APPLIED COMPUTATIONAL ELECTROMAGNETICS SOCIETY JOURNAL

October 2013
Vol. 28 No. 10
ISSN 1054-4887

The ACES Journal is abstracted in INSPEC, in Engineering Index, DTIC, Science Citation Index Expanded, the Research Alert, and to Current Contents/Engineering, Computing & Technology.

The illustrations on the front cover have been obtained from the research groups at the Department of Electrical Engineering, The University of Mississippi.

THE APPLIED COMPUTATIONAL ELECTROMAGNETICS SOCIETY
http://www.aces-society.org

EDITOR-IN-CHIEF

Atef Elsherbeni
University of Mississippi, EE Dept.
University, MS 38677, USA

ASSOCIATE EDITORS-IN-CHIEF

Sami Barmada
University of Pisa. EE Dept.
Pisa, Italy, 56126

Fan Yang
University of Mississippi, EE Dept.
University, MS 38677, USA

Mohamed Bakr
McMaster University, ECE Dept.
Hamilton, ON, L8S 4K1, Canada

Yasushi Kanai
Niigata Inst. of Technology
Kashiwazaki, Japan

Mohammed Hadi
Kuwait University, EE Dept.
Safat, Kuwait

Mohamed Abouzahra
MIT Lincoln Laboratory
Lexington, MA, USA

Ozlem Kilic
Catholic University of America
Washington DC, 20064, USA

Alistair Duffy
De Montfort University
Leicester, UK

Levent Gurel
Bilkent University
Ankara, Turkey

EDITORIAL ASSISTANTS

Matthew J. Inman
University of Mississippi, EE Dept.
University, MS 38677, USA

Mohamed Al Sharkawy
Arab Academy for Science and
Technology, ECE Dept. Alexandria,
Egypt

EMERITUS EDITORS-IN-CHIEF

Duncan C. Baker
EE Dept. U. of Pretoria
0002 Pretoria, South Africa

Allen Glisson
University of Mississippi, EE Dept.
University, MS 38677, USA

David E. Stein
USAF Scientific Advisory Board
Washington, DC 20330, USA

Robert M. Bevensee
Box 812
Alamo, CA 94507-0516, USA

Ahmed Kishk
University of Mississippi, EE Dept.
University, MS 38677, USA

EMERITUS ASSOCIATE EDITORS-IN-CHIEF

Alexander Yakovlev
University of Mississippi, EE Dept.
University, MS 38677, USA

Erdem Topsakal
Mississippi State University, EE Dept.
Mississippi State, MS 39762, USA

EMERITUS EDITORIAL ASSISTANTS

Khaled ElMaghoub
University of Mississippi, EE Dept.
University, MS 38677, USA

Anne Graham
University of Mississippi, EE Dept.
University, MS 38677, USA

Christina Bonnington
University of Mississippi, EE Dept.
University, MS 38677, USA

OCTOBER 2013 REVIEWERS

Ahmed Abdelrahman
Mohamed Abouzahra
Mohamed Al-Sharkaway
Guido Ala
Ercument Arvas
Ivan Bonev
Vedula Chakravarthy
Jiefu Chen
Daniel De Zutter
Gerald DeJean
Satya Dubey
Abdel Kader Hamid
Park Hyun Ho
Darko Kajfez
Yasushi Kanai
Michiko Kuroda
Sohrab Majidifar
Hend Malhat
Manoj Meshram
Claudio Montiel
Masoud Movahhedi
Arash Nejadpak
Pei Cheng Ooi
Zhen Peng
Andrew Peterson
Alain Reineix
Miao Sui
Hui Wang
Donald Wilton
John Young
Kezhong Zhao

THE APPLIED COMPUTATIONAL ELECTROMAGNETICS SOCIETY

JOURNAL

Vol. 28 No. 10 October 2013

TABLE OF CONTENTS

© 2013, The Applied Computational Electromagnetics Society

High-order Treatment of Junctions and Edge Singularities with the Locally-corrected Nyström Method

M. M. Bibby and A. F. Peterson

School of Electrical and Computer Engineering
Georgia Institute of Technology, Atlanta, GA, 30332-0250, USA
mbibby@ece.gatech.edu, peterson@ece.gatech.edu

***Abstract*–** High order techniques are known to be effective for the electromagnetic analysis of smooth structures. In the following, high order representations developed for the current density at edges and junctions are incorporated into the locally-corrected Nyström method. Conducting structures used for purposes of illustration include a strip, a structure with three fins and a junction, and a hexagonal cylinder. Results suggest that the accuracy of the numerical results obtained with the new approach is comparable to that obtained for problems with smooth surfaces.

***Index Terms*–**Edge singularities, high order representations, junction conditions, and singular basis functions.

I. INTRODUCTION

High-order numerical techniques are those in which the representation of the primary unknown is usually in terms of a polynomial of degree $p \geq 2$ and the convergence rate of the solution is much faster than $O(h^2)$, where h is the nominal cell dimension. These techniques have been effective for obtaining high accuracy and rapid convergence in numerical solutions of integral equations for electromagnetics [1-3], at least for smooth structures. Recent publications report a method-of-moments (MoM) procedure that permits similar improvement in accuracy for 2D structures with edges where the current density or charge density exhibits a singularity [4-5]. That approach used a high order representation containing appropriate fractional powers of polynomial terms in the cells adjacent to an edge where a current singularity occurs. For those structures, the rate of decrease in the error improves with reduced cell sizes as either the basis function or the representation order increases. In the following, a similar procedure is incorporated into the locally-corrected Nyström (LCN) method.

In Nyström approaches, the representation of the unknown quantity is provided indirectly by a quadrature rule. Degrees of freedom such as the fractional polynomial powers needed for edge singularities can be obtained by the use of quadrature rules specifically created to incorporate those terms. Extensions of the LCN for the special case of a knife-edge singularity were previously proposed by Gedney et al. [6], Gedney [7], and Tong and Chew [8]. The present work differs in that it is applicable to corners of any angle, and it incorporates quadrature rules that can integrate multiple singular terms at each edge in order to achieve true high order behavior. Results indicate that as the order of the representation for the current density increases, the accuracy of the solution improves at the same rates observed for smooth geometries.

The LCN method is usually implemented without imposing any condition on the continuity of the current density representation across cell boundaries. Consequently, one might question the extent to which the LCN results near a junction between three or more cells (such as the "fin" structure in Fig. 1) satisfy Kirchhoff's current law (KCL). In fact, high order behavior is not obtained unless the current density is modeled to the same accuracy level everywhere. In the following, an approach similar to that used at edges is applied to model the current density in cells adjacent to junctions.

Submitted On: Feb. 15, 2013
Accepted On: Aug. 29, 2013

1054-4887 © 2013 ACES

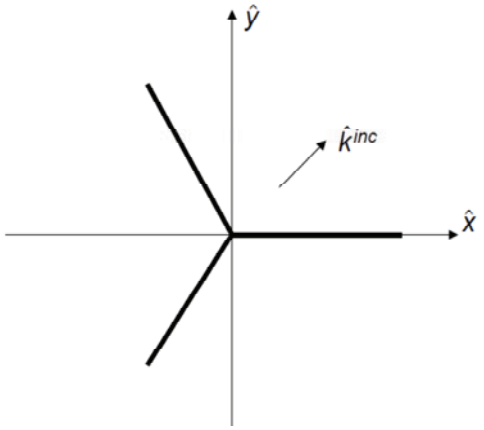

Fig. 1. A perfectly conducting structure, consisting of 3 fins and a junction. The structure is infinite in the *z* direction, and the angle between adjacent fins is 120 degrees.

A preliminary description of the treatment of edges, with examples that differ from those presented below, was given in [9] and [10]. The treatment of junctions using the MoM and LCN was briefly discussed in [11]. An extensive list of references on the treatment of edge singularities was included in [4]; a similarly extensive list of references on the LCN approach may be found in [10].

II. SINGULAR REPRESENTATION FOR EDGES

A solution for the surface current density induced on an infinite wedge is developed in [12]. Based on those results, a general asymptotic expression for the current density as a function of ρ on the face of a wedge (Fig. 2) with interior angle α, near the tip ($\rho = 0$), can be written for the transverse magnetic (TM)-to-*z* case as,

$$J_z : \sum_{m=0}^{\infty}\sum_{n=1}^{\infty} c_{mn}\rho^{2m+\upsilon_n-1} \tag{1}$$

where a cylindrical coordinate system (ρ, ϕ, z) is employed. In equation (1),

$$\upsilon_n = \frac{n\pi}{(2\pi-\alpha)}, \quad n = 1,\ 2,\ 3,\ \ldots \tag{2}$$

A similar expression for the transverse electric (TE)-to-*z* case is,

$$J_\rho : \sum_{m=0}^{\infty}\sum_{n=0}^{\infty} d_{mn}\rho^{2m+\upsilon_n} \tag{3}$$

where υ_n is defined as,

$$\upsilon_n = \frac{n\pi}{(2\pi-\alpha)}, \quad n = 0,\ 1,\ 2,\ \ldots \tag{4}$$

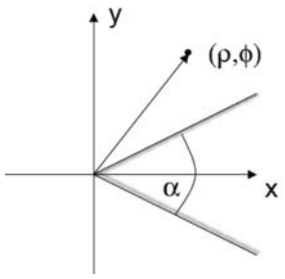

Fig. 2. Wedge tip geometry.

To properly model singular edge currents in the context of the MoM, reference [4] proposed basis functions for use in cells adjacent to geometric corners. For cells that are not adjacent to a corner of the contour, a Legendre expansion of order *q* is employed. In the corner cells, the representation is augmented by including some number of terms with non-integer exponents from equations (1) or (3). Empirical evidence [4-5] suggests that the singular behavior can be confined to single edge cells if those cells are sufficiently large (perhaps a quarter wavelength in dimension). Since the singular representation in equations (1) or (3) is sufficient only in a small neighborhood of the edge, for large cells it is necessary to mix regular (polynomial) terms with the singular terms to properly represent currents throughout that cell. The authors concluded in [5] that if *q* polynomial terms are used in non-corner cells, the local error near the corner can be reduced to the level of the error produced in the cells away from the corner by combining *q* regular terms and *q* singular terms in corner cells that are twice the size of the non-corner cells. The latter approach is used in the following to create quadrature rules that can be used within a Nyström discretization, and also as the basis functions used for local corrections.

Examples to follow will employ structures with interior wedge angles of 0 and 120 degrees. From equation (1), the transverse-magnetic-to-*z* (TM) current near 0 degree angle involves exponents, in increasing order, of

$$\left\{\frac{-1}{2},\ 0,\ \frac{1}{2},\ 1,\ \frac{3}{2},\ 2,\ \frac{5}{2},\ 3,\ \ldots\right\}. \tag{5}$$

For the transverse-electric-to-z (TE) case, the set of exponents for a 0 degree angle obtained from equation (3) is

$$\left\{0,\ \frac{1}{2},\ 1,\ \frac{3}{2},\ 2,\ \frac{5}{2},\ 3,\ \frac{7}{2},\ \ldots\right\}. \tag{6}$$

For the 120 degree case, TM currents require the exponents

$$\left\{\frac{-1}{4},\ \frac{1}{2},\ \frac{5}{4},\ \frac{7}{4},\ 2,\ \frac{5}{2},\ \frac{11}{4},\ \frac{13}{4},\ \ldots\right\}, \tag{7}$$

while TE currents require

$$\left\{0,\ \frac{3}{4},\ \frac{3}{2},\ 2,\ \frac{9}{4},\ \frac{11}{4},\ 3,\ \frac{7}{2},\ \ldots\right\}. \tag{8}$$

However, using the approach of [5], the representation for currents at an edge incorporates an equal number of singular terms and regular terms. When integer exponents occur in the series, and duplicate the regular terms in the basis set, we incorporate additional fractional exponents from the series in their place. Table I summarizes the suggested degrees of freedom for a 0 degree TM corner (a knife edge).

Table I: Exponents of the degrees of freedom used for a given order, for cells near a 0 degree corner (TM case). The corner cells involve twice as many degrees of freedom as the other cells, but are to be twice as large.

Order of representation q	Exponents used in non-corner cells	Exponents used in corner cells
1	0	–1/2, 0
2	0, 1	–1/2, 0, 1/2, 1
3	0, 1, 2	–1/2, 0, 1/2, 1, 3/2, 2
4	0, 1, 2, 3	–1/2, 0, 1/2, 1, 3/2, 2, 5/2, 3
5	0, 1, 2, 3, 4	–1/2, 0, 1/2, 1, 3/2, 2, 5/2, 3, 7/2, 4

Terms with the exponents in Table I are used to construct a hierarchical basis set as described in [4] and [10]. As an example, the "order-2" representations in the end cells for the 0 degree TM corner is obtained using the 4 functions

$$\left\{u-\frac{3}{2}u^{1/2}+\frac{3}{5}-\frac{1}{20}u^{-1/2},\ u-\frac{4}{3}u^{1/2}+\frac{2}{5},\ u-\frac{5}{6}u^{1/2},\ u\right\}, \tag{9}$$

where a local coordinate $0 \le u \le 1$ is employed with $u = 0$ at the corner, and a basic Gram-Schmidt procedure is used to produce an orthogonal set. (Since the $u^{-1/2}$ term cannot be integrated with itself, here basis functions incorporating the four terms are orthogonalized in the reverse order they appear in equation (5) to produce the set of equation (9). In the non-edge cells, an order-2 representation is obtained using the constant and linear Legendre polynomials,

$$\{1,\ 2u-1\} \tag{10}$$

to represent the currents.

III. LCN IMPLEMENTATION

The LCN approach was proposed in [1] and is described in many publications, including [10], so we omit a review of the technique. Reference [10] also describes the details of how we treat the electric-field integral equation (EFIE) and magnetic field integral equation (MFIE), including the Green's function singularities.

Two important aspects of an LCN approach necessary to implement the singular representation described above are a set of basis functions that can be used to "locally correct" the kernel of the integral operator when the sources reside in a cell containing a corner singularity, and a family of quadrature rules that can integrate the singular functions to high accuracy. The basis functions are obtained by combining the degrees of freedom associated with a particular wedge angle with polynomials, and orthogonalizing those terms using a Gram-Schmidt process, as described above for a 0 degree angle and discussed in [4] and [10] in more generality. Quadrature rules that can integrate the singular functions are usually not readily available, and for this work are synthesized from an expanded set of appropriate degrees of freedom, using a procedure similar to that of [13], which is also reviewed and explained in [10]. Several of these rules are provided below. Since a q-point quadrature rule can exactly integrate $2q$ independent terms, additional degrees of freedom from the family of terms for the relevant corner angle were employed in the generation of the quadrature rules. As in the non-singular case, when the quadrature rules are related to the basis functions in this manner, the accuracy of the overall LCN analysis will be limited by the basis functions used within the local correction procedure, and not by the quadrature rules.

The region over which the basis functions described above are used to "locally correct" the

singular kernel is the *local correction footprint*. In this work, local corrections are used whenever the observer or test point is within 0.15 λ of any part of the source cell, where λ denotes the wavelength. Otherwise, the actual Green's function is sampled in accordance with the classical Nyström procedure. The 0.15 λ footprint was selected after extensive numerical experiments. A more sophisticated scheme would adapt the size of the local correction footprint as needed to maintain a smooth transition between the synthetic and actual kernels.

To demonstrate the accuracy of the results that follow, we solve a 2:1 over-determined system of equations using a least-square algorithm [2], and calculate the normalized residual error (*NRE*) for the result from the residual of the over-determined system, as originally suggested by Bunch and Grow [14-15]. The *NRE* is defined for the TM-to-*z* electric-field integral equation (EFIE) on a perfectly conducting target as in [2],

$$NRE = \frac{\sqrt{\int \left| E_z^{inc} + E_z^{s} \right|^2 dt}}{\sqrt{\int \left| E_z^{inc} \right|_{\max}^2 dt}} \cong \frac{\sqrt{\sum_{i=1}^{N_{tp}} w_i \left| E_z^{inc}(t_i) + E_z^{s}(t_i) \right|^2}}{\left| E_z^{inc} \right|_{\max} \sqrt{\sum_{i=1}^{N_{tp}} w_i}} \quad (11)$$

where $\{t_i\}$ and $\{w_i\}$ denote Gauss-Legendre quadrature nodes and weights. N_{tp} is the total number of points included in the measure. For a global measure of *NRE*, N_{tp} is the total number of test points on the target. Alternatively, the *NRE* can be determined on a cell-by-cell basis; in that case equation (11) is computed for each cell with N_{tp} equal to the number of test points within that cell. As noted above, the number of test points in a corner cell is twice the number of test points in other cells not adjacent to a corner. For the MFIE or the transverse-electric (TE) EFIE, equation (11) is modified in an obvious way to implement the appropriate residual.

LCN unknowns are the samples of current density at the nodes of a quadrature rule. Since the integral equation is enforced at twice as many match points as unknowns, the test points are not the nodes defining the unknown samples. In this study, test points are the nodes of a Gauss-Legendre rule with the appropriate number of points, even in the end cells where a different quadrature rule is used to define the LCN discretization. Appendix A describes an interpolation approach used to distribute the weights associated with the identity operator in the MFIE.

The rate at which the global *NRE* decreases as a function of cell size or number of unknowns can be used to judge the extent to which high order behavior is exhibited by the results. Consider two results, the first yielding NRE_1 with N_1 unknowns, and the second exhibiting NRE_2 with N_2 unknowns. The incremental slope of the associated error curve may be obtained from successive results using,

$$Slope_q = \frac{\log_{10}(NRE_2) - \log_{10}(NRE_1)}{\log_{10}(N_2) - \log_{10}(N_1)} \quad (12)$$

where the subscript serves as a reminder that the expansions are of order q. For scatterers with smooth surfaces [2], and targets with edges treated by the MoM approaches of [4-5], values of equation (12) often approximate integers as N increases. Similar behavior is observed with the LCN results.

We use an over-determined system of equations to compute the *NRE* and its slope and estimate the accuracy of a result. If the error estimate is not needed, LCN results can be obtained more efficiently with square systems of equations [10].

IV. EXAMPLE: SCATTERING FROM A CONDUCTING STRIP

To illustrate the approach, consider the scattering of a uniform TM plane wave from a flat, perfectly conducting strip with width of 7 wavelengths. The numerical solution is obtained by an application of the LCN approach to the EFIE. Gauss-Legendre quadrature rules are used within the LCN process for interior cells, while the special rules generated for knife-edge corners (α = 0) are used in end cells. These quadrature rules for q = 1–3 are given in [10]. End cells are twice the dimension of other cells and use twice as many degrees of freedom (special quadrature rules for Nyström sampling and a number of singular terms equal to the number of regular terms in the functions used for the local corrections).

A high accuracy reference solution for the induced current J_z^{exact} on a conducting strip can be obtained in terms of an eigenfunction series of Mathieu functions [16]. To assess the accuracy of

the current density, Fig. 3 shows the error as a function of position on a strip modeled with 26 cells for two cases (the results are actually the superposition of the currents on either side of the strip). In the first case (the upper plots in Fig. 3), the end cell discretizations are obtained from the conventional LCN quadrature (Gauss-Legendre) rules, with the local correction provided by Legendre polynomial functions. In other words, no special edge treatment is applied. In the second case, the representation in the end cells is provided using quadrature rules that can integrate the mixture of exponents appearing in equation (5), and the local corrections are obtained using functions such as those in equation (9).

Figure 3 shows that if the conventional LCN representation is used in the end cells, there is no significant improvement in the results beyond order $q = 2$. However, when the singular representation is used in the end cells, there is a continuous improvement in the accuracy of the results as q increases, and the average error has improved by a factor of 10^{-9} for $q = 8$. We define the global normalized error in the current density (*NEJ*) as,

$$NEJ = \frac{\left\| J_z^{exact} - J_z^{num} \right\|}{\left| 2\hat{n} \times \bar{H}^{inc} \right|_{\max}} = \frac{\sqrt{\frac{1}{N_{tp}} \sum_{i=1}^{N_{tp}} w_i \left| J_z^{exact}(t_i) - J_z^{num}(t_i) \right|^2}}{\left| 2\hat{n} \times \bar{H}^{inc} \right|_{\max}} \quad (13)$$

where $\{t_i\}$ and $\{w_i\}$ denote Gauss-Legendre quadrature nodes and weights. Figure 4 shows the global *NEJ* as a function of the number of unknowns and the order q. As expected for higher order representations, these curves decrease with a steeper slope as q increases, despite the singularities at the strip ends. Although the slopes become somewhat erratic for higher values of q, they appear to approach integer values for lower q values and generally decrease as q increases.

Figure 5 shows results for the same strip when illuminated by a normally-incident TE wave, obtained from the LCN solution of the EFIE. The singular representations employed for the TE polarization are based on the exponents in equation (6), and do not include the $u^{-1/2}$ term used for the TM case. The basis functions and quadrature rules may be found in [10] up to $q = 3$. Although the edge singularity is weaker in the TE case and the current density is bounded, a polynomial representation cannot reduce the error by more than a factor of 10^{-2}. However, the singular expansions facilitate a continuous improvement as the order increases, and reduce the average error by 10^{-8} for $q = 8$.

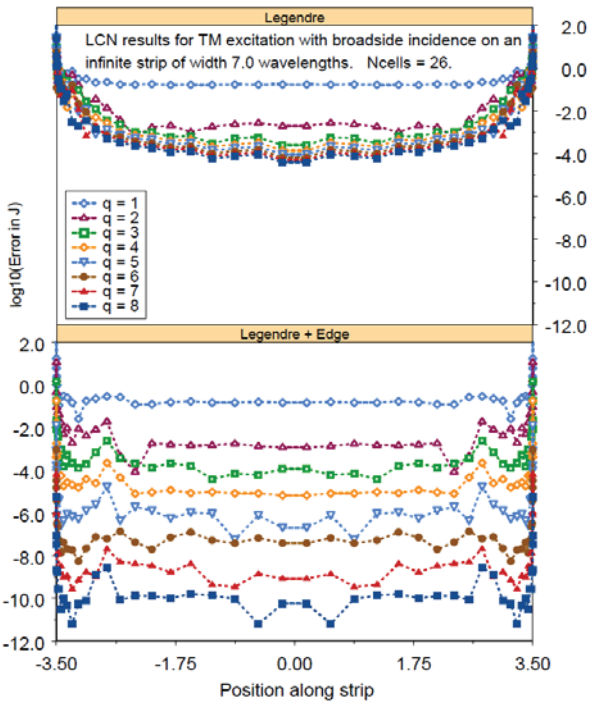

Fig. 3. Error in the current density as a function of position and order q, for a perfectly conducting 71 strip illuminated by a normally-incident TM plane wave. 26 cells are used to model the strip, with the end cells twice as large as the others. The upper figure shows the error when the end cells are treated with the same representation used in other cells; the lower figure shows the error when the singular representation is used in the end cells.

V. EXAMPLE: SCATTERING FROM A CONDUCTING 3-FIN STRUCTURE

Figure 1 shows a "3-fin" structure consisting of three perfectly conducting strips connected at the origin. For TE excitation, current is expected to flow across the junction between the strips. Since the LCN representation does not impose explicit current continuity between junctions, this structure provides a test bed for the satisfaction of Kirchhoff's current law at the junction. In fact, both the open ends of the strips and the junction ends of the strips must be treated specially to obtain high order accuracy in this case. The 3-fin will be treated using the EFIE.

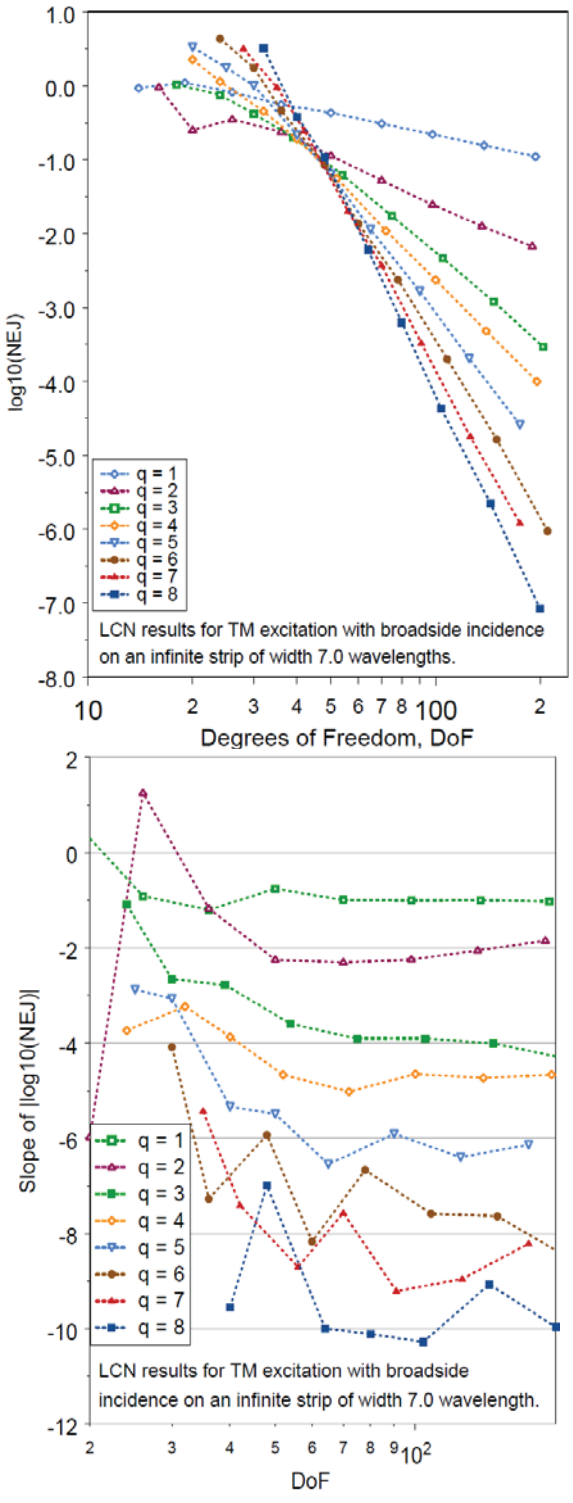

Fig. 4. (a) Global normalized error in the current density, *NEJ*, as a function of degrees of freedom and representation order q, for a perfectly conducting 7 λ strip illuminated by a normally-incident plane TM wave and (b) slopes of the *NEJ* curves in (a).

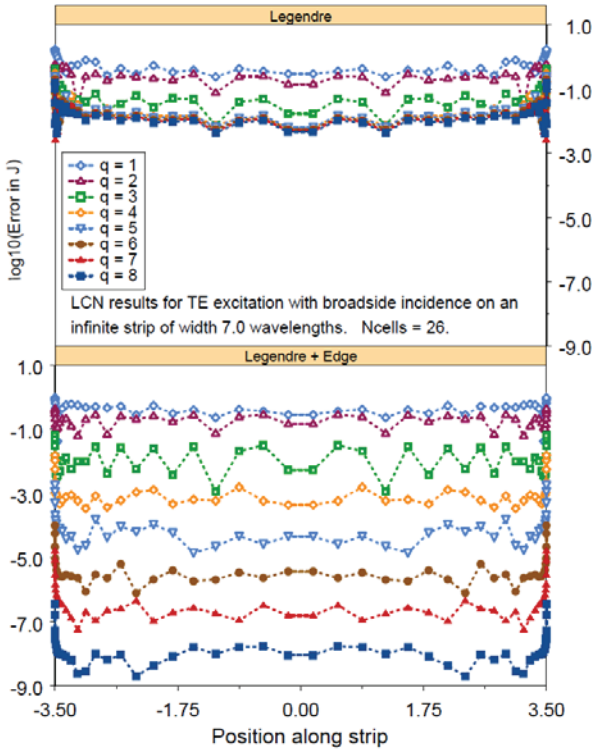

Fig. 5. Error in the TE current density as a function of position and q, for a perfectly conducting 7 λ strip illuminated by a normally-incident plane wave. 26 cells are used to model the strip, with the end cells twice as large as the others. The upper figure shows the error when the end cells are treated with the same representation used in other cells; the lower figure shows the error when the singular representation is used in the end cells.

Suppose that each strip of the 3-fin is 7 λ in width, and each is divided into cells with the end cells and junction cells twice as large as the others. The same singular representations are used in the end cells as used for the single TE strip in the preceding section; representations in the junction cells are based on terms with exponents in equation (8) from the wedge solution for a 120 degree interior angle. Orthogonal basis functions used for the local corrections for the 120 degree TE case are given by the set in Table II.

In Table II, functions B_1 and B_2 are used for local corrections in cells adjacent to the fin junction for q = 1. B_1 through B_4 are used for q = 2, etc. Table III presents quadrature rules for implementing the Nyström discretization in the junction cells, assuming u = 0 denotes the corner.

Since the 3-fin structure does not have an exact solution, we use the *NRE* to judge the relative accuracy of the results. Figure 6 shows the *NRE* as a function of position along one of the three fins of the structure, for four situations. In the first (upper plot), a conventional nonsingular representation is used in all cells of the model. In the second, a conventional representation is used in all cells except the edge cells, which are treated using a singular representation for a knife edge. In the third, a conventional representation is used in all cells except the junction cells, where the singular representation for a 120 degree wedge is employed. Finally, the fourth case (bottom plot) employs the singular representation for the knife-edge in the edge cells and the singular representation for the 120 degree wedge in the junction cells.

Table II. Basis functions for 120 degrees, TE case.

$$B_1 = u^{3/4}$$

$$B_2 = u^{3/4} - \frac{7}{10}$$

$$B_3 = u^{3/4} - \frac{1}{5} - \frac{13}{14}u^{3/2}$$

$$B_4 = u^{3/4} - \frac{1}{26} + \frac{4}{7}u^{3/2} - \frac{99}{65}u$$

$$B_5 = u^{3/4} - \frac{8}{429} + \frac{16}{11}u^{3/2} - \frac{648}{325}u - \frac{2584}{5775}u^{9/4}$$

$$B_6 = u^{3/4} - \frac{5}{528} + \frac{95}{22}u^{3/2} - \frac{1377}{520}u + \frac{323}{105}u^{9/4} - \frac{6561}{1144}u^2$$

From Fig. 6, it is apparent that the overall accuracy does not improve substantially beyond $q = 2$ unless the edge cells employ the singular representation, and that true high order behavior requires that the junction cells also use the enhanced treatment. Figure 7 shows the global *NRE* as a function of the total number of degrees of freedom in the representation, when both edge cells and junction cells employ the singular representations. As in the previous cases, the *NRE* data show increasing slopes with order q and the slopes approximate integer values.

Table III. Weights and nodes associated with the generalized quadrature rule for the TE case, wedge angle = 120 degrees.

nodes	u_i	w_i
2	0.13672511222849918533	0.37951320305834680660
(q=1)	0.72219266699689013444	0.62048679694165319340
4	0.01926255761438994475	0.06029440891031772626
(q=2)	0.16721235939430592191	0.25171152151926467369
	0.51263727731319399021	0.40879441442668019898
	0.88533792190675015565	0.27919965514373740106
6	0.00445775138948688208	0.01445955504231629716
(q=3)	0.04504111963567514576	0.07632091915597698975
	0.17358207080404601792	0.18539035944199733131
	0.41224567448376463466	0.28274134250464589399
	0.70683287748179531992	0.28508835965386458933
	0.93749552578180260021	0.15599946420119889846

At the junction of the 3-fin, the currents flowing into the center point should add to zero, to satisfy Kirchhoff's current law for the TE case. Figure 8 shows the sum of the currents at the center, as a function of degrees of freedom (as the cells are refined) and order q, when both edge cells and junction cells employ the singular representations. From the figure, it is apparent that the satisfaction of KCL improves with increases in both mesh density and in the order q.

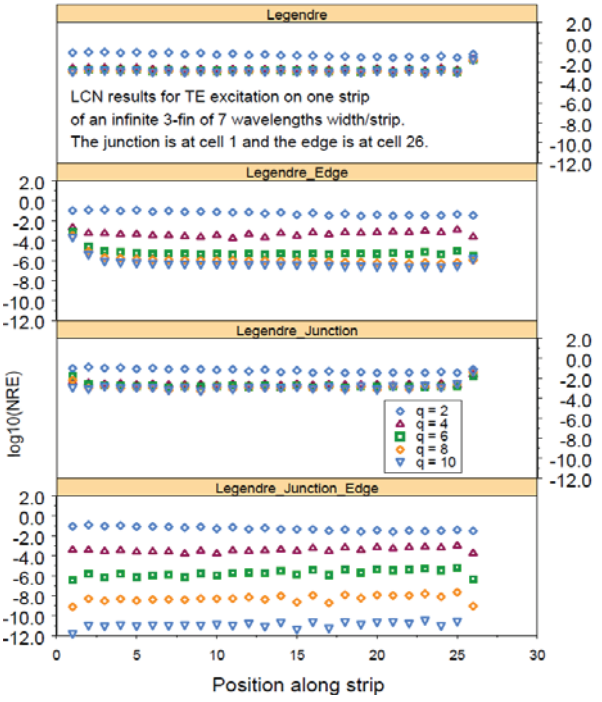

Fig. 6. Local *NRE* results for one fin of the 3-fin structure when illuminated by a TE wave propagating 20 degrees from the x-axis, for four different combinations of representations.

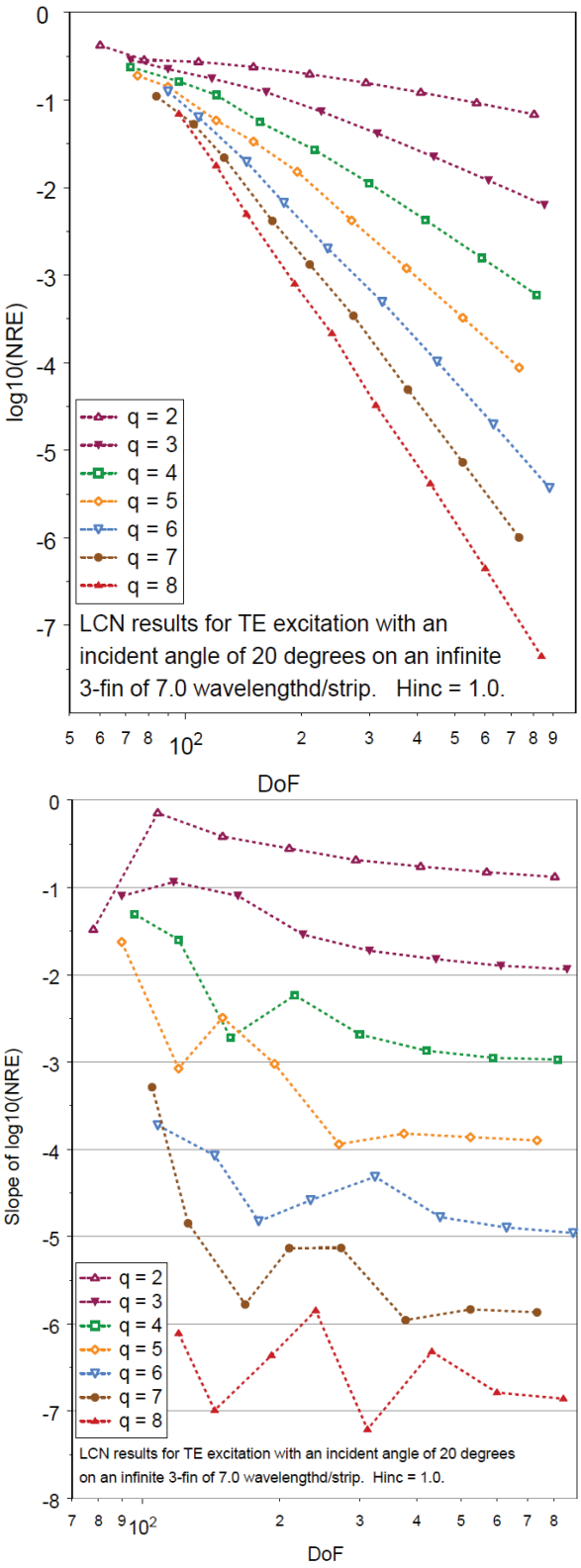

Fig. 7. Global NRE results for the 3-fin when illuminated by a TE wave propagating 20 degrees from the x-axis.

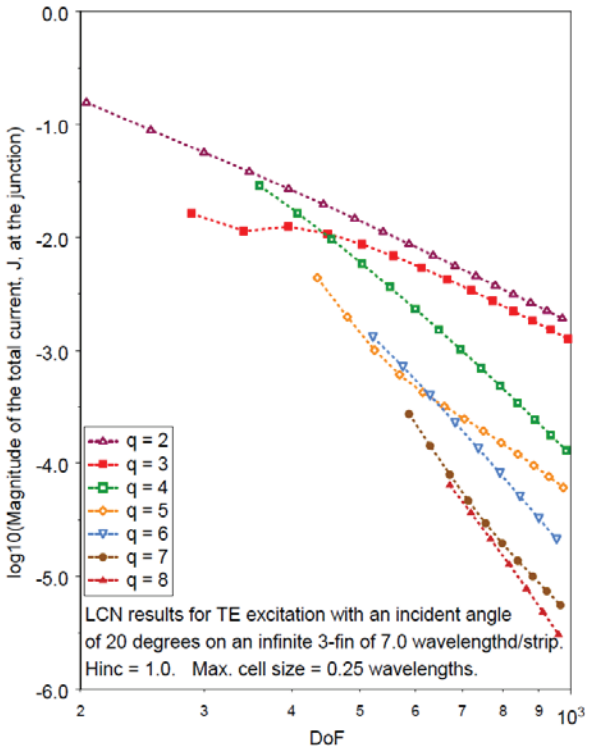

Fig. 8. Sum of the junction currents for the 3-fin, illustrating the extent to which KCL is satisfied as cells are refined for various representation orders q.

In summary, study of the 3-fin structure suggests that junction continuity can be ensured to high order only if the proper junction behavior is incorporated into the representation in the cells at the junction. Treatment using regular cells on either side of a junction will suffice only in the case of two coplanar cells. On the other hand, if it is desired to insulate two cells from each other (an infinitesimal gap), end conditions equivalent to those used at the ends of a TE strip will be required to model that behavior to high order.

VI. EXAMPLE: SCATTERING FROM A HEXAGONAL CONDUCTING CYLINDER

Several examples of the LCN treatment of conducting cylinders with edges are illustrated in [10], including cylinders with triangular and square cross sections. As a final example, we consider the LCN solution of the MFIE for a perfectly conducting hexagonal cylinder, when each face of the cylinder is 3.5 λ in width, and a TM wave is incident symmetrically upon one of

the corners between faces. The corners of the hexagon exhibit 120 degree wedge angles, and orthogonal basis functions used for the local corrections for the 120 degree TM case are given by the set in Table IV. In Table IV, functions B_1 and B_2 are used for local corrections for $q = 1$, B_1 through B_4 are used for $q = 2$, etc. Table V presents quadrature rules for implementing the Nyström discretization in the edge cells, assuming $u = 0$ is the corner.

Table IV: Basis functions for 120 degrees, TM case.

$$B_1 = u^{-1/4}$$

$$B_2 = u^{-1/4} - \frac{3}{2}$$

$$B_3 = u^{-1/4} - 3 + \frac{5}{2}u^{1/2}$$

$$B_4 = u^{-1/4} - \frac{9}{2} + 10u^{1/2} - 7u$$

$$B_5 = u^{-1/4} - \frac{216}{35} + \frac{200}{7}u^{1/2} - 72u + \frac{1716}{35}u^{5/4}$$

$$B_6 = u^{-1/4} - \frac{2187}{280} + \frac{825}{14}u^{1/2} - \frac{1053}{4}u + \frac{1287}{5}u^{5/4} - \frac{187}{4}u^2$$

Table V. Weights and nodes associated with the generalized quadrature rule for the TM case, wedge angle = 120 degrees.

nodes	u_i	w_i
2	0.06048307438790956835	0.23887432757190171923
(q=1)	0.63793952019398706980	0.76112567242809828077
4	0.00555344256643894865	0.02400445850565570990
(q=2)	0.10317714071097559074	0.20343338712212968209
	0.43540065702647568767	0.43755946702900373626
	0.86077917841276450835	0.33500268734321087175
6	0.00101938730710741485	0.00451930945029498980
(q=3)	0.02223334550546676504	0.04851941270439041254
	0.12189892349088265974	0.16084006407326768690
	0.34991308210221298855	0.28863159936577654207
	0.66542732067496877426	0.31703773119016205046
	0.92738778900338639928	0.18045188321610831823

Figure 9 shows the global NRE data for this problem, while Fig. 10 shows the NRE as a function of position for various values of order q. On each face of the hexagonal cylinder, the error is relatively uniform, and improves with increasing q. A plot of the magnitude of the current density on three of the six faces of the hexagonal cylinder is shown in Fig. 11.

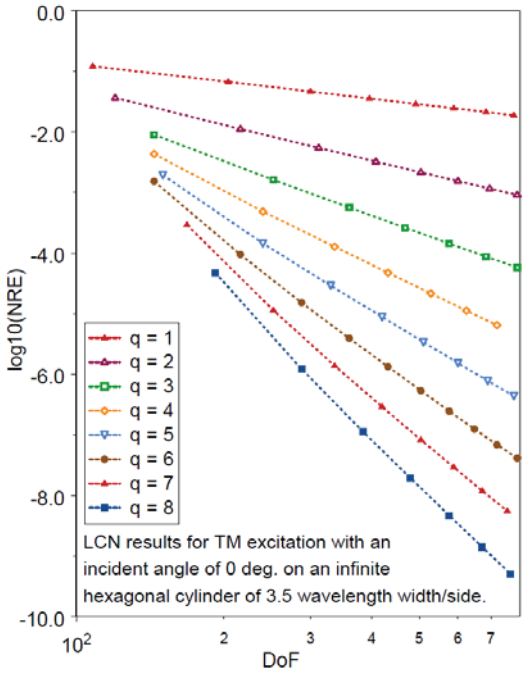

Fig. 9. Global NRE for the hexagonal cylinder, obtained by solving the TM MFIE with LCN.

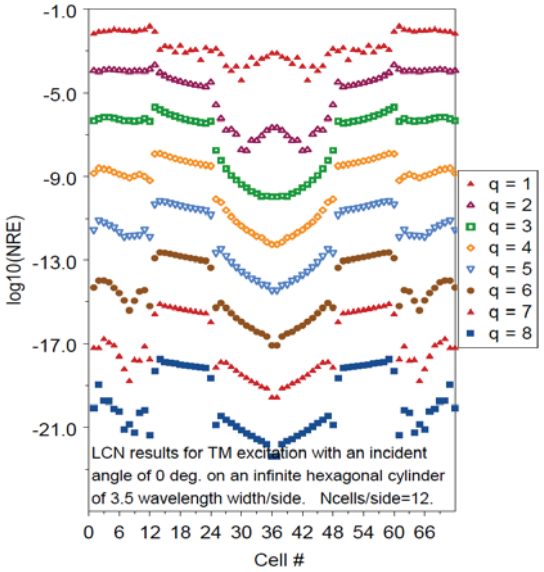

Fig. 10. Local NRE for the hexagonal cylinder example.

VII. CONCLUSIONS

A technique for representing edge and junction effects has been incorporated into the locally-corrected Nyström method. This procedure is shown to produce high order behavior for problems with singularities in the current or charge density at bends or corners. Results having

more than 8 digits of agreement with exact solutions were obtained for the strip examples. Current and charge must also be properly modeled at junctions to maintain high accuracy. For the TE case, where current flows across a junction, as the accuracy of the results improves with representation order the extent to which Kirchhoff's current law is satisfied also improves.

The treatment of more complicated (non-symmetric) junctions remains a topic for future work. It is expected that it may be necessary to incorporate fractional exponents for the full set of wedge angles to properly model the currents in that situation.

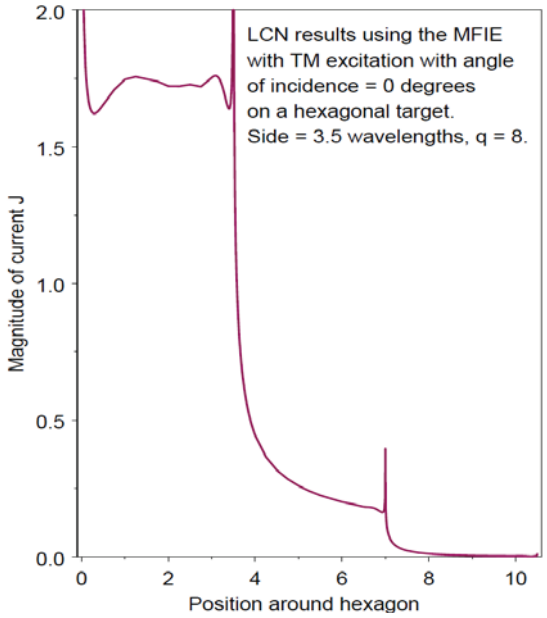

Fig. 11. LCN solution for the current magnitude obtained from the MFIE for a perfectly conducting hexagonal cylinder, when each face of the cylinder is 3.5l in width, and an TM wave with unit H_z is incident symmetrically upon one of the corners between faces. The solution for q = 8 is shown over one half of the computational domain.

APPENDIX A. INTERPOLATION TECHNIQUE USED TO IMPLEMENT IDENTITY OPERATORS WHEN OBSERVATION POINTS DO NOT COINCIDE WITH QUADRATURE NODES

When the observation points coincide with quadrature nodes, the Nyström treatment of equations such as the MFIE that have an identity-type operator is obvious: the unknown samples become part of the discrete equation. When observation points do not coincide with quadrature nodes, the basis set used to implement local corrections may be used to provide an interpolation. Suppose that the current density $J(u)$ is defined at samples $\{u_1, u_2, \ldots, u_p\}$. We seek the coefficients $\{\alpha_i\}$ in the expression

$$J(u_0) = \alpha_1 J(u_1) + \alpha_2 J(u_2) + \mathsf{L} + \alpha_p J(u_p) = \mathbf{s}^T \begin{bmatrix} \alpha_1 \\ \alpha_2 \\ \mathsf{M} \\ \alpha_p \end{bmatrix} \quad \text{(A.1)}$$

where

$$\mathbf{s}^T = \begin{bmatrix} J(u_1) & J(u_2) & \mathsf{L} & J(u_p) \end{bmatrix}. \quad \text{(A.2)}$$

If the samples $\{J(u_i)\}$ are known, we obtain a set of coefficients $\{\beta_i\}$ from the system,

$$\mathbf{Mb} = \begin{bmatrix} B_1(u_1) & B_2(u_1) & \mathsf{L} & B_p(u_1) \\ B_1(u_2) & B_2(u_2) & & B_p(u_2) \\ \mathsf{M} & & & \mathsf{M} \\ B_1(u_p) & B_2(u_p) & \mathsf{L} & B_p(u_p) \end{bmatrix} \begin{bmatrix} \beta_1 \\ \beta_2 \\ \mathsf{M} \\ \beta_p \end{bmatrix} = \mathbf{s}, \quad \text{(A.3)}$$

where $\{B_i\}$ are the basis functions. The matrix operator $\mathbf{M}$ used on the left-hand side of (A.3) is the same system used in the local correction process for the cell in question [10]. Although the $\{J(u_i)\}$ are not known, in principle we can use the coefficients $\{\beta_i\}$ to determine,

$$J(u_0) = \sum_{i=1}^{p} \beta_i B_i(u_0) = \mathbf{b}^T \begin{bmatrix} B_1(u_0) \\ B_2(u_0) \\ \vdots \\ B_p(u_0) \end{bmatrix} = \mathbf{s}^T \mathbf{M}^{-T} \begin{bmatrix} B_1(u_0) \\ B_2(u_0) \\ \vdots \\ B_p(u_0) \end{bmatrix} \quad \text{(A.4)}$$

where we solved equation (A.3) to obtain $\mathbf{b} = \mathbf{M}^{-1}\mathbf{s}$. By equating (A.1) and (A.4), we obtain the coefficients in equation (A.1) as,

$$\begin{bmatrix} \alpha_1 \\ \alpha_2 \\ \mathsf{M} \\ \alpha_p \end{bmatrix} = \mathbf{M}^{-T} \begin{bmatrix} B_1(u_0) \\ B_2(u_0) \\ \mathsf{M} \\ B_p(u_0) \end{bmatrix}. \quad \text{(A.5)}$$

These coefficients $\{\alpha_i\}$ are the weights used to distribute the identity operator among the current density samples when the observation point u_0 is not in the set $\{u_1, u_2, \ldots, u_p\}$.

REFERENCES

[1] L. Canino, J. Ottusch, M. Stalzer, J. Visher, and S. Wandzura, "Numerical solution of the Helmholtz equation in 2D and 3D using a high-order Nyström discretization," *J. Comp. Physics* , vol. 146, pp. 627-663, 1998.

[2] M. Bibby and A. Peterson, "On the use of over-determined systems in the adaptive numerical solution of integral equations," *IEEE Trans. Antennas Propagat.*, vol. 53, pp. 2267-2273, July 2005.

[3] E. Klopf, N. Sekeljic, M. Illic, and B. Notaros, "Optimal modeling parameters for higher order MoM-SIE and FEM-MoM electromagnetic simulations," *IEEE Trans. Antennas Propagat*., vol. 60, pp. 2790-2801, June 2012.

[4] M. Bibby, A. Peterson, and C. Coldwell, "High order representations for singular currents at corners," *IEEE Trans. Antennas Propagat* ., vol. 56, pp. 2277-2287, August 2008.

[5] M. Bibby, A. Peterson, and C. Coldwell, "Optimum cell size for high order singular basis functions at geometric corners," *ACES Journal*, vol. 24, pp. 368-374, August 2009.

[6] S. Gedney, J. Ottusch, P. Petre, J. Visher, and S. Wandzura, "Efficient high order discretization schemes for integral equation methods," *Digest of the 1997 IEEE Antennas and Propagation Society International Symposium*, Montreal, PQ, pp. 1814-1817, July 1997.

[7] S. Gedney, "Application of the high-order Nyström scheme to the integral equation solution of electromagnetic interaction problems," *Proceedings of the IEEE International Symposium on Electromagnetic Compatibility* , Washington, DC, pp. 289-294, August 2000.

[8] M. Tong and W. Chew, "Nyström method with edge condition for electromagnetic scattering by 2D open structures," *Progress in Electromagnetic Research*, vol. 62, pp. 49-68, 2006.

[9] M. Bibby, A. Peterson, and C. Coldwell, "High-order treatment of corner singularities with the locally-corrected Nyström method," *Digest of the 2009 IEEE Antennas and Propagation Society International Symposium*, Charleston, SC, June 2009.

[10] A. Peterson and M. Bibby, *An Introduction to the Locally-Corrected Nyström Method*, San Rafael: Morgan & Claypool Synthesis Lectures, 2010.

[11] A. Peterson, M. Bibby, and C. Coldwell, "Satisfaction of end, continuity, and junction conditions by implicit and explicit subsectional Legendre expansions," *Proceedings of the 25 th Annual Review of Progress in Applied Computational Electromagnetics*, Monterey, CA, March 2009.

[12] R. Harrington, *Time Harmonic Electromagnetic Fields*, New York: McGraw-Hill, pp. 238-242, 1961.

[13] J. Ma, V. Rokhlin, and S. Wandzura, "Generalized Gaussian quadrature rules for systems of arbitrary functions," *SIAM J. Numer. Anal*., vol. 33, pp. 971-996, June 1996.

[14] K. Bunch and R. Grow, "Numerical aspects of the boundary residual method," *Int. J. Num. Modelling*, vol. 3, pp. 57-71, 1990.

[15] K. Bunch and R. Grow, "On the convergence of the method of moments, the boundary-residual method, and the point-matching method with a rigorously convergent formulation of the point matching method," *ACES Journal*, vol. 8, no. 2, pp. 188-202, 1993.

[16] J. Bowman, T. Senior, and P. Uslenghi, *Electromagnetic and Acoustic Scattering by Simple Shapes*, New York, Hemisphere Publishing, 1987.

Malcolm M. Bibby received the B.Eng. and Ph.D. degrees in Electrical Engineering from the University of Liverpool, in 1962 and 1965, respectively, and an MBA from the University of Chicago. He is currently an Adjunct Professor in ECE at Georgia Tech. He has been interested in the numerical aspects of antenna design and electromagnetics for more than 30 years.

Andrew F. Peterson received the B.S., M.S., and Ph.D. degrees in Electrical Engineering from the University of Illinois, Urbana-Champaign in 1982, 1983, and 1986 respectively. Since 1989, he has been a member of the faculty of the School of Electrical and Computer Engineering at the Georgia Institute of Technology, where he is now Professor and Associate Chair for Faculty Development. Within ACES, he has served at various times as a member of the Board of Directors, the Finance Committee Chair, the Publications Committee Chair, and the President. He also served as a technical co-chair for the 25th Annual Review of Progress in Applied Computational Electromagnetics (ACES 2009). He was elevated to ACES Fellow in 2008.

Minimizing The 3D Solenoidal Basis Set in Method of Moments Based Volume Integral Equation

A. Obi [1], R. Lemdiasov [2], and R. Ludwig [3]

[1] GE Global Research, Niskayuna, NY12309, USA
aghogho.obi@ge.com

[2] PhiHealth, Richardson, TX75075, USA
lemdiasov@gmail.com

[3] Department of Electrical and Computer Engineering
Worcester Polytechnic Institute, Worcester, MA01609, USA
ludwig@ece.wpi.edu

Abstract ─ A method for completely minimizing a 3D-solenoidal basis set, and identifying its linearly independent basis functions in method of moments (MoM) based volume integral equation (VIE) is presented. The method uses the connecting information of the geometric mesh and the properties of the 3D solenoidal basis function to remove the null space of the basis set. Consequently, the approach is not prone to numerical inaccuracies due to finite machine precision resulting from matrix manipulations. In addition, our method is not restricted to simply connected or contiguous mesh regions; it is applicable to a wide variety of complicated mesh regions featuring holes and voids. Finally, an expression for determining the minimum number of linearly independent solenoidal basis functions in a given tetrahedral mesh is presented.

Index Terms – Divergence-free, method of moments (MoM), and solenoidal edge basis function.

I. INTRODUCTION

When applying VIE based method of moments (MoM) formulations in electromagnetic problems involving arbitrary shaped three-dimensional (3D) bodies, the solution domain is best discretized using a number of tetrahedral elements [1]. In each tetrahedral element, a basis function is defined to best approximate the properties of the electromagnetic quantity of interest. It has been shown that the choice of an appropriate basis function is of critical importance when applying MoM formulations [2-4]. The most widely used basis function for 3D VIE modeling is the Schaubert-Wilton-Glisson (SWG) basis function defined in [1]. It is well suited for modeling the electric flux density **D** as it enforces the boundary condition of a continuous normal component of **D** on the faces of the tetrahedra where it is defined. However, the SWG basis function does not have the property of zero-divergence, which is demanded of **D** in a dielectric. This has encouraged a number of authors to use a divergence-free or solenoidal basis function that more accurately describes the physics within a dielectric [5, 6]. One such basis function is the 3D solenoidal basis introduced by de Carvalho*et al* [7, 8] for modeling the electromagnetic scattering of inhomogeneous dielectrics. Kulkani*et al* [2] demonstrated considerably better performance of the 3D-solenoidal basis function compared with the SWG basis function, including the fact that there was a significant reduction (1.67 to 2 times) of the number of unknowns for the same tetrahedral mesh. Although, their analysis was promising, they stressed the difficulty of implementing a preliminary conditioning operation to remove the null space associated with the solenoidal basis set.

Submitted On: March 26, 2013
Accepted On: Sept. 29, 2013

1054-4887 © 2013 ACES

Several approaches were proposed and implemented in order to identify the linearly independent 3D solenoidal basis functions in a given tetrahedra mesh. In [2], the Gram or covariance is formed and reduced by row operations to an echelon form using Gauss-Jordan elimination with partial pivoting. This is a complex method involving matrix manipulations that are prone to numerical inaccuracies due to finite machine precision. As a result, methods utilizing only the connecting information in the geometric mesh have been developed by several authors. In one method, reference [5] constructed an undigraph using the nodes and edges in the geometric mesh, and created a generating tree linking the nodes and edges. The limitation of this method is that it is only applicable to simply connected mesh regions (or mesh regions without holes). In another method, reference [3] proposed a solution where the nodes of the mesh are counted and tested, one-by-one, with a set of established criteria. Unfortunately, this method like the previous one is not applicable to objects and regions with holes.

In this paper, we expand on the work reported in [3] and introduce a simple, yet robust method for determining the linearly independent 3D solenoidal basis functions in a given tetrahedral mesh. The proposed method is based on the connecting information in the geometric mesh and the properties of the 3D solenoidal basis function. As such, it is not prone to numerical inaccuracies resulting from complex matrix manipulations. It is also applicable to all mesh regions with multiple holes and voids. Specifically, it can be used to accurately determine the number of voids in a given tetrahedral mesh. In addition, an accurate expression for determining the minimum number of linearly independent basis functions in a given mesh is presented.

II. THEORY AND FORMULATION

A. Basis definition

The 3D-solenoidal basis function is defined within a tetrahedron of volume V as shown in Fig. 1. It is a constant vector field that is perpendicular to the basis edge vector as depicted in Fig. 1. In this case, vector $\overrightarrow{\boldsymbol{CD}}$ denotes the basis edge vector while vector $\overrightarrow{\boldsymbol{AB}}$, represents the opposite edge vector parallel to the constant vector field. For any given point within the tetrahedron, the basis function with respect to the corresponding basis edge vector can be expressed mathematically as,

$$\boldsymbol{f}(\mathbf{r}) = \frac{\mathbf{e}}{3\boldsymbol{V}}\mathbf{u}(\mathbf{r}) \tag{1}$$

where

$$\mathbf{u}(\mathbf{r}) = \begin{cases} \mathbf{1} & \mathbf{r} \in \boldsymbol{V} \\ \mathbf{0} & \mathbf{r} \notin \boldsymbol{V} \end{cases}. \tag{2}$$

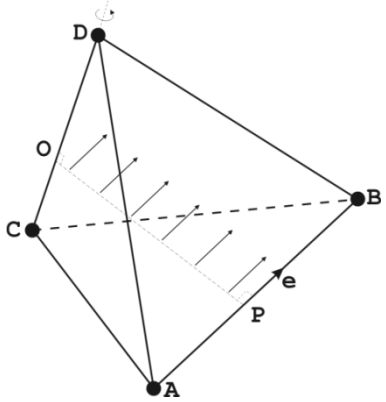

Fig. 1. Definition of the 3D solenoidal basis function in a tetrahedron.

The basis function $\boldsymbol{f}(\mathbf{r})$ defined in equation (1) is such that its divergence within the tetrahedron is zero, i.e., $\boldsymbol{f}(\mathbf{r})$ is solenoidal. Also, $\boldsymbol{f}(\mathbf{r})$ has the desired property that the normal component of its flux is continuous across any internal face boundary, and the total flux of its normal component through any face that is not parallel to $\boldsymbol{f}(\mathbf{r})$ is equal to one. In a typical tetrahedral mesh region consisting of multiple interconnecting tetrahedra, equation (1) can be modified to include the contributions from all neighbouring tetrahedra that share a common basis edge vector giving,

$$\mathbf{F}_{\boldsymbol{i}}(\mathbf{r}) = \sum_{\boldsymbol{k}=\mathbf{1}}^{\boldsymbol{N_T}} \frac{\mathbf{e}_{\boldsymbol{k}}}{3\boldsymbol{V}_{\boldsymbol{k}}}\mathbf{u}_{\boldsymbol{k}}(\mathbf{r}) \tag{3}$$

where N_T is the total number of tetrahedra connected to the i^{th} edge. With the definition of equation (3), any physical electromagnetic quantity that is solenoidal can be approximated in the discretized region using the 3D solenoidal basis function. Examples of physical quantities include the electric flux density **D** in a pure dielectric, the magnetic flux density **B**, the curl of the magnetic field ($\nabla \times \mathbf{H}$) or the total volumetric current density, and the curl of the electric field ($\nabla \times \mathbf{E}$).

B. Size of the basis set

It was shown in [2] that the size of the 3D-solenoidal basis set is far smaller than the number of edges in the mesh region. The number of linearly independent solenoidal basis functions is given by,

$$\boldsymbol{N_{Basis} \leq N_{Faces} - N_{Tetrahedra}} \quad (4)$$

where N_{Basis} is the number of linearly independent solenoidal basis functions, N_{Faces} is the number of faces, and $N_{Tetrahedra}$ is the number of tetrahedra in the mesh. When the meshregion is not simply connected, i.e., is made up of holes and voids, equation (4) can be modified into,

$$\boldsymbol{N_{Basis} = N_{Faces} - N_{Tetrahedra} - N_{Voids}} \quad (5)$$

where N_{Voids} is the number of voids in the mesh. Equation (5) can be explained by considering a mesh region with no voids. A simple void can be created by removing an internal tetrahedron from the mesh. In this case, the previous number of independent solenoidal basis function will not change since the normal component of flux from the remaining neighbouring tetrahedra into the void is unchanged. Consequently, the number of voids has to be accounted for as in equation (5) since there is no change in the number of faces. The simple void can be made larger by the continuous removal of one tetrahedron and the faces it introduced in the region bounding the simple void. In this case, equation (5) is unaltered because each time a tetrahedron is removed, the exact number of faces it introduced in the mesh is also removed. Using a similar argument, the inclusion of a hole has no effect on equations (4) or (5). This can be explained by considering a simple hole that is created by removing exactly one tetrahedron and the faces it introduced in the mesh region. This simple hole can be extended by the continuous removal of exactly one tetrahedron and the faces it introduced in the region bounding the simple hole. In this case, the number of independent solenoidal basis function is still given by equations (4) or (5), since the number of tetrahedra and faces removed remain balanced.

C. Minimization Algorithm

Consider a mesh region containing a single tetrahedron as shown in Fig. 2. Formally, there are six defined solenoidal basis functions corresponding to the six labeled edges. In $\Re^3$ space, only three of these functions are linearly independent, and a more natural choice of these functions would be $\mathbf{F}_4(\mathbf{r})$, $\mathbf{F}_5(\mathbf{r})$, and $\mathbf{F}_6(\mathbf{r})$ defined on edges 4, 5, and 6 as shown in Fig. 2. In addition, edges 4, 5, and 6 form the basis function face of the tetrahedra. We define the seed node N_1 as the node that is opposite to the basis function face associated with the tetrahedron. Also, we describe the neighbouring edges of node N_1 as those edges that contain node N_1: edges 1, 2, and 3 respectively. A typical mesh region can be constructed by the addition of more tetrahedra to the single tetrahedron structure of Fig. 2. When tetrahedra are added, they will share nodes, edges or faces depending on the mesh geometry.

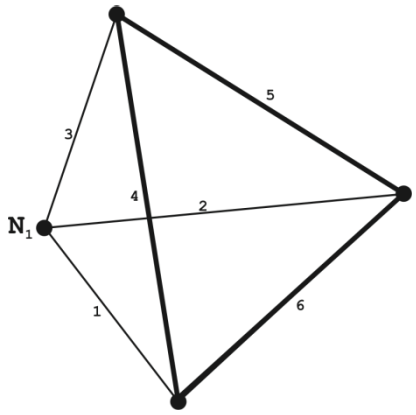

Fig. 2. 3D solenoidal basis functions defined as bold lines on the opposite face to seed node N_1.

According to [3], all tetrahedra having the same seed node are grouped together to form a structure very similar to an icosahedron (soccer ball structure [3]) where the seed node is at the center of the structure. The basis functions associated with all the tetrahedra in this structure are defined on the edges of the exterior faces. Subsequently, nodes on these exterior faces are used in turn as seed nodes to create more structures and this process continues as described in [3]. However, as more of these icosahedra like structures are formed, a situation will arise when a newly formed structure shares a node, an edge or a face with one or more previously formed structures. When this occurs, (5) is no longer satisfied,leading to an incorrect result. If the mesh region is simply connected or contiguous, then this problem can be avoided by appropriate seed node selection as discussed in [3]. In order to resolve this problem for non-contiguous mesh regions with multiple holes and voids, we introduce

additional solenoidal basis functions in the structure when it shares one or more edges, or faces with one or more previously formed structures. These additional functions are determined by the nature of the contact between the structures. For simplicity, we will consider two possible scenarios for contact: edge contact and face contact between any two tetrahedra of the structure as shown in Fig. 3. Using equation (5) on the edge contact configuration shown in Fig. 3 (a) indicates that six and not five solenoidal basis functions are required. In order to find out which additional basis functions are required while still adhering to the icosahedra approach, we observe that basis function $\mathbf{F}_6(\mathbf{r})$ will be modified by the contact based on equation (3). Since the new tetrahedron shares an edge with the previous defined one, $\mathbf{F}_6(\mathbf{r})$ is modified accordingly into,

$$\mathbf{F_6(r)}_{New} = \mathbf{F_6(r)}_{Previous} + \frac{\mathbf{e_9}}{3V_9}\mathbf{u_9(r)}\,. \quad (6)$$

This modification will destabilize the previous choice of basis functions in the structure, and basis functions $\mathbf{F}_4(\mathbf{r})$, $\mathbf{F}_5(\mathbf{r})$, $\mathbf{F}_6(\mathbf{r})$, $\mathbf{F}_{10}(\mathbf{r})$, and $\mathbf{F}_{11}(\mathbf{r})$ no longer linearly combine to produce the dependent basis $\mathbf{F}_1(\mathbf{r})$, $\mathbf{F}_2(\mathbf{r})$, and $\mathbf{F}_3(\mathbf{r})$. However, since

$$\begin{aligned}\frac{\mathbf{e_9}}{3V_9}\mathbf{u_9(r)} &= \mathbf{F_7(r)} \pm \mathbf{F_{10}(r)} \\ &= \mathbf{F_8(r)} \pm \mathbf{F_{11}(r)}\,, \end{aligned} \quad (7)$$

we can choose either $\mathbf{F}_7(\mathbf{r})$ or $\mathbf{F}_8(\mathbf{r})$ as an additional basis function so that the dependent bases can now be determined. Similarly, it can be shown that for the contact configuration in Fig. 3 (b), two additional solenoidal basis functions must be chosen from the set $\{\mathbf{F}_7(\mathbf{r}), \mathbf{F}_8(\mathbf{r}), \mathbf{F}_9(\mathbf{r})\}$, since we have that,

$$\mathbf{F_7(r)} \pm \mathbf{F_8(r)} \pm \mathbf{F_9(r)} = \mathbf{0}. \quad (8)$$

Using the results from these configurations, we describe an algorithm to determine the linearly independent solenoidal basis functions from the set of all edges. A flow diagram of the algorithm is depicted in Fig. 4. The first process is to specify an arbitrary node as the head node and insert it into an empty linked list. Next, we pick the head or first node from the list as the first seed node, and we find all tetrahedra sharing this node. A two-step validation test is then performed on all tetrahedra found. The first step involves checking each tetrahedron found for one or more neighbouring edges that are not shared with any tetrahedra of a previous seed node, and one or more nodes on the basis function face that are already in the linked list. This is the mesh continuity test as defined in [3]. If no tetrahedron is found that satisfies these conditions then the test is successful. On the other hand, if one or more tetrahedra fail the test then we apply the next step of validation. The introduction of this second step is the key contribution of this paper that differentiates it from the work in [3]. The second step examines each tetrahedron that failed the mesh continuity test to determine how they touch the other tetrahedra from previously listed seed nodes. For this test to be successful, all tetrahedra must touch other tetrahedra from previously listed seed nodes as shown in either contact configuration of Fig. 3. If one or more tetrahedra touch in any other way, the seed node is removed and inserted at the end of the linked list and the process is repeated with a new seed node. Upon a successful outcome from validation testing, the appropriate edges of the basis function faces or neighbouring edges of all tetrahedra found are selected as basis function, and the nodes on the basis function faces are inserted into the linked list. This process is repeated until all nodes in the mesh are exhausted.

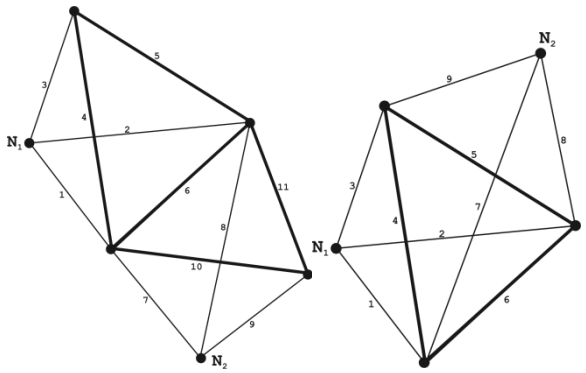

(a) (b)

Fig. 3. Possible contact configuration of two tetrahedra from seed nodes N_1 and N_2: (a) tetrahedra share an edge and (b) tetrahedra share a face.

III. EXAMPLES AND TESTING

In this section, we challenge our algorithm using different tetrahedra meshes of simple and complex geometrical structures containing multiple holes and voids. These meshes were created with the software package Netgen [9]; they are depicted in Fig. 5. The algorithm was implemented and executed on an Intel Core i5-2520M 2.5 GHz PC with 4.0 GB of RAM running

Open Suse 12.1. We tabulate the mesh parameters of each discretized region, as well as the output from the algorithm into Table I .In every case considered, the algorithm is able to identify the independent 3D solenoidal basis functions. Also, we observe that equation (5) is in agreement with the output from the algorithm. The algorithm is indeed very robust, and is applicable to a very broad class of complex meshes with multiple holes and voids, as seen. Moreover, the complete minimum number of independent solenoidal bases is always smaller than the number of edge bases in the discretization (typically by a factor ranging between 16% and 20%), resulting in further reduction in memory resources. The execution time for large meshes is in the order of a few seconds, and is less than a second for smaller meshes (fewer than 19,000 edges). These results are an indication of superior performance when compared to linear algebraic methods using the same PC hardware. Finally, the algorithm is very straight forward to implement, and does not suffer from numerical inaccuracies due to floating point matrix operations since it uses the connecting information in the mesh.

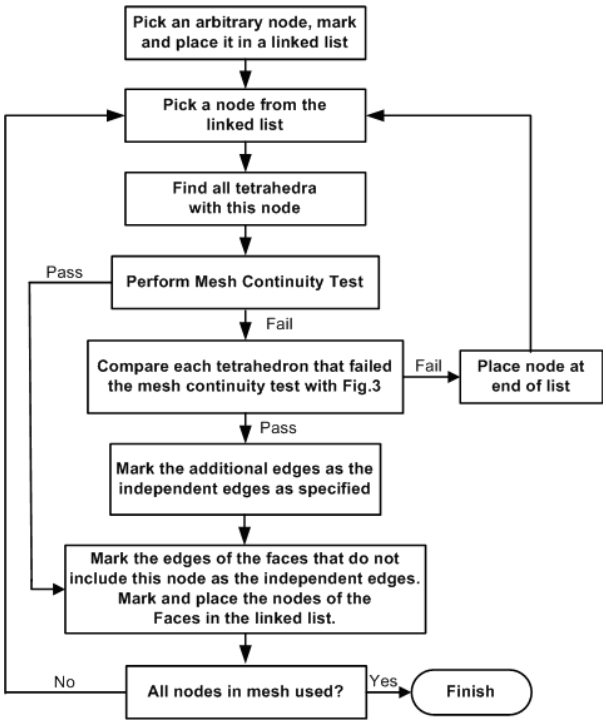

Fig. 4. Algorithm for identifying linearly independent basis functions.

Table I. Output from the algorithm for the mesh regions shown in Fig. 5.

Mesh Region	N_{Edges}	N_{Faces}- $N_{Tetrahedra}$– N_{Voids}	N_{Basis} (Algorithm output)	**Time** (s)
Fig.5(a)	12864	10723	10723	< 1
Fig.5(b)	11065	9253	9253	< 1
Fig.5(c)	187547	156001	156001	199
Fig.5(d)	24177	19455	19455	1
Fig.5(e)	34957	28240	28240	4
Fig.5(f)	13001	10544	10544	< 1

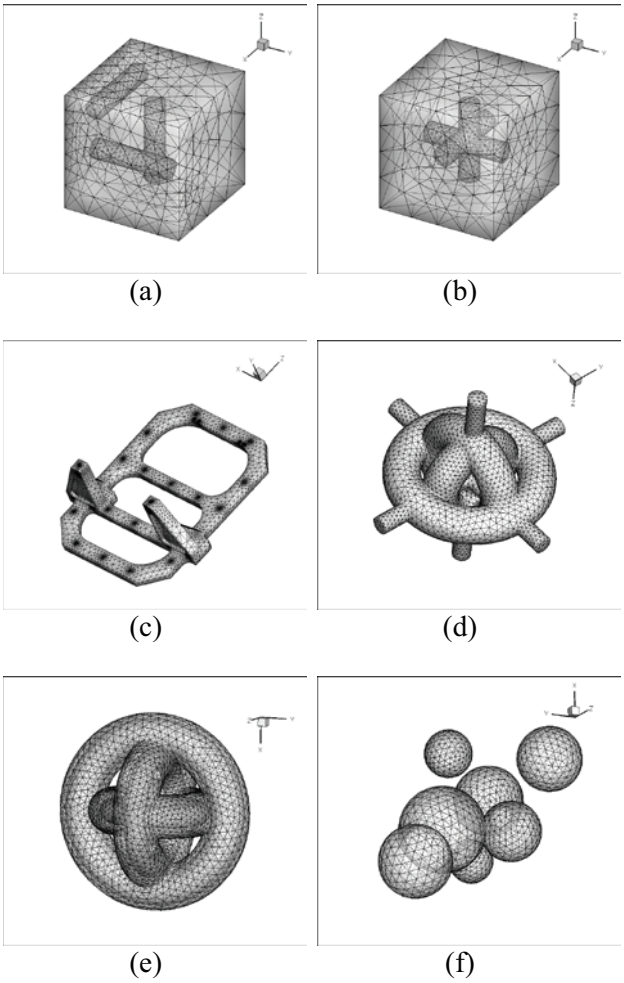

Fig. 5. Mesh regions generated with NETGEN: (a) cube with three cylindrical voids, (b) cube with a single void of merged cylinders, (c) steel frame with multiple holes, (d) gyroscope, (e) three connected tori with single connecting void, and (f) group of five connecting spheres and two separated spheres.

IV. CONCLUSION

In this paper, we presented a novel method for the determination of the minimum number of 3D-solenoidal basis functions in a given tetrahedral discretization. The method was derived using the connecting information in the mesh structure and the properties of the 3D-solenoidal basis function. The method is able to identify the independent basis functions even in the presence of holes and voids within the mesh structure. To our knowledge, this is the only algorithm that is insensitive to the presence of holes and voids in the mesh discretization. In addition, it provides significant savings in computational resources when compared to algorithms involving complex matrix manipulations. Finally, it is worthy of note that the contact configurations of Fig. 3 can be expanded to accommodate other ways tetrahedra from two or more seed nodes can come into contact. This will provide an improvement in the speed of the algorithm at the expense of an increase in the complexity of identifying the type of contact, and the additional basis edges resulting from that contact. The chosen contact configuration is simple and sufficient to guarantee proper functioning of the algorithm in any region.

REFERENCES

[1] D. Schaubert, D. Wilton, and A. Glisson, "A tetrahedral modeling method for electromagnetic scattering by arbitrary shaped inhomogeneous dielectric bodies," *IEEE Trans. Antennas Propagat*., vol. 32, no. 1, pp. 77-85, Jan. 1984.

[2] S. Kulkani, R. Lemdiasov, R. Ludwig, and S. Makarov, "Comparison of two sets of low-order basis functions for tetrahedral VIE modeling," *IEEE Trans. Antennas Propagat.*, vol. 52, no. 10, pp. 2789-2795, Oct. 2004.

[3] R. Lemdiasov and R. Ludwig, "The determination of linearly independent rotational basis functions in volumetric electric field integral equations," *IEEE Trans. Antennas Propagat.*, vol. 54, no. 7, pp. 2166-2169, July 2006.

[4] J. Ding, R. Chen, J. Zhu, Z. Fan, and D. Ding, "A redundant loop basis for closed structures with application to MR basis," *ACES Journal* , vol. 26, no. 3, March 2011.

[5] M. Li and W. Chew, "Applying divergence-free condition in solving the volume integral equation," *Progr. In Electr. Research*, PIER 57, pp. 311-333, 2006.

[6] B. Rubin, "Divergence-free basis for representing polarization current in finite-size dielectric regions," *IEEE Trans. Antennas Propagat*., vol. 41, no. 3, pp. 269-277, March 1993.

[7] S. Carvalho and L. Mendes, "Method of moments with solenoidal basis functions: An approach to analyze the scattering by inhomogeneous dielectrics," *in Compu. Electro. Conf.*, no. 420, April, 1996.

[8] S. Carvalho and L. Mendes, "Scattering of EM waves by inhomogeneous dielectric with the use of the method of moments and 3-D solenoidal basis functions," *Microw. Opt. Techn. Lett.*, vol. 23, no. 1, pp. 42-46, 1999.

[9] NETGEN, http://www.hpfem.jku.at/netgen/.

Aghogho Obi is currently a Research Engineer with GE Global Research in Niskayuna, NY. He obtained his M.S. and Ph.D degrees in Electrical and Computer Engineering from Worcester Polytechnic Institute, Worcester, MA in 2004 and 2008, respectively. His research interests include the numerical modeling of electromagnetic sensors, electromagnetic navigation system design for minimally invasive surgery and algorithm development in embedded systems.

Rostislav A. Lemdiasov received the M.S. degree in Mechanical Engineering (2000) and the Ph.D. degree (2004) in Electrical Engineering from Worcester Polytechnic Institute, Worcester, MA. His research interests lie in numerical simulation of the high-frequency RF fields as well as in design of the gradient coils for MRI. He is currently working for PhiHealth, Richardson, TX, as a Design Engineer. His responsibilities include design of MRI RF coils as well as other electronics related to MRI.

Reinhold Ludwig, Ph.D. is the Chief Scientific Officer and Co-founder of Insight MRI. Dr. Ludwig is a Professor of Electrical and Computer Engineering with joint appointment in Biomedical Engineering at Worcester Polytechnic Institute, Worcester, MA. He has been a consultant for a number of corporations, venture funds, and the US government. Dr. Ludwig has published extensively on electromagnetic modeling, MRI coil design, including a seminal book on RF electronics; he holds 10 patents.

Simple and Efficient BZT-Higher-Order PML Formulations for the Metal Plate Buried in Three-Dimensional Dispersive Soil Space Problems

N. Feng[1], Q. H. Liu[2], and C. Zhu[1]

[1] Institute of Electromagnetics and Acoustics
Xiamen University, Xiamen, 361005, P. R. China
fengnaixing@gmail.com, zhuchhxd@xmu.edu.cn

[2] Department of Electrical and Computer Engineering
Duke University, Durham, NC 27708, USA
qhliu@ee.duke.edu

Abstract–Efficient and unsplit-field higher-order PML formulations using the stretched coordinate perfectly matched layer (SC-PML) formulations and the bilinear Z-Transform (BZT) method are presented for truncating the finite-difference time-domain (FDTD) lattices. This method is completely independent of the material properties of the FDTD computational domain and hence can be applied to the modeling of arbitrary media without any modification because of the D-B constitutive relations used. The higher-order PML has the advantages of both the conventional PML and the complex frequency-shifted PML (CFS-PML) in terms of absorbing performances. Two 3D FDTD simulations of the metal plate buried in dispersive soil space FDTD domains have been carried out to validate these formulations. It is shown that the proposed PML formulations with the higher-order scheme are efficient in terms of attenuating both the low- frequency propagating waves and evanescent waves and reducing late-time reflections.

Index Terms–Bilinear Z-transform (BZT) method, finite-difference time-domain (FDTD), and perfectly matched layer (PML).

I. INTRODUCTION

Since the introduction of the perfectly matched layer (PML) absorbing boundary condition by Berenger [1], various modified PMLs have been presented to terminate the finite-difference time-domain (FDTD) lattices. Among the various implementations of PMLs, the stretched coordinate PML (SC–PML) by Chew and Weedon [2] has the advantage of simple implementation in the corners and edges of PML regions. Furthermore, Ramadan applied Z-transform to implement PML [3]. Recently, complex frequency-shifted PML (CFS–PML), introduced by Kuzuoglu and Mittra [4] and implemented by simply shifting the frequency- dependent pole off the real axis and into the negative-imaginary half of the complex plane, has drawn considerable attention due to the fact that this PML is efficient in attenuating low-frequency evanescent waves and reducing late-time reflections [5]. However, the CFS-PML would have a poor absorption of low-frequency propagating waves as shown in [6-8]. To overcome the limitations of both the conventional PML and the CFS-PML, the higher-order PML was proposed by Correia, which retains the advantages of both the CFS-PML and conventional PML in [8]. It has shown that the 2nd-order PML is highly effective in absorbing both evanescent and low-frequency propagating waves in both open-region and periodic problems in [9]. In [9], the 2nd-order PML based on the SC-PML was implemented by using the split-field PML formulations and the auxiliary differential equation (ADE) method. However, besides the drawback of more requirements of the memory and the computational time, the

Submitted On: May 29, 2012
Accepted On: Nov. 12, 2013

1054-4887 © 2013 ACES

higher-order PML implementation proposed in [9] was difficult to be extended to the case with more than two poles because the polynomial expansion was employed.

In this paper, efficient and unsplit-field higher-order PML formulations are proposed based on the SC-PML formulations and the bilinear Z-transform method. The proposed BZT PML algorithm is different from the proposed PML algorithm in [9] and [12-19], the proposed BZT PML algorithm is based on D-B formulations, and consequently, the proposed higher-order PML formulations require less memory and computational time as compared with that in [9]. Two 3D numerical simulation for the metal plate buried in dispersive soil space FDTD domains are given to validate the proposed formulations, as the investigation on the performance of the higher-order PML for dispersive soil half-space problem is very rare in the literatures. Only the 2nd-order case is described in this paper, but this approach is easy to be applied to any number of poles.

II. FORMULATION

In the SC-PML regions, the *x*-projection of Ampere's law for the frequency-domain modified Maxwell's equations can be written as,

$$j\omega\varepsilon_0\varepsilon_r E_x = \frac{1}{S_y}\frac{\partial H_z}{\partial y} - \frac{1}{S_z}\frac{\partial H_y}{\partial z}. \tag{1}$$

To make the PML completely independent of the material properties of the FDTD computational domain, equation (1) can be written in terms of the electric flux density D as,

$$j\omega\varepsilon_0 D_x = \frac{1}{S_y}\frac{\partial H_z}{\partial y} - \frac{1}{S_z}\frac{\partial H_y}{\partial z} \tag{2}$$

where $D_x = \varepsilon_r E_x$, ε_r is the relative permittivity of the FDTD computational domain. Consequently, this PML can be applied to truncate arbitrary media and all that is needed is to modify $D_x = \varepsilon_r E_x$ under consideration. The method is available in [11] to obtain E from D. S_η $(\eta = y, \text{or } z)$ is the complex stretched coordinate variable.

For the conventional PML, S_η is defined as,

$$S_\eta = \kappa_\eta + \sigma_\eta / j\omega\varepsilon_0 \tag{3}$$

where $\sigma_\eta \geq 0$ is the conductivity profile different from zero only in the PML region to provide attenuation for the propagating waves and $\kappa_\eta \geq 1$ is different from 1 only in the PML region to attenuate the evanescent waves.

With the CFS scheme, S_η is defined as,

$$S_\eta = \kappa_\eta + \sigma_\eta / (\alpha_\eta + j\omega\varepsilon_0) \tag{4}$$

where α_η is assumed to be positive real.

The idea of the higher-order PML was proposed in [9] by generalizing this metric for the case where more than one pole was present. For the 2nd-order PML, S_η is defined as,

$$S_\eta = S_{1\eta}\cdot S_{2\eta} = \left(\kappa_{1\eta} + \frac{\sigma_{1\eta}}{\alpha_{1\eta} + j\omega\varepsilon_0}\right) \cdot \left(\kappa_{2\eta} + \frac{\sigma_{2\eta}}{\alpha_{2\eta} + j\omega\varepsilon_0}\right). \tag{5}$$

Transforming equation (2) from the frequency domain to the *Z*-domain, we obtain,

$$\frac{1-z^{-1}}{\Delta t}\varepsilon_0 D_x = S_y(z)\cdot\frac{\partial H_z}{\partial y} - S_z(z)\cdot\frac{\partial H_y}{\partial z} \tag{6}$$

where Δt is the time step and $S_\eta(z), (\eta = y, z)$, is the *Z*-transform of $1/S_\eta$, which can be obtained by first transforming $1/S_\eta$ to the s-domain using the relation $j\omega \to s$, and then applying the bilinear transform method [10] using the relation $s \to (2/\Delta t)(1-z^{-1})/(1+z^{-1})$,

$$S_\eta(z) = w_{1\eta}\left(\frac{1-a_{1\eta}\cdot z^{-1}}{1-b_{1\eta}\cdot z^{-1}}\right)\cdot w_{2\eta}\left(\frac{1-a_{2\eta}\cdot z^{-1}}{1-b_{2\eta}\cdot z^{-1}}\right) \tag{7}$$

where

$$w_{m\eta} = \frac{2\varepsilon_0 + \alpha_{m\eta}\Delta t}{2\varepsilon_0\kappa_{m\eta} + \alpha_{m\eta}\kappa_{m\eta}\Delta t + \sigma_{m\eta}\Delta t},\quad m=1,2$$

$$a_{m\eta} = \frac{2\varepsilon_0 - \alpha_{m\eta}\Delta t}{2\varepsilon_0 + \alpha_{m\eta}\Delta t},\quad m=1,2,$$

$$b_{m\eta} = \frac{2\varepsilon_0\kappa_{m\eta} - \alpha_{m\eta}\kappa_{m\eta}\Delta t + \sigma_{m\eta}\Delta t}{2\varepsilon_0\kappa_{m\eta} + \alpha_{m\eta}\kappa_{m\eta}\Delta t + \sigma_{m\eta}\Delta t},\quad m=1,2.$$

Substituting equation (7) into equation (6), we obtain,

$$\frac{1-z^{-1}}{\Delta t}\varepsilon_0 D_x = w_{1y}\left(\frac{1-a_{1y}\cdot z^{-1}}{1-b_{1y}\cdot z^{-1}}\right)\cdot w_{2y}\left(\frac{1-a_{2y}\cdot z^{-1}}{1-b_{2y}\cdot z^{-1}}\right)\cdot\frac{\partial H_z}{\partial y} - w_{1z}\left(\frac{1-a_{1z}\cdot z^{-1}}{1-b_{1z}\cdot z^{-1}}\right)\cdot w_{2z}\left(\frac{1-a_{2z}\cdot z^{-1}}{1-b_{2z}\cdot z^{-1}}\right)\cdot\frac{\partial H_y}{\partial z}. \tag{8}$$

Introducing four auxiliary variables $Q_{x\eta}$ and $P_{x\eta}$ $(\eta = y, z)$,

$$Q_{xy} = \frac{w_{1y} w_{2y} \Delta t}{\varepsilon_0} \cdot \left(\frac{1}{1 - b_{1y} \cdot z^{-1}} \right) \cdot \frac{\partial H_z}{\partial y} = b_{1y} \cdot z^{-1} Q_{xy} + \frac{w_{1y} w_{2y} \Delta t}{\varepsilon_0} \cdot \frac{\partial H_z}{\partial y} \quad (9)$$

$$P_{xy} = \left(\frac{1 - a_{2y} \cdot z^{-1}}{1 - b_{2y} \cdot z^{-1}} \right) Q_{xy} = b_{2y} \cdot z^{-1} P_{xy} + Q_{xy} - a_{2y} \cdot z^{-1} Q_{xy} \ , \quad (10)$$

$$Q_{xz} = \frac{w_{1z} w_{2z} \Delta t}{\varepsilon_0} \cdot \left(\frac{1}{1 - b_{1z} \cdot z^{-1}} \right) \cdot \frac{\partial H_y}{\partial z} = b_{1z} \cdot z^{-1} Q_{xz} + \frac{w_{1z} w_{2z} \Delta t}{\varepsilon_0} \cdot \frac{\partial H_y}{\partial z} \ , \quad (11)$$

$$P_{xz} = \left(\frac{1 - a_{2z} \cdot z^{-1}}{1 - b_{2z} \cdot z^{-1}} \right) Q_{xz} = b_{2z} \cdot z^{-1} P_{xz} + Q_{xz} - a_{2z} \cdot z^{-1} Q_{xz} \ . \quad (12)$$

Considering that the z^{-1} operator corresponds to a single-step delay in the discrete time domain, equation (9) to equation (12) can be written in the FDTD form, respectively, as equation (13) to equation (16), where

$$Q_{xy}\Big|_{i+1/2,j,k}^{n+1} = b_{1y(j)} \cdot Q_{xy}\Big|_{i+1/2,j,k}^{n} + u_{y(j)} \cdot \left(H_z\Big|_{i+1/2,j+1/2,k}^{n+1/2} - H_z\Big|_{i+1/2,j-1/2,k}^{n+1/2} \right), \quad (13)$$

$$P_{xy}\Big|_{i+1/2,j,k}^{n+1} = b_{2y(j)} \cdot P_{xy}\Big|_{i+1/2,j,k}^{n} + Q_{xy}\Big|_{i+1/2,j,k}^{n+1} - a_{2y(j)} \cdot Q_{xy}\Big|_{i+1/2,j,k}^{n}, \quad (14)$$

$$Q_{xz}\Big|_{i+1/2,j,k}^{n+1} = b_{1z(k)} \cdot Q_{xz}\Big|_{i+1/2,j,k}^{n} + u_{z(k)} \cdot \left(H_y\Big|_{i+1/2,j,k+1/2}^{n+1/2} - H_y\Big|_{i+1/2,j,k-1/2}^{n+1/2} \right), \quad (15)$$

$$P_{xz}\Big|_{i+1/2,j,k}^{n+1} = b_{2z(k)} \cdot P_{xz}\Big|_{i+1/2,j,k}^{n} + Q_{xz}\Big|_{i+1/2,j,k}^{n+1} - a_{2z(k)} \cdot Q_{xz}\Big|_{i+1/2,j,k}^{n} \ . \quad (16)$$

Equation (8) can be written as,

$$D_x\Big|_{i+1/2,j,k}^{n+1} = D_x\Big|_{i+1/2,j,k}^{n} + P_{xy}\Big|_{i+1/2,j,k}^{n+1} - a_{1y(j)} \cdot P_{xy}\Big|_{i+1/2,j,k}^{n} - \left(P_{xz}\Big|_{i+1/2,j,k}^{n+1} - a_{1z(k)} \cdot P_{xz}\Big|_{i+1/2,j,k}^{n} \right) \quad (17)$$

where $u_y = w_{1y} w_{2y} \Delta t / \varepsilon_0 \Delta y$ and $u_z = w_{1z} w_{2z} \Delta t / \varepsilon_0 \Delta z$. Δy and Δz are space step. A similar method can be used for other regions of SC-PML.

In order to perform a comparison between the proposed higher-order PML formulations and the higher-order PML formulations proposed in [9] in terms of the amount of the auxiliary variables, we assume an FDTD computational domain of L × M × N cells with W-cell thick PML used on each one of the sides of domain. In the SC-PML region, the higher-order PML formulations proposed in [9] totally requires $288W^3 + 112(LW^2+MW^2+NW^2) + 40(LMW+LNW+MNW)$ auxiliary variables, however, the proposed higher-order PML formulations totally requires $192W^3 + 64(LW^2+MW^2+NW^2) + 16(LMW+LNW+MNW)$ auxiliary variables. As a result, the proposed higher-order PML formulations save $96W^3 + 48(LW^2+MW^2+NW^2)+24(LMW+LNW+MNW)$ auxiliary variables as compared with the higher-order PML formulations proposed in [9]. Saving auxiliary variables multiply by each variable, which occupies number of bytes in memory, which can be concluded that the proposed higher-order PML formulations save memory as compared with the higher-order PML formulations proposed in [9]. Obviously, if an FDTD computational domain (L, M, and N) is constant, saving memory will increase as the increase of PML layers. Similarly, if PML layers are constant, saving memory will increase as the increase of FDTD computational domain (L, M, and N).

It is obvious that, because of no polynomial expansion, the proposed implementation of the higher-order PML is easier than that in [9] to be extended to the case with more than two poles.

III. NUMERICAL RESULT

To show the validity of the proposed formulations, we implement a 3D FDTD simulation for the metal plate buried in an inhomogeneous, dispersive, and conductive soil half-space problem in a highly elongated FDTD grid. The metal plate size is $40 \times 10 \times 2$. The dielectric constant of soil is specified as the second-order Debye model with an added conductivity term $\varepsilon_r(\omega) = \varepsilon_\infty + \sigma / j\omega\varepsilon_0 + \sum_{p=1}^{2} A_p / (1 + j\omega\tau_p)$, where $\varepsilon_\infty = 4.15$ is the infinite frequency permittivity, A_1=1.8 and A_2=0.6 are the pole amplitudes, τ_1 =3.79 nsec and τ_2=0.151 nsec are the relaxation time and σ=1.11

ms/m is the conductivity. The half-space occupies 50 % of the vertical height of the horizontally elongated simulation region. The space is discretized with the FDTD lattice with $\Delta x = \Delta y = \Delta z = 0.05$ m and time step is $\Delta t = 77$ ps. The simulation is done with a $126 \times 46 \times 26$ grid including 10-cell thick PML layers, as shown in Fig. 1. Assuming that the origin is at a corner of the FDTD grid, a vertically polarized point source located at (13, 13, 13) (above the soil) is excited by a differentiated Gaussian pulse with a half pulse bandwidth $= 1155$ ps. Within the PML, σ_η and κ_η are scaled using a fourth-order polynomial scaling and α_η is a constant. The relative reflection error (in decibels) versus time is computed at an observation point located at (113, 33, 12) using error (decibels) $R_{dB}(t) = 20\log_{10}(|E_z^R(t) - E_z^T(t)|/|E_{z\_\max}^R|)$ where $E_z^T(t)$ is the field computed using the test domain, and $E_z^R(t)$ is the reference field based on an extended lattice, and $E_{z\_\max}^R$ is the maximum value of the reference solution over the full-time simulation. For the 2nd-order PML, the relative reflection error between the formulations in [9] and the proposed formulations is first computed over 1500 time steps for $\sigma_{1\eta\text{opt}} = 0.175/150\pi\Delta x$, $\kappa_{1\eta} = 1$, $\alpha_{1\eta} = 0$, $\sigma_{1\eta} = \sigma_{1\eta\text{opt}}\rho^4$, $\alpha_{2\eta} = 0.0055 + \sigma_{1\eta}$, $\sigma_{2\eta} = \sigma_{2\eta\text{opt}}\rho^2$, $\kappa_{2\eta} = 1 + \kappa_{2\eta\text{opt}}\rho^2$, $\kappa_{2\eta\text{opt}} = 10$ and $\sigma_{2\eta\text{opt}} = 4/150\pi\Delta x$. Where the σ_{opt} is chosen as $\sigma_{\text{opt}} = (m+1)/150\pi\Delta x$ and ρ is zero at the interface of the PML and the FDTD computational domains and 1 at the end. This same example is repeated with the SC-PML ($\alpha_\eta = 0$, $\kappa_{\max} = 11$ and $\sigma_{\max} = 0.18$ S/m) and the convolution PML in [5] ($\alpha_\eta = 0.0055$, $\sigma_{\max} = 0.24$ S/m and $\kappa_{\max} = 7$). In this paper, σ and κ are evaluated as the average value in the cell around the index location [1]. These optimum parameters are chosen empirically to obtain the lowest reflection. The results are illustrated in Fig. 2.

The maximum relative reflection errors of the conventional SC-PML, the CPML, the 2nd-order PML in [9], and the proposed 2nd-order PML are -45dB, -52dB, -62dB and -70dB, respectively. It can be concluded from Fig. 2 that the absorbing performance of the proposed 2nd-order PML formulations have 18 dB and 25 dB improvement in terms of the maximum relative error as compared with the CPML and the SC-PML, respectively, and holds much lower reflection error for the late-time region than the CPML and the SC-PML. Table I and II are using different perfectly matched layer algorithm procedures, which occupy of memory and different time steps, and computational time, respectively. Obviously, when FDTD computational domain is invariant, saving memory will increase with the increase of PML layers and saving time will increase with the increase of time steps.

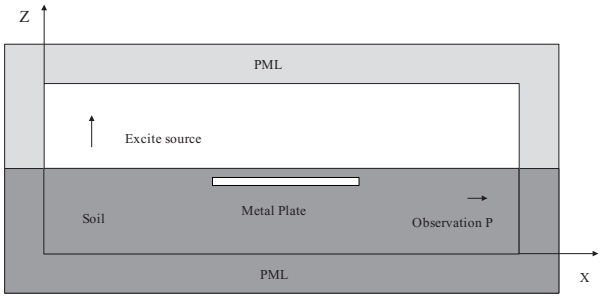

Fig. 1. A metal plate buried in an inhomogeneous, dispersive, and conductive soil half-space problem.

Table I: Memory requirements (bytes) for the different PML implementations.

	PML layers=10	PML layers=16
2nd-order PML in [9]	49,506K	105,509K
Proposed 2nd-order PML	30,848K	65,244K
CPML	24,084K	49,664K
SC-PML	24,084K	49,672K

In the second numerical example, in order to validate the proposed formulations, the problem of the electromagnetic scattering by a highly elongated object is studied. Particularly, a thin 100 mm $\times$ 25 mm plate is immersed in a background media [5] with constitutive parameters ε and σ. For the purposes of this study, constitutive parameters for soil are assumed, giving σ =0.273 and ε_r =7.73. The plate is illuminated by a vertically polarized electric current element placed just above one corner of the plate. The current source is given a differentiated Gaussian time signature with a 6 GHz bandwidth. The simulation is done with a

$126 \times 51 \times 26$ grid including 10-cell-thick PML layers placed only three cells from the scatter on all sides with the space steps $\Delta x = \Delta y = \Delta z = 5$ mm, as shown in Fig. 3. Within the PML, σ_i and κ_i are scaled using an mth order polynomial scaling. It is noted that α is not scaled, and is constant through the PML.

Table II: Computational time (s) for different PML implementations (PML layers = 10).

	Time steps =2000	Time steps =4000
2nd-order PML in [9]	757.90	1390.48
Proposed 2nd-order PML	484.18	828.30
CPML	312.48	625.08
SC-PML	314.55	626.53

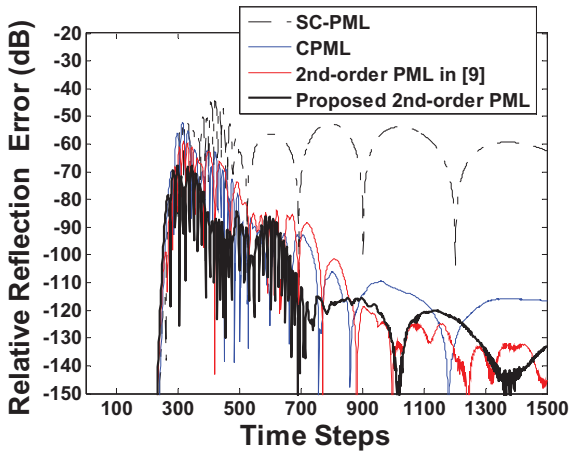

Fig. 2. The relative reflection error of the conventional SC-PML, the CPML, the 2nd-order PML in [9] and the proposed 2nd-order PML for a metal plate buried on an inhomogeneous, dispersive, and conductive soil half-space problem.

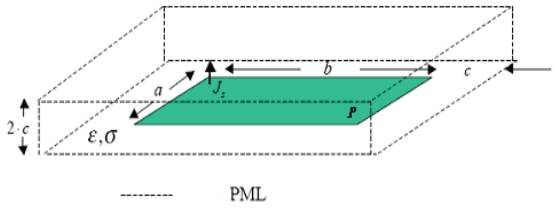

Fig. 3. Shows the FDTD grid geometry in this simulation.

To study the reflection error due to the proposed PMLs, a reference problem is also simulated. To this end, the same mesh is extended 75 cells out in all dimensions, leading to a 272 × 201 × 176 cell lattice. The proposed PMLs are used to terminate this lattice with optimal PML parameters to minimize any spurious reflection. The fields within the lattice are then excited by an identical source, and the time-dependent fields are recorded within the region representing the original lattice. The relative reflection error (in dB) versus time is computed at an observation point in the corner of the computational domain using $R_{dB}(t)=20\log_{10}\left(\left|E_x(t)-E_{\text{xref}}(t)\right|\Big/\left|E_{\text{x\_refmax}}\right|\right)$ where $E_x(t)$ represents the time-dependent discrete electric field of the observation point, $E_{\text{xref}}(t)$ is a reference solution based on an extended lattice, and $E_{\text{x\_refmax}}$ represents the maximum value of the reference solution over the full-time simulation. The relative error computed is recorded in Fig. 4. The relative reflection error is first computed over 1800 time iterations. This same example is repeated with SC-PML (α_η =0 $\kappa_{\max}$ =14 and $\sigma_{\max}$ =2.290 S/m) and the convolution PML (CPML) [5] (α_η =0.04 $\kappa_{\max}$ =11 and $\sigma_{\max}$ =4.198 S/m). For the 2nd-order PML including the proposed PML formulations and the formulations in [9], the following parameters are chosen: $\kappa_{1\eta}$ =1, $\alpha_{1\eta}=0$, $\sigma_{1\eta\text{opt}}=0.175/150\pi\Delta x$, $\sigma_{1\eta}=\sigma_{1\eta\text{opt}}\rho^4$, $\kappa_{2\eta\text{opt}}=14$, $\kappa_{2\eta}=1+\kappa_{2\eta\text{opt}}\rho^2$, $\alpha_{2\eta}=0.04+\sigma_{1\eta}$, $\sigma_{2\eta\text{opt}}=4/150\pi\Delta x$ and $\sigma_{2\eta}=\sigma_{2\eta\text{opt}}\rho^2$, where ρ is zero at the interface of the PML and the FDTD computational domains and 1 at the end. In all computations of this paper, σ and κ are evaluated as the average value in the cell around the index location [1]. These optimum parameters are chosen empirically to obtain the lowest reflection.

These results are illustrated from Fig. 4. The maximum relative reflection errors of the conventional SC-PML, the CPML, the proposed 2nd-order PML and the 2nd-order PML in [9] are -50dB, -86dB, -93dB, and -93dB, respectively. It can be concluded from Fig. 4 that the absorbing

performance of the proposed 2nd-order PML formulations has more 7dB and 43dB improvement in terms of the maximum relative error as compared with the CPML and the SC-PML, respectively, and holds much lower reflection error for the late-time region than the SC-PML.

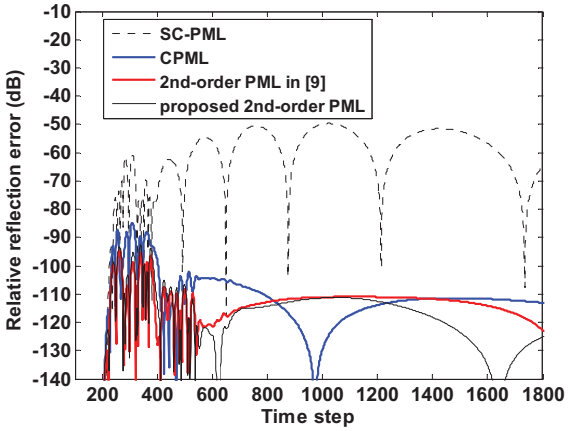

Fig. 4. The relative reflection error of the conventional SC-PML, the CPML, the 2nd-order PML in [9] and the proposed 2nd-order PML.

Tables III and IV are using different perfectly matched layer algorithm procedures, which occupy memory and different time steps, which occupy of computational time, respectively. Obviously, when FDTD computational domain is invariant, saving memory will increase with the increase of PML layers and saving time will increase with the increase of time steps.

Table III: Memory requirements (bytes) for the different PML implementations.

	PML layers=10	PML layers=16
2nd-order PML in [9]	43,803K	98,748K
Proposed 2nd-order PML	31,288K	65,832K
CPML	25,343K	53,323K
SC-PML	26,332K	55,428K

IV. CONCLUSION

Efficient and unsplit-field higher-order PML formulations based on the SC-PML and the bilinear Z-transform method has been presented. It can be shown in the numerical simulation that the proposed 2nd-order PML formulations hold good absorbing performance in terms of attenuating both the low-frequency propagating waves and evanescent waves, and also require less memory and computational time as compared with that in [9].

Table IV: Computational time (s) for the different PML implementations (PML layers=10).

	Time steps =1000	Time steps =2000
2nd-order PML in [9]	707.37	1443.65
Proposed 2nd-order PML	500.98	1031.18
CPML	378.07	777.51
SC-PML	381.70	780.51

ACKNOWLEDGMENT

This work is supported by the Natural Science Foundation of China (NSFC) under Grant 412400 29 and 61301008.

REFERENCES

[1] J. Bérenger, "A perfectly matched layer for the absorption of electromagnetic waves," *J. Computat. Phys.*, vol. 114, no. 2, pp. 185-200, Oct. 1994.

[2] W. Chew and W. Weedon, "A 3-D perfectly matched medium from modified Maxwell's equations with stretched coordinates," *Microw. Opt. Technol. Lett.*, vol. 7, no. 13, pp. 599-603, Sep. 1994.

[3] O. Ramadan and A. Oztoprak, "Z-transform implementation of the perfectly matched layer for truncating FDTD domains," *IEEE Microw. Wireless Compon. Lett.*, vol. 13, no. 9, pp. 402-404, Sep. 2003.

[4] M. Kuzuoglu and R. Mittra, "Frequency dependence of the constitutive parameters of causal perfectly matched anisotropic absorbers," *IEEE Microw. Guided Wave Lett.* , vol. 6, no. 12, pp. 447-449, Dec. 1996.

[5] J. Roden and S. Gedney, "Convolution PML (CPML): An efficient FDTD implementation of the CFS-PML for arbitrary media," *Microw. Opt. Technol. Lett.*, vol. 27, no. 5, pp. 334-339, Dec. 2000.

[6] E. Bécache, P. Petropoulus, and S. Gedney, "On the long-time behavior of unsplit perfectly matched layers," *IEEE Trans. Antennas Propag.*, vol. 52, no. 5, pp. 1335-1342, May 2004.

[7] J. Bérenger, "Numerical reflection from FDTD-PMLs: a comparison of the split PML with

the unsplit CFS PML," *IEEE Trans. Antennas Propag.*, vol. 50, no. 3, pp. 258-265, March 2002.

[8] D. Correia and J. Jin, "Performance of regular PML, CFS-PML, and second-order PML for waveguide problems," *Microw. Opt. Technol. Lett.*, vol. 48, no. 10, pp. 2121-2126, Oct. 2006.

[9] D. Correia and J. Jin, "On the development of a higher-order PML," *IEEE Trans. Antennas Propag.*, vol. 53, no. 12, pp. 4157-4163, Dec. 2005.

[10] J. Proakis and D. Manolakis, *Digital Signal Processing: Principles, Algorithms and Applications*, 3rd ed. Englewood Cliffs, NJ: Prentice Hall, 1996.

[11] D. Sullivan, "Frequency-dependent FDTD methods using Z transforms," *IEEE Trans. Antennas Propag.*, vol. 40, no. 10, pp. 1223-1230, 1992.

[12] O. Montazeri, M. Bakr, and Y. Haddara, "A PML for electroacoustic waves in piezoelectric materials using FDTD," *The Applied Computational Electromagnetics Society (ACES) Journal*, vol. 26, no. 6, pp. 464-472, June 2011.

[13] N. Okada and J. Cole, "Nonstandard finite difference time domain algorithm for Berenger's perfectly matched layer," *The Applied Computational Electromagnetics Society (ACES) Journal*, vol. 26, no. 2, pp. 153-159, Feb. 2011.

[14] J. Cole and D. Zhu, "Improved version of the second-order Mur absorbing boundary condition based on a nonstandard finite difference model," *The Applied Computational Electromagnetics Society (ACES) Journal*, vol. 24, no. 4, pp. 375-381, August 2009.

[15] M. Wong and A. Sebak, "The floating PML applied to practical FDTD applications," *The Applied Computational Electromagnetics Society (ACES) Journal*, vol. 23, no. 2, pp. 110-119, June 2008.

[16] M. Inman, A. Elsherbeni, J. Maloney, and B. Baker, "Practical implementation of a CPML absorbing boundary for GPU accelerated FDTD technique," *The Applied Computational Electromagnetics Society (ACES) Journal*, vol. 23, no. 1, pp. 16-22, March 2008.

[17] T. Kaufmann, K. Sankaran, C. Fumeaux, and R. Vahldieck, "A review of perfectly matched absorbers for the finite-volume time-domain method," *The Applied Computational Electromagnetics Society (ACES) Journal*, vol. 23, no. 3, pp. 184-192, Sep. 2008.

[18] N. Feng and J. Li, "Novel and efficient FDTD implementation of higher-order perfectly matched layer based on ADE method," *J. Computat. Phys.*, vol. 232, no. 1, pp. 318-326, Jan. 2013.

[19] G. Fan and Q. Liu, "A well-posed PML absorbing boundary condition for lossy media," *in Proc. IEEE Antennas Propagat. Soc. Int. Symp. Dig.*, vol. 3, pp. 2-5, Boston, MA, July 8–13, 2001. *It is also published in Antennas Wireless Propag. Lett.*, vol. 2, pp. 97-100, 2003.

Naixing Feng received the B.S. degree in Electronic Science and Technology and the M.S. degree in Micro- Electronics and Solid-State electronics from Tianjin Polytechnic University, Tianjin, China, in 2010 and 2013, respectively. He is currently working toward his PhD degree in Radio Physics at Xiamen University, Xiamen. His current research interests include computational electromagnetics and acoustics.

Qing Huo Liu received his B.S. and M.S. degrees in physics from Xiamen University in 1983 and 1986, and Ph.D. degree in electrical engineering from the University of Illinois at Urbana-Champaign in 1989.

His research interests include computational electromagnetics and acoustics, inverse problems, geophysical subsurface sensing, biomedical imaging, electronic packaging, and the simulation of photonic and nano devices. He has published over 500 papers in refereed journals and conference proceedings. He was with the Electromagnetics Laboratory at the University of Illinois at Urbana-Champaign as a Research Assistant from September 1986 to December 1988, and as a Postdoctoral Research Associate from January 1989 to February 1990. He was a Research Scientist and Program Leader with Schlumberger-Doll Research, Ridgefield, CT from 1990 to 1995. From 1996 to May 1999 he was an Associate Professor with New Mexico State University. Since June 1999, he has been with Duke University where he is now a Professor of Electrical and Computer Engineering.

Dr. Liu is a Fellow of the IEEE, a Fellow of the Acoustical Society of America, a member of Phi Kappa Phi, Tau Beta Pi, a full member of U.S. National Committee of URSI Commissions B and F. Currently he serves as the Deputy Editor in Chief of Progress in Electromagnetics Research, an Associate Editor for IEEE Transactions on Geoscience and Remote Sensing, and an Editor for Computational Acoustics. He was a Guest Editor in Chief of Proceedings of the IEEE for a special issue on large-scale computational electromagnetics published in 2013. He received the 1996 Presidential Early Career Award for Scientists and Engineers (PECASE) from the White House, the 1996

Early Career Research Award from the Environmental Protection Agency, and the 1997 CAREER Award from the National Science Foundation.

Chunhui Zhu received the Ph.D. degree in control science and engineering from Harbin Institute of Technology, in 2012. From October 2009 to October 2011, she was with the electrical engineering at Duke University, Durham, NC, as a visiting student. Since January 2013, she has been with Xiamen University, where she is currently an assistant professor of department of electronic science. Her research interest is fast algorithms for computational electromagnetics and their applications in engineering.

Analysis of EM Scattering from 3D Bi-Anisotropic Objects above a Lossy Half Space Using FE-BI with UV Method

J. Zhu [1], M. M. Li [2], Z. H. Fan [2], and R. S. Chen [2]

[1] College of Communications and Information Engineering
Nanjing University of Posts and Telecommunications, Nanjing, 210006, China
zhujian82@njupt.edu.cn

[2] Department of Communication Engineering
Nanjing University of Science and Technology, Nanjing 210094, China
eechenrs@mail.njust.edu.cn

Abstract ─ In this paper, the finite-element boundary integral (FE-BI) method with UV method is applied to analyze the electromagnetic scattering from arbitrary three-dimensional bi-anisotropic objects located above a lossy half space. The form of electric field in bi-anisotropic materials is provided and cast into linear equations by finite element method (FEM), which is valid for any complex materials. The boundary integral equation (BI) is used to truncate the computational domain by using a half-space dyadic Green's function via the discrete complex image method (DCIM). A fast numerical approach, the UV method, is employed to decrease the memory requirement and the total CPU time for FE-BI solution. Numerical results are carried out so as to validate our developed algorithm. Further, the effects of different material parameters on the scattering characteristics of typical bi-anisotropic object in half space are examined and compared.

Index Terms - Bi-anisotropic media, electro-magnetic scattering, FE-BI, half-space, and UV method.

I. INTRODUCTION

Artificial microwave complex materials, including isotropic/bi-isotropic, anisotropic/bi-anisotropic media, have been many potential applications in the fields of antennas, alteration of the radar cross sections, since the media parameter provides an extra degree of freedom to control the scattering properties of targets [1-2].

Many numerical techniques have been extensively studied for investigation of electromagnetic scattering from complex material objects in free space, such as the finite difference time domain method (FDTD) [3], the finite element method (FEM) [4], the method of moment (MoM) [5-7], the volume-surface integral equation (VSIE) [8] and the hybrid finite-element boundary integral method (FE-BI) [9]. However, to the best of our knowledge, very few works are directly related to the applications of numerical methods to investigate complex material objects located above a lossy half space, especially containing the bi-anisotropic media. FDTD and FEM based on differential equation are very flexible in terms of material geometry and composition. However, they are vulnerable to the impact of boundary truncation for scattering analysis [11]. MoM is the most popular approach, which has been developed for the electromagnetic scattering by a 3-D chiral object in the presence of a lossy half space [12, 13]. However, MoM is still quite cumbersome to be applied to the case of strongly inhomogeneous dielectric objects. Moreover, this method relies on the closed-form Green's functions, which are very difficult to obtain for general bi-anisotropic media [12].

The hybrid method FE-BI is well known as a powerful tool to solve the complex scattering problems [9, 10, 14], which deals with the inside fields via FEM flexibly and applies boundary integral equation with an appropriate Green's

Submitted On: Sept. 3, 2012
Accepted On: Oct. 31, 2013

1054-4887 © 2013 ACES

function to truncate the computational domain for the unbounded domain. In this paper, FE-BI has been extended to study electromagnetic scattering from arbitrary bi-anisotropic objects located above a lossy half space. In the boundary integral formulations, one of the most complicated issues is evaluation of the half-space dyadic Green's function [12, 13, 17-20]. Each component of the dyadic is represented in general via a Sommerfield integral (SI), the direct numerical evaluation of which makes a MoM analysis prohibitive. The numerical integration of SI is time consuming since the integrand is both highly oscillating and slowly decaying. Therefore, the discrete complex image method (DCIM) [15] is employed to overcome this difficulty.

However, the final FE-BI system of equations consists of a partly-full, partly-sparse matrix, the equation of that is difficult to solve efficiently for iterative methods. Fortunately, the difficulty can be overcome by use of the fast multipole method (FMM) [16]. In [12, 13, 17, 18], FMM has been extended for general targets in the presence of a lossy half space. The "far" terms are evaluated via an approximation to the dyadic Green's function, using a single appropriately weighted image in the real space [17]. However, this real-image representation of the Green's function is appropriate for expansion when the source and observation points are separated by a wavelength or more [16]. This determines the large minimum group size of the FMM, which leads to a low efficiency. In this paper, the rank-based methods, the multilevel UV method [21] is applied to overcome the above difficulty for the approximation to the half-space Green's function in the "far" terms. The computational complexity and memory requirement of the multilevel UV method is $O(rN\log N)$, where r is the typical rank at the largest level [21]. The multilevel UV method is the impedance matrix decomposition based method and kernel function independent. The half-space Green's function in the "far" terms is evaluated via DCIM, and the multilevel UV method needs only to deal with the final low-ranked far matrix. Thus, the approximation error is controllable via the threshold in the UV matrix compression [21]. The multilevel UV method is easy to be applied in the existing FE-BI code without large change of the algorithms.

The paper is organized as follows. The formulation employed to solve the problem is reported in section II, together with an introduction of the multilevel UV method for FE-BI analysis. In section III, numerical results are carried out so as to validate our developed algorithm. The final remarks are included in section IV.

II. FORMULATION

An arbitrary complex media object above a half space is considered. The relative permittivity and permeability of the object and the lower half-space are denoted by $(\overline{\overline{\varepsilon}}, \overline{\overline{\mu}}, \overline{\overline{\xi}}, \overline{\overline{\zeta}})$ and $(\varepsilon_{gr}, \mu_{gr})$. FEM is used to describe the electric field in volume V. A boundary integral equation about the equivalent electric current **J** and magnetic current **M** on the surface of the object is solved by MoM to complement FEM equations.

A. Weak form of wave equation in complex media

The electric and magnetic fields **E** and **H** radiated by the surface current **J** and **M** in an unbounded bi-anisotropic media are governed by the following constitutive relations [4, 10],

$$\begin{aligned} \mathbf{D} &= \overline{\overline{\varepsilon}} \bullet \mathbf{E} + \overline{\overline{\xi}} \bullet \mathbf{H} \\ \mathbf{B} &= \overline{\overline{\zeta}} \bullet \mathbf{E} + \overline{\overline{\mu}} \bullet \mathbf{H}, \end{aligned} \tag{1}$$

where $\overline{\overline{\varepsilon}}$ and $\overline{\overline{\mu}}$ are the permittivity and permeability tensors, respectively. $\overline{\overline{\xi}}$ and $\overline{\overline{\zeta}}$ are the tensors describing the magnetoelectric coupling effects in bi-anisotropic media. The wave equation has the following equation,

$$\mathcal{L} \bullet \mathbf{E} = -j\omega \mathbf{J}_i \tag{2}$$

where $\mathcal{L} = \left(-\nabla + j\omega\overline{\overline{\xi}}\right) \bullet \overline{\overline{\mu}}^{-1} \bullet \left(\nabla + j\omega\overline{\overline{\zeta}}\right) + \omega^2 \overline{\overline{\varepsilon}}$.

By taking the inner product with test functions E^a both sides of equation (2), then we have the following weak form of vector electric wave equation,

$$\begin{aligned} F\left(\mathbf{E}, \mathbf{E}^a\right) = & < \mu^{-1} \bullet \left(\nabla \times \mathbf{E}^a + j\omega\overline{\overline{\xi}} \bullet \mathbf{E}^a\right), \nabla \times \mathbf{E} + j\omega\overline{\overline{\zeta}} \bullet \mathbf{E} > \\ & + \omega^2 < \mathbf{E}^a, \overline{\overline{\varepsilon}} \bullet \mathbf{E} > - < \mathbf{E}^a, j\omega \mathbf{J}_i > - < j\omega \mathbf{J}_i{}^a, \mathbf{E} > \\ & - j\omega \int \left(\hat{n} \times \mathbf{E}^a\right)^* \bullet \mathbf{H}^{ext} dS. \end{aligned} \tag{3}$$

B. Half-space boundary integral formulation

The electric and magnetic fields outside S can be calculated by the surface boundary integral at the

surface S. As a scatterer, this object is illuminated by a total "incident field" including two components, one is the incident field ($\boldsymbol{E}^{inc}, \boldsymbol{H}^{inc}$) and the other is the reflected field ($\boldsymbol{E}^{ref}, \boldsymbol{H}^{ref}$) in the presence of the half space. The combined-field integral equation (CFIE) is used as follows,

$$\begin{aligned}\hat{t}\cdot\left(\mathbf{E}^{inc}(\mathbf{r})+\mathbf{E}^{ref}(\mathbf{r})\right)=\hat{t}\cdot[&\frac{1}{2}\mathbf{E}(\mathbf{r})+jk_0\iint_S\overline{\overline{\mathbf{K}}}_{ii}^{A}(\mathbf{r},\mathbf{r}')\cdot\mathbf{J}_S(\mathbf{r}')dS'\\&+\frac{j}{k_0}\oiint_S\nabla'\cdot\mathbf{J}_S(\mathbf{r}')\nabla K_{ii}^{\phi e}(\mathbf{r},\mathbf{r}')dS'\\&+\iint_S\nabla\times\overline{\overline{\mathbf{G}}}_{ii}^{F}(\mathbf{r},\mathbf{r}')\cdot\mathbf{M}_S(\mathbf{r},\mathbf{r}')dS'],\end{aligned}\tag{4}$$

$$\begin{aligned}\hat{n}\times\left(\overline{\mathbf{H}}^{inc}(\mathbf{r})+\overline{\mathbf{H}}^{ref}(\mathbf{r})\right)=\hat{n}\times[&\frac{1}{2}\overline{\mathbf{H}}(\mathbf{r})+jk_0\iint_S\overline{\overline{\mathbf{K}}}_{ii}^{F}(\mathbf{r},\mathbf{r}')\cdot\mathbf{M}_S(\mathbf{r}')dS'\\&+\frac{j}{k_0}\oiint_S\nabla'\cdot\mathbf{M}_S(\mathbf{r}')\nabla K_{ii}^{\phi m}(\mathbf{r},\mathbf{r}')dS'\\&-\iint_S\nabla\times\overline{\overline{\mathbf{G}}}_{ii}^{A}(\mathbf{r},\mathbf{r}')\cdot\mathbf{J}_S(\mathbf{r},\mathbf{r}')dS'],\end{aligned}\tag{5}$$

where $\mathbf{J}_S=\eta\hat{n}\times\mathbf{H}$ and $\mathbf{M}_S=\mathbf{E}\times\hat{n}$ are the electric current and the equivalent magnetic current over the surface S, respectively. $\overline{\overline{\mathbf{K}}}_{ii}^{A}, \overline{\overline{\mathbf{G}}}_{ii}^{F}, \overline{\overline{\mathbf{K}}}_{ii}^{F}, \overline{\overline{\mathbf{G}}}_{ii}^{A}$ and $K_{ii}^{\phi e}$ and $K_{ii}^{\phi m}$ are the dyadic and the scalar Green's functions for the half-space region, which can be evaluated efficiently via the complex-image technique [15].

RWG [22] and Whitney basis functions [23] are used to expand the current and electric field. Combining equations (3) to (5), the final FE-BI matrix equation is obtained,

$$\begin{bmatrix}K_{II} & K_{IS} & 0\\ K_{SI} & K_{SS} & B\\ 0 & P & Q\end{bmatrix}\begin{Bmatrix}E_I\\ E_S\\ J_S\end{Bmatrix}=\begin{Bmatrix}0\\ 0\\ b\end{Bmatrix}\tag{6}$$

where $\{E_i\}$ is a vector containing the discrete electric field inside V, $\{E_S\}$, and $\{J_S\}$ are vectors containing the discrete electric and current on S, respectively, and finally K_{II}, K_{IS}, K_{SI}, K_{SS}, and B denote the corresponding highly sparse FEM matrices, and {b} is a vector related to the incident field.

C. The multilevel UV method

The dense matrices [P] and [Q] generated by BI equation, which is a bottleneck of the FE-BI method that severely limits the capability of the FE-BI method in dealing with large objects. However, with the discrete complex image, the half-space Green function can be expanded to the exponential form, and then the half-space Green function varies smoothly with distance. Therefore, by grouping with the octree structure, similar to [18, 21], the dense matrices [P] and [Q] can split into many low-rank submatrix blocks, which can be low rank compression. In this paper, the multilevel UV method is applied to reduce the computational complexity and memory requirement of the BI part.

The multilevel UV method is a rank-based method. Generally, the interaction matrix is full-ranked when the observation groups are in the near field of the source group, while the interaction matrix between them is low-ranked when the observation groups are in the far field. Application of the UV decomposition to the low-ranked impedance matrix will result in significant memory and computational time savings. The basic principles of the UV decomposition can be found more detail in [21].

The whole object is divided into levels with the octree algorithm. Figure 1 illustrates a three level octree structure for a two-dimensional domain. The highest level has four blocks and the lowest level has $4l$ blocks where l is the number of levels. As proposed in [16], for the observation block (block 1) at level-1, the corresponding impedance matrix **Z**, which refers to the matrices [P] and [Q] in FE-BI, can be decomposed into l (l is the number of levels) sparse matrices,

$$\mathbf{Z}=\mathbf{Z}^0+\mathbf{Z}^1+\cdots+\mathbf{Z}^{l-1},\tag{7}$$

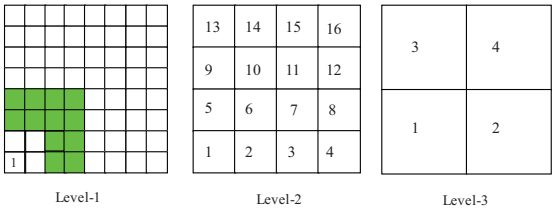

Fig. 1. A three level octree structure.

Since Z^0 is the near impedance matrix for the interactions of self and neighboring blocks at level-1, Z^0 is full-ranked and stored directly. Z^1 and so forth are the impedance matrices for the interactions of the far field, which is defined as the parent block's near field and the current block's far field. As shown in Fig. 1, the far field of block 1 at level-1 is the blocks 2, 5, and 6 at level-2 , since block 1 at level-2 is the parent block of block 1 at level-1 and the blocks 2, 5, and 6 are the neighbors of block 1 at level-2. Similarly, the far field of block 1 at level-1 is the region of blocks 3, 4, and 2 at level-3. The far field interactions are only evaluated at the peer level. The concept of the far field used above is

the same as it in the multilevel fast multipole algorithm (MLFMA) [16].

For Z^1 and so forth, the matrices are operated with two different ways according to their size, when applying the UV method. When the size of the matrix is small, it will be computed directly and its rank r is evaluated by singular value decomposition (SVD), then the **U** and **V** matrixes can be obtained. When the size of the matrix is large, the column and row sampling according to rank estimates is performed and SVD on the sampled matrix is implemented instead. So it should be noted that average ranks of the matrix blocks and the approximation precision increase by the decrease of truncation error. In the code, the rank of the first pair of groups is evaluated and the others are assumed the same as the first pair to further reduce the time for evaluating the rank. The above technique is feasible, since only the coarse estimation of the rank is needed in the UV algorithm [21]. The $m \times n$ matrix is then decomposed into **U**($m \times r$) and **V**($r \times n$) matrices, which leads to the significant time and memory savings when the matrix is low-ranked.

III. NUMERICAL RESULTS AND DISCUSSIONS

In this section, numerical examples are considered to demonstrate the accuracy and flexibility of our FE-BI algorithm for the analysis of electromagnetic scattering from arbitrary objects in half space. For the precision of the UV method. The truncation error of SVD is 1e-4 in the codes for these numerical examples. All numerical experiments are performed on a Pentium 4 with 2.9 GHz CPU and 2 GB RAM in double precision.

At first, Fig. 2 shows the bistatic scattering cross section of a bi-isotropic chiral sphere in the case of VV-polarizations. The chiral sphere is situated 40 cm above a lossy half space with a diameter of 0.6 m. The half space is characterized by ε_{gr} = 5.0 – j0.2 and σ_g = 0.01 S/m and at 300 MHz. The total number of unknowns is 45227 consisting of 40700 for the finite-element discretization and 4527 for BI. Two-level UV method is employed with the minimum group size 0.076 λ_0. The chiral body is assumed to have a relative chirality ξ_r and parameters $\varepsilon = \varepsilon_0\varepsilon_r / \left(1-\xi_r^2\right)$, $\mu = \mu_0\mu_r / \left(1-\xi_r^2\right)$, $\xi = -j\sqrt{\varepsilon\mu}\xi_r / \left(1-\xi_r^2\right)$, $\zeta = -\xi$, where $\varepsilon_r = 3.0$, $\mu_r = 1.0$ and $\xi_r = 0.3, 0.5, 0.8$. As shown in Fig. 2, the numerical results of the bistatic RCS is compared with those obtained by MoM [12]. It is obvious that an excellent agreement is obtained between them. Therefore, our algorithm has been proven to be accurate enough. The efficiency of the UV method for FE-BI solution is verified by comparing with the FE-BI without UV method. It takes 798.3 minutes to compute using FE-BI without UV method but only 265.2 minutes are need for the UV method. The memory requirement is 625.41 MB for BI part without UV method, but 211.38 MB for BI part with UV method.

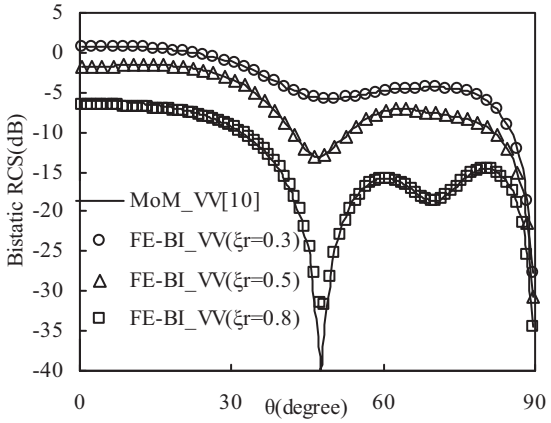

Fig. 2. Bistatic scattering cross section in the case of VV-polarization of a homogeneous chiral sphere above a lossy half space.

To validate our algorithm for computing the electromagnetic scattering of bi-anisotropic targets, the scattering cross section of a bi-anisotropic omega cylinder is computed and compared to the results in [10]. The bi-anisotropic omega media has constitutive tensors are in the form as follows,

$$\overline{\overline{\varepsilon}} = \varepsilon_0 \begin{bmatrix} \varepsilon_1 & 0 & 0 \\ 0 & \varepsilon_2 & 0 \\ 0 & 0 & \varepsilon_3 \end{bmatrix}, \quad \overline{\overline{\mu}} = \mu_0 \begin{bmatrix} \mu_1 & 0 & 0 \\ 0 & \mu_2 & 0 \\ 0 & 0 & \mu_3 \end{bmatrix}, \quad (8)$$

$$\overline{\overline{\xi}} = \begin{bmatrix} 0 & 0 & 0 \\ -j\Omega & 0 & 0 \\ 0 & 0 & 0 \end{bmatrix}, \quad \overline{\overline{\zeta}} = \begin{bmatrix} 0 & j\Omega & 0 \\ 0 & 0 & 0 \\ 0 & 0 & 0 \end{bmatrix},$$

where $\varepsilon_1 = 2.0, \varepsilon_2 = 3.0, \varepsilon_3 = 2.0$, $\mu_1 = 1.2, \mu_2 = 1.2, \mu_3 = 1.0$ and Ω = 0.0, 0.5, and 1.0. Figures 3 and 4 show the bistatic scattering cross section of the finite omega cylinder in a free space, in the case of VV- and HH-polarizations [10]. The cylinder is meshed

into 4948 triangles and 34317 tetrahedrons. In Fig 3, the results obtained by our algorithm are in good agreement with those in [10].

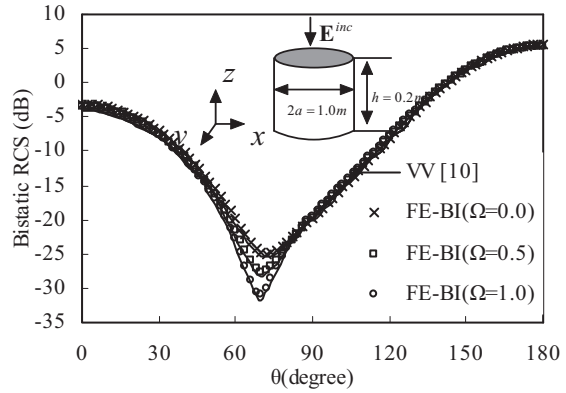

Fig. 3. Bistatic scattering cross section of a finite omega cylinder in free space in the case of VV-polarization.

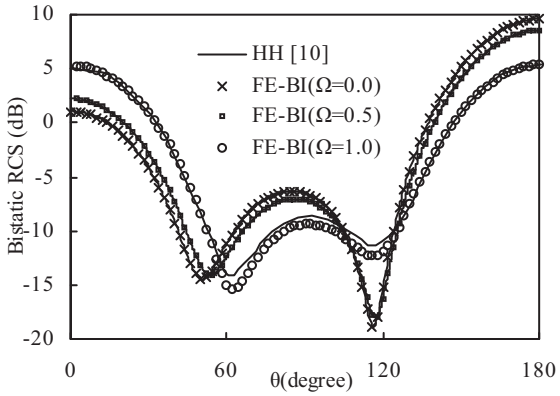

Fig. 4. Bistatic scattering cross section of a finite omega cylinder in free space in the case of HH-polarization.

Further, the bistatic scattering cross sections of the cylinder located at 0.3 m above a half space is studied via the FE-BI, as shown in Fig. 5. In the solution of FE-BI, two-level UV method is employed with the minimum group size 0.126 λ. The efficiency of the UV method for FE-BI solution is verified by comparing with the FE-BI without UV method. It takes more than 24 hours to compute using FE-BI without UV method but only 594.3 minutes are needed for the UV method. The memory requirement is 1.681 GB for BI part without UV method, but 387.28 MB for BI part with UV method.

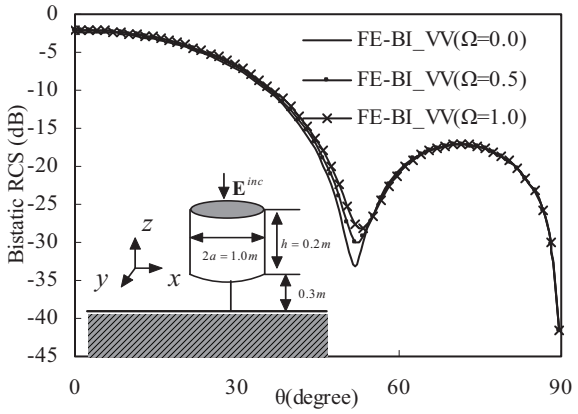

Fig. 5. Bistatic scattering cross section of a finite omega cylinder in half space in the case of VV-polarization.

Figure 5 at first shows the bistatic scattering cross section in the case of VV-polarization. It is shown that the Ω parameter has little effect on the scattering pattern in half space as well as in free space, shown in Fig. 3. As shown in Fig. 4, for the HH-polarization, the scattering pattern in free space can be modified effectively by the Ω parameter. However, as shown in Fig. 6, for the HH-polarization, the Ω parameter has less effect on the scattering pattern in half space than it has in free space. Moreover, it is interesting to note that the values of the HH-polarization RCS in free space increase with increasing magnitude of the Ω parameter, as observed in Fig. 4. However, the values of the HH-polarization RCS in half space slightly decrease with the increasing magnitude of the Ω parameter, as observed in Fig. 6. Of course, the scattering characteristics of a bi-anisotropic object depend on the combination of many different parameters, such as the four constitutive tensors, the incident wave form, the direction and polarization state etc. [10].

IV. CONCLUTION

In this paper, the FE-BI method has been developed for the analysis of electromagnetic scattering from arbitrary bi-anisotropic objects located above a lossy half space. The accuracy of the proposed method has been proven by comparison with published data. The multilevel UV method has been successfully applied to FE-BI to decrease the memory requirement and CPU time of solution. The effect of bi-anisotropic

parameters on the scattering characteristics is examined by considering the canonical examples. The present analysis shows that for VV-polarization scattering pattern, the bi-anisotropic parameters have less effect either in free space or half space. For HH-polarization scattering pattern, the bi-anisotropic parameters have great effect in free space, but it has actually little effect in free space in this analysis. Further, the present analysis may be useful in choosing appropriate bi-anisotropic materials to control the scattering characteristics in half space.

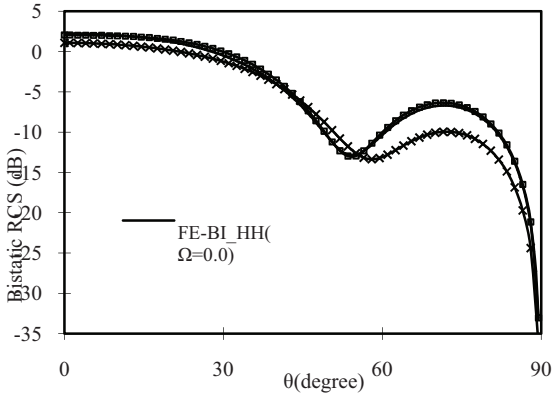

Fig. 6. Bistatic scattering cross section of a finite omega cylinder in half space in the case of HH-polarization.

ACKNOWLEDGMENT

This work was supported in part by Jiangsu Natural Science Foundation of BK2011757 and Jiangxi Natural Science Foundation of 20122BAB211018.

REFERENCES

[1] J. Volakis, A. Chatterjee, and L. Kempel, *Finite Element Method for Electromagnetics: Antennas, Microwave Circuits and Scattering Applications*, IEEE Press, New York, 1998.

[2] F.-G. Hu, C.-F. Wang, and Y.-B. Gan, "Efficient calculation of electromagnetic scattering from cavities coated with bianisotropic media using FE-BI method with higher-order tetrahedral elements," *IEEE Antennas and Propagation Society International Symposium*, pp. 3883-3886, July 2006.

[3] A. Semichaevsky, A. Akyurtlu, D. Kern, D. Werner, and M. Bray, "Novel BI-FDTD approach for the analysis of chiral cylinders and spheres," *IEEE Trans. Antennas Propag.*, vol. 54, no. 3, pp. 925-932, March 2006.

[4] F. Bilotti, L. Vegni, and A. Toscano, "Radiation and scattering features of patch antennas with bianisotropic substrates," *IEEE Trans. Antennas Propag.*, vol. 51, no. 3, pp. 449-456, March 2003.

[5] D. Wang, P. Lau, E. Yung, and R. Chen, "Scattering by conducting bodies coated with bi-isotropic materials," *IEEE Trans. Antennas Propag.*, vol. 55, no. 8, pp. 2313-2319, Aug. 2007.

[6] D. Worasawate, J. Mautz, and E. Arvas, "Electromagnetic scattering from an arbitrarily shaped three-dimensional homogeneous chiral body," *IEEE Trans. Antennas Propag.*, vol. 51, no. 5, pp. 1077-1084, 2003.

[7] I. Bogaert, "Accurate computation and tabulation of the scalar Green function for bi-anisotropic media and its derivatives," *28th Annual Review of Progress in Applied Computational Electromagnetics*, pp. 422-426, Columbus, Ohio, April 2012.

[8] X. Deng, C. Gu, and Y. Zhou, "Electromagnetic scattering by arbitrary shaped three-dimensional conducting objects covered with electromagnetic anisotropic materials," *Applied Computational Electromagnetics Society Journal*, vol. 26, no. 11, pp. 886-892, Nov. 2011.

[9] X. Yuan, D. Lynch, and J. Strohbehn, "Coupling of finite element and moment methods for electromagnetic scattering from inhomogeneous objects," *IEEE Trans. Antennas Propagat.*, vol. 38, pp. 386-393, March 1990.

[10] Y. Zhang, X. Wei, and E. Li, "Electromagnetic scattering from three-dimensional bianisotropic objects using hybrid finite element-boundary integral method," *J. of Electromagn. Waves and Appl.*, vol. 18, no. 11, pp. 1549-1563, 2004.

[11] S. Caorsi and R. Raffetto, "Perfectly matched layers for the truncation of finite-element meshes in layered half-space geometries and applications to electromagnetic scattering by buried objects," *Microwave Opt. Technol. Lett.*, vol. 19, no. 6, pp. 427-434, Dec. 1998.

[12] X. Wang, D. Werner, L.-W. Li, and Y.-B. Gan, "Interaction of electromagnetic waves with 3-D arbitrarily shaped homogeneous chiral targets in the presence of a lossy half space," *IEEE Trans. Antennas Propag.*, vol. 55, no. 12, Dec. 2007.

[13] R. Chen, Y. Hu, Z. Fan, D. Ding, D. Wang, and E. Yung, "An efficient surface integral equation solution to EM scattering by chiral objects above a lossy half space," *IEEE Trans. Antennas Propagt.*, vol. 57, no. 11, pp. 3586-3593, Nov. 2009.

[14] G. Pelosi, G. Toso, and R. Coccioli, "Finite-element boundry-integral analysis of electromagnetic scattering by a buried dielectric object," *Microwave and Optical Technology Letters*, vol. 24, no. 6, March 2000.

[15] D. Fang, J. Yang, and G. Delisle, "Discrete image theory for horizontal electric dipole in a multilayer medium," *Proc. Inst. Elect. Eng. H*, vol. 135, no. 5, pp. 297-303, Oct. 1988.
[16] W. Chew, J. Jin, E. Midielssen, and J. Song, *Fast and Efficient Algorithms in Computational Electromagnetics*, Boston, MA: Artech House 2001.
[17] Z. Liu, J. He, Y. Xie, A. Sullivan, and L. Carin, "Multilevel fast multipole algorithm for general targets on a half-space interface," *IEEE Trans. Antennas Propag.*, vol. 50, no. 12, pp. 1838- 1849, Dec. 2002.
[18] M. Li, H. Chen, C. Li, R. Chen, and C. Ong, "Hybrid UV/MLFMA analysis of scattering by PEC targets above a lossy half-space," *Applied Computational Electromagnetics Society Journal*, vol. 26, no. 1, pp. 17-25, Jan. 2011.
[19] D. Ding, J. Ge, and R. Chen, "Well-conditioned CFIE for scattering from dielectric coated conducting bodies above a half-space," *Applied Computational Electromagnetics Society Journal*, vol. 25, no. 11, pp. 936-946, Nov. 2010.
[20] L. Felsen and N. Marcuvitz, *Radiation and Scattering of Waves Piscataway*, NJ: IEEE Press ch. 4, 1996.
[21] L. Tsang, Q. Li, P. Xu, D. Chen, and V. Jandhyala, "Wave scattering with UV multilevel partitioning method: 2. Three-dimensional problem of nonpenetrable surface scattering," *Radio Sci.*, vol. 39, pp. RS5011, 2004.
[22] S. Rao, D. Wilton, and A. Glisson, "Electromagnetic scattering by surfaces of arbitrary shape," *IEEE Trans. Antennas Propag.*, vol. 30, pp. 409-418, 1982.
[23] J. Jin, *The Finite Element Method i n Electromagnetics. 2nd ed.,* New York: John Wiley & Sons, Inc., 2002.

Jian Zhu received the B.S. and Ph.D degrees in electromagnetic fields and microwave technology from Nanjing University of Science and Technology (NUST), China, in 2004 and 2010, respectively.
She is currently a lecturer of Nanjing University of Posts and Telecommunications. Her current research interests include CEM and antennas.

Meng-Meng Li was born in Jiangsu Province, the People's Republic of China in 1984. He received B.S. degree in physics from Huaiyin normal college in 2007, and is currently working toward the PH.D. degree at Nanjing University of Science and Technology. His research interests focus on fast solution of integral equations, modeling of microwave integrated circuits and UWB antennas.
Mr Li received the student paper award from the 2012 International Conference on Microwave and Millimeter Wave Technology.

Z. H. Fan was born in Jiangsu, China, in 1978. He received the M.Sc and Ph.D degrees in electromagnetic field and microwave technique from Nanjing University of Science and Technology (NJUST), Nanjing, China, in 2003 and 2007, respectively. During 2006, he was with the Center of wireless Communication in the City University of Hong Kong, Kowloon, as a Research Assistant. He is currently a Lecturer with the Electronic Engineering of NJUST. He is the author or coauthor of over 20 technical papers. His current research interests include computational electromagnetics, electromagnetic scattering and radiation.

Ru-shan Chen received the B.S. and M.S. degrees in electronic from Southeast University, China, in 1987 and 1990, respectively, and the Ph.D. degree from the Department of Electronic Engineering, City University of Hong Kong (CUHK), Hong Kong SAR, China, in 2001. In 1990, he joined the Department of Electronic Engineering, Nanjing University of Science and Technology (NUST), China. Since 1996, he has been a Visiting Scholar with the Department of Electronic Engineering, CUHK. In 1999, he was promoted Full Professor of NUST, and in 2007, he was appointed Head of the Department of Communication Engineering.
His research interests mainly include CEM and millimeter wave systems. He has authored or coauthored more than 200 papers, including over 140 papers in international journals. Dr. Chen is the recipient of the Foundation for China Distinguished Young Investigators in 2003. In 2008, he became a Chang-Jiang Professor under the Cheung Kong Scholar Program of China.

Linear Dielectric Resonator Array Fed by N-Way Bow-Tie Shaped Dielectric Resonator Power Divider

L. Hady Salman [1], A. Kishk [2], and D. Kajfez [1]

[1] Department of Electrical Engineering, The University of Mississippi, MS 38677, USA
[2] Department of Electrical and Computer Engineering, Concordia University,
Montreal, QC, Canada H3G 1M8
kishk@encs.concordia.ca

***Abstract*–**The concept of using high order modes of a bow-tie shaped dielectric resonator in the design of N-way power divider is presented in this paper. The design of 6-way power divider operating at X-band frequency range is illustrated, simulated and tested for concept validation. The combination of probe type excitation and microstrip technology is used to excite an H-polarized resonating mode around 10 GHz. Both input matching and in phase tapered power distribution are experimentally maintained within 150 MHz frequency band around the resonant frequency. Measured scattering parameters magnitude and phase of the proposed 7-port structure are shown to verify the expected simulation results. Also, the proposed power divider is used to excite an antenna array of six rectangular dielectric resonators using narrow slots coupled to the power divider output through microstrip lines. Good agreement between simulated and measured results is obtained for application validation.

***Index Terms*–**Antenna array feed, bow-tie shaped dielectric resonators, higher-order modes, power divider, and X-band.

I. INTRODUCTION

Dielectric resonators (DRs) have been used in the design of microwave components such as microwave filters and stabilized oscillators [1-3]. These ceramic resonators are made of low loss, temperature-stable and of high dielectric constant materials [4-5]. However, for antenna applications, such dielectric resonators can be of low radiation Q-factor. Hence, high radiation efficiency device characteristics are obtained [6-8]. All these properties made them suitable for multi- functional applications as either radiator and/or resonator for microwave circuits [9-12].

High-order mode dielectric resonators were studies for several years due to their desirable properties in the design of microwave and millimeter devices. They have been used for measurements of dielectric loss tangent and for sensing applications in the microwave and millimeter wave regions due to their high Q-factor and strong field concentration in the surrounding area of the dielectric boundaries [13-14]. Among such high-order modes are the so-called dielectric resonator whispering-gallery modes (WGMs), which are usually travelling along the dielectric resonator's boundary with oscillating field distributed between the outer boundary and the inner caustic of the resonator.

These high-order modes have practical use in many optical, millimeter and even sub-millimeter electronic systems [15]. Recent research work was devoted in the use of such H-polarized WGM in the design of N-way microwave power divider with equal in-phase and out-of-phase power distribution [16-17]. The objective of this work is to investigate the availability of exciting an H-polarized high order mode with high radial index to be used in the design of microwave tapered power divider.

In this paper, an extension to [18] for a bow-tie shaped dielectric resonator operating in the H-polarized high-order radial field variation mode is presented. The bow-tie shaped dielectric resonator is enclosed by cylindrical cavity to obtain an N-ports microwave power divider. The resonator is placed on top of a rectangular ground plane and excited by microstrip feeding network to be

Submitted On: Feb. 20, 2012
Accepted On: March 16, 2013

1054-4887 © 2013 ACES

printed on a microwave substrate and coupled to the dielectric resonator through conducting probes penetrating inside the resonator at certain designed positions with fixed heights. An early stage of fabricating the physical layout for the proposed structure is shown in Fig. 1 for 6-way power divider. The proposed design is assumed to produce in-phase tapered power distribution at the output ports while the spacing distance between the adjacent output ports are kept to be half wavelength apart to feed linear antenna array.

A brief description of the proposed geometry and the design procedure using ANSYS HFSS commercial software [19] are provided in section II. In section III, simulated results are compared with the measured results for further concept validation in addition to demonstrating the advantages of using shielded cavity resonator to suppress radiation losses and enhance the coupling to the resonating mode. In section IV, the design of 6-elements linear rectangular dielectric resonator antenna array is described.

II. DESCRIPTION OF PROPOSED POWER DIVIDER

The proposed X-band power divider geometry is shown in Fig. 2. The bottom layer is sketched in solid lines while the top layer is in dashed lines to have a better understanding of the designed configuration. The proposed power divider consists of a bow-tie shaped dielectric resonator with 24 mm sector radius, 5 mm height, and 23° sector angle placed on top of a rectangular RT/duroid 6010LM dielectric substrate with dielectric constant 10.2 and 0.625 mm thickness. The resonator is exposed to the grounded side of the microstrip feeding network.

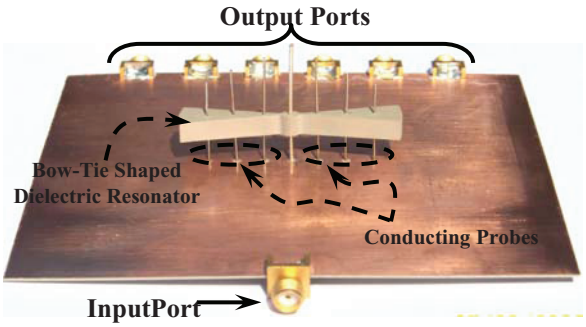

Fig. 1. Early fabrication stage for the proposed X-band 6-way power divider using bow-tie shaped dielectric resonator (side view).

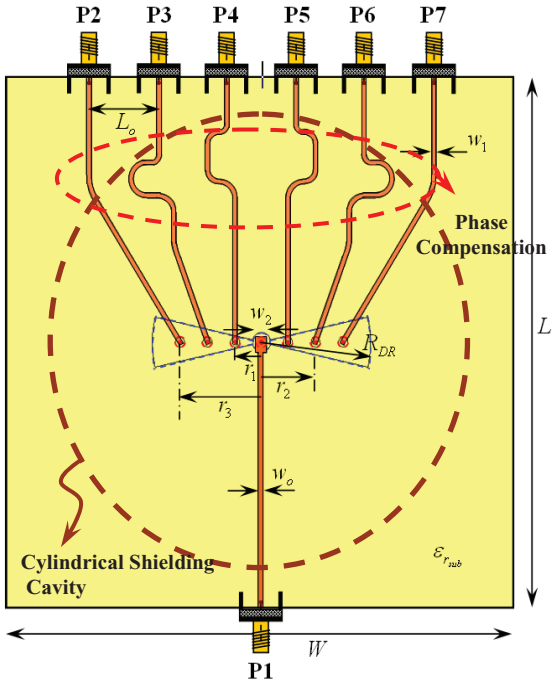

Fig. 2. Bottom view of the proposed X-band 6-way tapered higher order dielectric resonator power divider.

The design procedure was done in two successive phases. The first phase focused on the design of the dielectric resonator and compromises its shape to meet the desired specifications. The second phase involved the design of the microstrip feeding network that is printed on the other side of the dielectric substrate. In phase and symmetrical tapered power distribution are obtained at the different output ports while acceptable impedance matching at the input port is achieved as shown in Fig. 2. This power divider is more compact in size compared to other traditional power dividers. The design is not restricted to 2^n-output ports.

It is important to understand the electrical nature of the excited higher order mode to help in choosing the dielectric resonator's shape and the appropriate excitation or coupling technique. A sector-shaped dielectric resonator is designed and excited through coaxial probe at the center. Thus, higher-order transverse magnetic mode with three radial magnetic loops on each side of the probe and of different field strength are recognized around 10 GHz.

For transverse magnetic modes with larger radial mode index, the magnetic field lines are circularly oriented with successive out of phase

field loops (in y-axis). The number of these loops is equal to the radial index of the excited mode, which are three in this case. Due to the fact that symmetrical tapering scheme is required, a bow-tie shaped resonator is suggested as shown in Fig. 1. The magnetic field distribution inside the bow-tie shaped dielectric resonator at the resonant frequency of the excited mode is shown in Fig. 3, where out-of-phase magnetic field loops are observed while exciting the resonator from port 1 and terminating the other ports with matched loads.

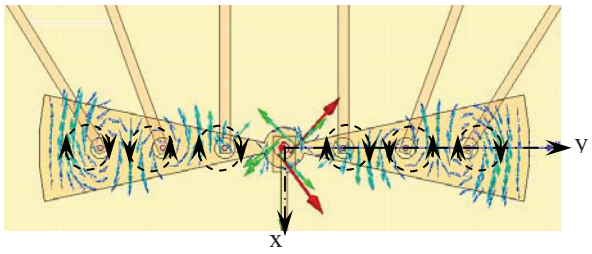

Fig. 3. Magnetic field representation of the excited high-order dielectric resonator mode inside the bow-tie shaped resonator at 10 GHz.

An easy method to couple with the H-polarized high-order mode is by using coaxial probes as reported in [16]. Conducting probes are inserted inside the dielectric resonator at the center of each magnetic loop. Parametric studies were conducted at the beginning to obtain the proper positioning and height of the six conducting probes for acceptable coupling to the resonating mode while maintaining the probe radius to be 0.27 mm. The conducting probes were placed at distances of 6, 12, and 18 mm away from the center of the resonator as shown in Figs. 1, and 3. It was found that the optimum length of the conducting probes to penetrate inside the resonator, ***Hp***, is 1 mm for appropriate coupling to the desired mode. The design of the non-radiating microstrip feeding network on the bottom side of the dielectric substrate was modeled. Conducting "vias" were used to connect between the inserted probes and the open ended terminals of the non-radiating microstrip lines.

The output ports were connected to three pairs of symmetrical microstrip lines around the x-axis from the other side of the dielectric substrate with 50 Ω SMA connectors as shown in Fig. 2. The input port was also connected to a microstrip pad of width w_2. In-phase power distribution at the output ports was obtained by introducing different sections of meandering lines as part of the feeding network design. The spacing distance, L_o, between the successive adjacent ports is kept to be half a wavelength around 10 GHz for the antenna array application. Table I lists all the design parameters that have been used in Fig. 2. Since it was stated in previous work [16-17] that radiation losses from the bow-tie shaped dielectric resonator are significant, a cylindrical conducting cavity of 45 mm radius and 10 mm height was used to shield the resonator and prevent any radiation losses as shown in Fig. 4. The cavity design parameters were chosen while maintaining acceptable impedance matching at the input port while reducing any disturbance to the excited mode due to the designed shielding cavity.

Table I: The proposed 6-way power divider design parameters.

Design Parameter	Parameter Value (mm)	Design Parameter	Parameter Value (mm)
W	110	w_o	0.6
L	110	w_1	1
L_o	15	w_2	2.2
r_1	6	r_3	18
r_2	12	R_{DR}	24

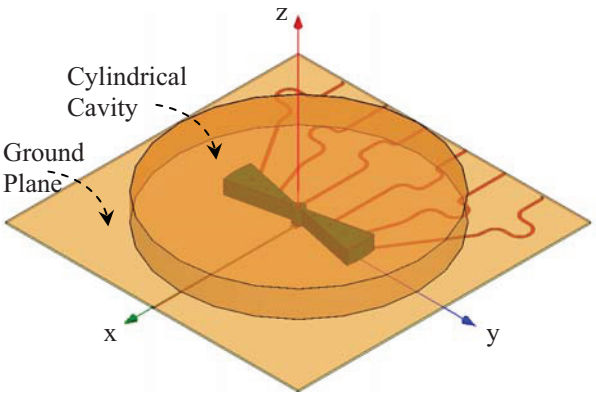

Fig. 4. Illustration of simulated 6-way power divider with the proposed cylindrical shielding cavity to suppress the radiation losses of the bow-tie dielectric resonator.

III. POWER DIVIDER RESULTS

A homemade bow-tie shaped dielectric resonator was machined according to the selected design parameters listed in Table I. The resonator was machined to have three holes of 0.27mm

radius at each side of the resonator while the middle hole was of 1 mm radius to host the input probe. Measurements were conducted on the fabricated design for verification.

Figure 5 illustrates the simulated and measured scattering parameters of the power divider. It can be noticed that tapering in the coupled power is achieved within the range of 2dB between the different output ports. The concept of using the bow-tie resonator was intended to achieve tapering for the power. However, the measured tapering level was smaller than anticipated. It could be controlled further by changing the probes' lengths, but this will add to the practical difficulty of adjusting the probe's length with our in house limited facilities.

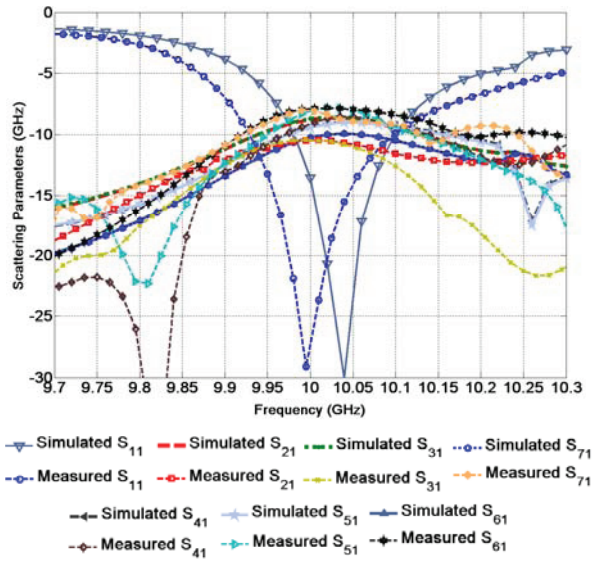

Fig. 5. Measured and simulated reflection and coupling coefficients for the shielded 7-port X-band in-phase power divider.

The advantages of the resonant-type power divider are the high efficiency of the power distribution and the assurance that the output signals are exactly in-phaseor out-of-phase with respect to each other before entering the microstrip lines feeding network. Assuming that the input source andthe output ports are properly matched, the efficiency of the power divider can be obtained as,

$$\eta = \frac{\sum_{i=2}^{7} |S_{1i}|^2}{1 - |S_{11}|^2}. \quad (1)$$

By using the measured values of the scattering parameters shown in Fig. 5, the efficiency at 10 GHz comes out to be 62 %. It is believed that a significant portion of the losses occurs in the microstrip feeding network. In addition, phase measurements were also done for the different ports with respect to the input port and compared with the simulated results as shown in Fig. 6. Differences between the simulated and measured results can be noticed, which could be attributed to the fabrication tolerances.

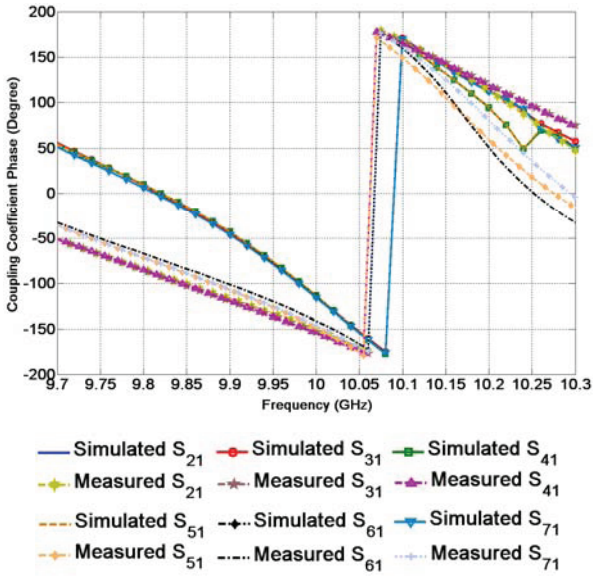

Fig. 6. Comparison between the measured and simulated coupling coefficients phase with respect to the input ports.

IV. ANTENNA ARRAY RESULTS

A rectangular dielectric resonator with length, L_{DR}, width, W_{DR}, and height, H_{DR} is placed on a rectangular ground plane and excited with rectangular narrow slot to resonate at 10 GHz. The slot is of length L_s and width W_s and is excited by a microstrip line that is terminated by an open stub of length L_t beyond the middle of the narrow slot as shown in Fig. 7. The proposed power divider is used as a feeder for the modeled linear rectangular DRA array. The spacing between the elements is maintained to be half a wavelength at 10 GHz.

The reflection coefficient of a single element is shown in Fig. 8 (a), and the radiation pattern of a single element over a finite ground plane is shown in Fig. 8 (b). All the dimensions are listed in Table II.

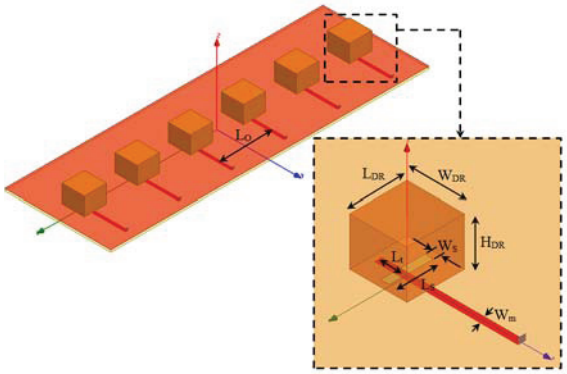

Fig. 7. Proposed rectangular dielectric resonator antenna array excited with narrow slots and coupled to microstrip feeding network.

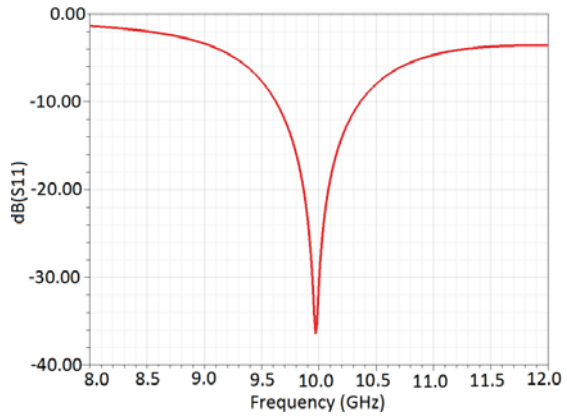

(a)

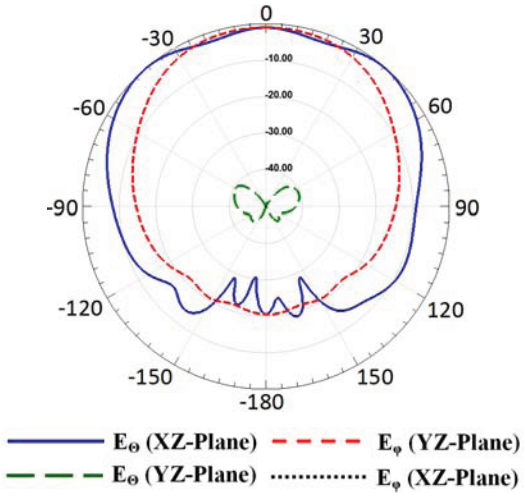

(b)

Fig. 8. Simulated results for a single rectangular DRA element excited by a narrow slot: (a) antenna reflection coefficient and (b) far filed radiation patterns.

Table II: Dimensions of single element DRA.

Design Parameter Symbol	Parameter Value (mm)	Design Parameter Symbol	Parameter Value (mm)
L	151.25	L_S	4.6
W	165	W_S	0.9
L_{DR}	6.3	L_t	6.375
W_{DR}	6.3	W_m	0.8
H_{DR}	5	D	14.73
R_{Cavity}	45	H_{Cavity}	10

Finally, Fig. 9 illustrates the complete design configuration simulated using ANSYS HFSS commercial software [19]. The physical layout of the antenna array with the proposed power divider in its final presentation is shown in Fig. 10 from both top and bottom views.

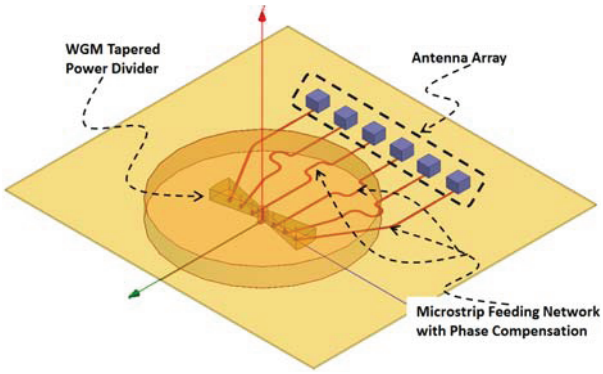

Fig. 9. Simulated rectangular DRA array fed by the proposed X-band power divider based on bow-tie shaped dielectric resonator.

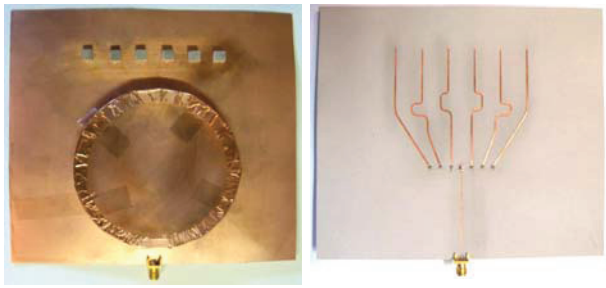

Fig. 10. Top and bottom views of the array and the power divider.

Figure 11 shows the measured and simulated reflection coefficients of the final proposed design configuration shown in Fig. 10. Acceptable matching to input impedance with 100 MHz impedance bandwidth around the designed resonant frequency is achieved. In addition, simulated and measured far field radiation patterns at 10 GHz for the designed array fed with the proposed power divider are shown in Fig. 12.

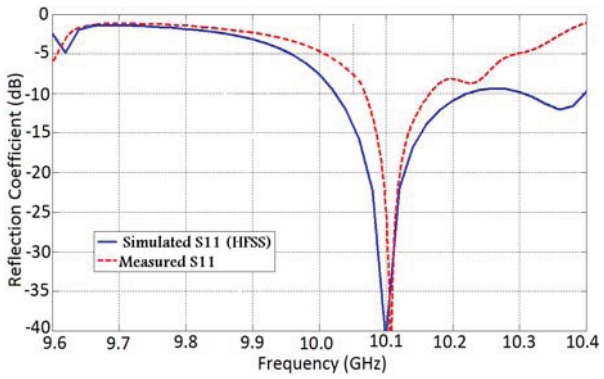

Fig. 11. Measured and simulated input reflection coefficient of the proposed rectangular DRA array fed by the 7-way power divider.

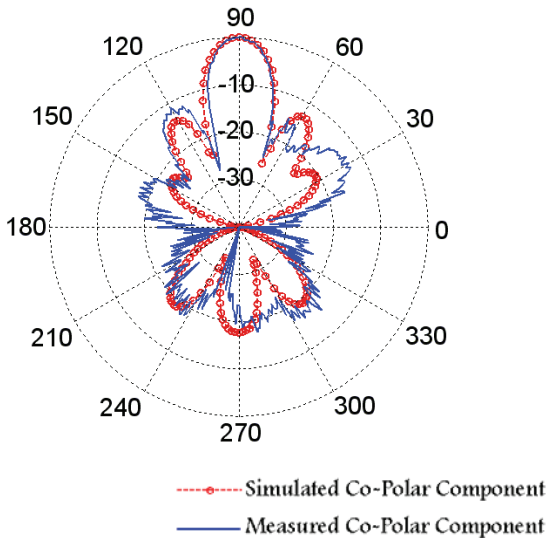

Fig. 12. Measured and simulated far field radiation patterns of the proposed antenna array.

Broadside type of radiation pattern with 12 dB side lobe level is achieved as shown in Fig. 12. Based on HFSS results, the computed directivity is 11.6 dB and the gain is 11.5 dB indicating very high radiation efficiency. As mentioned before, the tapering level can be controlled by the probe lengths or by the radial position of the probes from the center of the bow-tie resonator. These are possible techniques that can be investigated in the future.

V. CONCLUSION

An X-band high-order bow-tie shaped dielectric resonator enclosed by a cylindrical cavity was designed, built, and tested to perform as a 7-way tapered power divider. The excitation of the transverse magnetic mode was carried out by using microstrip feeding technology integrated with probe coupling technique. The amplitudes of both reflection and transmission coefficients were measured and compared with the simulated results. In addition, phase measurements were also done for the transmission coefficients. Finally, the application of the proposed power divider was demonstrated in feeding 6-element rectangular dielectric resonator antenna array. Antenna array reflection coefficient and far field radiation patterns were obtained and compared with measured data.

ACKNOWLEDGEMENT

This work was supported by the National Science Foundation under grant no. ECS-524293. The authors would like to acknowledge Rogers Corporation for providing free laminates of microwave substrates (http://www.rogerscorporation.com).

REFERENCES

[1] D. Kajfez and P. Guillon, Dielectric Resonators, Atlanta GA: Noble Publishing Co., 1998.

[2] A. Okayaya and L. Barash, "The dielectric microwave resonator," *Proceedings IRE*, vol. 50, pp. 2081-2092, Oct. 1962.

[3] L. Hady, A. Kishk, and D. Kajfez, "Dielectric resonator antenna in a polarization filtering cavity for dual function applications," *IEEE Transactions on Microwave Theory and Techniques*, vol. 56, no. 12, pp. 3079-3085, Dec. 2008.

[4] T. Iveland, "Dielectric resonator filters for application in microwave integrated circuits," *IEEE Transactions on Microwave Theory and Techniques*, vol. 19, no. 7, pp. 643-652, July 1971.

[5] D. Kajfez, "Linear fractional curve fitting for measurement of high Q factors," *IEEE Transactions on Mi crowave Theory and Techniques*, vol. 42, no. 7, pp. 1149-1153, July 1994.

[6] A. Kishk, H. Auda, and B. Ahn, "Radiation characteristics of cylindrical dielectric resonator antenna with new applications," *IEEE Antennas and Propagation Magazine*, vol. 31, no. 1, pp. 7-16, Feb. 1989.

[7] A. Kishk, A. Glisson, and G. Junker, "Bandwidth enhancement for split cylindrical dielectric resonator antennas," *PIER*, vol. 33, pp. 97-118, 2001.

[8] R. Chair, A. Kishk, and K. Lee, "Wideband stair-shaped dielectric resonator antennas," *IET Microwaves, Antenna and Propagation*, vol. 1, no. 2, pp. 299-305, 2007.

[9] L. Hady, A. Kishk, and D. Kajfez, "Dual-band compact DRA with circular and monopole-like linear polarizations," *IEEE Transactions on Antennas and Propagation*, vol. 57, no. 9, pp. 2591-2598, Sep. 2009.

[10] E. Lim, and K. Leung, "Novel utilization of the dielectric resonator antenna as an oscillator load," *IEEE Transactions on Antennas and Propagation*, vol. 55, no. 10, pp. 2686-2691, Oct. 2007.

[11] E. Lim, and K. Leung, "Novel application of the hollow dielectric resonator antenna as a packaging cover," *IEEE Transactions on Antennas and Propagation*, vol. 54, no. 2, pp. 484-487, Feb. 2006.

[12] L. Hady, D. Kajfez, and A. Kishk "Triple mode use of a single dielectric resonator," *IEEE Transactions on Antennas and Propagation*, vol. 57, no. 5, pp. 1328-1334, May 2006.

[13] M. Zinieris and R. Sloan, "High-order modes in dielectric resonators for measurement of loss tangent," *IEE Proceedings-Science, Measurement and Technology*, vol. 147, no. 2, pp. 91-94, 2000.

[14] C. Vedrenne, "Whispering-gallery modes of dielectric resonators," *IEE Proceedings H–Microwaves, Optics and Antennas*, vol. 129, pp. 183-187, Aug. 1982.

[15] D. Cros and P. Guillon, "Whispering gallery dielectric resonator modes for W-band devices," *IEEE Transactions on Microwave Theory and Techniques*, vol. 38, no. 11, pp. 1667-1674, Nov. 1990.

[16] L. Hady, A. Kishk, and D. Kajfez, "Five-way power divider based on dielectric resonator whispering-gallery modes," *IEEE MTT-S International Microwave Symposium Digest*, pp. 481-484, June 2009.

[17] L. Hady, A. Kishk, and D. Kajfez, "Power dividers based on dielectric resonator whispering-gallery modes fed by probe or slot type of coupling," *IEEE Transactions on Mi crowave Theory and Technique*, vol. 57, no. 12, pp. 3404-3409, Dec. 2009.

[18] L. Hady, A. Kishk, and D. Kajfez, "X-band microwave power divider based on bow-tie shaped dielectric resonator high-order modes," *IEEE MTT-S International Microwave Symposium Digest*, pp. 1732-1735, May 2010.

[19] Commercial software HFSS distributed by ANSYS Inc.: http://www.ansys.com.

Modeling of Weakly Conducting Thin Sheets in the Discontinuous Galerkin Method for Shielding Effectiveness Evaluation

M. Boubekeur [1], A. Kameni [1], A. Modave [2], L. Bernard [1], and L. Pichon [1]

[1] Laboratoire de Génie Electrique de Paris, UMR 8507 CNRS, SUPELEC, Université Paris-Sud
Université Pierre et Marie Curie, 11 rue Joliot-Curie, 91192 Gif-sur-Yvette, France
Mohamed.boubekeur@lgep.supelec.fr , abelin.kameni@lgep.supelec.fr , laurent.bernard@lgep.supelec.fr,
lionel.pichon@lgep.supelec.fr

[2] Université de Liège, Department of Electrical Engineering and Computer Science, Applied and
Computational Electromagnetics, Liège 4000, Belgium
a.modave@ulg.ac.be

Abstract ― This paper presents a modeling of weakly conducting thin sheets in the time domain discontinuous Galerkin method. This interface condition is used to avoid the mesh of resistive sheets in order to evaluate the shielding effectiveness in high frequency electromagnetic compatibility problems. This condition is valid when the thickness of the sheet is smaller than the skin depth. This approach is validated by a comparison with an analytical solution. A 1D two sheets example, 2D and 3D cavities are treated to illustrate the efficiency of the condition.

Index Terms – Discontinuous Galerkin, resistive sheet, and shielding effectiveness.

I. INTRODUCTION

The accurate evaluation of the shielding effectiveness of enclosures of complex shapes is a crucial issue in many electromagnetic compatibility (EMC) problems. It requires adequate numerical approaches. The ability to model features that are small relative to the cell size is often important in electromagnetic simulations. This may lead to subsequent increase in memory and execution time due to a refined mesh around small details of the geometry. This is particularly true for thin sheets, which may involve a mesh of bad quality.

In order to avoid the spatial discretization of thin sheets, different interface conditions have been proposed. In the frequency domain, analytical solutions [1, 2] can be included in a three dimensional model [3]. Many papers have been devoted to extend the approach in the time domain using an inverse Fourier or Laplace transform combined to a convolution product with the FDTD method [4-6]. Nevertheless, the stair casing error present in the FDTD method may affect significantly the numerical results.

The discontinuous Galerkin (DG) method is a powerful approach for solving time dependent problems. It is based on the local resolution of the equations in each cell and uses flux terms to connect adjacent elements [7-9]. It has the advantage of the unstructured mesh and high spatial order unlike the conventional FDTD. Such a high level spatial scheme can reduce the dispersive error induced by the low level of the spatial approximation in the FDTD.

Composite materials become widely used in aerospace and aircraft industries. They are generally composed by a resin matrix reinforced by conducting fibres [10, 11]. These materials offer low weight but are not as electrically conductive as metallic ones. So they have a significant impact on the electromagnetic behaviour of the enclosures. The effect of such a low conductivity on the envelope resonances needs to be studied.

In [12] a resistive sheet was proposed for a DG method based on hexahedral elements. It showed its advantages in terms of accuracy and

Submitted On: April 12, 2013
Accepted On: Aug. 16, 2013

1054-4887 © 2013 ACES

memory storage compared with the FDTD method but suffers from the use of cubic cells.

In this paper a specific interface condition is proposed to replace a thin resistive cell in a DG method based on an unstructured mesh. The formalism is developed in the general 3D case, it is then implemented for simplex elements in 2D (triangles) and 3D (tetrahedral). It allows to take into account conductors with a thickness smaller than the skin depth. This method is implemented in a DG module of GMSH [13].

II. PROBLEM FORMULATION

The Maxwell's equations are solved in the time domain as,

$$\begin{cases} \varepsilon\,\partial_t\vec{\mathbf{E}} - \nabla\times\vec{\mathbf{H}} = -\vec{\mathbf{J}} \\ \mu\,\partial_t\vec{\mathbf{H}} + \nabla\times\vec{\mathbf{E}} = 0 \end{cases}, \tag{1}$$

where ε is the permittivity of the medium and μ its permeability. The current density of the conductive medium is such as $\vec{\mathbf{J}} = \sigma\vec{\mathbf{E}}$, with σ is the conductivity.

For the computational applications, the fields are discretized on a mesh made of triangular or tetrahedral elements, with first-order basis functions. The time-stepping is performed with the leapfrog scheme. The numerical scheme is based on the variational formulation of equation (1) given by, in each tetrahedral element T,

$$\begin{cases} \int_T \varepsilon\frac{\vec{\mathbf{E}}^{n+1}-\vec{\mathbf{E}}^{n}}{\Delta t}.\vec{\boldsymbol{\varphi}} = [\int_T \vec{\mathbf{H}}^{n+\frac{1}{2}}.\nabla\times\vec{\boldsymbol{\varphi}} \\ + \int_{\partial T}\left(\vec{\mathbf{n}}\times\vec{\mathbf{H}}\right)^{num,n+\frac{1}{2}}.\vec{\boldsymbol{\varphi}} - \int_T \sigma\vec{\mathbf{E}}^{n}.\vec{\boldsymbol{\varphi}}] \\ \int_T \mu\frac{\vec{\mathbf{H}}^{n+\frac{1}{2}}-\vec{\mathbf{H}}^{n-\frac{1}{2}}}{\Delta t}\vec{\boldsymbol{\phi}} = -[\int_T \vec{\mathbf{E}}^{n}.\nabla\times\vec{\boldsymbol{\phi}} \\ + \int_{\partial T}\left(\vec{\mathbf{n}}\times\vec{\mathbf{E}}\right)^{num,n}.\vec{\boldsymbol{\phi}}] \end{cases}, \tag{2}$$

where $\left(\vec{\mathbf{n}}\times\vec{\mathbf{E}}\right)^{num}$ and $\left(\vec{\mathbf{n}}\times\vec{\mathbf{H}}\right)^{num}$ are the numerical flux that must be evaluated with a particular discretization. There are generally two choices, which make the scheme dissipative or dispersive,

$$\begin{cases} \left(\vec{\mathbf{n}}\times\vec{\mathbf{H}}\right)^{num,n+\frac{1}{2}} = \vec{\mathbf{n}}\times\frac{\left\{Z\vec{\mathbf{H}}^{n+\frac{1}{2}}\right\}}{\{Z\}} - \alpha\left(\vec{\mathbf{n}}\times\frac{(\vec{\mathbf{n}}\times[\![\vec{\mathbf{E}}^{n}]\!])}{\{Z\}}\right) \\ \left(\vec{\mathbf{n}}\times\vec{\mathbf{E}}\right)^{num,n} = \vec{\mathbf{n}}\times\frac{\{Y\vec{\mathbf{E}}^{n}\}}{\{Y\}} + \alpha\left(\vec{\mathbf{n}}\times\frac{\left(\vec{\mathbf{n}}\times\left[\!\left[\vec{\mathbf{H}}^{n-\frac{1}{2}}\right]\!\right]\right)}{\{Y\}}\right) \end{cases}, \tag{3}$$

where $\vec{\boldsymbol{n}}$ the outward normal, $Z = 1/Y = \sqrt{\mu/\varepsilon}$,$[\![u]\!] = \frac{u^{+}-u^{-}}{2}$ and $\{u\} = \frac{u^{+}+u^{-}}{2}$. The subscript "–" denotes the values for fields in the current element, while "+" is for the adjacent element. For α = 0, centred flux are obtained and the numerical scheme is dispersive [14]. For α = 1, upwind flux are obtained and the numerical scheme is dissipative [8]. In this work, upwind fluxes are used. For expensive reference simulations (when the sheet is meshed and 3D cavity), an implicit Runge-Kutta scheme that permits a large time step is considered.

III. CONSTRUCTION OF THE INTERFACE CONDITION

The electromagnetic field equations in the sheet are considered in 1D and in the frequency domain,

$$\begin{cases} \partial_x E_y = -j\omega\mu H_z \\ \partial_x H_z = -(\sigma + j\omega\varepsilon)E_y \end{cases}, \tag{4}$$

where ε, μ, and σ are respectively the permittivity, the permeability, and the conductivity of the sheet (Fig. 1).

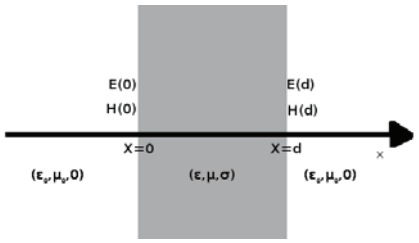

Fig. 1. Resistive sheet.

So the intrinsic impedance of the sheet is,

$$\eta = \sqrt{\frac{j\omega\mu}{(\sigma+j\omega\epsilon)}}, \tag{5}$$

and the planar propagation constant is,

$$\gamma = \sqrt{j\omega\mu(\sigma + j\omega\varepsilon)}. \tag{6}$$

For low frequency, the impedance and the propagation constant can be written as,

$$\begin{cases} \eta = \sqrt{\frac{j\omega\mu}{\sigma}} \\ \gamma = \sqrt{j\omega\mu\sigma} \end{cases}. \tag{7}$$

Using the analytical 1D solution [5], the electromagnetic fields on the two sides of the shield are connected by,

$$\begin{pmatrix} H_z(\omega,0) \\ H_z(\omega,d) \end{pmatrix} = M \begin{pmatrix} E_y(\omega,0) \\ E_y(\omega,d) \end{pmatrix} \quad (8)$$

where M is the admittance matrix,

$$M = \begin{pmatrix} y_1(\omega) & -y_2(\omega) \\ y_2(\omega) & -y_1(\omega) \end{pmatrix}. \quad (9)$$

y_{11} and y_{21} have the following expression,

$$\begin{aligned} y_1(\omega) &= -(\eta \tanh(\gamma d))^{-1} \\ y_2(\omega) &= -(\eta \sinh(\gamma d))^{-1}. \end{aligned} \quad (10)$$

The asymptotic behaviour of y_{11} and y_{21}, when $\omega \to 0$,

$$\begin{aligned} y_1 \sim y_1^{LF} &= -\frac{i}{\omega\mu d} - \frac{\sigma d}{3} + O(\omega) \\ y_2 \sim y_2^{LF} &= -\frac{i}{\omega\mu d} + \frac{\sigma d}{6} + O(\omega) \end{aligned}. \quad (11)$$

For the low frequencies, $(y_2 - y_1) \approx \frac{\sigma d}{2}$. The error of this approximation depends on γd. The real and imaginary parts of γd are equal to $\frac{d}{\delta}$, where $\delta = \sqrt{\frac{2}{\mu\sigma\omega}}$ is the skin depth. So the error of the approximation is determined by the rate $\frac{d}{\delta}$. For our problem, we choose $\frac{d}{\delta} \leq 1$. In the worst case (i.e., $d = \delta$), the error on $(y_2 - y_1)$ is then approximately 3 %.

The continuity of the electric field is supposed, and a simplified relation is deduced,

$$\begin{cases} E_y(\omega,0) = E_y(\omega,d) \\ H_z(\omega,d) - H_z(\omega,0) = \sigma d \frac{E_y(\omega,0) + E_y(\omega,d)}{2}. \end{cases} \quad (12)$$

For the time domain application, due to the linearity of the relation, it stays unchanged,

$$\begin{cases} E_y(t,0) = E_y(t,d) \\ H_z(t,d) - H_z(t,0) = \sigma d \frac{E_y(t,0) + E_y(t,d)}{2}. \end{cases} \quad (13)$$

The relation of equation (12) can be formulated with the tangential components of the fields,

$$\begin{cases} \vec{n} \times \vec{E}^+ = \vec{n} \times \vec{E}^- \\ \vec{n} \times \vec{H}^+ - \vec{n} \times \vec{H}^- = Y_s \vec{n} \times \vec{n} \times \frac{(\vec{E}^- + \vec{E}^+)}{2}, \end{cases} \quad (14)$$

where $\vec{n}$ is the outward unit normal of the $(\vec{E}^-, \vec{H}^-)$ element and $Y_s = \sigma d$. The propagation of a plane wave with normal incidence is considered from "-" incident medium to "+". The resulting flux terms for the proposed interface condition are obtained using equation (13) and flux term in equation (3) with $\alpha = 0$. $(\vec{n} \times \vec{E})^{num}$ stays unchanged relative to equation (3) thanks to the continuity of the electric field. To define $(\vec{n} \times \vec{H})^{num}$, $\vec{n} \times \frac{\{Z\vec{H}\}}{\{Z\}}$ is replaced by $\vec{n} \times \vec{H}^+$ computed using equation (14),

$$\begin{cases} (\vec{n} \times \vec{H})^{num} = \vec{n} \times \vec{H}^- + Y_s \vec{n} \times \vec{n} \times \{\vec{E}\} \\ (\vec{n} \times \vec{E})^{num} = \vec{n} \times \frac{\{Y\vec{E}\}}{\{Y\}} \end{cases}. \quad (15)$$

IV. 1D TEST EXAMPLE

A. Validation test

To validate this condition, we consider $\vec{E} = (0, 0, E_z)$ and $\vec{H} = (0, H_y, 0)$, and two domains separated by a sheet of 1 mm thickness (Fig. 1). This sheet is illuminated by a planar cosine pulse with frequency $f = 100$ MHz. The transmitted and reflected fields are computed for $\sigma \in [1,500]$ S/m. The minimal skin depth is 2.25 mm. Figure 2 illustrates the comparison between the transmitted field of the computed solution and the analytical solution, which is calculated in the frequency domain. The difference between the analytical and computed solution is negligible.

For the same example, the frequency is varied from 100 MHz to 1000 MHz, for conductivity $\sigma = 100$ S/m. The shielding effectiveness for the electric field is defined by the following expression,

$$SE_E = 20 \log_{10} \left| \frac{\vec{E}_i}{\vec{E}_t} \right|, \quad (15)$$

where $\vec{E}_i$ is the incident electric field and $\vec{E}_t$ is the transmitted electric field.

The error on the shielding effectiveness of the sheet between analytical and computed solution remains less than 1%. These examples validate the interface condition when the skin depth is larger than the thickness of the sheet.

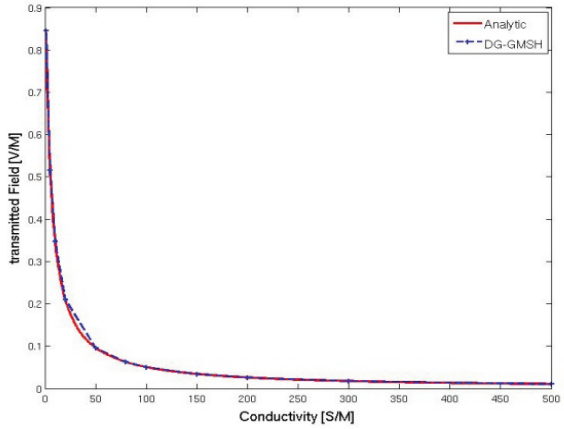

Fig. 2. Transmitted field.

B. Double sheets

The incident electromagnetic field is similar to the first example. Three domains separated by two sheets of 1 mm thickness and conductivity $\sigma = 50\ \mathrm{S/m}$ are considered. The distance between the two sheets is 10 cm (Fig. 3). The incident field is a Gaussian pulse $E_z = e^{-a(t-t_0)^2}$ centered at $t_0 = 5.10^{-9}$s, with the parameter $a = \frac{9.10^{16}\log(100)}{(0.75)^2}\ \mathrm{s}^{-2}$. In this example, three solutions are compared (Fig. 4). The first one corresponds to the situation where the sheet is meshed. This problem is solved with DG method. The second one is solved with finite integration technique (FIT) [15]. The third one corresponds to the interface condition and is solved with DG method. A good agreement is obtained with the interface condition; the computational time is reduced by a factor of 10. This is due to the fact that in the case where the sheet is meshed a great number of elements are required. Moreover, an implicit scheme is needed to avoid a reduced time step. The FIT method solution has the same behaviour but the maximum value is less important than for the other solutions.

V. 2D CAVITY

An illustration of this DG scheme is presented in a 2D case with the interface condition. Let us consider a cavity whose dimensions are 50 cm × 40 cm. A 10 cm aperture is located on the front side. The thickness of the wall is 1 mm (Fig. 5). The incident field is a product between cosine and a sinus cardinal. $E_z = \mathrm{sinc}\big(w_r(t-t_0)\big)\cos\big(w_c(t-t_0)\big)$ with $w_r = 300$ MHz and $w_c = 700$ MHz. This field is centered at $t_0 = 5.10^{-8}$ s, and excites a large frequency band $f \in [400,1000]$ MHz.

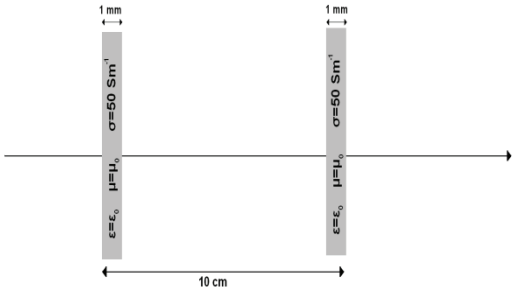

Fig. 3. Double conductive sheet.

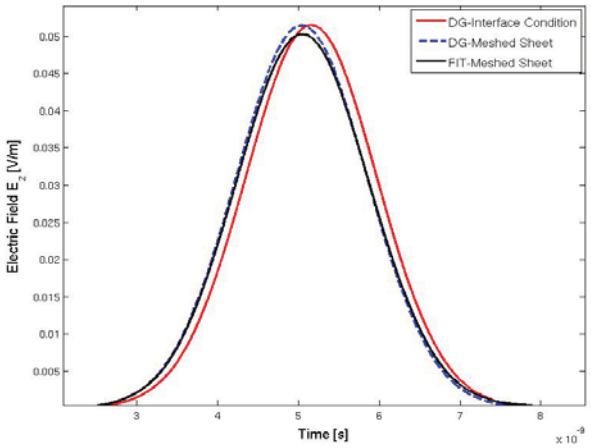

Fig. 4. Transmitted field in the midpoint between the sheets.

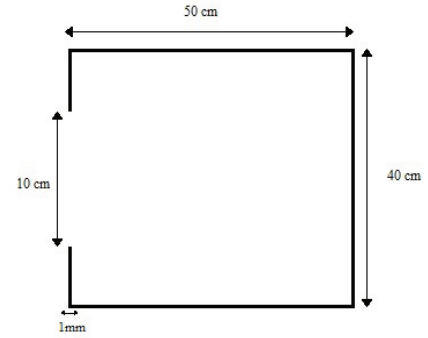

Fig. 5. 2D cavity.

A fast Fourier transform (FFT) is applied to the total field at the center of the cavity. Different cases are considered. The perfect electric conductor (PEC) case is computed with DG

method and FIT method. The cases of finite conductivity values are computed with the interface condition with DG method.

In Fig. 6 the shielding effectiveness is plotted at the center of the cavity for the different cases. The results obtained with the PEC interface condition in DG method (red) is close to that obtained with FIT (blue). For finite values of conductivity $\sigma = 100\ \mathrm{S/m}$ (green) and $\sigma = 10\ \mathrm{S/m}$ (black), it can be noted that the resonance peaks are attenuated due to the conductivity. This behaviour is in accordance to that observed in a composite shield studied in the frequency domain [16]. In Fig. 7 the total electric field is compared at the center of the cavity when it is illuminated by the Gaussian pulse used in the 1D example. The different cases considered are the PEC wall in DG (red) and FIT (blue), the conductive wall with $\sigma = 10\ \mathrm{S/m}$ (purple) and $\sigma = 50\ \mathrm{S/m}$ (black) in DG with interface condition.

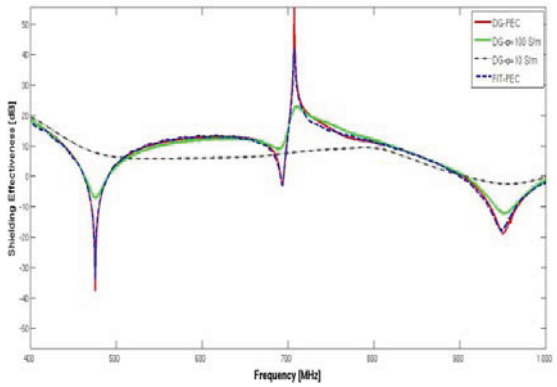

Fig. 6. Shielding effectiveness in the center of the cavity.

For the PEC wall, the field penetrates only by the aperture. In case of resistive walls the fields propagate through the walls and aperture. So the fields inside the cavity decrease faster with time for low conductivities.

VI. 3D CAVITY

Let us consider 3D cavity (Fig. 8), whose dimensions are $a = 300$ mm, $b = 120$ mm, $d = 300$ mm, $l = 100$ mm, $w = 5$ mm and $t = 1$ mm[17]. This cavity is illuminated by an incident Gaussian pulse $E_z = e^{-a(t-t_0)^2}$ centered at $t_0 = 1{,}5.10^{-9}$s, with the parameter $a = \frac{(11.10^9)^2}{4\log(100)}\ \mathrm{s}^{-2}$. The electric field is computed at the center of the cavity. Different cases of conductivity of the sheet are compared, $\sigma = 100\ \mathrm{S/m}$, $\sigma = 50\ \mathrm{S/m}$ and PEC.

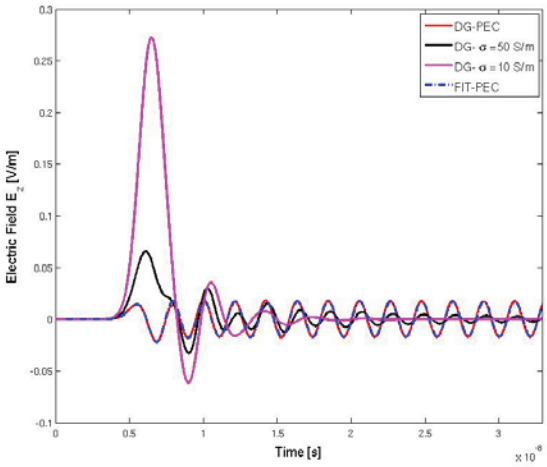

Fig. 7. Electric field in the center of the cavity.

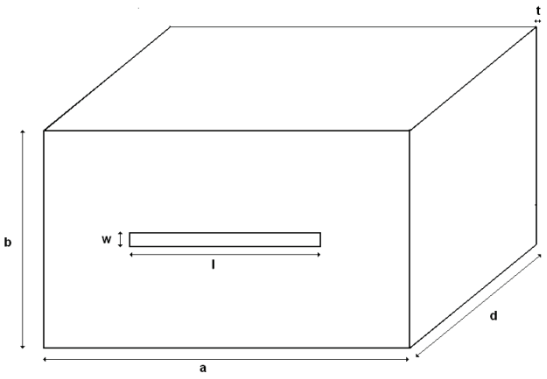

Fig. 8. 3D cavity.

A FFT is applied to the electric field, and the shielding effectiveness is plotted in Fig. 9. The result obtained with the PEC case (red) is similar to the analytical formulation (blue) [17]. For the case of finite conductivities, the shielding effectiveness is less important and the resonance peaks are attenuated due to the transmission of the shield.

In Fig. 10, the time domain electric fields are compared for the same cases. For the PEC case (black), the electric field is low, because it penetrates only by the aperture. For the other cases, the electric field remains important for low conductivities and decreases faster with time.

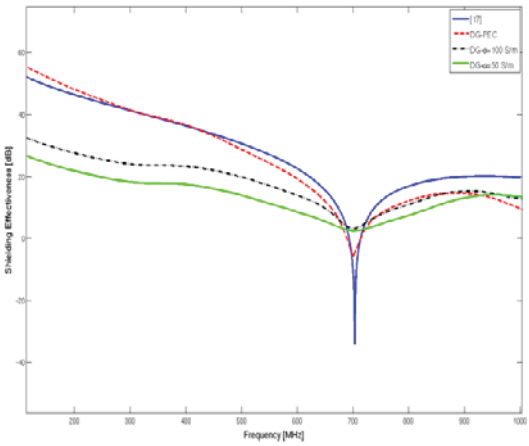

Fig. 9. Shielding effectiveness in the center of the cavity.

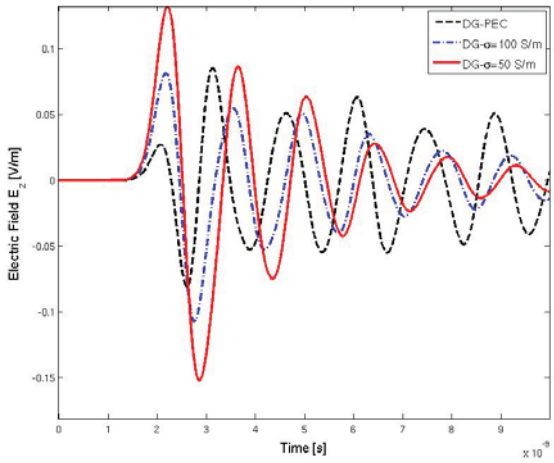

Fig. 10. Electric field in the center of the cavity.

VII. CONCLUSION

An interface condition avoiding the mesh of thin resistive sheets is presented and allows a reduction of the computational cost when computing shielding effectiveness. It takes into account a sheet with a thickness smaller than the skin depth. The interface condition has been implemented in a 2D and 3D discontinuous Galerkin method, and has been validated for different scattering problems. The future developments will extend the interface condition for the case of dielectric composite material.

REFERENCES

[1] K. Mitzner, "Effective boundary conditions for reflection and transmission by an absorbing shell of arbitrary shape," *IEEE Trans. Antennas and Propag.*, vol. 16, no. 6, pp. 706-712, 1968.

[2] R. Schulz, V. Plantz, and D. Brush, "Shielding theory and practice," *IEEE Trans. Electromagn. Comp.*, vol. 30, no. 3, pp. 187-201, 1988.

[3] F. Bocquet, L. Pichon, A. Razek, and G. Tanneau, "3D FEM analysis of electromagnetic wave scattering from a dielectric sheet in EMC problems," *IEEE Trans. Magn.*, vol. 34, no. 5, pp. 2791-2794, 1998.

[4] S. Van der Berghe, F. Olyslager, and D. De Zutter, "Accurate modeling of thin conducting layer in FDTD," *IEEE Microwave and G uided Wave Letters*, vol. 8, no. 2, pp. 75-77, 1998.

[5] M. Sarto, "A new Model for the FDTD analysis of the shielding performances of thin composite structures," *IEEE Trans. Electromagnetic Comp.*, vol. 44, no. 4, pp. 298-306, 1999.

[6] M. Feliziani, F. Maradei, and G. Tribellini, "Field analysis of penetrable conductive shields by the finite-difference time-domain method with impedance network boundary conditions (INBS's)," *IEEE Trans. Electromagnetic Comp.*, vol. 44, no. 4, pp. 307-319, 1999.

[7] B. Cockburn, S. Hou, and C.-W. Shu, "TVB Runge-Kutta local projection discontinuous Galerkin finite element method for conservation laws IV: The multidimensional case," *Math. Comp.,* no. 54, pp. 545-581, 1990.

[8] J. Hesthaven and T. Warburton, "Nodal high-order methods on unstructured grids: time domain solution of Maxwell's equations," *J. Comp. Phys.*, vol. 181, no. 1, pp. 186-221, 2002.

[9] D. Gedney, C. Luo, J. Roden, R. Crawford, B. Guernsey, J. Miller, T. Kramer, and E. Lucas, "The discontinuous Galerkin finite-element time-domain method solution of Maxwell's equations," *ACES Journal*, vol. 24, no. 2, pp. 129-142, 2009.

[10] V. Préault, R. Corcolle, L. Daniel, and L. Pichon, "Effective permittivity of shielding composite materials for microwave frequencies," *IEEE Trans. Electromagnetic Comp.* (accepted)

[11] C. Holloway, M. Sarto, and M. Johansson, "Analyzing carbon-fiber composite materials with equivalent-layer models," *IEEE Trans. Electromagnetic Comp.*, vol. 47, no. 4, pp. 833-844, 2005.

[12] L. Pebernet et al, "Discontinuous Galerkin method applied to electromagnetic compatibility: introduction of thin wire and thin resistive materials," *IET Sci. Meas. Technol.*, vol. 2, no. 6, pp. 395-401, 2001.

[13] A. Kameni, A. Modave, M. Boubekeur, V. Preault, L. Pichon, and C. Geuzaine, "Evaluation of shielding effectiveness of composite wall with a time domain discontinuous Galerkin method," *The*

European Physical Journal - Applied Physics. (accepted for publication)

[14] L. Fezoui, S. Lanteri, S. Lohrengel, an S. Piperno, " Convergence and stability of a discontinuous Galerkin time-domain method for the 3D heteregeneous Maxwell's equations on unstructured meshes," *M2AN*, vol. 39, no. 6, pp. 1149-1176, 2005.

[15] L. Bernard, R. Torrado, and L. Pichon, "Efficient implementation of UPML in generalized finite-difference time-domain method," *IEEE Trans. Magn.*, vol. 46, no. 8, pp. 3492-3495, 2010.

[16] W. Abdelli, X. Mininger, L. Pichon, and H. Trabelsi, "Impact of composite materials on the shielding effectiveness of enclosures," *ACES Journal*, vol. 27, no. 4, pp. 369-375, 2012.

[17] M. Robinson, T. Benson, C. Christopoulos, J. Dawson, M. Ganley, A. Marvin, S. Porter, and D. W. Thomas, "Analytical formulation for the shielding effectiveness of enclosures with apertures," *IEEE Trans. Electromagn. Compat*., vol. 40, no. 3, pp. 240-248, 1998.

Mohamed Boubekeur received his Master in Mathematical Modeling option Numerical analysis and PDE in Pierre et Marie Curie University, he is currently a PhD student at LGEP. His current research interests include electromagnetic compatibility shielding, Modeling of wave propagation for thin sheet.

Abelin Kameni is an Engineer from "Ecole D'Ingénieurs en Modélisation Mathématique et Mécanique (MATMECA)" in 2004. He received the Msc degree in Mathematical modeling from University of Bordeaux in 2005. In 2009 he earned a PhD in Electrical Engineering of Université Henri Poincarré from Nancy and joined the Laboratoire de Génie Electrique of Paris (LGEP) in 2010 as Assistant Professor. His research interests concern numerical methods applied to electromagnetic problems.

Axel Modave is a physics engineer from the University of Liège in 2008. He is currently a PhD student in the Applied and Computational Electromagnetics group at the University of Liège. His research interests concern numerical methods for wave-like problems in electromagnetic and mechanics.

Laurent Bernard received the B.Sc. and M.Sc. degrees from the Institut National Polytechnique de Grenoble in 2004. In 2007, he received the Ph.D. from the Ecole Centrale de Lyon and the Universidade Federal de Minas Gerais (co-supervision). He is currently Research Engineer at the CNRS and works with the LGEP (Laboratoire de Génie Electrique de Paris). His research interests concern mesh-based numerical methods for electromagnetics and coupled problems.

Lionel Pichon is an Engineer from Ecole Supérieure d'Ingénieurs en Electronique et Electrotechnique (ESIEE) in 1984. In 1985 he joined the Laboratoire de Génie Electrique de Paris (LGEP) where he earned a PhD in electrical engineering in 1989. He got a position at the CNRS (Centre National de la Recherche Scientifique) in 1989. He is now Directeur de Recherche at the CNRS (Senior Scientist). Since 2002 he is one of the animators of the Groupement de Recherche CNRS, known as GDR Ondes, where is involved a large network of laboratories and researchers related to the modeling of wave propagation from mathematical theory to numerical solutions for particular applications.

Compact CPW-Fed Antenna with Circular Polarization Characteristics in WLAN Frequency Band

M. Majidzadeh, J. Nourinia, and Ch. Ghobadi

Department of Electrical Engineering
Urmia University, Urmia, Iran
Maryam_Majidzadeh37@yahoo.com, J.Nourinia@urmia.ac.ir, Ch.Ghobadi@urmia.ac.ir

Abstract ─ A novel co-planar waveguide (CPW)-fed antenna with circular polarization (CP) characteristics in the 5.1 GHz − 5.8GHz is presented. By adding a vertical stub and a rotated L shaped stub to the antenna structure, a bandwidth of 5 GHz − 8GHz (46 %) for S_{11} < -10 dB is achieved and also circular polarization characteristics is generated in the 5.1 GHz − 5.8 GHz, which completely covers the wireless local area network (WLAN) frequency band. The antenna has a very simple structure and occupies a compact area of 25 × 25 × 1 mm^3. The very simple structure and small size are of the marvelous merits of the proposed antenna. The antenna design process, impedance bandwidth and axial ratio (AR) bandwidth enhancement process are discussed in detail.

Index Terms - Circular polarization, CPW-feed line, and WLAN applications.

I. INTRODUCTION

Communication industry has experienced sea-change during the last decades. One of the key components of every communication system is the antenna, which has not been an exception and has undergone great changes over the years of its progress. With the assignment of 3.1 GHz − 10.6 GHz as UWB frequency band, which caused the accelerating growth of communication systems, the need for novel antennas with compact size, low weight, high efficiency, and good radiation properties have been emerged. An antenna, if properly designed, can be highly impressive in the performance of a communication system. Hence, a lot of effort has been put into designing antennas and considerable valuable works have been reported in the literature. Microstrip-fed antennas [1-4] and CPW-fed antennas [5-8] are of the most common antenna types that are designed to be used in communication appliances. One of the important issues in communication systems is the provision of right orientation between the transmitter and receiver antennas. Circularly polarized antennas are good solutions to this problem. By the use of CP antennas, there will be no need to consider the orientation between the transmitter and receiver. Apart from this, overcoming the multipath fading problem, higher performance, and better mobility and weather penetration with respect to the linearly polarized (LP) antennas are of the admirable CP antennas features [9, 10]. Recently, a lot of CP antennas have been proposed. For instance in [11], a CPW-fed CP antenna is presented that has a 48.8 % axial ratio. In [12], the authors propose an antenna with C-shaped grounded strips aiming at generating CP characteristics. An antenna with enhanced axial ratio is introduced in [13]. In [14], an annular ring antenna with microstrip feed line is presented.

In this paper we propose a novel antenna structure. The proposed antenna is fed by a 50 Ω CPW feed line. The antenna is printed on a 25×25×1 mm^3 FR4 substrate and operates over the frequency band of 5 GHz − 8 GHz for S_{11} < -10 dB, which is achieved by the inclusion of a vertical stub and a rotated L-shaped stub in the antenna structure. The addition of a rotated L-shaped element, also creates the circular polarization characteristics in the frequency band of 5.1 GHz − 5.8 GHz (WLAN). The proposed antenna with the circular polarization property is a suitable candidate for communication systems,

Submitted On: Jan. 29, 2013
Accepted On: Oct. 31, 2013

1054-4887 © 2013 ACES

which are to be used in WLAN frequency band. The most salient feature of the presented work which differentiates it from the previously designed antennas is the very simple structure and small size. The remainder of the paper is outlined as follows: the structure and design process of the antenna are discussed in section II. The simulation results of parametric study, measured results, and their comparison are presented in section III. Eventually, section IV concludes the paper.

II. ANTENNA DESIGN

The schematic of the proposed CP antenna is shown in Fig. 1 (a). The fabricated antenna is also shown in Fig. 1 (b). The proposed antenna is printed on a cheap FR4-epoxy substrate with permittivity of 4.4, loss tangent of 0.002 and thickness of 1 mm. A CPW feed line with the length and width of 16.6 mm and 2.4 mm respectively, is adopted to feed the study antenna. First, a basic structure is designed as the main topology. Then a vertical stub is added to the basic antenna structure to enhance the impedance bandwidth and then a rotated L-shaped stub is included to both, enhance the impedance bandwidth and generate the CP property. What makes this antenna distinctive from the conventional CP antennas is the simple structure respect to the other CP antennas. Also, small area of the antenna is an important feature that makes the antenna design process easy and cost effective as well as making its installation easy and economical on the communication equipment. The values of all the antenna parameters are given in detail in Fig. 1.

III. RESULTS AND DISCUSSIONS

The performance of the CP antenna has been investigated using Ansoft High Frequency Structure Simulator (HFSS). The impedance bandwidth, axial ratio, gain, and radiation pattern of the proposed antenna have been measured and analyzed. The measured results are obtained using the Agilent 8722ES network analyzer.

A. Antenna design steps

To better understand the antenna performance and analyze the effect of different parts on its performance, the design process is divided into three steps. In each step, one part is added to the antenna to reach the final design. The three steps are shown in Fig. 2. S_{11} and axial ratio curves for the antennas in Fig. 2 are shown in Fig. 3 (a) and (b).

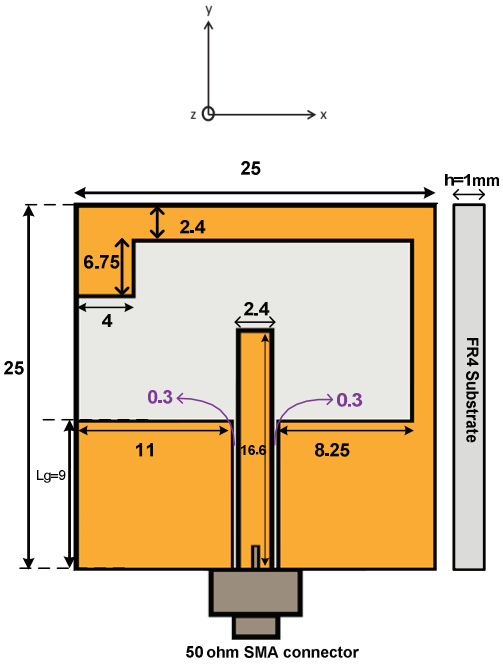

(a)

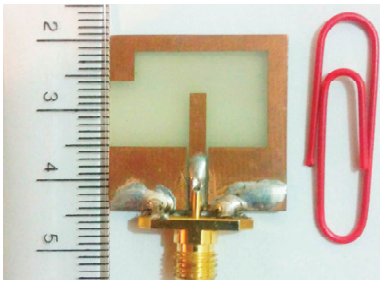

(b)

Fig. 1. (a) The schematic geometry of the proposed antenna and (b) the fabricated antenna.

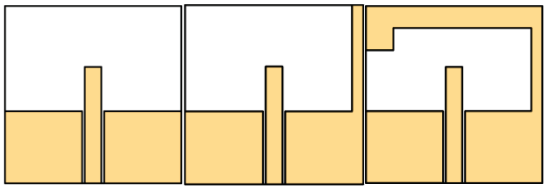

(a) (b) (c)

Fig. 2. The geometry of the three design steps of the proposed antenna; (a) step 1, (b) step 2, and (c) step 3.

As it is seen from Fig. 2, three geometries are considered until reaching the final antenna structure. In step 1, which is shown in Fig. 2 (a), just a simple feed line and two rectangular parts as the ground plane are included in the antenna body. From the simulated results in Fig. 3, this antenna operates over the frequency band of 6.1 GHz – 7.9 GHz and there is no circular polarization. In step 2, a vertical stub is added to the right side of the ground plane. The addition of this stub, creates a new path for the current and excites a new resonance in the 5.3 GHz, leading to bandwidth enhancement. The bandwidth of the antenna in this step extends from 5 GHz to 7.5 GHz. Still, no circular polarization is seen. Finally, in step 3, which is the final structure, a rotated L-shaped stub is also included. With this change, the bandwidth has reached to 5 GHz – 8 GHz. Apart from the bandwidth enhancement obtained by the modification made in last step, circular polarization is also generated in the frequency band of 5.2 GHz – 5.8 GHz.

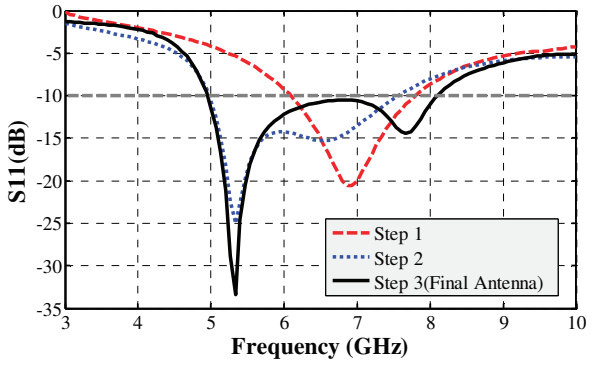

(a)

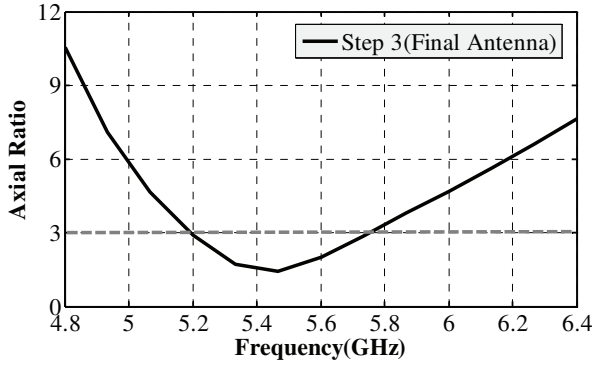

(b)

Fig. 3. (a) S_{11} curve of the three proposed antennas in Fig. 2 and (b) the axial ratio of the proposed antennas in Fig. 2.

B. The CP mechanism

To explain the CP operation mechanism of the proposed antenna, surface current distribution is simulated on the antenna at the frequency of 5.5 GHz and in four phases of 0°, 90°, 180°, and 270°. The simulated results are shown in Fig. 4. As it is clear from this figure, in 0° phase, the dominant current on the antenna flows in +y direction. In 90° phase, the current changes its direction and flows in the –x direction. In 180° and 270°, the magnitude of the current is the same as 0° and 90°, respectively, but its orientation is reverse, that is –y and +x. Based on the simulated surface current distribution, it is seen that the current turns counter clockwise as the phase increases from 0° to 270° by a step of 90°. This shows that the presented CP antenna generates RHCP in +z direction and LHCP in –z direction.

C. The ground plane length

The ground plane length that is named as L_g in Fig. 1, is the parameter that is studied in this section. Figure 5 shows the effect of this parameter on the antenna performance. Three values are chosen for L_g and the S_{11} and AR bandwidths are simulated and shown in Fig. 5 (a) and (b). It is clear that the lower edge frequency band of both S_{11} and AR have shifted towards higher frequencies as the L_g increases from 8 mm to 10 mm with a step of 1 mm. The higher edge has also been influenced by this change and has shifted to higher frequencies. Only when L_g is 9 mm, highest impedance bandwidth and a complete CP coverage of 5.2 GHz – 5.8 GHz (WLAN) is covered. In fact, when this parameter is varied, the coupling of the ground plane with the feed line and the rotate L-shaped element is influenced, which affects the antenna performance.

D. Simulated and measured results

The antenna with the given values in Fig. 1 has been fabricated and tested. Figure 6 shows the simulated and measured S_{11} and axial ratio bandwidth. It is seen that the simulated and measured S_{11} curves are in good agreement and the small difference is due to the soldering and fabrication faults. Also, the measured axial ratio bandwidth is slightly more than the AR obtained from simulation. According to the measured results, the frequency band of 5 GHz – 8 GHz is completely covered by the antenna and the axial

ratio is extended from 5.1 GHz – 5.8 GHz, which is about 13 %.

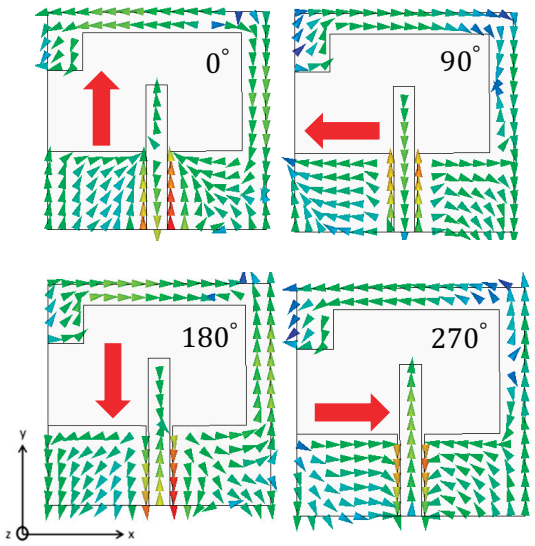

Fig. 4. Surface current distribution on the antenna at 0°, 90°, 180°, and 270°.

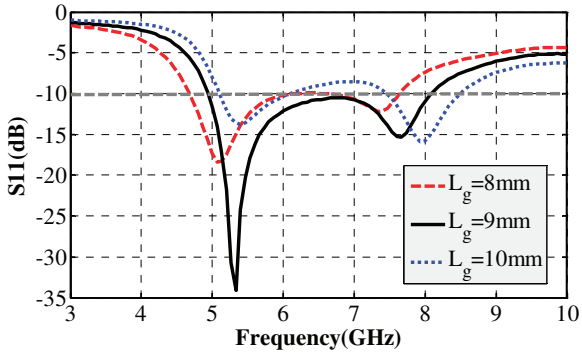

(a)

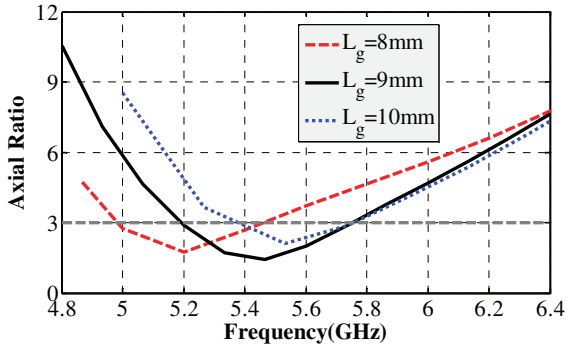

(b)

Fig. 5. (a) S_{11} curves and (b) axial ratio for different values of L_g.

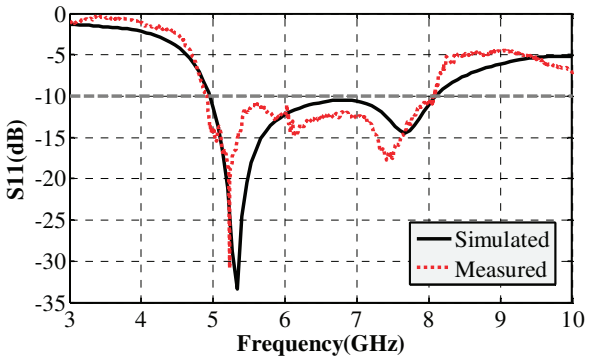

(a)

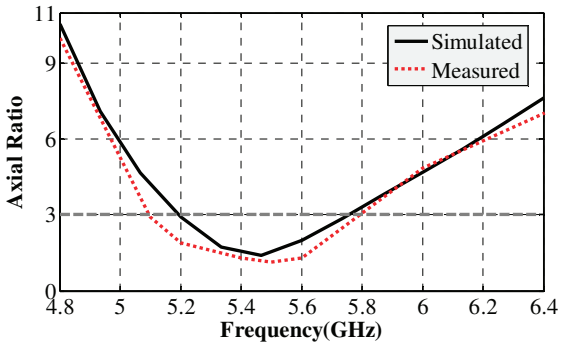

(b)

Fig. 6. (a) Simulated and measured S_{11} and (b) simulated and measured AR.

The antenna gain is also measured and compared with the simulated results in Fig. 7. It is seen that the measured gain is acceptable in the frequency band of 5.1 GHz – 5.8 GHz, where the CP property is achieved. The measured RHCP and LHCP radiation patterns of the antenna at 5.5 GHz in the xz- and yz-plane are plotted in Fig. 8. Acceptable radiation pattern is obtained for the antenna, making it suitable for communication industry.

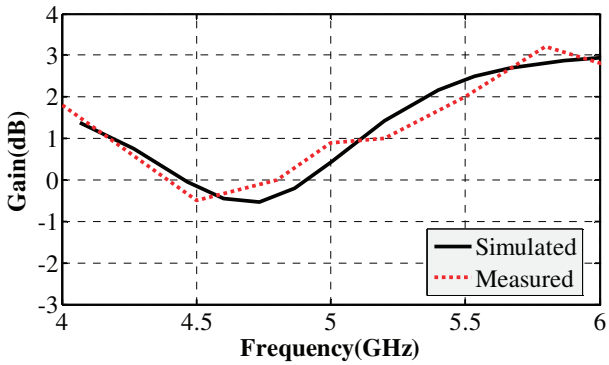

Fig. 7. Simulated and measured antenna gain.

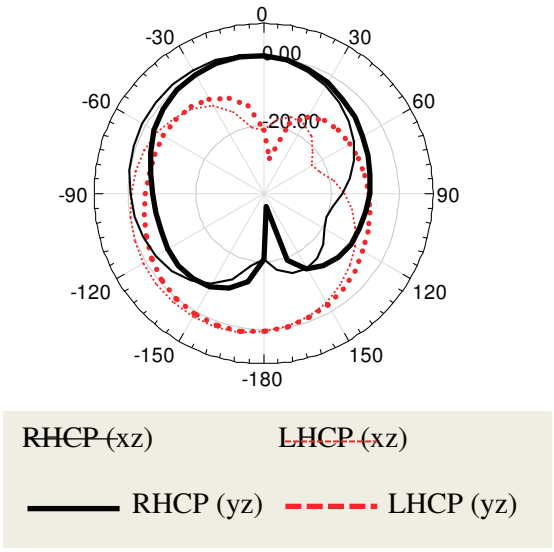

Fig. 8. Measured RHCP and LHCP radiation pattern of the CP antenna in the xz- and yz-plane at 5.5 GHz.

IV. CONCLUSION

A novel compact CPW-fed antenna with CP characteristics in WLAN frequency band is introduced in this work. The antenna has admirable characteristics making it a suitable option for communication systems. Small size and very simple structure are of the clear advantages of this antenna over the previously designed CP antennas. Also, acceptable gain and good radiation properties are other features of the presented antenna. The study antenna exhibits impedance bandwidth between 5 GHz to 8 GHz and its axial ratio extends from 5.1 GHz to 5.8 GHz, completely covering the WLAN frequency band. The agreement of the simulated and measured results show that the presented structure is a good candidate for communication systems.

REFERENCES

[1] M. Majidzadeh and Ch. Ghobadi, "Compact microstrip-fed monopole antenna with modified slot ground plane for UWB applications," *Applied Computational Electromagnetics Society (ACES)*, vol. 27, no. 10, pp. 801-807, 2012.

[2] R. Azim, M. Islam, and N. Misran, "Design of a planar UWB antenna with new band enhancement technique," *Applied Computational Electromagnetics Society (ACES)*, vol. 26, no. 10, pp. 856-862, Oct. 2011.

[3] M. Ojaroudi, S. Yazdanifard, N. Ojaroudi, and M. Naser-Moghaddasi, "Small square monopole antenna with enhanced bandwidth by using inverted T-shaped slot and conductor-backed plane," *IEEE Trans. Antennas Propagat.*, vol. 59, no. 2, pp. 670-674, Feb. 2011.

[4] D. Javan and O. Ghouchani, "Cross slot antenna with U-shaped tuning stub for ultra wideband applications," *Applied Computational Electromagnetics Society (ACES)*, vol. 24, no. 4, pp. 427-432, August 2009.

[5] M. Majidzadeh and Ch. Ghobadi, "Wide band CPW-fed circular patch antenna with tapered ground plane," *International Journal of Natural and Engineering Science (IJNES),* vol. 3, pp. 105-108, 2012.

[6] S. Mohammadi, J. Nourinia, Ch. Ghobadi, and M. Majidzadeh, "Compact CPW-fed rotated square-shaped patch slot antenna with band-notched function for UWB applications," *Electronics Lettres*, vol. 47, no. 24, pp. 1307-1308, 2011.

[7] S. Mohammadi, J. Nourinia, Ch. Ghobadi, and M. Majidzadeh, "A novel compact CPW-fed slot antenna with a pair of parasitic patches for UWB applications," *20th Iranian Conference on Electrical Engineering (ICEE)*, pp. 1409-1413, 2012.

[8] Z. Shun-Shi, L. Xian-Ling, and W. Wang, "Compact elliptical monopole antenna with impedance bandwidth in excess of 21:1," *IEEE Trans. Antennas Propagat.*, vol. 55, pp. 3082-3085, 2007.

[9] K. Wong, F. Chang, and T. Chiou, "Low-cost broadband circularly polarized probe-fed patch antenna for WLAN base station," *in Proc. IEEE Antennas Propag. Soc. Int. Symp*., vol. 2, pp. 526-529, 2002.

[10] K. Lau and K. Luk, "A novel wideband circularly polarized patch antenna based on L-probe and slot-coupling techniques," *in Proc. IEEE Antennas Propag. Soc. Int. Symp*., vol. 3, pp. 878-881, 2003.

[11] J. Sze, Ch. Hsu, Zh. Chen, and Ch. Chang, "Broadband CPW-fed circularly polarized square slot antenna with lightening-shaped feedline and inverted-L grounded strips," *IEEE Trans. Antennas Propagat.*, vol. 58, no. 3, pp. 973-977, 2010.

[12] Y. Chen, Y. Jiao, G. Zhao, F. Zhang, Zh. Liao, and Y. Tian, "Dual-band dual-sense circularly polarized slot antenna with a C-shaped grounded strip," *IEEE Letters on Antenna and Propagat*., vol. 10, pp. 915-918, 2011.

[13] Sh. Pan, J. Sze, and P. Tu, "Circularly polarized square slot antenna with a largely enhanced axial-ratio bandwidth," *IEEE Letters on Antenna and Propagat.*, vol. 11, pp. 969-972, 2011.

[14] J. Sze and W Chen, "Axial-ratio-bandwidth enhancement of a microstrip-line-fed circularly polarized annular-ring slot antenna," *IEEE Trans. Antennas Propagat.*, vol. 59, no. 7, pp. 2450-2456, 2011.

Maryam Majidzadeh was born on 18 September, 1987 in Urmia, Iran. She received her B.S. and M.Sc. degrees in Electrical Engineering from Urmia University in 2009 and 2012, respectively. She is currently a Ph.D. student in Electrical Communication Engineering at the same university. Her research interests are in designing of UWB antenna, bandwidth enhancement and antenna miniaturization techniques, Circular Polarized antennas and numerical method in electromagnetics.

Javad Nourinia received his B.Sc. in Electrical and Electronic Engineering from Shiraz University and M.Sc. degree in Electrical and Telecommunication Engineering from Iran University of Science and Technology, and Ph.D. degree in Electrical University of Science and Technology, Tehran Iran in 2000. From 2000, he was an assistant professor and now he is a professor in the Department of Electrical Engineering of Urmia University, Urmia, Iran. His primary research interests are in antenna design, numerical methods in electromagnetic and microwave circuits.

Changiz Ghobadiwas born on 1 June, 1960 in Iran. He received the B.S. degree in Electrical and Electronic Engineering and M.S. degree in Electrical and Telecommunication Engineering from Isfahan University of Technology, Isfahan, Iran and Ph.D. degree in Electrical-Telecommunication from University of Bath, Bath, UK in 1998. From 1998 he was an Assistant Professor and now is a professor in the Department of Electrical Engineering, of Urmia University, Urmia, Iran. His primary research interests are in antenna design, radar and adaptive filters.

Comprehensive Parametric Study of a Novel Dual-Band Single Feed Planar Inverted-F Antenna

T. Yousefi and N. Komjani

Department of Electrical Engineering
Iran University of Science and Technology, Tehran, Iran
Tara.e.yousefi@gmail.com, n_komjani@iust.ac.ir

***Abstract*–**This paper presents a new configuration of a dual frequency, single feed, planar inverted-F antenna, which is suitable for implementation in different handsets. A parametric study, using finite element simulation software, high frequency structure simulator, has been carried out on each of the frequencies of this antenna and closed formulas in terms of antenna parameters have been obtained, which makes the designing process much easier. The proposed antenna has been fabricated according to the obtained formulas. Both, numerical simulation and experimental data are presented.

***Index Terms*–** Dual-band, microstrip antenna, mobile antenna, and planar inverted-F antenna (PIFA).

I. INTRODUCTION

It is a well-known fact that the demand for wireless communication systems is ever-growing. Therefore, compact antennas employed in these systems have become the center of attention of numerous researchers. In many places around the world, cellular communication systems operate in two distinct frequency bands simultaneously. For example, some cellular phones work in GSM at 0.9 GHz and DSC1800 at 1.8 GHz. Two separate antennas can be used, with one of them resonating at GSM and the other at DSC, but this is not space efficient. At present both GSM and DSC provide services in the same network, which means that antennas that work in these two bands simultaneously are needed.

Designing such a dual band antenna presents a challenge, because it should operate properly in both frequency bands, while being small enough to fit in different handsets. Despite their low manufacturing cost and light weight, microstrip antennas [1-3] are not suitable for dual-band cellular handsets, because they are bulky at the lower frequency bands.

The solution is using planar inverted-F antennas (PIFAs) [4, 5], which are a modification of microstrip antennas. PIFAs have attracted much interest due to their small size, easy manufacturing, moderate gain, being less prone to breakage, and their potential to work at several frequencies with only minor modification. PIFAs are in fact, grounded half-quarter wavelength path antennas consisting of a finite ground-plane, a radiating top layer, and a short-circuiting mechanism that connects the top radiator to the ground-plane. The ease of design in order to obtain multiple resonances has made PIFA a very popular choice for mobile handset antennas. However, when we are dealing with multiple resonance frequencies, tuning them proves to be tricky [6-10]. Therefore, obtaining closed formulas in terms of the antenna parameters, which give us the operating frequencies will definitely make the designing process much easier [11].

In this paper a new configuration of a dual-band planar inverted-F antenna is proposed and parametrically evaluated. Studying the effects of antenna parameters on its operating frequencies, will help us find the key control elements and will result in easier frequency tuning. Moreover, by collecting the data from the parametric evaluation of each of the PIFA frequencies, closed formulas in terms of the key control antenna parameters are presented. By using these formulas, designing a

Submitted On: Nov. 5, 2012
Accepted On: Sept. 1, 2013

1054-4887 © 2013 ACES

dual-band PIFA with desired operating frequencies is achievable.

II. ANTENNA DESIGN

The design procedure for this antenna is simple and straight forward. The first step is to start with a simple classical PIFA, which is basically a short circuited quarter wave patch that works only in GSM. By short circuiting a quarter wave patch, the current at the end of the patch does not have to be zero so a current-voltage distribution of a half wave patch is obtainable with reducing the required space needed on the phone by half.

A single band PIFA is shown in Fig. 1 and as the name implies it is distinguished by the loop formed by the short right angle elements, which resembles the letter "F". Slits are made in this patch, which results in branches which are basically resonating paths. The smaller path resonates at DSC and the longer path resonates at GSM resulting in a dual band planar inverted F antenna.

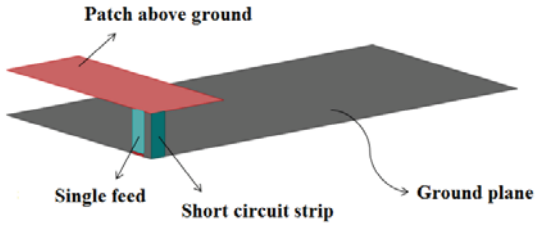

Fig. 1. Classic single band single feed PIFA.

III. ANTENNA STRUSTURE

The geometry of the proposed antenna is shown in Fig. 2. The top radiating element consists of several branches, which allow the antenna to work at two distinct frequencies. The total planar dimensions of the radiating top layer, which is made of copper are w and L, and the antenna height is shown with h. In order to see the effects of the substrate permittivity, ε_r, it has gradually changed from 1 to 4 in the simulations.

There are different shorting mechanisms, like using shorting pins, shorting plates, or a shorting wall [7]. In this antenna, a short-circuiting plate has been used, which is a vertical conducting strip with dimensions $W_S \times h$. This short circuiting plate connects the patch to the ground plane. The initial antenna dimensions have been chosen so that the operating frequencies are approximately 0.9 GHz and 1.8 GHz. In the next section, these dimensions will be changed for parametric evaluation.

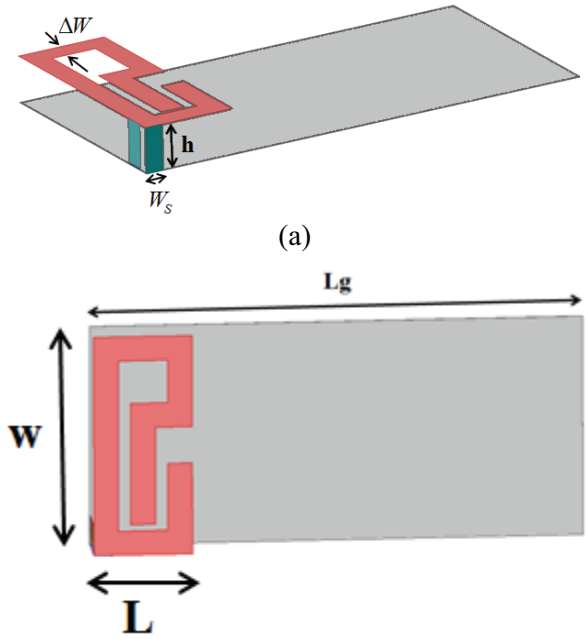

Fig. 2. (a) Side view of the dual band PIFA and (b) top view of the dual band PIFA.

IV. NUMERICAL RESULTS

A. Parametric study

This section includes the parametric evaluation of the PIFA in terms of substrate relative permittivity, antenna height, ground plane dimensions, feed position, strip width, and the overall length of the radiating element. It will be shown that the resonance frequencies of the proposed structure can be controlled with the proper choice of its parameters [11-14]. The numerical results given in this section, has been obtained by using finite element simulation software, high frequency structure simulator, ANSOFT HFSS13 [15], which employs the adaptive finite element method. It will be seen that by varying the parameters, the designed antenna shows a dual-band performance in different operating frequencies; and by evaluating the effects of these parameters and collecting the data, closed formulas have been obtained in the following sections.

Ground plane dimension effects:

The antenna ground plane has an important effect on its performance. Currents excited on the radiating element will induce currents on the ground plane and the magnetic field is produced as the result of interaction between the radiating element and its image in the ground plane. The ground plane acts as a perfect reflector of energy only when it's infinite, but in practical situations, its dimensions are comparable to the radiating element and is used to control the resonance frequencies [12, 13]. The effect of ground plane dimensions has been shown in Fig. 3. If the length of the ground plane is considerably smaller than λ/4, tuning of the antenna will get increasingly difficult and the overall performance will deteriorate.

Antenna height and substrate permittivity effect:

PIFA bandwidth is inversely proportional to its quality factor: Q = stored energy/power loss. Substrates with higher ε_r, store more energy and radiate less. This is similar to assuming that the PIFA is equivalent to a lossy capacitor with high ε_r, resulting in a higher Q and lower bandwidth. Similarly, by increasing the substrate thickness, considering the inverse proportion of the capacity and the thickness, the energy increases while the quality factor decreases [16]. These effects have been shown in Figs. 4 and 5, respectively. The electrical properties of the substrate as well as the thickness of the substrate can affect the gain and bandwidth of the antenna. A thin substrate with a high ε_r will result in a weak radiation and a narrow bandwidth. Substrates with high loss tangent result in lossy antennas and consequently lower gains. Therefore, these kinds of antennas are usually mounted on thick low ε_r and low δ substrates just like what has been done in this paper.

Substrates with higher dielectric constant store energy rather than radiating it. We can model a patch antenna with a lossy capacitor with a high Q. It is obvious that a high Q factor results in a narrow band width. Although microstrip antennas mounted on high dielectric constant substrates have benefits like smaller size, they suffer from lower radiation efficiency and narrow bandwidth. The antenna bandwidth is inversely proportional to the Q-factor. This Q-factor is defined for a resonator as follows,

$$Q = \frac{energy\ \ stored}{power\ \ lost}\ . \qquad (1)$$

A substrate with bigger width and lower ε_r like air can result in a wider bandwidth and better radiation efficiency by lowering the Q-factor, and it can also solve the antenna surface excitation. The radiating element is usually made of copper and the substrate serves as a mechanical support for the radiating element. The dielectric constants of the substrates are usually between 1 and 10 and can be separated into three groups.

1- Some dielectric constants are between 1 and 2. These substrates are usually air, polystyrene foam, and dielectric honeycomb.
2- Relative dielectric constants between 2 to 4. These materials consist of dielectric reinforced Teflon.
3- Materials with relative dielectric constants between 4 and 10. These materials can be ceramic, quartz, or alumina.

The microstrip antenna theory ([1-5]) shows a degradation in antenna performance with increasing ε_r. Substrates with higher ε_r will decrease the antenna size at the cost of lower gain and matching bandwidth. These parameters can be observed in two ways. First the dimensions of the antenna and the resonance frequency are fixed while the effect are studied. In previous researches the comparison between the effects of Duroid, FR4, mica, silicon nitrate, alumina, rogers3210, silicon, and gallium arsenide substrate show that for a PIFA with fixed dimensions, antennas with the air, duroid, and FR4 substrate have an acceptable matching bandwidth, but the FR4 substrate has low gain and the other substrates, with higher ε_r cannot resonate without a change in the antenna structure [17-18]. It can be seen that the impedance bandwidth decreases with the increase in ε_r. If we study the effects of the substrate with a fixed resonance frequency and tuning the dimensions we can see that the maximum gain and return loss is obtained by using the substrates with lower dielectric constants. As stated before, an increase in ε_r results in an antenna with a higher Q-factor. Consequently, we have only studied the effect of substrates with dielectric substrates between 1 and 4 and it can be seen that the best result can be obtained with an antenna with air substrate.

Strip and short circuit plate width effects:

The width of the shorting plate has a very important effect on frequency tuning [19]. As shown in Fig. 6, by reducing the shorting plate width, the resonance frequency decreases. Strip width is another parameter that allows an independent control of resonance frequencies because it has an opposite effect on them; i.e., by increasing the strip width, the lower resonance frequency decreases and the higher frequency increases. This effect has been shown in Fig. 7.

Antenna overall length:

As expected, the overall length of the radiating element has the most important effect on tuning the resonance frequencies [20]. By increasing this length, both of the resonance frequencies will decrease. This effect has been shown in Fig. 8.

B. Formula derivation

In the previous section the effect of PIFA parameters on its resonance frequencies has been studied. As shown earlier one of the parameters (strip width) has an opposite effect on the resonance frequencies so it could be used to independently tune them and achieve the desired f_1/f_2. The parameters have been finely varied and extensive data has been gathered. Fitting the data has resulted in closed formulas for each of the resonance frequencies. In these formulas, h is the antenna height, L_g is the length of the ground plane, ε_r is the substrate permittivity, L is the overall radiating length, and Δw and W_S are the strips and the ground plane widths, respectively

$$f_1 = 2.2 \times \frac{0.7h + L_g}{\varepsilon_r^{\frac{1}{4}}(1.5L + \Delta w + W_s)}, \quad (2)$$

$$f_2 = 9.06 \times \frac{0.2h + 0.5L_g + 0.2\Delta w}{\varepsilon_r^{\frac{1}{4}}(1.5L + 1.8W_s)}. \quad (3)$$

By using these formulas, a PIFA has been designed, which works in GSM at 0.9 GHz and DSC1800 at 1.8 GHz. The values obtained for the parameters in millimeters are: $h = 8, W_s = 10, \Delta w = 4, \varepsilon_r = 1, L = 132, L_g = 81$

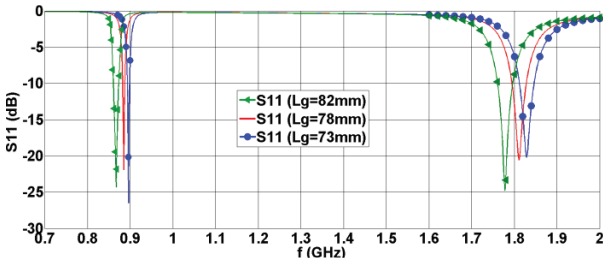

Fig. 3. Ground plane dimension effects on the resonance frequencies.

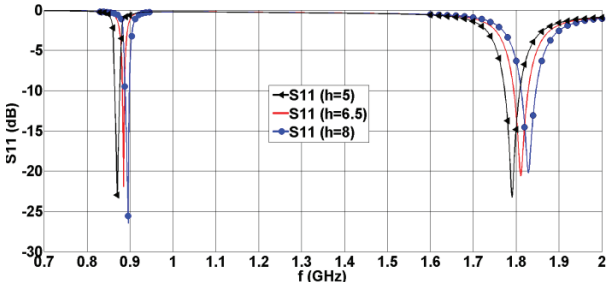

Fig. 4. Antenna height effects on the resonance frequencies.

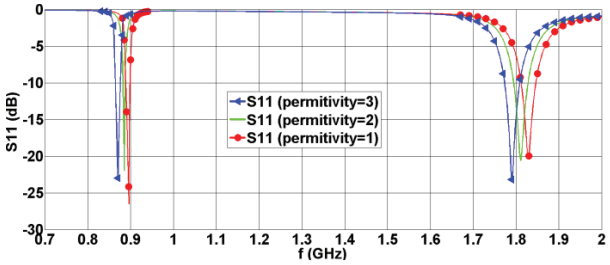

Fig. 5. Substrate permittivity effect on the resonance frequencies.

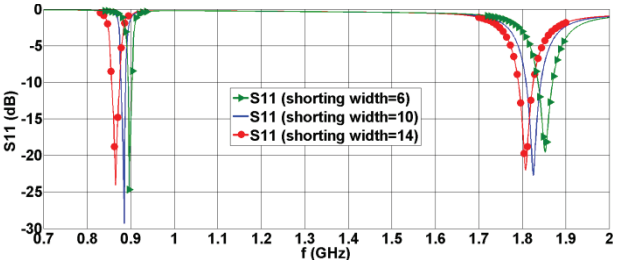

Fig. 6. Short circuit plate width effects on the resonance frequencies.

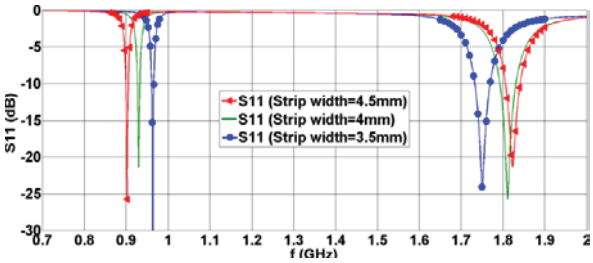

Fig. 7. Strip width effects on the resonance frequencies.

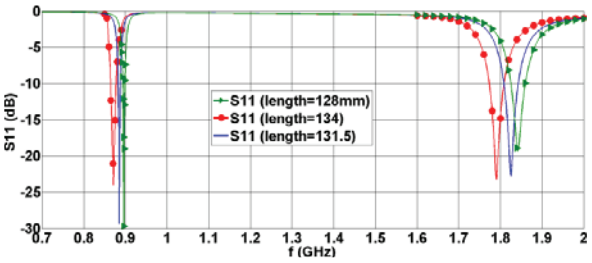

Fig. 8. Antenna overall length effects on the resonance frequencies.

C. Credibility range and accuracy of the formulas

In this section the frequency credibility range of the closed form formulas are evaluated for each of the resonance frequencies. First, the antenna is designed and simulated multiple times in HFSS; each time obtaining resonance frequency pairs with the first frequency between 670 MHz and 1100 MHz and the second one between 1570 MHz and 2000 MHz, and the antenna parameters in each simulation has been gathered. The parameters obtained by the simulation have been used in the formulas and the resulting frequency pairs have been compared to the simulated ones in order to find the validity range of the proposed formulas. The results have been shown in Fig. 9.

In order to study the accuracy of the formulas, the accurate values of the parameters according to full wave simulation are used in the formulas and the resulting frequency has been compared to the accurate frequency. The figures have been obtained by calculating the difference between the frequencies resulted from the formula to the accurate frequency obtained from simulation. Tables I and II, show the accuracy of the formulas in percentage in each frequency band. As expected from the figures, the formulas are accurate in the operation frequency bands.

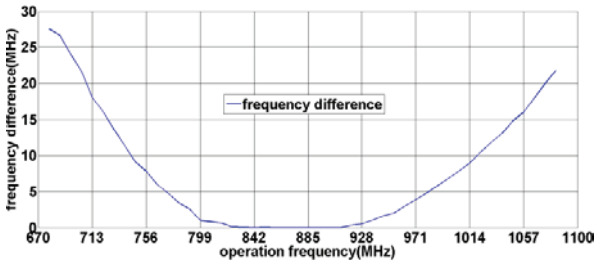

(a)

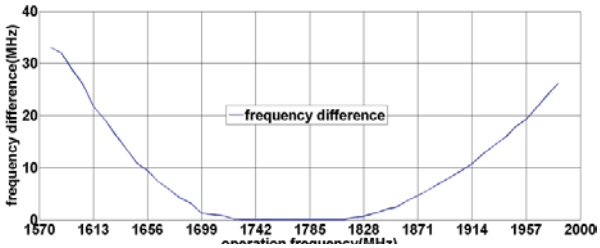

(b)

Fig. 9. (a) Credibility range for f1 and (b) ccredibility range for f2.

Table I: Accuracy of formulas for the lower frequency band.

Frequency range(MHz)	Percentage of error
f<740	$\Delta f > 1.3\%$
740<f<760	$0.9\% < \Delta f < 1.3\%$
760<f<800	$0.1\% < \Delta f < 0.9\%$
800<f<930	$\Delta f < 0.1\%$
930<f<980	$0.1\% < \Delta f < 0.5\%$
980<f<1030	$0.5\% < \Delta f < 1\%$
f>1030	$\Delta f > 1\%$

Table II: Accuracy of formulas for the higher frequency band.

Frequency range(MHz)	Percentage of error
f<1650	$\Delta f > 0.6\%$
1650<f<1680	$0.3\% < \Delta f < 0.6\%$
1680<f<1700	$0.07\% < \Delta f < 0.3\%$
1700<f<1830	$\Delta f < 0.07\%$
1830<f<1870	$0.07\% < \Delta f < 0.3\%$
1870<f<1900	$0.3\% < \Delta f < 0.6\%$
f>1900	$\Delta f > 0.6\%$

In order to evaluate the accuracy another example has been given. By using these formulas, another PIFA has been designed, which works in GSM at 0.85 GHz and DSC at 1.75 GHz. The values obtained for the parameters in millimeters are: h = 6 mm, W_S = 10.3, Δw = 6, ε_r = 1, L =

134, and L_g = 80. Simulating the proposed PIFA with the mentioned parameters, results in 0.8502 GHz and 1.7498 GHz frequencies, which shows the accuracy of the formulas. The Antenna can be designed to work in any frequency pair stated in the tables or figures and the parameters must be chosen accordingly for each frequency pair. It should be kept in mind that although many values might be chosen for the parameters; these values have a direct effect on the performance of the antenna. As stated earlier, the antenna has the best performance by choosing the highest value for h, and the lowest value for ε_r and a very small L_g will result in overall performance deterioration [21]. There is no specific limitation in L, Δw and W_s therefore, these parameters can be used to obtain the desired frequencies.

D. Antenna gain variation with frequency

Furthermore, the antenna gain variation with frequency at each band has been studied. Figure 10 shows the simulated antenna gain versus frequency in GSM and DCS bands. As shown in Fig. 10 , maximum gains are 2.4 dBi and 3.95 dBi at 0.9 GHz and 1.8 GHz center frequencies of each frequency band and the total gain is above 2.2 dBi in the working bands. It can be observed that the antenna gain is sufficient for mobile terminals. The gain in the DSC band is higher than the GSM band and that was predictable because of the higher electrical length of the antenna at the DCS band.

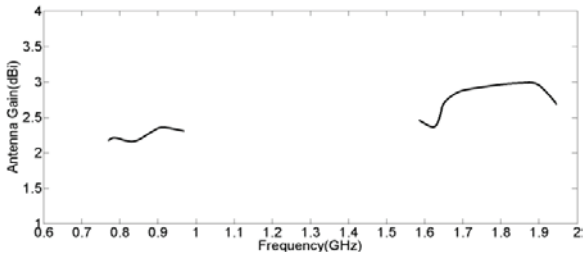

Fig. 10. Antenna gain variation with frequency.

V. FABRICATION AND MEASUREMENT

The antenna parameters have been found by using the formulas for GSM and DSC1800, namely 0.9 GHz and 1.8 GHz, respectively, and it has been fabricated according to the obtained dimensions. The fabricated antenna is shown in Figs. 11 (a) and (b). The comparison between the measured and simulated S11-parameters in Fig. 12 shows a complete agreement between the simulation and fabrication results, which proves the accuracy of the analysis and the formulas. The measured radiation pattern of the antenna at both frequencies is presented in Fig. 13. The radiation pattern in both planes is almost omni-directional, which means good coverage in both frequency bands.

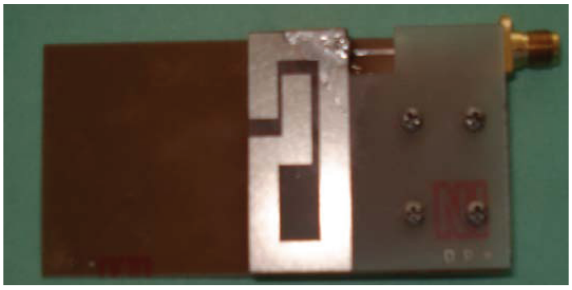

(a)

(b)

Fig. 11. The fabricated dual band PIFA; (a) top view and (b) side view.

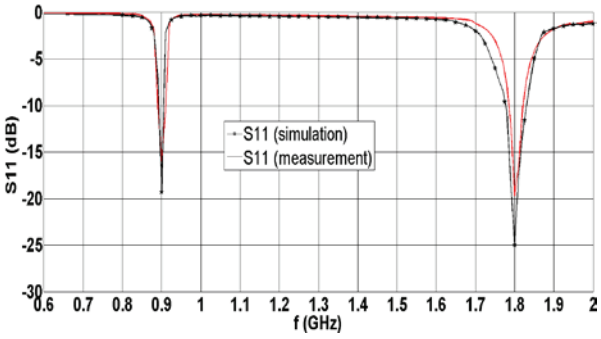

Fig. 12. Numerical simulation and measurement results.

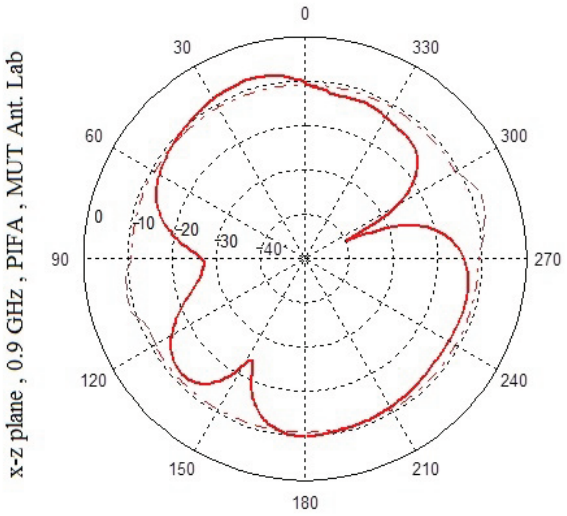

(a)

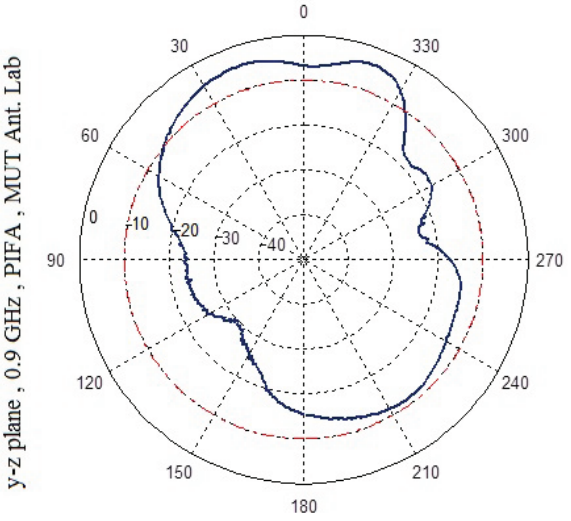

(b)

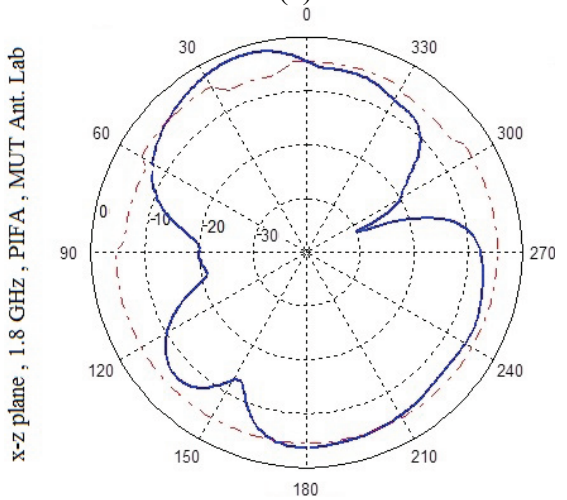

(c)

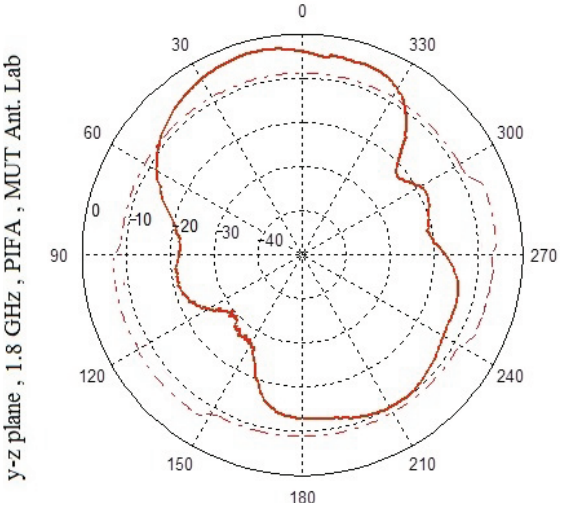

(d)

VI. CONCLUSION

In this paper a dual frequency, single feed, planar inverted-F antenna has been presented. This antenna is well suited to telephone handsets used in today's mobile communication systems operating in two frequency bands for example both GSM and DCS 1800 bands. The PIFA has been parametrically evaluated in terms of substrate relative permittivity, antenna height, ground plane dimensions, strip width, shorting plate width, and the effective dimension of the radiating element. It has been shown that the resonance frequencies of the proposed structure can be controlled with the proper choice of its parameters resulting in closed form formulas, which are very useful in designing this antenna. The proposed antenna has been fabricated according to the obtained formulas. Both numerical simulation and experimental data show the accuracy of analysis and formulas.

REFERENCES

[1] J. James and P. Hall, *Handbook of Microstrip Antennas*, Peter Peregrinus Ltd., London, UK, 1989.

[2] D. Pozar and D. Schaubert, *Microstrip Antennas: The Analysis and Design of Microstrip Antennas and Arrays*, IEEE press, New York, USA, 1995.

[3] I. Bahl and P. Bhartia, *Microstrip Antennas*, Artech House, Nonvood, MA, 1980.

[4] V. Nguyen, R. Bhatti, and S. Park, "A simple PIFA-based tunable internal antenna for personal communication handsets," *IEEE Ant. and Wir. Prop. Lett.*, vol. 7, pp. 130-133, May 2008.

[5] G. Kossiavas, R. Staraj, P. Le Thuc, C. Luxey, and A. Diallo, "Enhancement of the isolation between

two closely spaced mobile phone internal antennas by a neutralization effect," *22nd Annual Review of Progress in Applied Computational Electromagnetics (ACES)*, pp. 733-737, Miami, FL, March 2006.

[6] S. Liam, O. Boon P. Koh, P. Song, and L. Lau, "From a simple IFA to a dual band PIFA," *International Workshop on Antenna Technology: Small Antennas and Novel Metamaterials*, IWAT 2008.

[7] N. Karmakar, "Shorting strap tunable single feed dual-band stacked patch PIFA," *IEEE Ant. and Wir. Prop. Lett.*, vol. 2, pp.68-71, 2003.

[8] S. Haverals and T. Gilles, "Design and realisation of a quad band antenna for mobile telephony applications," *26th Annual Review of Progress in Applied Computational Electromagnetics (ACES)*, pp. 586-591, Tampere, Finland, April 2010.

[9] S. Ali, H. Kanj, D. Wang, and W. Geyi, "Design and analysis of a novel pent-band antenna for handheld applications," *24th Annual Review of Progress in Applied Computational Electromagnetics (ACES)*, pp. 899-902, Niagara Falls, Canada, March 30 - April 4, 2008.

[10] S. Jeon, H. Lee, S. Park, S. Lee, and N. Kim, "Design of mobile phone antenna with multi-band for SAR reduction," *23rd Annual Review of Progress in Applied Computational Electromagnetics (ACES)*, pp. 1739-1745, Verona, Italy, March 2007.

[11] H. Chattha, Y.Huang, Xu. Zhu, and Y. Lu "An empirical equation for predicting the resonant frequency of planar inverted-F antennas," *IEEE Ant. and Wir. Prop. Lett.*, vol. 8, pp. 856-860, 2009.

[12] M. Abedin and M. Ali, "Modifying the ground plane and its effect on planar inverted-F antennas (PIFAs) for mobile phone handsets," *IEEE Ant. and Wir. Prop. Lett.*, vol. 2, pp. 226-229, 2003.

[13] M. Huynh and W. Stutzman, "Ground plane effects on planar inverted-F antenna (PIFA) performance," *IEE Proceedings on Microwaves, Antennas, and Propagation*, 8 Augst 2003.

[14] S. Ibnyaich, J. Elbakouchi, A. Ghammaz, and M. Hassani, "Effects of changing dimensions on the planar inverted-F antenna performances," *Faible Tension Faible Consommation (FTFC)*, pp. 119-122, May-June 2011.

[15] HFSS 3D Full-Wave Electromagnetic Field Simulation ver. 13.

[16] J. He and K. Chung, "Design of a dual-band microstrip-fed meandered-tail PIFA for WLAN applications," *Antennas and Propagation Society International Symposium*, 2009.

[17] Y.-T. J.-Charles ,V. Ungvichian, and J. Barbosa, "Effects of substrate permittivity on planar inverted-F antenna performances," *Journal of Computers*, vol. 4, no. 7, July 2009.

[18] Y.-T. J.-Charles, V. Ungvichian, and A. Barbosa, "A study of substrate permittivity effects on the gain of planar inverted-F antennas," *IEEE Southeast Con.*, Huntsville, Alabama, April 2008.

[19] H. Chattha, Y. Huang, and Y. Lu "PIFA bandwidth enhancement by changing the widths of feed and shorting plates," *IEEE Ant. and Wir. Prop. Lett.*, vol. 8, pp.638-640, 2009.

[20] Y. Yu and J. Tarng, "A novel modified multiband planar inverted-F antenna," *IEEE Ant. and Wir. Prop. Lett.*, vol. 8, pp.189-192, 2009.

[21] I. Bonev, O. Franek, M. Christensen, and G. Pedersen, "Impact of the mobile phone dimensions on the hearing aids compatibility," *Applied Computational Electromagnetics Society (ACES) Journal*, vol. 25, no. 11, pp. 984-989, Nov. 2010.

Detail-Oriented Design of a Dual-Mode Antenna with Orthogonal Radiation Patterns Utilizing Theory of Characteristic Modes

A. Araghi and G. Dadashzadeh

Department of Electrical Engineering
Shahed University, Tehran, Iran
a.araghi@shahed.ac.ir, gdadashzadeh@shahed.ac.ir

Abstract ─ In this paper, theory of characteristic modes (TCMs) is used to perform modal analysis of a trapezium-shaped PEC plate. So it follows that a wide-spread overview about the electromagnetics behavior of the plate is provided. The first seven characteristic currents and corresponding resonance frequencies of the structure are obtained. All modes are orthogonal to each other. By applying the reactive loading, the first two modes are forced to be resonating close to each other at frequency of about 3.5 GHz, which is suitable for WiMax applications. To excite aforementioned modes on the structure, an appropriate configuration of microstrip feed lines is utilized. Due to the orthogonality property of current modes, the created radiation patterns are also orthogonal to each other. Since two characteristic currents are excited on the structure's body, it is expected to achieve two orthogonal radiation patterns too, which could result in a dual-mode antenna. To carry out the above-mentioned modal analysis, a specific method of moments (MoM) code has been developed and applied. The proposed antenna is simulated by well-known full-wave package Ansoft HFSS and results clarification of the expectations about the orthogonality in patterns.

Index Terms – Dual-mode antenna, method of moments (MoM), and theory of characteristic modes (TCMs).

I. INTRODUCTION

Design of antennas for wireless communication systems has attracted lots of interests. Obviously, the inclusion of multiple technologies in wireless devices will significantly increase the antenna's functionality. The more progress in system design, the much more attention in antenna selection. Since the advent of numerical based electromagnetic simulators, the approach of antenna design has been totally altered. At the moment, some huge amount of functions are performed by these simulators, which may results in vague understanding of the antenna performance especially whenever self optimizer tools in these simulators are utilized.

In many occasions the designer requires some wide spread insight about the antenna operation in different frequencies or may be the response of radiating part to various configurations of feedings. Making a profit of mentioned information enables the designer to choose the best conceivable option among all possibilities of an antenna to offer. This cannot be easily achieved by simulators and of course is quite time consuming.

Modal analysis could be an effective solution to cope with this problem due to the wide spread insight, which is provided by about the behavior of analyzed body. For a long time ago while now, modal analysis has been used in electromagnetics for the analysis of close structures (e.g., waveguides and cavities) in which it is quite simple to reach close solutions by applying boundary conditions [1, 2]. Nonetheless, it is not that easy to calculate different modes in open structures (e.g., antennas or scatterers) and it is usually quite time-consuming. Probably, this is one of the reasons that why modal analysis is not commonly used for antenna design at the present time. However, getting involved with the computation's difficulties of modes on open

Submitted On: Nov. 26, 2012
Accepted On: Sept. 1, 2013

1054-4887 © 2013 ACES

structures has its own values since it results in a wide-spread insight about the overall electromagnetic behavior of the analyzed body. Fulfillment of modal analysis in electromagnetic structures can be obtained via some limited number of approaches, for instances, which are spherical modes [3], modal expansion method [4], and eigen functions of conducting bodies. One subdivision of the classical eigen function analysis, termed as characteristic modes, was introduced first by Harrington in the early 1970s [5, 6]. The characteristic modes are real current modes that can be computed numerically for conductive structures of arbitrary shapes and are commonly named characteristic currents. Since characteristic currents form a set of orthogonal currents on an analyzed body, they create a set of orthogonal radiation patterns as well. As a direct result of this phenomenon, if one can form some characteristic currents on an analyzed body, achieving orthogonal patterns is expected [7, 8].

Generally, resonance frequency of different modes is dependent on physical characteristics of the analyzed structure and is the natural behavior of that body. However, utilizing reactive loading approach [9] enables us to have a control on almost every intended mode's resonance frequency.

The core objective of this paper is to indicate that the modal analysis of a structure can orient the whole design procedure. Accordingly, as an arbitrary structure, a trapezium-shaped conducting plate is analyzed by the theory of characteristic modes (TCMs) and its first seven modes are obtained in the first step. Then, an overview of the general modal behavior of the structure is given. After that, oriented reactive loading is carried out on the plate to make some changes on the resonance frequency of two intended modes among all those seven. At last, a feeding structure for the excitation is suggested. By exciting those mentioned specific modes, two orthogonal radiation patterns are achieved, which results in a dual-mode antenna.

II. MODAL ANALYSIS OF A TRAPEZIUM-SHAPED PEC PLATE

In this section, to provide a better understanding, at first a brief study on theory of characteristic modes is presented, and after that, first seven characteristic modes of a trapezium-shaped conducting plate are calculated using a developed proper MoM [10] code. Based on the obtained results, reactive loading on the analyzed body is performed to alter the resonance frequency of the first two modes. This reactive loading is fulfilled to have a dual-mode antenna (in this case, dual-mode means dual orthogonal radiation patterns) and it is also essential to make both modes similar from resonance frequency point of view. Hence, reactive loading is used to set the resonance frequency of first two modes at about 3.5 GHz so that make the antenna (which will be designed based on the mentioned modal analysis) suitable for WiMax applications.

A. Brief study on theory of characteristic modes (TCMs)

By the method explained in [5, 6], characteristic modes or characteristic currents can be calculated by the eigen functions of the following particular eigen value matrix equation,

$$[X]\overrightarrow{J_n} = \lambda_n [R]\overrightarrow{J_n} \tag{1}$$

where λ_n is eigen value, $\overrightarrow{J_n}$ is nth eigen vector or characteristic current, and [R] and [X] are the real and imaginary parts of the generalized impedance matrix [Z], which is produced in traditional MoM analysis of a structure. In fact equation (1) is derived from a particular weighted eigen value operator equation [5, 6]. The traditional MoM applies the inversion of [Z] (with considering the excitation point) to compute the created current on the body of analyzed structure. However, the result which is derived from equation (1) is a set of creatable currents on that body without considering any excitation. To put it in other words, equation (1) introduces the inherent behavior of an electromagnetics structure apart from the way of excitation and its own problems; i.e., impedance matching, soldering point, and etc.

One of the most important things, which should be taken into consideration in equation (1) is how eigen values λ_n respond to alteration of frequency. λ_n's variation range is from $-\infty$ to $+\infty$, and λ_n s of smallest magnitude are more important from radiation and scattering problems point of view. As given in [5, Eq. (20)], the modes with positive λ, predominantly store magnetic energy, whereas those with negative λ, mainly store electric energy. The mode having $\lambda = 0$ is called the resonant mode.

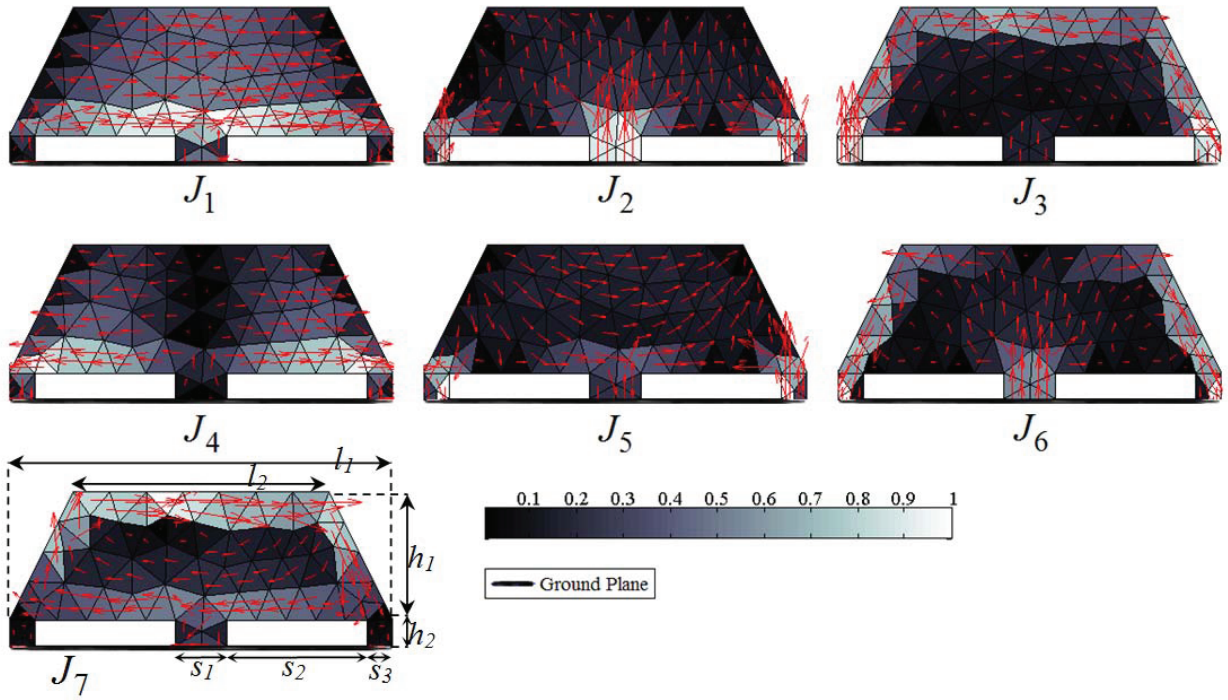

Fig. 1. Normalized first seven characteristic currents of a trapezium-shaped conducting plate near the ground plane.

In other words, at a specific frequency, the eigen value of a particular mode becomes zero and the mode is at resonance. Another representation of λ_n's is α_n's, which are called characteristic angles [11]. The formulation is as follows,

$$\alpha_n = 180^\circ - \tan^{-1}(\lambda_n). \quad (2)$$

It is obvious that at resonant frequency, characteristic angle (α_n) becomes 180°. Furthermore, due to [12] the frequencies related to angles between 135° and 225° represent the mode's bandwidth. To study the modal behavior of a conducting body, the first seven modes would suffice due to the weakness of amplitude and intense oscillation of the modes with higher number.

B. Applying TCMs on a trapezium-shaped PEC plate and reactive loading

Before getting involved with mode's calculation, pointing out to some prerequisites would be instrumental. At first, to meet all TCMs properties, it is a must that, the analyzed body is surrounded by air ($\varepsilon_r = 1$) [5]. Under this circumstance, TCMs guarantees that each characteristic current ($\overrightarrow{J_n}$) results in corresponding characteristic field ($\overrightarrow{E_n}$), which is orthogonal to all other characteristic fields (i.e., orthogonal radiation patterns). As a result, at the beginning, a trapezium-shaped plate close to an infinite PEC plate (ground plane) is placed in an air surrounded area far away from any object or scatterer. Afterward, the modal behavior of this structure is carried out by utilizing TCMs.

Secondly, in this work, modal analysis of the plate is performed to express some operational information, which are supposed to result in a proposal of an antenna (existence of the ground plane, which is mentioned above is also for this reason). Therefore, a way to make it possible to excite appropriate modes on the plate's body should be considered at the outset of design procedure. Consequently, three stands have been put under the trapezium-shaped plate to make it possible to push the current via them to the plate.

Owe to the above-mentioned issues, by developing a MoM code that uses 133 RWG [13] basis functions, the first seven characteristic currents and corresponding characteristic angles of the discussed plate with dimensions of l_1 = 30 mm, l_2 = 20 mm, h_1 = 10 mm, h_2 = 2 mm, s_1 = 4 mm, s_2

= 11 mm, and s_3 = 2 mm have been calculated, and the results are illustrated in Figs. 1 and 2, respectively.

According to Fig. 1, there are two modes with horizontally direction currents (J_1 and J_4), one vertically direction current mode (J_2), three loop shaped current modes (J_3, J_6, and J_7), and one special mode (J_5) in which the current shape is to some extent a mixture of horizontal and loop shaped. It is important to point out that, the outer current's loop in J_3 is closed via the ground plane. Generally, loop-shaped currents result in creation of passive modes [14] so that the corresponding characteristic angle never hits the 180° point; Fig. 2 vividly represents this issue (α_3, α_6, and α_7). The exact resonance frequency of other modes is as follows; J_1:6.1 GHz, J_2 : 5.6 GHz, J_4 : 7.9 GHz, and J_5 : 12 GHz. Commonly the resonance frequency of first mode is less than the second mode, but in this specific structure, ground plane shifts the resonance frequency of the second mode to a value less than the first mode's resonance: with the aid of image-theory, it is possible to eliminate the ground plane and replace the symmetrical shape of the plate instead. By doing so, it becomes apparent that two slots (the empty rooms between plate's body and ground plane in Fig. 1), which are actually two reactive loads, are blocking the J_2's movement and shifts this mode's resonance to less values. These slots have no considerable effects on J_1's resonance due to the current direction of this mode.

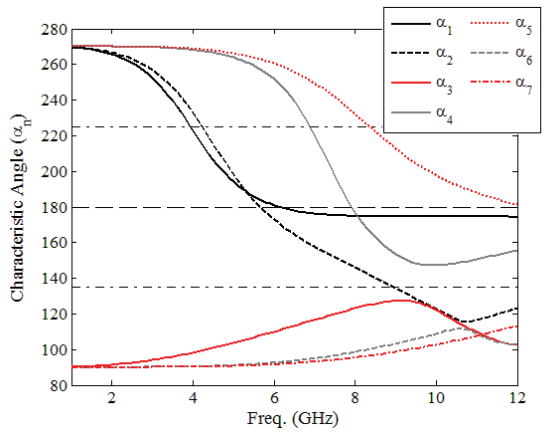

Fig. 2. First seven characteristic angles of the trapezium-shaped conducting plate near the ground plane.

At this time a general overview about the natural behavior of discussed structure is provided. The most valuable result from our point of view is that there are two modes, which resonate close to each other (J_1 and J_2). However, their resonance frequencies are not suitable for the intended applications, i.e., WiMax. Hereafter, we focus on these two modes and by doing reactive loadings, we try to shift these mode's resonance frequency close to 3.5 GHz.

To decrease the resonance frequency of the first mode, a vertical slot would be effective according to this fact that the direction of this current mode is horizontal. Therefore, a slot at the middle of the plate is created from its top till the middle stand (Fig. 3), the slot width is l_{s1} = 2 mm. This slot makes the first mode J_1 to be exactly resonated at frequency of 3.5 GHz (Fig. 4). However, there is no considerable change on resonance frequency of the second mode due to the direction of its current. J_1 and J_2 in modified structure are presented in Fig. 3. The other vertically current mode is J_4, so the resonance frequency of this mode is also reduced to less value (5.2 GHz) in this new shape of plate.

At last, it is worth mentioning that slot's creation on the plate makes the seventh mode active in contrary with Fig. 1's structure. As it can be observed from Fig. 3, according to the existence of the slot, J_7 changes its configuration from loop shaped one (Fig. 1) to vertically current and this makes the mode to be an active mode, which resonate at about 12 GHz.

The final step is to make the second mode to resonate close to the first mode at about 3.5 GHz. To meet this condition, the proposed structure alongside with first and second characteristic currents on the body's structure are presented in Fig. 5 (l_{s2} = 2 mm, h_3 = 4 mm, other dimensions are same as previous structures in Figs. 1 and 3). Correspondingly, Fig. 6 represents the behaviour of characteristic angles in this new structure. As it is clear from the figure, new added horizontal slots result in a reduction at resonance frequency of all modes that their current directions are vertical. There are still two reactive modes (J_3 and J_6) and the resonance frequency of the other modes are as follow; J_1 : 3.5 GHz, J_2 : 3.65 GHz, J_4 : 4.1 GHz, J_5 : 4.8 GHz, and J_7 : 5.1 GHz. So at this moment our predefined goal is achieved, i.e., two resonating modes at about 3.5 GHz. Now if some configuration of currents similar to those ones presented in Fig. 5 can be shaped on the structure, it is expected to obtain two orthogonal radiation patterns.

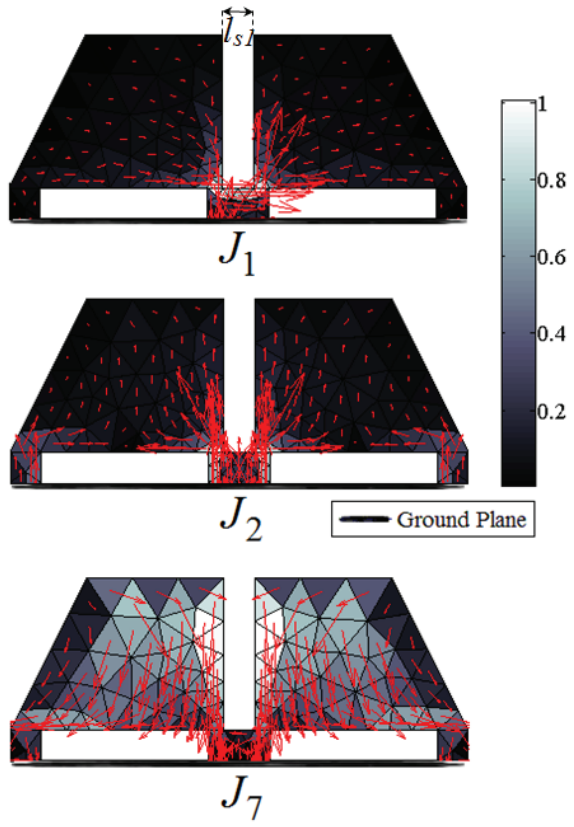

Fig. 3. Normalized first, second, and seventh characteristic current of a reactively loaded trapezium-shaped conducting plate near the ground plane.

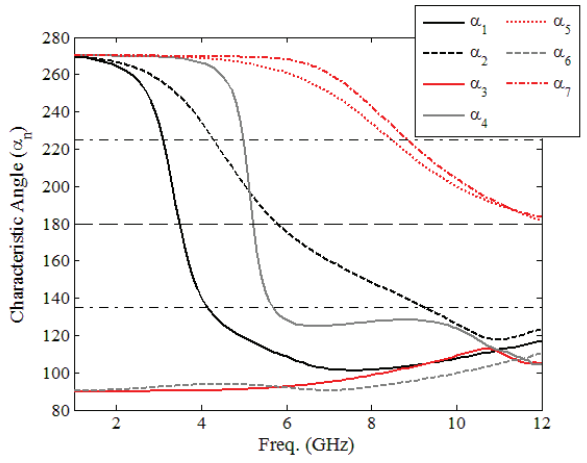

Fig. 4. First seven characteristic angles of the reactively loaded trapezium-shaped conducting plate of Fig. 3.

III. ANTENNA DESIGN

Once the modes J_1 and J_2 on the structure presented in Fig. 5 have been extracted, the next step is to find optimum feeding scheme to excite these modes on the antenna. To do this, the proposed antenna structure is shown at a glance in Fig. 7. As it can be observed, there are four separated ports, which connected to the radiating part (the trapezium-shaped plate) via four microstrip transmission lines, printed on a Rogers RT/duroid 5870 substrate with thickness of h = 0.787 mm and ε_r = 2.33. To consider an infinite ground plane (which have taken into consideration the numerical modal analysis) in the antenna structure, other dimensions of substrate are $l_x = l_y$ = 80 mm, which result in an adequately large plan in

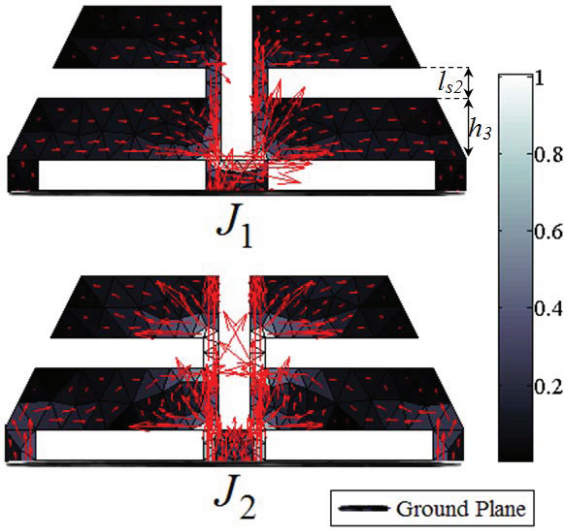

Fig. 5. Normalized first and second characteristic currents of a reactively loaded trapezium-shaped conducting plate near the ground plane.

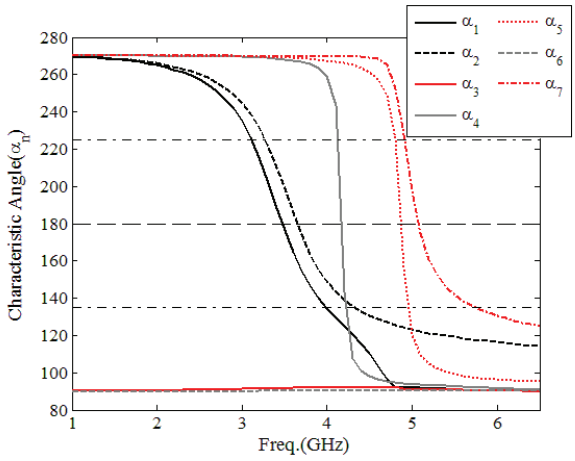

Fig. 6. First seven characteristic angles of the reactively loaded trapezium- shaped conducting plate of Fig. 5.

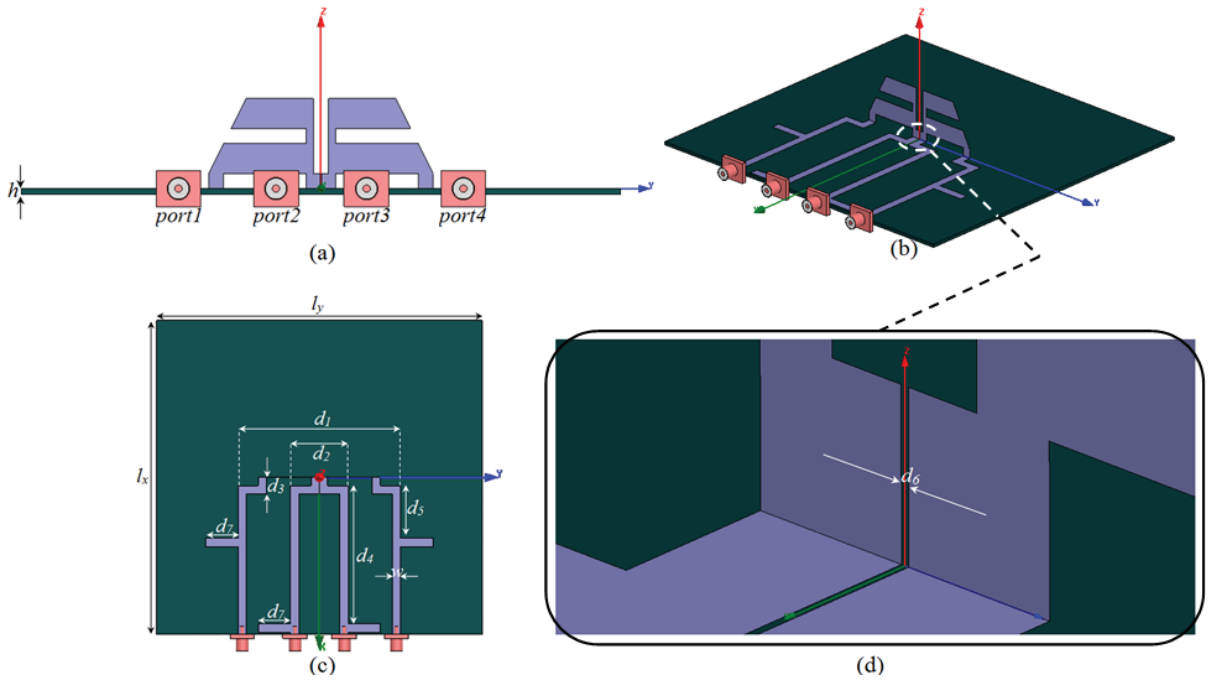

Fig. 7. Proposed antenna structure and its characteristics.

comparison with the wavelength. In order to be able to excite first and second modes on the structure's body in a better way, a thin slot is created at the middle of the radiating part with width of d_6 = 0.1 mm (Fig. 7 (d)) to decrease the unwanted current's follow from *port2* to *port3*. Both this slot and the substrate's thickness have not been analyzed in TCMs and of course their existence shifts the corresponding resonance frequency of the desired modes. However, owing to the fact that without these mentioned elements, the antenna structure cannot be completely achieved, they have been kept on the structure and instead, their undesirable effects have been compensated by using of four stubs that can be seen in Fig. 7. Other antenna's parameters, which are presented in Fig. 7 (c) are as follow: d_1 = 40 mm, d_2 = 14.1 mm, d_3 = 4 mm, d_4 = 34 mm, d_5 = 13 mm, d_7 = 8 mm, and w = 2 mm. The antenna physical structure is symmetric with respect to *xz* plane and the dimensions, which are not specified in the figure are the same as those represented in Figs. 1, 3, and 5.

IV. RESULTS

To obtain the dual-mode operation, some alternations in phases of the ports have been performed. In other words, to create J_2 ($Mode_2$) on the trapezium-shaped plate, all ports are excited with the same initiate phase. Furthermore, creation of J_1 ($Mode_1$) on the body is achievable by producing 180° phase difference in *ports2* and *4* with respect to *ports1* and *3*. Table I presents the feeding configuration that can be employed at ports.

Table I: Feeding configuration (amplitude and phase) for the excitation of 1st and 2nd modes.

	port1	***port2***	***port3***	***port4***	**Excited current**
$Mode_1$	$1\angle 0^\circ$	$1\angle 180^\circ$	$1\angle 0^\circ$	$1\angle 180^\circ$	J_1
$Mode_2$	$1\angle 0^\circ$	$1\angle 0^\circ$	$1\angle 0^\circ$	$1\angle 0^\circ$	J_2

The proposed antenna is simulated by the full-wave well known package Ansoft HFSS. The current distributions of first and second modes on the trapezium-shaped plate are obtained as illustrated in Fig. 8, which are both acceptably similar with those presented in Fig. 5. Apart from this, Fig. 9 represents the *S*-parameters of the antenna, which revealed that the antenna can work well at 3.5 GHz.

At this moment, with regard to the fact that two characteristic currents are created on the analyzed structure, it is expected that the corresponding radiation patterns will be orthogonal to each other and Fig. 10 clarifies the correctness of this issue. As it can be observed from Fig. 10, the orthogonality

condition of patterns is obtained very well at both *phi* = 0° and 90° planes, which makes the antenna to operate in two modes, which are different in radiation pattern. As it has been cleared before, associated with each mode, there is a specific configuration of feeding. So it follows that changing the initiate phase of feeding's ports as presented in Table. I, results in switching between modes in the proposed dual-mode antenna.

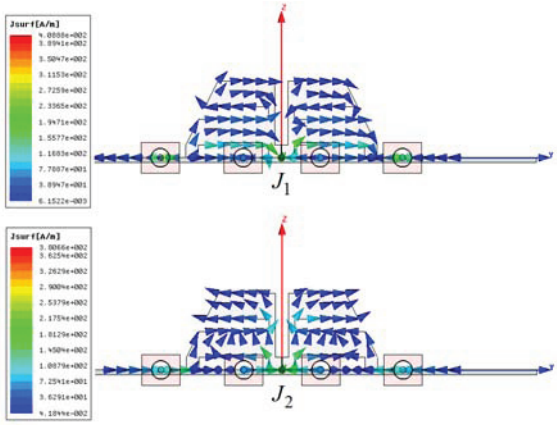

Fig. 8. The excitation of first and second modes on the proposed antenna structure.

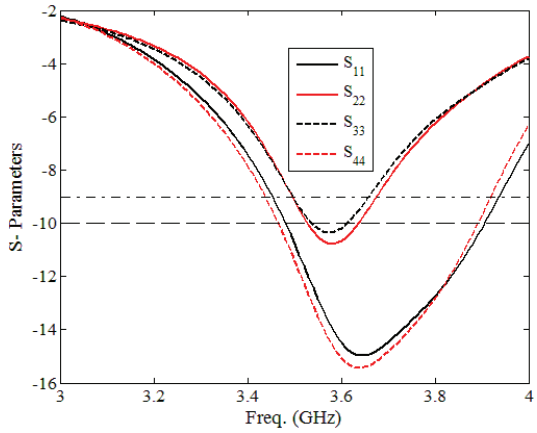

Fig. 9. Scattering parameters of the proposed antenna structure.

V. CONCLUSION

Modal analysis of a structure is exploited to design an antenna whose advantage is operating in two modes. Each mode has a radiation pattern, which is orthogonal to the other mode. The first seven characteristic modes of a trapezium-shaped radiator are obtained by a specific MoM code. With the aid of a general overview about the electromagnetic behavior of the analyzed body, reactive loading is performed in order to set the resonance frequency of first two modes to be identical. From the TCMs, it is expected that each characteristic current leads to a radiation pattern that is orthogonal to the radiation pattern of other characteristic current. As a result, a specific feeding structure is proposed to excite the discussed first two modes on the structure's body so that a dual-mode antenna is obtained, which benefits from two orthogonal radiation patterns. By choosing an appropriate initiate phase of the feeding's ports, switching between modes is achievable.

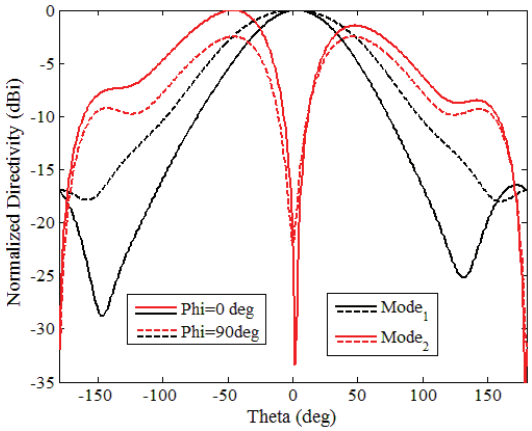

Fig. 10. Normalized radiation patterns of the proposed antenna in first and second modes.

ACKNOWLEDGMENT

The authors would like to express their gratitude to the reviewers for their valuable advice and helpful comments.

REFERENCES

[1] D. Pozar, *Microwave Engineering*, John Wiely and Sons, 2005.

[2] M. Swillam, M. Bakr, and X. Li, "Modal sensitivity analysis of guided wave structures using one FDTD simulation," *25th Annual Review of Progress in Applied Computational Electromagnetics (ACES)*, pp. 286-290, Mar. 2009.

[3] R. Harrington, "Effect of antenna size on gain, bandwidth and efficiency," *J. Res. Nat. Bur. Stand. Radio Propag.*, vol. 64, pp. 1-12, Jan. 1960.

[4] D. Wilton and R. Mittra, "A new numerical approach to the calculation of electromagnetic scattering properties of two dimensional bodies of arbitrary cross section," *IEEE Trans. Antennas Propag.*, vol. 20, no. 2, pp. 310-317, May 1972.

[5] R. Harrington and J. Mautz, "Theory of characteristic modes for conducting bodies," *IEEE Trans. Antennas Propag.*, vol. 19, no. 5, pp. 622-628, Sep. 1971.
[6] R. Harrington and J. Mautz, "Computation of characteristic modes for conducting bodies," *IEEE Trans. Antennas Propag.*, vol. 19, no. 5, pp. 629-639, Sep. 1971.
[7] E. Antonino-Daviu, M. Cabedo-Fabres, M. Gallo, M. Ferrando-Bataller, and M. Bozzeti, "Design of a multimode MIMO antenna using characteristic modes," in *Proc. 3rd EuCAP*, 2009, pp. 1840-1844.
[8] A. Araghi and G. Dadashzadeh, "Oriented design of an antenna for MIMO applications using theory of characteristic modes," *IEEE Antennas and Wireless Propag. Letters*, vol. 11, pp. 1040-1043, Sep. 2012.
[9] R. Harrington and J. Mautz, "Control of radar scattering by reactive loading," *IEEE Trans. Antennas Propag.*, vol. 20, no. 4, pp. 446-454, July 1972.
[10] R. Harrington, *Field Computation by Moment Method*, New York: Macmillan, 1968.
[11] E. Newman, "Small antenna location synthesis using characteristic modes," *IEEE Trans. Antennas Propag.*, vol. 27, no. 4, pp. 622-628, July 1979.
[12] M. Cabedo-Fabres and A. Valero-Nogueira, "Systematic design of antennas using the theory of characteristic modes," Ph.D. dissertation, Univ. Politec. Valencia, Valencia, Spain, 2007.
[13] S. Rao, D. Wilton, and A. Glisson, "Electromagnetic scattering by surfaces of arbitrary shape," *IEEE Trans. Antennas Propag.*, vol. 30, no. 3, pp. 409-418, May 1982.
[14] M. Cabedo-Fabres, E. Antonino-Daviu, A. Valero-Nogueira, and M. Ferrando-Bataller, "The theory of characteristic modes revisited: A contribution to the design of antennas for modern applications," *IEEE Antennas Propag. Mag.*, vol. 49, no. 5, pp. 52-68, Oct. 2007.

Ali Araghi was born on Oct. 20, 1985. He received his B.Sc. degree from Islamic Azad University -Rey Branch and M.Sc. degree from Shahed University, Tehran, Iran, respectively in 2009 and 2012, both in Communication Eng. Since Jan. 2012 he has been collaborating with ICT Research Institute on wave propagation analysis in different environments and wireless sensor networks. His research interests include the modal analysis of open structures, numerical methods, wave propagation, array and phase array antenna, and printed antennas with linear and circular polarization.

Gholamreza Dadashzadeh was born in Urmia, Iran, in 1964. He received the B.Sc. degree in communication engineering from Shiraz University, Shiraz, Iran, in 1992 and M.Sc. and Ph.D. degrees in communication engineering from Tarbiat Modarres University, Tehran, Iran, in 1996 and 2002, respectively. From 1998 to 2003, he has worked as the Head Researcher of the Smart Antenna for Mobile Communication Systems and the wireless local-area network 802.11 project with the radio communications group of Iran Telecommunication Research Center (ITRC). From 2004 to 2008, he was the Dean of the Communications Technology Institute, ITRC. He is currently an Assistant Professor with the Department of Electrical Engineering, Shahed University, Tehran. He has published more than 70 papers in referred journals and international conferences in the area of antenna design and smart antennas. Dr. Dadashzadeh is a member of the Institute of Electronics, Information, and Communication Engineers of Japan and the Iranian Association of Electrical and Electronics Engineers. He received the first degree of national researcher in 2007 from Iran's Ministry of Information and Communications Technology.

Investigations on Corrugation Issues in SIW based Antipodal Linear Tapered Slot Antenna for Wireless Networks at 60 GHz

P. Shrivastava, D. Chandra, N. Tiwari, and T. Rama Rao

RADMIC, Department of Telecommunication Engineering
SRM University, Chennai - 603203, India
purvashrivastava09@gmail.com, dev0702@gmail.com, nitizaz@gmail.com

Abstract ― In recent days, substrate integrated waveguide (SIW) technology is attracting a lot of interest in the development of millimeter-wave (MmW) based circuits due to its inherent advantages. Tapered slot antenna (TSA) with antipodal geometry is used to surmount the impedance matching constraint and to enhance electrical performance including gain, side lobes levels, and main beam pattern. This paper focuses on the design of antipodal linear tapered slot antenna (ALTSA) using SIW technique at 60 GHz for wireless local area network (WLAN) and wireless personal area network (WPAN) applications. The size of the proposed antenna is very compact (43.29 mm × 9.93 mm × 0.381 mm) and the substrate used is RT/ Duroid 5880. Corrugations have been investigated on both the edges to improve antenna gain, front-to-back ratio, and radiation patterns. Numerical simulations are performed using 3D-EM tools, high frequency structure simulator (HFSS) and CST microwave studio (CST MWS). The obtained results reveal that when corrugation is introduced in the antenna there is a significant improvement of 3 dB in gain, respectively. This study has been reported earlier in other frequency bands but rarely any literature has been reported of such development at 60 GHz.

Index Terms - ALTSA, corrugation, CST MWS, front to back ratio, HFSS, MmW, and SIW.

I. INTRODUCTION

The evolution of new generation wireless communication systems is highly dependent on the deployment of millimeter-wave (MmW) based radio technologies. With the available bandwidth of 7 GHz, the unlicensed 60 GHz band (57 GHz – 64 GHz) is of great interest for the new generation wireless local area network (WLAN) and wireless personal area network (WPAN), which will allow multimedia downloads at ultra-high speed with data rate of 1 Gbps [1]. The propagation characteristics of the 60 GHz band are characterized by high levels of oxygen absorption and rain attenuation. This limits the range of communication systems using this band. However, it will allow a high level of frequency re-use and therefore makes it attractive for a variety of short-range wireless communication applications [2].

Recently, there has been a great deal of interest in antennas for millimeter wave applications. Tapered slot antenna (TSA) has been widely used to take advantage of high gain, low side-lobe level characteristics, ease of implementation, and broadband characteristics [3]. TSA is a popular choice for applications such as ground penetration surveillance, medical imaging security, road surface scanning [4], and numerous wireless communication applications [5]. Many of the new radar systems reaching the fleet over the next few years will use frequency or phase-sensitive antennas and antennas that can electronically scan the azimuth as well as elevation. TSA can be a good candidate for such antenna systems.

Many designs for taper have been proposed and developed by researchers all over the world [6-9]. One such type of antenna is antipodal linear tapered slot antenna (ALTSA). Researchers around the globe have given high attention to ALTSA

Submitted On: March 9, 2013
Accepted On: Sept. 23, 2013

1054-4887 © 2013 ACES

for its salient performances, which includes narrow beamwidth, high element gain, and wide bandwidth [10]. It has been reported that a reduced antenna width is associated with degradation in radiation pattern, which is a significant problem for the design of compact TSAs [11]. ALTSA has been investigated widely in academic and industry focusing the ultra-wideband (UWB) and very high frequency (VHF) range [8-12], hardly any work is present in the extremely high frequency (EHF) range. Substrate integrated waveguide (SIW) technology has been proposed for MmW circuits and investigated by researchers from various parts of the world in the past 15 years [13]. In [14], a simple technique for propagation characteristics for SIW has been studied and proposed. Waveguides are basically a device for transporting electromagnetic energy from one region to another. In this study, it is composed of two rows of metalized via-holes, which are connected with two metal plates on the top and bottom sides. The mechanism on which SIW operates is very much similar to a rectangular waveguide. SIW inherits most of the advantages of the conventional metallic waveguides like complete shielding, low loss, high quality factor and high power-handling capability [15].

TSA with corrugation structure have been used to reduce tapered slot antenna width without any significant degradation in the radiation pattern [11-13]. In applications such as MmW radar and communication systems using directional antenna, it is preferred that the antenna should have a high front to back ratio (F/B) and directivity. Corrugation has been proven successful in TSA structures for F/B ratio, gain, and beamwidth improvement [16].

Selection of simulation tool can be made based upon the simulation data uncertainties, simulation time, model design limitation, and hardware requirement. Due to complex MmW antenna design, computational electromagnetic (CEM) field model is inevitable. CEM models the interaction of magnetic and electric field with physical objects and their environment to find the numerical approximation of Maxwell's equation. High frequency structure simulator (HFSS) based on finite element method (FEM) and CST microwave studio (CST MWS) based on finite difference time domain method (FDTD) are specialized software that solve the subset of Maxwell's equations [17].

Thus, this paper focuses on the effect of corrugation in SIW fed ALTSA, designed for WLAN and WPAN applications at 60 GHz. Comparison of results using electromagnetic solvers HFSS and CST MWS have been made for accuracy and simulation time. Section II deals with design, simulation and measured results are presented in section III, followed by conclusions in section IV.

II. ALTSA ARCHITECTURE AND DESIGN

The ALTSA is designed on 0.381 mm RT/Duroid 5880 substrate with dielectric constant ε_r = 2.2 and tan δ = 0.0004. Figure 1 depicts a configuration of the proposed ALTSA with the SIW feeding, which consists of two flares. On one side, the input track is flared to produce half of the linear TSA and then on the other side of substrate the ground plane is flared in the opposite direction. One of the advantages of the antipodal geometry is that it does not need to layout any stubs on the printed circuit board (PCB) to achieve impedance matching.

The input impedance of the ALTSA is high and that of the SIW is low, which causes a mismatch problem. To solve this problem, the flares are designed in a way that they overlap each other. The SIW feeding structure has two periodic rows of metalized cylindrical vias connecting the upper and lower flares of ALTSA, which acts as dielectric filled rectangular waveguide. The center frequency of proposed antenna is 60 GHz and length of tapered slot line is 4.5 λ. Table 1 provides various parameters of SIW based ALTSA.

The performance of ALTSA depends upon the thickness t and the dielectric permittivity ε_r [18] as given in equation (1),

$$f_{substrate} = \frac{t(\sqrt{\epsilon_r} - 1)}{\lambda}. \quad (1)$$

For better performance it should lie within a range given by equation (2),

$$0.005 \leq f_{substrate} \leq 0.03 . \quad (2)$$

When the distance between the via-holes are electrically small (< 0.2 λ), SIW can be replaced by rectangular waveguide [13]. SIW can be

commonly used as transmission line, which is similar to rectangular waveguide in terms of mode and cut-off frequency properties.

The cut-off frequency is a frequency at which all lower frequencies are attenuated by the waveguide and above the cut-off frequency all higher frequencies propagate within the waveguide. The cut-off frequency depends on the shape and size of the cross section of waveguide. The larger the waveguide, the lower the cut-off frequency of antenna. The effective width of the SIW structure W_s [18] is calculated based on equation (3),

$$W_s = W_{SIW} - 1.08\frac{D}{P} + 0.1\frac{D}{W_{SIW}} \quad (3)$$

where, D is the diameter of the via, P is the space between the vias and W_{SIW} is the SIW width. The cut-off frequency is given by equation (4)

$$f_{c,mn} = \frac{c}{2\sqrt{\varepsilon_r}}\sqrt{\left(\frac{m}{a}\right)^2 + \left(\frac{n}{b}\right)^2}, \quad (4)$$

where, c is the speed of light and ε_r is the relative permittivity.

Table 1: Dimension of ALTSA.

Parameter	Dielectric Substrate: RT/duriod (ε_r =2.20, h=0.381mm)	
	Symbol	Value mm
ALTSA Length	L1	44.61
SIW Length	L2	22.36
Taper Length	L3	4.93
Microstrip Line Length	L4	1.2
ALTSA Width	W1	9.93
Overlapping Area Width	W2	1.8
Taper Width	W3	3.12
Microstrip Line Width	W4	0.8
SIW Width	W_{SIW}	6.2
Diameter of Vias	D	0.6
Pitch of Vias	P	0.90

Both D and P should be measured precisely to ensure loss free radiation between the metallic vias because of diffraction. Following equations (5) and (6) allows us to do the same [18],

$$D \le \frac{\lambda_g}{5}, \quad (5)$$

where, λ_g is the guided wavelength and,

$$P \le 2D. \quad (6)$$

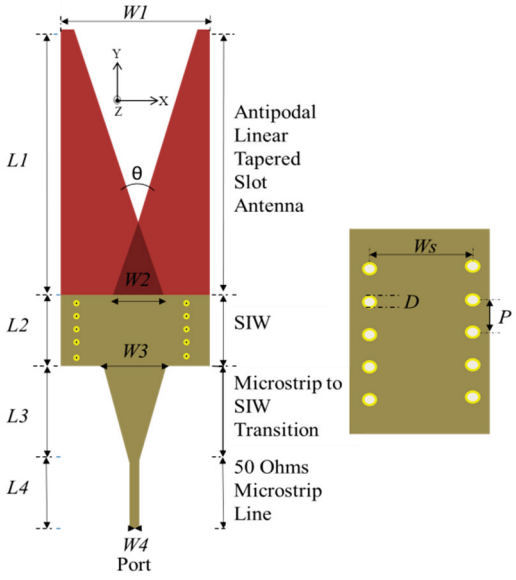

Fig. 1. Proposed ALTSA design.

The size of the excitation port also plays a vital role in performance of antenna. There are several rules for determining the port size. The port peripheries should touch the ground plane of the transmission line and the width of the port should be wide enough to avoid the adjacency of the signal strip and port periphery [15]. For matching the low characteristic impedance of SIW a linearly tapered microstrip is used. The microstrip is designed based upon the equations given in [19].

A. Corrugation structures

Further, outer rectangular corrugation structures are applied to the ALTSA design. On small antennas, undesired surface currents on the outlines lead to near field radiation and thereby lead to reduced gain as well as high side lobe levels [11, 12]. For antenna pattern improvement the concept of corrugation structures have been studied. Corrugations have been proven successful in tapered slot antenna structures for improvement of gain and front to back ratio [16]. Corrugations are well known in the design of

horn antennas in order to suppress higher modes. Therefore, they guarantee the polarization pureness of the antenna [18].

B. Outer rectangular corrugation

Figure 2 shows the ALTSA with outer rectangular corrugation structure. The length and the width are selected to be 1.25 mm (RC_l) and 0.5 mm (RC_W), respectively with 0.5 mm spacing (RC_S) between the rectangular corrugations, made on the outer edges of the ALTSA.

III. SIMULATIONS AND RESULTS

The HFSS and CST MWS are the simulation softwares (SS) used to simulate the ALTSA at 60 GHz. In the current implementation, the antenna is first designed and simulated using HFSS. For the validation of simulated results obtained, the antenna with same dimension is designed and simulated using CST MWS. HFSS simulation offers a reliable mesh adaptation algorithm and several simulation coverage criteria. For CST simulation, mesh definition has a significant influence on representation of areas that includes ports.

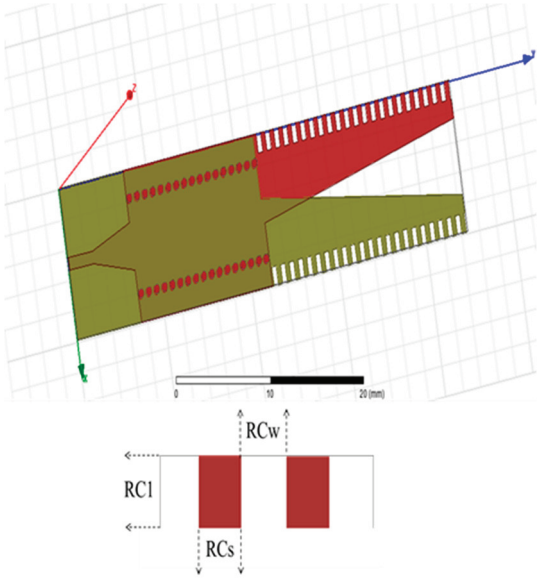

Fig. 2. ALTSA with outer corrugation.

In these areas, mesh step is decreased until the relevant mesh vertices are accurately positioned as start and end points for integration across ports. Due to ALTSA geometry and higher frequency, it is observed that a high number of meshes are needed to accurately model the structure and simulate the electromagnetic response. The total computing time is about 30 minutes for both the 3D-EM tools and the computing platform is Intel Core i7 with 24 GB random access memory (RAM). The simulation result indicates the return loss, distribution of current, and gain of ALTSA.

Figure 3 shows the plain and corrugated ALTSA fabricated on an RT/Duroid 5880 dielectric substrate with thickness of 0.381 mm. The simulated return loss shown in Figs. 4 and 5 illustrate that the return loss for corrugated ALTSA is good at 60 GHz band and the bandwidth is approximately 3 GHz, which is around 38.5 % of the total spectrum under observation in both the SS. E-plane is the plane containing the electric field vector and the direction of maximum radiation. The electric field or "E" plane determines the polarization or orientation of the radio wave.

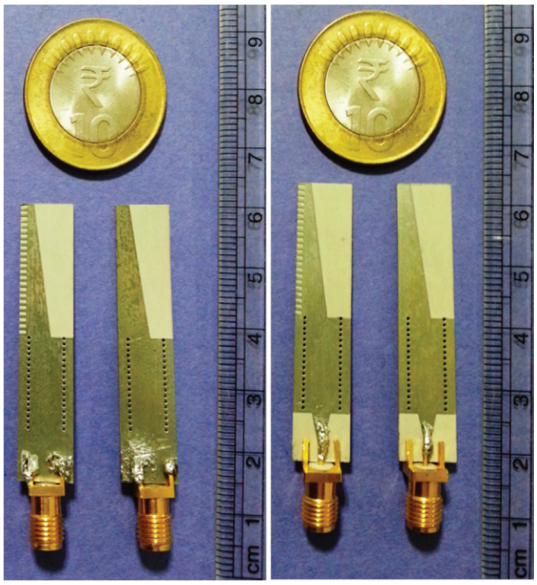

(a) (b)

Fig. 3. Photographs of plain ALTSA and ALTSA with corrugation, (a) upper side and (b) lower side.

For a vertically-polarized antenna, the E-plane usually coincides with the vertical/elevation plane. For a horizontally-polarized antenna, the E-Plane usually coincides with the horizontal/azimuth plane. E- and H-planes should be 90 degree apart. The magnetizing field or "H" plane lies at a right

angle to the "E" plane. For a vertically polarized antenna, the H-plane usually coincides with the horizontal/azimuth plane. For a horizontally-polarized antenna, the H-plane usually coincides with the vertical/elevation plane. This is important, since MmW applications need a good stability of radiation pattern and directivity.

In an antenna pattern, the half power beam width is the angle between the half-power (-3 dB) points of the main lobe, when referenced to the peak effective radiated power of the main lobe. The 3dB beamwidth for plain ALTSA and ALTSA with outer rectangular corrugation is within the range of $32^{o} \approx 38^{o}$, while the SLL is between -4 dB and -9 dB in both the SS.

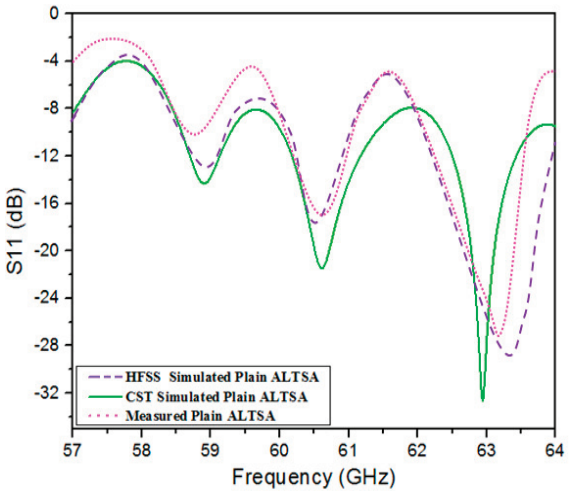

Fig. 4. Simulated and measured S_{11} parameters of plain ALTSA.

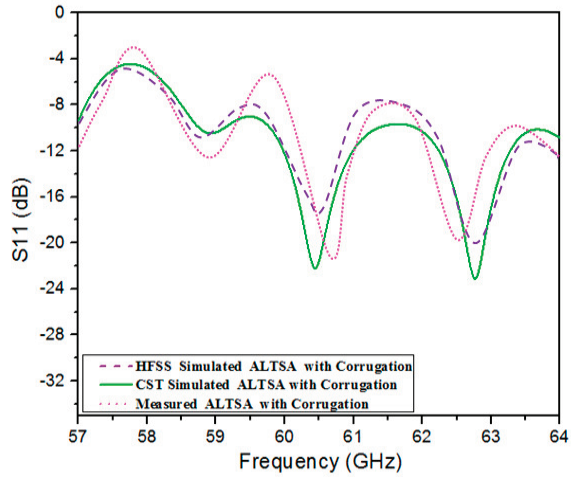

Fig. 5. Simulated and measured S_{11} parameters of ALTSA with corrugation.

Figure 6 shows current distribution in ALTSA in HFSS and CST MWS. It is observed that corrugation on outer edges of ALTSA contributes higher gain. The gradually flared edges can be considered to accommodate a continuous change of wavelength over a broad frequency range, which results in the broadband impedance matching performance. Figures 7 and 8 show the simulated and measured gain of ALTSA along the boresight, which is observed to be 13.2 dB in HFSS and 13 dB in CST MWS for plain ALTSA while the measured gain is observed to be 12.6 dB. A slight difference in two simulated results can be observed, which is basically due to the different numerical methods employed in CST MWS and HFSS. Similarly, for the corrugated ALTSA the gain is observed to be 16.2 dB in HFSS and 16.1 dB in CST MWS. The measured gain is observed to be 16 dB. Simulated and measured results indicate that corrugation effects have significant impact on return loss, radiation pattern, and antenna gain.

IV. CONCLUSIONS

In this research work, ALTSA with and without outer rectangular corrugations are designed and simulated utilizing Ansys's HFSS and CST MWS for 60 GHz wireless communications. The simulated results were compared with the measured values obtained from the fabricated antenna. The results from simulation and measurement were observed and the performance of the antenna in relation to gain and beamwidth has been analyzed. The corrugations on the outer edges of the antenna change the surface current distribution increasing the gain. The proposed antenna has low side and back lobes, and a high gain. For validation, the results of HFSS and CST MWS simulations were compared with the measured results and are observed to be in good agreement.

ACKNOWLEDGEMENT

Authors are very much appreciative to the DRDO, Govt. of India for providing financial backing in executing this research work.

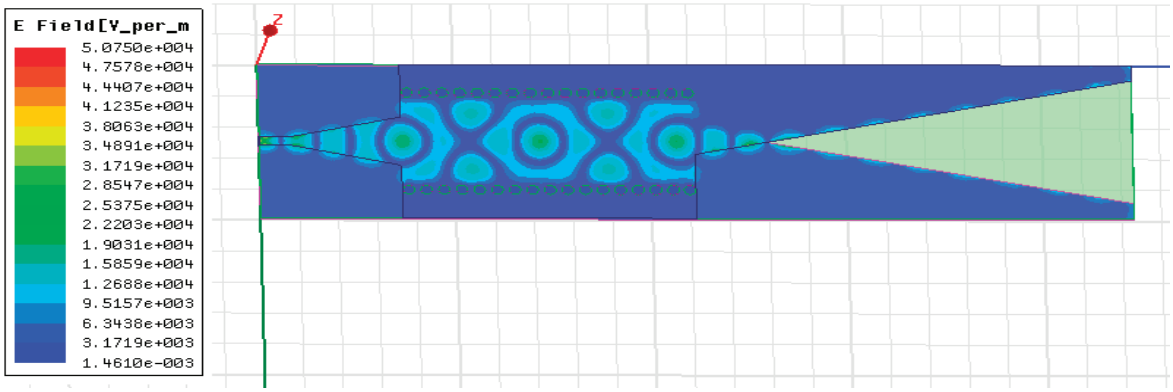

(a)

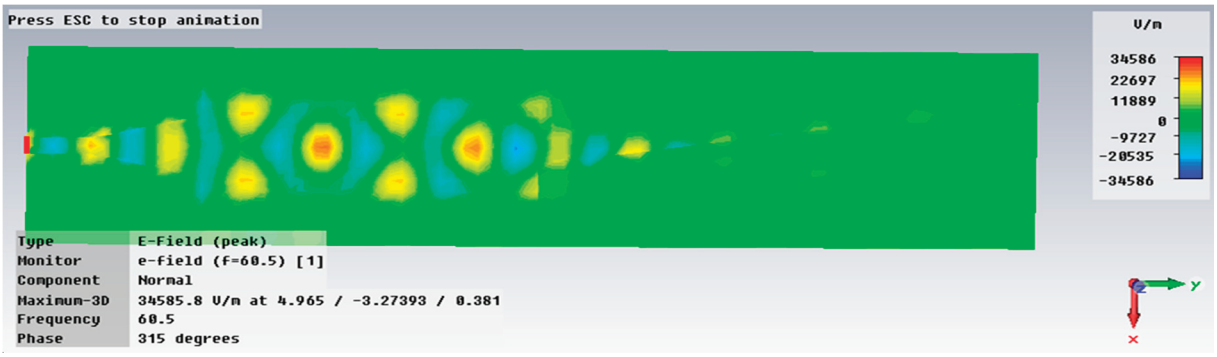

(b)

Fig. 6. Current distribution on plain ALTSA simulated in (a) HFSS and (b) CST MWS.

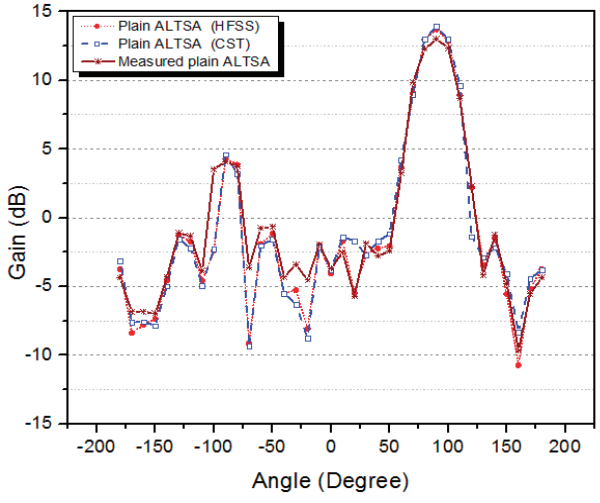

Fig. 7. Simulated and measured gain of plain ALTSA.

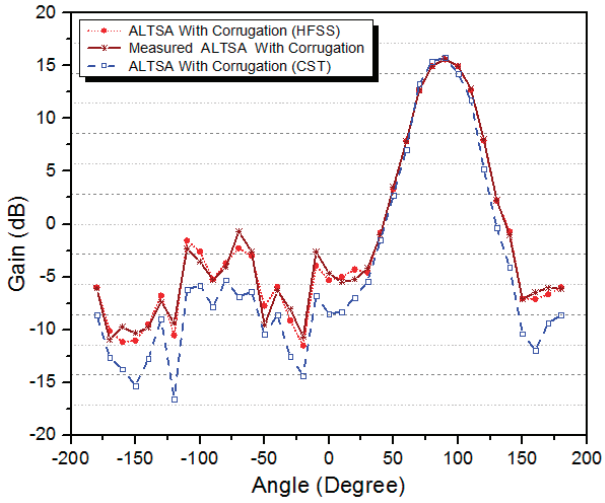

Fig. 8. Simulated and measured gain of corrugated ALTSA.

REFERENCES

[1] K. Huang and D. Edwards, *Millimetre Wave Antennas for Gigabit Wireless Communications*, 1st ed., John Wiley, Chichester, 2008.

[2] S. Yong, P. Xia, and A. Garcia, *60 GHz Technology for Gbps WLAN and WPA*, 1st ed., John Wiley, Chichester, 2011.

[3] T. Namas and M. Hasanovic, "Ultrawideband antipodal vivaldi antenna for road surface scanner based on inverse scattering," in *Proc. 28th Annual Review of Progress in Applied Computational Electromagnetics*, Ohio, pp. 882-887, 2012.

[4] C. Rodenbeck, S. Kim, W. Tu, M. Coutant, S. Hong, and M. Chang, "Ultrawideband low cost phased array radars," *IEEE Trans. Microw. Theory and Tech.*, vol. 53, no. 12, pp. 3697-3703, Dec. 2005.

[5] D. Chang, B. Zeng, and J. Liu, "Modified antipodal Fermi antenna with piecewise linear approximation and shaped-comb corrugation for ranging applications," *IET Microwaves, Antennas and Propag.*, vol. 4, no. 3, pp. 399-407, Mar. 2010.

[6] N. Symeon, G. Ponchak, J. Papapolymerou, and M. Tentzeris, "Conformal double exponentially tapered slot antenna (DETSA) on LCP for UWB applications," *IEEE Trans. on Antennas and Propag.*, vol. 54, no. 6, pp. 1663-1669, June 2006.

[7] S. Sugawara, Y. Maita, K. Adachi, and K. Mizuno, "A mm-wave tapered slot antenna with improved radiation pattern," *Proc. Intnl. Microwave Symp. Digest, IEEE MTT-S,* Denver, pp. 959-962, 1997.

[8] N. Ghassemi and K. Wu, "Planar high-gain dielectric-loaded antipodal linearly tapered slot antenna for E- and W-band gigabyte point-to-point wireless services," *IEEE Trans. on Antennas and Propag.*, vol. 61, no. 4, pp. 1747-1755, 2013.

[9] W. Coburn and A. Zaghloul, "Numerical analysis of stacked tapered slot antennas," in *Proc. 28th Annual Review of Progress in Applied Computational Electromagnetics*, Ohio, pp. 112-117, 2012.

[10] Z. Hao, W. Hong, J. Chen, X. Chen, and K. Wu, "A novel feeding technique for antipodal linearly tapered slot antenna array," in *Proc. International Microwave Symposium Digest, IEEE MTT-S*, China, pp. 3, 2003.

[11] T. Djerafi and K. Wu, "Corrugated substrate integrated waveguide (SIW) antipodal linearly tapered slot antenna array fed by quasi-triangular power divider," *Progress In Electromagnetics Research* C, vol. 26, pp. 139-151, 2012.

[12] S. Sugawara, Y. Maita, K. Adachi, and K. Mizuno, "Characteristics of a mm-wave tapered slot antenna with corrugated edges," in *Proc. International Microwave Symposium Digest, IEEE MTT-S*, Baltimore, pp. 533-536, 1998.

[13] M. Bozzi, L. Perregrini, K. Wu, and P. Arcioni, "Current and future research trends in substrate integrated waveguide technology," *Radio Engineering*, vol. 18, no. 2, pp. 201-209, 2009.

[14] E. Mehrshahi and M. Salehi, "A simple technique for propagation characteristics of substrate integrated waveguide," *Applied Computational Electromagnetics Society Journal*, vol. 25, no. 8, pp. 690-695, 2010.

[15] C. Jiang, "Microwave and millimetre wave integrated circuit system in packaging," *DTU Electrical Engineering, Technical University of Denmark*, Jan. 2010.

[16] T. Huang and H. Hsu, "Antipodal dual exponentially tapered slot antenna (DETSA) with stepped edge corrugations for front-to-back ratio improvement," in *Proc. Asia Pacific Microwave Conference*, Taiwan, pp. 685-688, 2011.

[17] F. Shamshad and M. Amin "Simulation comparison between HFSS, CST and WIPL-D for design of dipole, horn and parabolic reflector antenna," *Advances in Computational Mathematics and its Applications ACMA,* vol. 1, no. 4, pp. 203-207, 2012.

[18] D. Yoon, Y. Hong, Y. An, J. Jang, U. Pak, and J. Yook, "High-gain planar tapered slot antenna for Ku-band applications," in *Proc. Asia-Pacific Microwave Conference*, Yokohama, pp. 1914-1917, 2010.

[19] D. Deslandes and K. Wu, "Integrated microstrip and rectangular waveguide in planar form," *IEEE Microwave and Wireless Components Lett.*, vol. 11, no. 2, pp. 68-70, Feb. 2001.

Purva Shrivastava received her B.E in Electronics and Communication Engineering from Rajiv Gandhi Technical University, Bhopal, India and M.Tech in Telecommunication Networks with honors from SRM University, Chennai, India. Currently she is pursuing Ph.D from Department of Telecommunication Engineering at SRM University, India. Her area of interest includes antennas and propagation and wireless communications.

Devanshu Chandra received his B.Tech (Electronics and Communication) from Uttar Pradesh Technical University (UP), and is currently pursuing M.Tech (Telecommunication Networks) from SRM University. His field of interest includes RF and Wireless Communications.

Nishesh Tiwari is currently pursuing Ph.D. from Department of Telecommunication Engineering at SRM University, India. He received his M.Tech Degree in Telecommunication Networks from SRM University. He received his B.Tech. Degree in Electronics and Communication Engineering from Sikkim Manipal University, India, in 2009. He is a Student member of IEEE Communications Society. His current research interests are Antennas and Propagation and Wireless Sensor Networks.

T. Rama Rao currently, working as Professor and Head of the Telecommunication Engineering Department, SRM University, India. He received his PhD degree on 'Radio Wave Propagation studies for Fixed and Mobile Communications over Southern India' from Sri Venkateswara University, Tirupati, India in the year 2000. Prof. Rama Rao is a Member of the IEEE; an IETE Fellow; Senior Member of ACEEE, Member of, Life Member of the ISCA, Member of IACSIT, Member of ACM and Member of WWRF – Wireless World Research Fourm. He was the recipient of "Young Scientist" award for the XXVIth URSI General Assembly, University of Toronto, Canada, held during August 1999. And, he has been selected as a participant to attend the 'School on Data and Multimedia Communications using Terrestrial and Satellite Radio links' organized by the ICTP (International Centre for Theoretical Physics), Trieste, Italy, 7-25 Feb. 2000. Dr. Rama Rao worked with Aalborg University, Denmark as 'Assistant Research Professor'; with Universidad Carlos III de Madrid, Spain and at the University of Sydney, Australia as 'Visiting Professor'. Also, worked as 'Post Doc Research Fellow' at National Chio Tung Univeristy, Hsinchu, Taiwan. He has a long-standing research history on Radiowave Propagation Studies for Wireless Communications. His research interests are Antennas, Radio Channel Measurements & Modeling, Broadband Wireless Communications and Mobile Cellular Telecommunications. He authored papers in reputed journals/transactions and international/national conferences.

Wide Stop-Band Microstrip Lowpass Filter with Sharp Roll-off Using Hairpin Resonators

M. Hayati and H. S. Vaziri

Electrical Engineering Department, Faculty of Engineering, Kermanshah Branch, Islamic Azad University, Kermanshah, Iran

mohsen_hayati@yahoo.com, hamid_423@yahoo.co.uk

Abstract ─ A compact microstrip lowpass filter with wide stop-band and sharp roll-off skirt is presented. The structure consists of a combination of modified Hairpin units. The cut-off frequency is 3.1 GHz. The proposed low-pass filter has a very good performance such as extended stop-band bandwidth from 3.36 GHz to 21.5 GHz with the insertion-loss higher than -20.0 dB, sharp roll-off, low insertion-loss, and high return-loss in the pass-band. The filter is designed, fabricated, and tested and the measured results are in good agreement with the EM-simulation results.

Index Terms - Hairpin unit, lowpass filter, microstrip, sharp roll-off, and wide stop-band.

I. INTRODUCTION

Microwave lowpass filters are one of the most important building blocks in modern microwave systems because of their ability to suppress unwanted harmonics and spurious signals. To answer the demands of modern communication systems, LPFs have been studied for many years. Resonators are the basic parts of filters and so different kinds of them such as stepped impedance, pseudo inter-digital and defected ground structures (DGS) have been designed and used to improve the performance of filters. Conventional LPFs suffer from gradual roll-off and narrow stop-band bandwidth [1]. Other disadvantages like high insertion-loss and fabrication complexity are also the problems that make the filters to be far from the ideal form [2]. The main advantages of Hairpin resonators are compact size and ease of fabrication since they were proposed for the first time in 1970's. In [3], a LPF using Hairpin resonator is presented. The filter's structure is simple but it suffers from a gradual roll-off and narrow stop-band bandwidth. In [4], the filter's performance is improved by adding a pair of coupled stepped impedance resonators (SIRs). Compared with the previous structure, this filter has a sharper response but the return-loss has become lower and the stop-band bandwidth is still narrow. In the filters proposed in [5-7], some characteristics like the stop-band bandwidth are enhanced but all those filters suffer from gradual roll-off.

In this paper, the new structure is presented to design a lowpass filter using Hairpin resonators. The simulated and measured results show a sharp roll-off and an extended stop-band bandwidth.

II. NOVEL HAIRPIN UNIT STRUCTURE

Figure 1 shows the structure of the conventional hairpin resonator and its S-parameters simulation results.

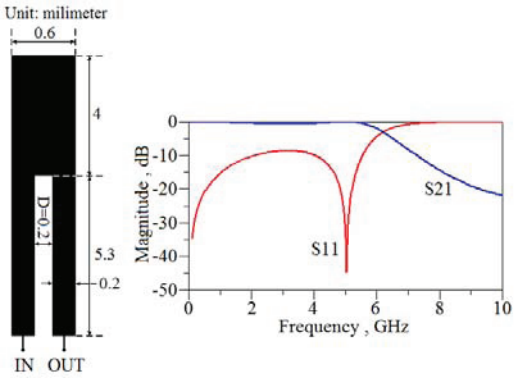

Fig. 1. Conventional hairpin resonator and its S-parameters results.

Submitted On: Dec. 28, 2012
Accepted On: Sept. 21, 2013

1054-4887 © 2013 ACES

As it is clear, the structure is simple and consists of a single transmission line and symmetric parallel coupled lines. This simple structure can be modeled by an LC circuit easily [1] and this is one of the advantages of using hairpin resonators. The equivalent LC circuit of the conventional hairpin unit is shown in Fig. 2.

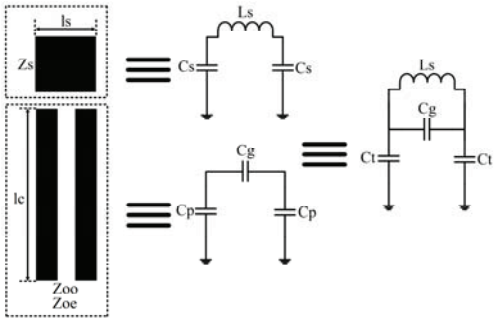

Fig. 2. The equivalent LC circuit of the conventional hairpin unit.

As it is shown, the single transmission line can be modeled as a capacitive-inductive π-network and the parallel coupled lines can be modeled as a capacitive π-network. The values of different parameters in the LC circuits are calculated in [1, 8], and they are summarized as follows,

$$Ls = \frac{Z_S \sin(2\beta_S l_S)}{\omega} \text{ (H)} \quad (1)$$

$$Cs = \frac{1-\cos(2\beta_S l_S)}{\omega Z_S \sin(2\beta_S l_S)} \text{ (F)}, \quad (2)$$

$$Cg = \frac{(Z_{oe}-Z_{oo})}{2\omega Z_{oe} Z_{oo} \cot(\beta_C l_C)} \text{ (F)}, \quad (3)$$

$$Cp = \frac{1}{\omega Z_{oe} \cot(\beta_C l_C)} \text{ (F)}. \quad (4)$$

Z_S is the characteristic impedance of the single transmission line and Z_{oo} and Z_{oe} are the odd- and the even-modes' impedance of the parallel coupled lines. β_S is the phase constant of the single transmission line and β_C is the phase constant of the coupled lines. In Fig. 2, Ct = Cp + Cs.

In this paper, to enhance the filter's performance and getting close to the ideal form, the structure of the conventional Hairpin resonator is modified by adding two extra stubs, to each side of the top part of the resonator. The new structure is shown in Fig. 3 (a).

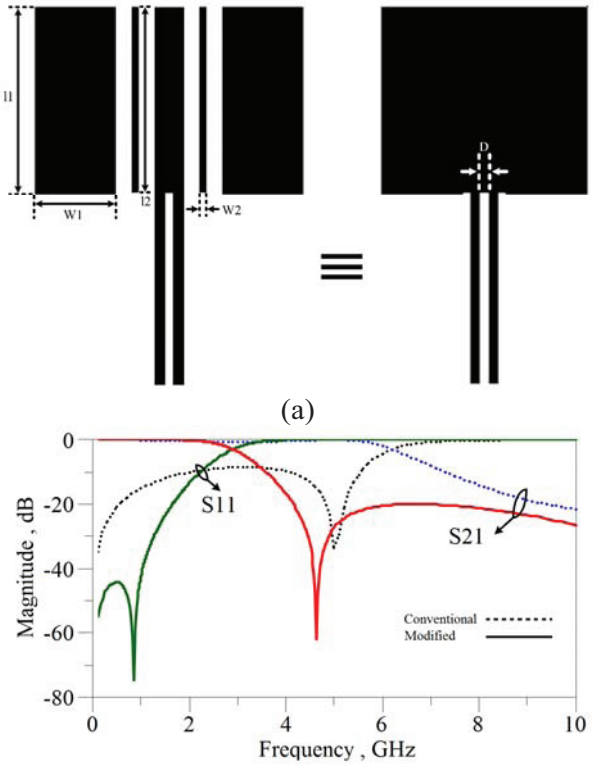

Fig. 3. (a) Modified hairpin resonator and (b) comparison between the results of the conventional and modified hairpin resonator.

The dimensions in Fig. 3 (a) are: W1 = 1.8, W2 = 0.2, l1 = 4.2, and l2 = 4.1 (all in millimeter). Figure 3 (b) shows a comparison between the simulation results of the modified resonator and the conventional hairpin resonator. As it is obvious in Fig. 3 (b), in comparison with the conventional structure, the modified structure has better performance. For example the return-loss in the pass-band is lower and transmission zeros have moved to lower frequencies and so the resonator has a sharper roll-off.

Modeling microstrip structures with LC circuits is very important. However, it is usually very hard to model microstrip circuits with lumped-elements but it has many advantages. An LC model can help the designers describe the behavioral characteristics of a microstrip structure better and perform analysis easier and faster. It is

especially very useful for optimizing the values of different parts because as it is mentioned, the analysis of an LC circuit in comparison with microstrip structures is very fast. In addition, in some circuits both lumped-elements and microstrip structures exist and to analyze such circuits, it is useful to model the microstrip structures with LC circuits.

The equivalent LC circuit for the proposed resonator is shown in Fig. 4 (a), where their values are: L1 = 1.13 nH, L2 = 1.7 nH, C1 = 0.2 pF, C2 = 0.36 pF, C3 = 1 pF, C4 = 0.1 pF. The values of LC parameters are calculated from the basic equations of hairpin unit and transmission lines i.e., equations (1) to (4), and then the values are optimized to improve the accuracy of the response. Figure 4 (b) shows the comparison between the simulation results of the layout and the LC model of the proposed resonator. As it is obvious, there is a very good agreement between the circuit and the EM simulation results.

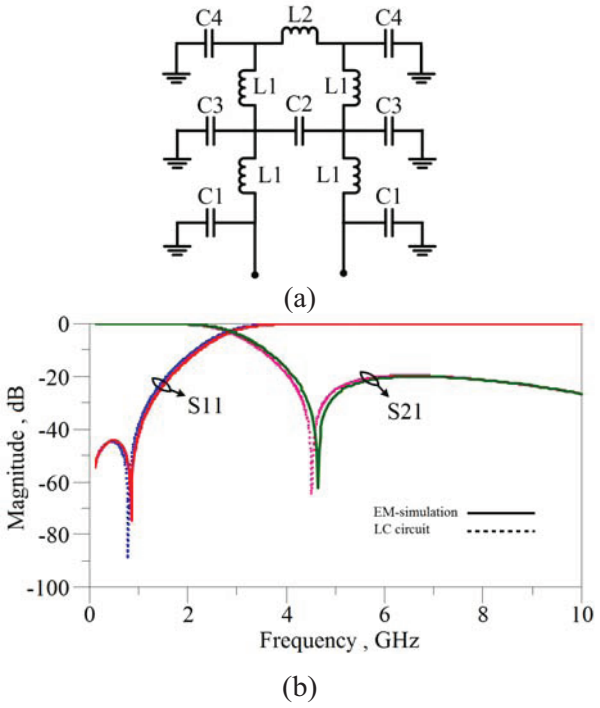

Fig. 4. (a) The equivalent LC circuit for the proposed resonator and (b) the comparison between the results of the LC circuit and EM simulation.

In hairpin resonators, the distance between the parallel lines is a very important parameter because any changes in the amount of this distance, will highly affect the response characteristics of the resonator and so it is important to study the effects of changing the value of this parameter on the response. This parameter is shown in Fig. 3 (a) as D.

Figure 5 (a) shows the simulation results of the proposed resonator for different values of D. As it is shown in this figure, by decreasing the value of D from 0.25 mm to 0.15 mm, the filter will have a sharper roll-off skirt. Because by decreasing the value of D, the coupling capacitance between the parallel lines will increase, which leads the transmission zeros to move to lower frequencies and so the roll-off will be sharper.

The coupling capacitance between the parallel lines is shown as C2 in Fig. 4 (a). In Fig. 5 (b), the effect of changing the value of C2 is presented and as it is expected, by increasing the value of C2, the transmission zeros will move to lower frequencies. And it confirms what was claimed before about D.

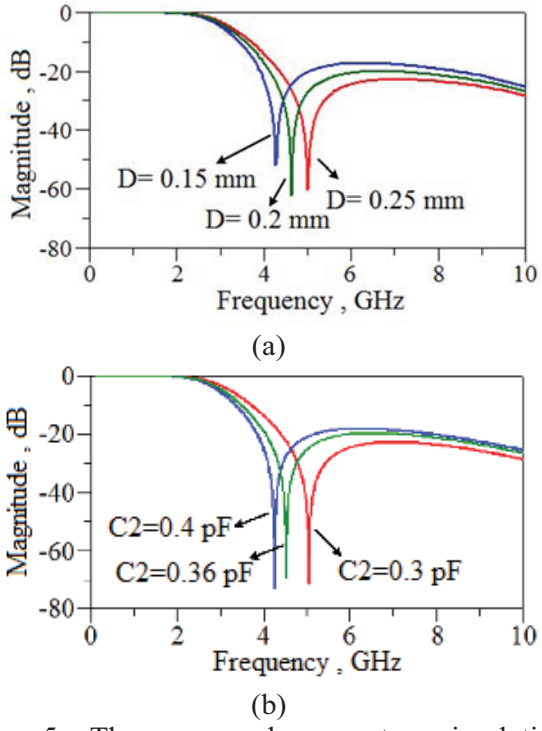

Fig. 5. The proposed resonator simulation results (a) as a function of D in microstrip structure and (b) as a function of C2 in the equivalent LC circuit.

As it is obvious in Fig. 5 (a), by decreasing the value of D, the insertion-loss in the stop-

band will decrease and so a proper value for D should be chosen to achieve the best performance for the filter. Finally, the value of D = 0.2 mm is chosen. The value of the cut-off frequency can be changed by changing some dimensions of the structure, but it should be considered that any changes in the dimensions of the resonator, will affect the response and the performance of the structure. A good method to change the cut-off frequency without changing the performance of the LPF is to change all the dimensions with the same scale. Figure 6 shows the response of the proposed resonator for different scale factors.

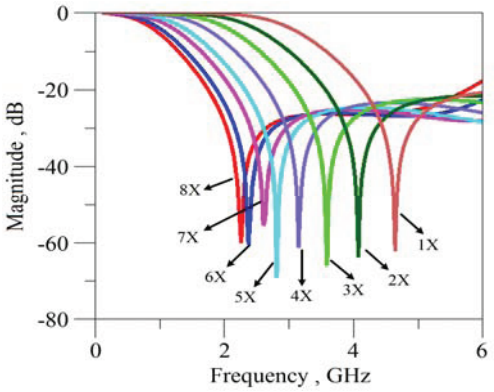

Fig. 6. The response of the proposed resonator for different scale factors.

It is seen in Fig. 6, as the dimensions of the proposed resonator become larger, the cut-off frequency will become smaller, while the response curves have almost the same shapes (that shows the same performance in the structures). Figure 7 shows a relationship between the value of the cut-off frequency and the scaling factor.

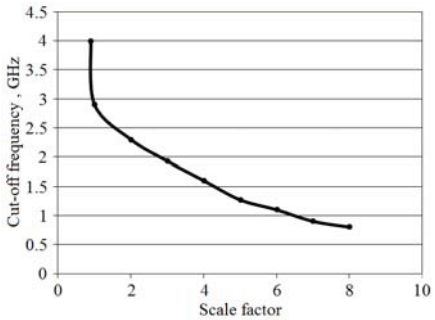

Fig. 7. The values of the cut-off frequency for different scaling factors.

Figure 7 is very useful to determine the dimensions of the structure to obtain a certain value for the cut-off frequency. According to Fig. 7, to increase the value of the cut-off frequency, it is needed to decrease the size of the structure and to decrease the value of cut-off frequency, the size of the structure should be increased. In Fig. 7, the response curve is an exponential type and so the change in the size of the resonator to increase the value of cut-off frequency will be very small, but to decrease the value of cut-off frequency there will be a bigger change in the size of the structure. Therfore, this method is more efficient especially when it is needed to increase the value of the cut-off frequency.

III. FILTER DESIGN

By using the proposed resonator, a new LPF with wide stop-band bandwidth and sharp roll-off is designed in this paper. In the first step, to improve the performance, a combination of two modified Hairpin units is used. One way to obtain a good performance and also a small size, is arranging the resonators in cascade model. So as it is shown in Fig. 8 (a), the coupled resonators have one common leg, which means: the output leg for the first resonator is as the input leg for the second one. The length of the legs also should be optimized to obtain the best possible performance. Figure 8 (b) shows the simulation results of the structure.

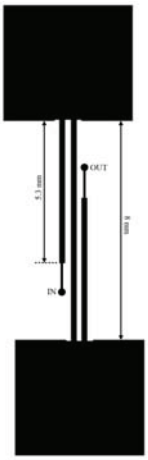

(a)

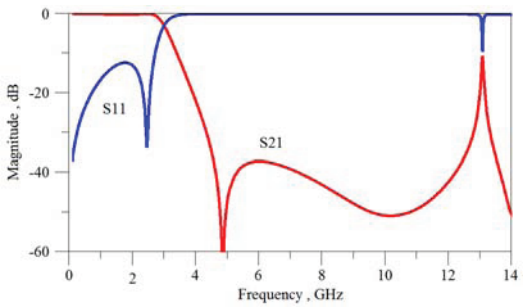

(b)

Fig. 8. The combination of two modified Hairpin resonators (a) layout and (b) simulation results.

As it is observed in Fig. 8 (b), the new structure has better response characteristics. The roll-off skirt is sharper and the stop-band bandwidth is wider but the return-loss in the pass-band is becoming low. In the next step, to extend the stop-band bandwidth, another modified Hairpin unit is designed. This unit and its simulation results are shown in Fig. 9.

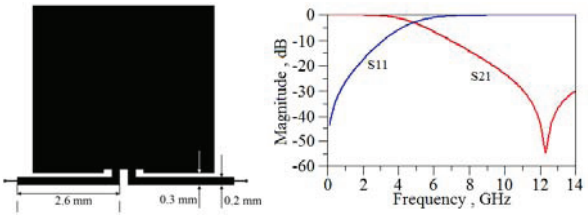

(a) (b)

Fig. 9. The second modified Hairpin unit (a) the structure and (b) simulation results.

In Fig. 9, the structure is achieved by bending the parallel lines at 90 degrees. As a result, the coupling capacitances between them will be removed and there will be new coupling capacitances between the lines and the top parts of the resonator. All these changes will highly affect the response characteristics of the structure and make the zero of S21 moves to higher frequencies and so the response characteristics of the resonator will be like what is shown in this figure.

By adding this new unit to the previous structure, a new combination is achieved. Figure 10 (a) shows this new structure and the simulation results are shown in Fig. 10 (b). The final structure is shown in Fig. 11.

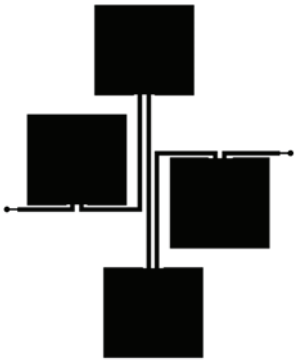

(a)

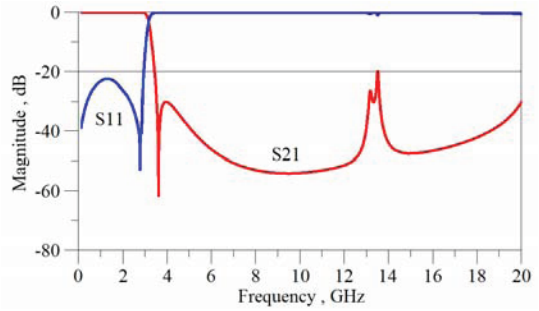

(b)

Fig. 10. The new structure (a) layout and (b) simulation results.

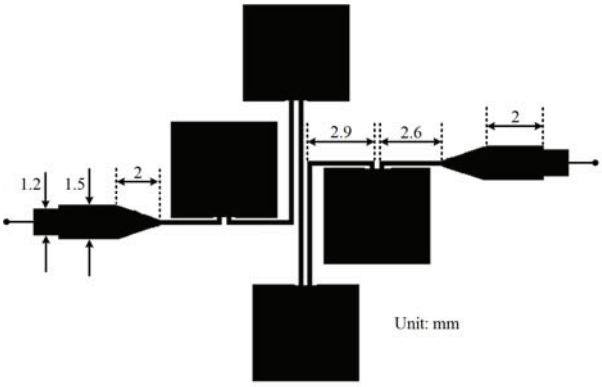

Fig. 11. The proposed lowpass filter.

As it is clear in Fig. 10 (b), there is a pole for S21 in the frequency of 13.5 GHz. The value of S21 in that frequency is lower than -20 dB. To increase this value to more than -20 dB, which extend the stop-band bandwidth (for the insertion-loss higher than -20 dB), it is needed to add some other parts to the structure. These parts are added to the feeding lines, which can be seen in Fig. 11. The parts with 1.5 mm wide are used for that

reason. The parts with 1.2 mm wide are used to have better impedance matching for 50 ohm ports.

Using the same method for the proposed resonator, the LC circuit model of the proposed lowpass filter is shown in Fig. 12 (a). In this figure the values of the elements are: C1 = 0.1 pF, C2 = 1 pF, C3 = 0.3 pF, C4 = 0.2 pF, C5 = 0.38 pF, C6 = 0.36 pF, C7 = 1 pF, C8 = 0.1 pF, C9 = 0.02 pF, L1 = 1.7 nH, L2 = 0.3 nH, L3 = 0.84 nH, L4 = 0.59 nH, L5 = 1.7 nH, L6 = 0.3 nH. Figure 12 (b) shows a comparison between the LC circuit model and EM-simulation results of the proposed filter.

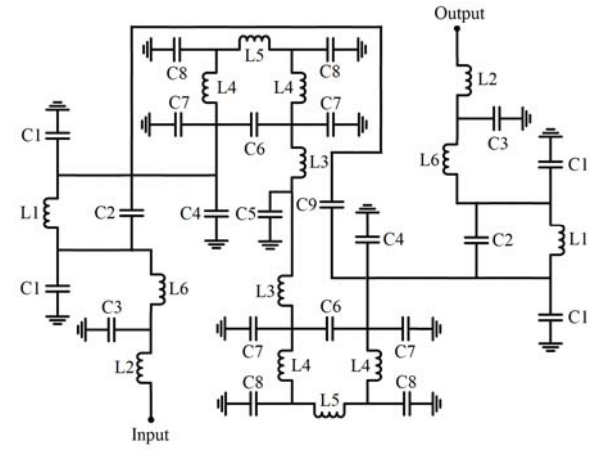

(a)

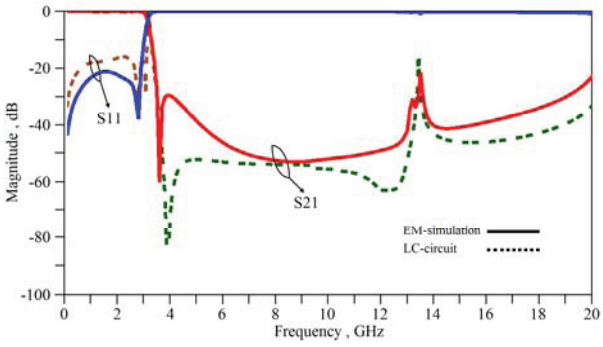

(b)

Fig. 12. (a) The equivalent LC circuit of the proposed filter and (b) the results.

This filter is designed on (RT/Duroid 5880) substrate with 2.22 dielectric constant, 15 mil heights, and 0.0009 loss tangents. The designed filter is fabricated using microelectronic technology and measured by the use of an Agilent network analyzer N5230A.

The simulated and measured results are shown in Fig. 13 (a) and the photograph of the filter is shown in Fig. 13 (b) and also the group-delay of the proposed filter is shown in Fig. 13 (c). As it is clear in Fig. 13 (a), the EM simulation results are in good agreement with the measured results.

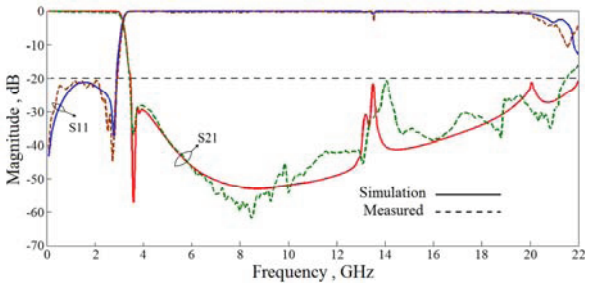

(a)

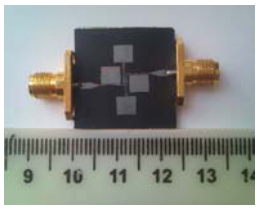

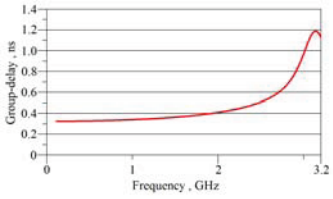

(b) (c)

Fig. 13. Proposed low-pass filter (a) the simulation and measurement results, (b) photograph, and (c) group-delay.

IV. RESULTS

Measured results show very good performance for the proposed filter. The insertion-loss from DC to 2.8 GHz is lower than -0.45 dB and the return-loss is higher than -20.7 dB. The transition from -3 dB to -20 dB is 0.26 GHz, which is equal to 65.38 dB/GHz that shows a sharp roll-off skirt and overall size of the fabricated filter is about 16.4 mm × 20 mm (0.246 λ_g × 0.3 λ_g). The group delay in the pass-band is from 0.3 ns to 1.18 ns.

Table I shows the comparison between the proposed filter and some other LPFs. As it is obvious, in comparison with the proposed filters in [2-13], this new filter has a very good performance. In Table I, all the stop-band bandwidths are calculated for the insertion-loss higher than -20 dB and as it is clear, compared with the other filters, the proposed filter has the sharpest roll-off skirt and also it has other advantages like: wide stop-band bandwidth and very good insertion-loss and return-loss in the pass-band.

Table I. Comparison between the proposed low-pass filter and some other filters.

Ref	Fc (GHZ)	R-O (dB/ GHz)	I-L (dB)	R-L (dB)	S-B (up to Fc)
2	3	18.9	1.4	24	4.7
4	1.5	18.8	0.5	10	2.13
5	2.5	24.2	0.45	14	3.44
6	1	48.5	0.4	20	4.1
7	0.5	56.6	0.5	16.3	7.6
8	2.4	34	1.2	5	low
9	4.16	19	0.1	20.18	2.48
10	1.67	24.28	0.5	12	2.63
11	2	18.9	0.6	12	5.32
12	2.95	16.19	0.1	20	5.42
13	2.75	48.5	0.5	17.5	1.7
This	3.1	65.38	0.45	20.7	5.85

R-O = roll-off, I-L = Insertion-loss, R-L = return-loss, and S-B = stop-band.

V. CONCLUSION

A compact low-pass filter with wide stop-band bandwidth and sharp roll-off is designed and fabricated. The simulated and measured results are in good agreement with each other. The filter has the cut-off frequency of 3.1 GHz, wide stop-band bandwidth (from 3.36 GHz to 21.5 GHz with the attenuation level above -20 dB), low insertion-loss, and high return-loss in the passband. The filter with these features can answer the demands of modern communication systems.

ACKNOWLEDGMENT

The authors would like to thank the Kermanshah Branch, Islamic Azad University for the financial support of this research project.

REFERENCES

[1] J. Hong and M. Lancaster, *Microstrip Filters for RF/Microwave Applications*, New York: Wiley, 2001.

[2] K. Song, Y.-Z. Yin, X. Yang, J.-Y. Deng, and H.-H. Xie, "Compact LPF with pair of coupling slots for wide stopband suppression," *Electronics Letters*, vol. 46, no. 13, pp. 922-924, 2010.

[3] L. Hsieh and K. Chang, "Compact lowpass filters using stepped impedance hairpin resonators," *Electronics Letters*, vol. 37, no. 4, pp. 899-900, 2001.

[4] M. Yang and J. Xu, "Design of compact, broad-stopband lowpass filter using modified stepped impedance hairpin resonators," *Electronics Letters*, vol. 44, no. 20, pp.1198-1199, 2008.

[5] S. Luo, L. Zhu, and S. Sun, "Stopband-expanded low-pass filters using microstrip coupled-line Hairpin units," *IEEE Microwave and Wireless Components Letters*, vol. 18, no. 8, pp. 506-508, 2008.

[6] L. Li, Z.-F. Li, and J.-F. Mao, "Compact lowpass filters with sharp and expanded stopband using stepped impedance Hairpin units," *IEEE Microwave and Wireless Components Letters*, vol. 20, no. 6, pp. 310-312, 2010.

[7] V. Velidi and S. Sanyal, "Sharp roll-off lowpass filter with wide stopband using stub-loaded coupled-line Hairpin unit," *IEEE Microwave and Wireless Components Letters*, vol. 21, no. 6, pp. 301-303, 2011.

[8] F. Wei, L. Chen, X.-W. Shi, Q.-L. Huang, and X.-H. Wang, "Compact lowpass filter with wide stop-band using coupled-line hairpin unit," *Electronics Letters*, vol. 46, no. 1, pp. 88-90, 2010.

[9] M. Hayati and A. Lotfi, "Compact lowpass filter with high and wide rejection in stopband using front coupled tapered CMRC," *Electronics Letters*, vol. 46, no. 12, pp. 846-848, 2010,

[10] X. Wei, P. Wang, M. Liu, and Y. Shi, "Compact wide-stopband lowpass filter using stepped impedance hairpin resonator with radial stubs," *Electronics Letters*, vol. 47, no. 15, pp. 862-863, 2011.

[11] M. Yang, J. Xu, Q. Zhao, L. Peng, and G. Li, "Compact, broad-stopband lowpass filters using SIRS-loaded circular Hairpin resonators," *Progress In Electromagnetics Research, PIER* 102, pp. 95-106, 2010.

[12] M. Challal, A. Boutejdar, M. Dehmas, A. Azrar, and A. Omar, "Compact microstrip low-pass filter design with ultra wide reject band using a novel

quarter-circle DGS shape," *Applied Computational Electromagnetics Society (ACES) Journal*, vol. 27, no. 10, pp. 808-815, Oct. 2012.

[13] W. Shao and J. Li, "Accurate modeling of a patterned ground and its application to microwave filters," *Applied Computational Electromagnetics Society (ACES) Journal*, vol. 27, no. 7, pp. 596-602, July 2012.

Mohsen Hayati received the BE in electronics and communication engineering from Nagarjuna University, India, in 1985, and the ME and PhD in electronics engineering from Delhi University, Delhi, India, in 1987 and 1992, respectively. He joined the Electrical Engineering Department, Razi University, Kermanshah, Iran, as an assistant professor in 1993. At present, he is an associate professor with the Electrical Engineering Department, Razi University. He has published more than 130 papers in international and domestic journals and conferences. His current research interests include microwave and millimeter wave devices and circuits, application of computational intelligence, artificial neural networks, fuzzy systems, neuro-fuzzy systems, electronic circuit synthesis, modeling and simulations.

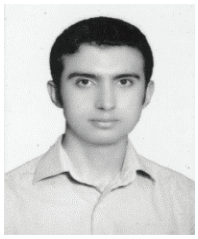

Hamid Sherafat Vaziri was born in Kermanshah, Iran in 1985. He received the B.Sc. and M.Sc. degree in Electrical Engineering from the Razi University, Kermanshah, Iran. His research interests include design and analysis of the microstrip filters, and antennas.

Analysis and Optimization of a 2-D Magnet Array with Hexagon Magnet

G. Liu, Y. Zhou, R. Zhou, W. Ming, and L. Huo

School of Mechanical Science and Engineering,
Huazhong University of Science and Technology, Wuhan 430074, China
lgd5401@gmail.com, yfzhou@mail.hust.edu.cn, rougangzhou@hust.edu.cn, mingwuyi81@gmail.com, liganghuo@126.com

Abstract ─ This paper introduces the hexagon permanent magnets, which are in *x*- or *y*- axis magnetized directions to the 2-D permanent magnet array for planar motor. Through the scalar magnetic potential equation, finite element method and effective amplitudes, the harmonic and analytical models are derived and verified. The reduction of the higher harmonics of *z*-component of the magnetic flux density with hexagon magnets is verified. Low higher harmonics of *z*-component of the magnetic flux density with hexagon magnets is optimized by the genetic algorithm. Comparing with the 2-D Halbach magnet arrays, the new magnet array has larger *z*-component of the magnetic flux density and smaller higher harmonics of *z*-component of the magnetic flux density, which can reduce the force ripples of planar motor.

Index Terms ─ Effective amplitude, force ripples, genetic algorithm, hexagon magnet, magnet array, and planar motor.

I. INTRODUCTION

In many industrial apparatus, like pick-and-place machines, lithography and inspection systems, objects are positioned and moved in a horizontal plane [1-10]. The magnetically levitated planar motors with 2-D permanent magnet array, which have the advantages of large range planar motion, simple structure, high speed, and high precision, have received increasing attention. Until now some types of planar motors, which can move freely in any directions in the plane have been proposed.

Cho et al. [2] proposed a magnet array for planar motor with compact structure to obtain high magnetic flux density. The magnetic field was obtained by using the scalar magnetic potential. But the harmonic model is too complex to apply in real time control. To deal with this problem, Cho et al. [3] substitute a 2-D sinusoidal wave with flux density exponentially decreasing across the air-gap length for the flux density distribution. In contrast with Cho et al, Jansen et al. [4, 5] proposed a new type of 2-D Halbach magnet array, derived an analytical model by taking the first harmonic of the magnetic flux density and optimized the 2-D Halbach magnet array by maximizing the magnetic flux density per unit of moving-part for low power dissipation. However, the higher harmonics of the magnet array is high, which is usually a main reason for the force ripples in planar motor [6]. To get a magnet array with high magnetic flux density and low higher harmonics, W. Min et al. [6] proposed a 2-D Halbach array with 4 segments per pole and adopting the genetic algorithm (GA) to minimize the higher harmonics. Y. Zhang [7] and L. Huang et al. [8] investigated different 1-D magnet array topologies and found the trapezoidal permanent magnet structures had a reduced number of high harmonic components. J. Peng et al. [9] proposed a 2-D Halbach array by using trapezoidal magnets. The trapezoidal magnets, which have a 45° magnetized direction are used to reduce the higher harmonics and increase the intensity of the magnetic field. The analytical model is derived by taking the amplitude of the magnetic flux density as the effective amplitude. The genetic algorithm is also used to minimize the higher harmonics.

Submitted On: March 15, 2013
Accepted On: Sept. 29, 2013

1054-4887 © 2013 ACES

The new 2-D magnet array proposed by this paper has the features of compact structure, without magnets of 45° magnetized direction and using hexagon magnets. The hexagon magnets are used to reduce higher harmonics and increase the intensity of the magnetic field. The harmonic model of the magnetic flux density for the new array is derived by Fourier series and the scalar magnetic potential [11], and verified by finite element method. The analytical model is derived by the effective amplitude. The genetic algorithm is used to minimize the higher harmonics in *z*-component of the magnetic flux density. Finally, the new array is compared with the 2-D Halbach array used by Jansen [4].

II. ANALYSIS OF MAGNETIC FLUX DENSITY

A. Analytical model

Figure 1 shows the magnet array with top view and cut-view. The magnetized direction of the magnets is denoted by the arrows from S-pole to N-pole, and S means the direction towards the paper and N means out of paper. The hexagon magnets are in the horizontal directions. The magnet array modeled as infinitely large with Fourier series by neglecting end effects. The residual magnetization vector of the magnet array with the permanent magnets can be expressed as,

$$\vec{M} = M_x \hat{x} + M_y y + M_z \hat{z}. \tag{1}$$

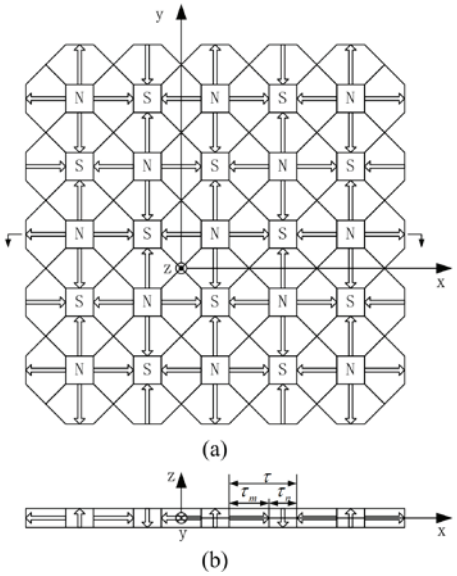

Fig. 1. Magnet array; (a) top and (b) cut-views.

Figure 2 shows the M_x projection distribution of the hexagon magnets. The projection distribution is derived by using Fourier series. The expression of M_x is,

$$\begin{aligned} M_x &= PMX_y \cdot PMX_x \cdot M \\ &= M\sum_{k=1}^{\infty}\sum_{l=1}^{\infty} a_{xk} b_{xl} \cos(k\omega x)\sin(l\omega y) \end{aligned}, \tag{2}$$

where $M=B_r/\mu_0$, $\omega=\pi/\tau$, k and l are the harmonic numbers for the x- and y-direction, respectively. While a_{xk} and b_{xl} are the projection distribution coefficients, τ is the pole pitch, τ_m is the length of the side of the magnets, which are magnetized in z-direction, and

$$a_{xk} = -\frac{4}{k\pi}\sin\frac{k\pi}{2}\cos\frac{k\omega\tau_m}{2} \tag{3}$$

$$b_{xl} = \frac{4}{l\pi}\sin^2\frac{l\pi}{2}\cos\big(l\omega v(x)\big). \tag{4}$$

The $v(x)$ is a function of the variable x due to the shape of hexagon magnet [9]. The distribution of variable x in a period with thick line is shown in Fig. 2 and expressed as

$$v(x) = \begin{cases} x+\tau & -\tau \le x < -0.5\tau \\ -x & -0.5\tau \le x < 0 \\ x & 0 \le x < 0.5\tau \\ -x+\tau & 0.5\tau \le x \le \tau \end{cases}. \tag{5}$$

The expression of cos ($l\omega v(x)$) is obtained using equation (5)

$$\begin{aligned} \cos\big(l\omega v(x)\big) &= \begin{cases} -\cos(u\omega x) & -\tau \le x < -0.5\tau \\ \cos(u\omega x) & -0.5\tau \le x < 0 \\ \cos(u\omega x) & 0 \le x < 0.5\tau \\ -\cos(u\omega x) & 0.5\tau \le x \le \tau \end{cases} \\ &= \lambda_{v(x)} \cos(u\omega x) \end{aligned}, \tag{6}$$

where $\lambda_{v(x)}$ is distribution coefficient. Figure 3 shows the distribution of $\lambda_{v(x)}$, and the expression is obtained by Fourier series

$$\lambda_{v(x)} = \sum_{u=1}^{\infty} \frac{4}{u\pi}\sin\frac{u\pi}{2}\cos(u\omega x), \tag{7}$$

where u is harmonic number.

M_y can be constructed by interchanging the variables x and y in the function of M_x. The M_z projection distribution of the cubic magnets is obtained by conventional approach with Fourier series and not list. The expressions of the residual magnetization vector of this array are,

$$M_x = -M\sum_{k=1}^{\infty}\sum_{l=1}^{\infty}\sum_{u=1}^{\infty} g(k)C\sin(l\omega y)\left(\cos(e_1\omega x) + \cos(e_2\omega x) + \cos(e_3\omega x) + \cos(e_4\omega x)\right) \quad (8)$$

$$M_y = -M\sum_{k=1}^{\infty}\sum_{l=1}^{\infty}\sum_{u=1}^{\infty} Cg(l)\sin(k\omega x)\left(\cos(e_5\omega y) + \cos(e_6\omega y) + \cos(e_7\omega y) + \cos(e_8\omega y)\right) \quad (9)$$

$$M_z = M\sum_{k=1}^{\infty}\sum_{l=1}^{\infty} a(k)a(l)\sin(k\omega x)\sin(l\omega y), \quad (10)$$

where τ_n is the length of the side of the hexagon magnets, and

$$C = \frac{16}{klu\pi^3}\sin^2\frac{k\pi}{2}\sin^2\frac{l\pi}{2}\sin\frac{u\pi}{2} \quad (11)$$

$$g(k) = \sin\frac{k\omega\tau_n}{2}, \quad (12)$$

$$a(k) = \frac{4}{k\pi}\sin^2\frac{k\pi}{2}\cos\frac{k\omega\tau_n}{2}, \quad (13)$$

$$e_1 = k + l + u, \quad (14)$$

$$e_2 = k + l - u, \quad (15)$$

$$e_3 = k - l + u, \quad (16)$$

$$e_4 = k - l - u, \quad (17)$$

$$e_5 = l + k + u, \quad (18)$$

$$e_6 = l + k - u, \quad (19)$$

$$e_7 = l - k + u, \quad (20)$$

$$e_8 = l - k - u. \quad (21)$$

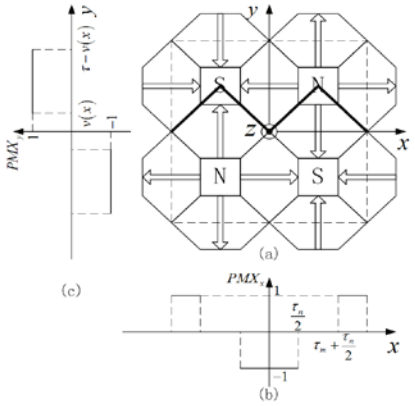

Fig. 2. M_x projection distribution of the hexagon magnets; (a) magnet array, (b) *x*-directoin, and (c) *y*-direction.

B. Governing and solving equation

To derive the magnetic flux density of the magnet array, the 3-D space is divided into three regions [11] of which a cross section is shown in Fig. 4. Regions 1 and 3 are in air. The permanent magnets in region 2 are located in between $m_b \le z \le m_t$. The assumption of air in the magnet array is not existed due to the compact structure.

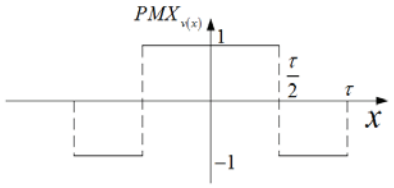

Fig. 3. Distribution of $\lambda_{v(x)}$.

The scalar magnetic potential equation is applied to this problem because there is no current. In regions 1 and 3, the next equations apply (only the equations for region 1 are shown),

$$\vec{H}_1 = -\nabla\Psi_1 \quad (22)$$

$$\nabla\times\vec{H}_1 = 0, \quad (23)$$

$$\vec{B}_1 = \mu_0\vec{H}_1, \quad (24)$$

$$\nabla\cdot\vec{B}_1 = 0, \quad (25)$$

where $\vec{B}_1$ is the magnetic flux density, $\vec{H}_1$ is the magnetic field strength, Ψ_1 is the scalar potential. In region 2,

$$\vec{H}_2 = -\nabla\Psi_2 \quad (26)$$

$$\nabla\times\vec{H}_2 = 0, \quad (27)$$

$$\vec{B}_2 = \mu_0\mu_r\vec{H}_2 + \mu_0\vec{M}, \quad (28)$$

$$\nabla\cdot\vec{B}_2 = 0, \quad (29)$$

where μ_r is the relative permeability. After the substitution of the scalar potential in equations (22) to (25) and equations (26) to (29), respectively, the following equations are obtained,

$$\nabla^2\Psi_1 = 0 \quad (30)$$

$$\nabla^2\Psi_2 = \nabla\cdot\frac{\vec{M}}{\mu_r} = \frac{M}{\mu_r}\times \left(\sum_{k=1}^{\infty}\sum_{l=1}^{\infty}\sum_{u=1}^{\infty} g(k)C\sin(l\omega y)\sum_{i=1}^{4} e_i\omega\sin(e_i\omega x) + \sum_{k=1}^{\infty}\sum_{l=1}^{\infty}\sum_{u=1}^{\infty} g(l)C\sin(k\omega x)\sum_{j=5}^{8} e_j\omega\sin(e_j\omega x)\right), \quad (31)$$

$$\nabla^2\Psi_3 = 0. \quad (32)$$

At infinite distance from the magnet array,

$$\Psi_1(z=\infty) = 0 \quad (33)$$

$$\Psi_3(z=-\infty) = 0. \quad (34)$$

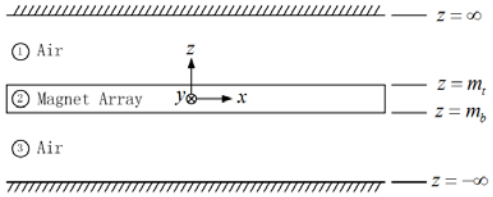

Fig. 4. Space divided into three regions.

The following boundary conditions apply on the interface between the magnets and the air (see also Fig. 4),

$$H_{1x}\left(z=m_t\right)=H_{2x}\left(z=m_t\right) \tag{35}$$

$$H_{1y}\left(z=m_t\right)=H_{2y}\left(z=m_t\right), \tag{36}$$

$$B_{1z}\left(z=m_t\right)=B_{2z}\left(z=m_t\right), \tag{37}$$

$$H_{2x}\left(z=m_b\right)=H_{3x}\left(z=m_b\right), \tag{38}$$

$$H_{2y}\left(z=m_b\right)=H_{3y}\left(z=m_b\right), \tag{39}$$

$$B_{2z}\left(z=m_b\right)=B_{3z}\left(z=m_b\right). \tag{40}$$

where m_t, m_b is the height of the magnet array.

The method of separation of variables is used to solve the Laplace equations. A solution of the scalar potential is substituted,

$$\begin{aligned}\Psi=&\sum_{k=1}^{\infty}\sum_{l=1}^{\infty}\sum_{u=1}^{\infty}\sin\left(l\omega y\right)\sum_{i=1}^{4}Z_i\left(z\right)\sin\left(e_i\omega x\right)\\&+\sum_{k=1}^{\infty}\sum_{l=1}^{\infty}\sum_{u=1}^{\infty}\sin\left(k\omega x\right)\sum_{i=5}^{8}Z_i\left(z\right)\sin\left(e_i\omega x\right)\\&+\sum_{k=1}^{\infty}\sum_{l=1}^{\infty}Z_0\left(z\right)\sin\left(k\omega x\right)\sin\left(l\omega y\right).\end{aligned} \tag{41}$$

In regions 1 and 3, substitution of equation (41) into equation (30) results in,

$$\begin{aligned}&\sum_{k=1}^{\infty}\sum_{l=1}^{\infty}\sum_{u=1}^{\infty}\sin\left(l\omega y\right)\sum_{i=1}^{4}\left(\frac{d^2Z_i\left(z\right)}{dz^2}-\lambda_i^{\,2}Z_i\left(z\right)\right)\sin\left(e_i\omega x\right)+\\&\sum_{k=1}^{\infty}\sum_{l=1}^{\infty}\sum_{u=1}^{\infty}\sin\left(k\omega x\right)\sum_{i=5}^{8}\left(\frac{d^2Z_i\left(z\right)}{dz^2}-\lambda_i^{\,2}Z_i\left(z\right)\right)\sin\left(e_i\omega y\right)+\\&\sum_{k=1}^{\infty}\sum_{l=1}^{\infty}\sin\left(k\omega x\right)\sin\left(l\omega y\right)\left(\frac{d^2Z_0\left(z\right)}{dz^2}-\lambda_0^{\,2}Z_0\left(z\right)\right)=0\end{aligned} \tag{42}$$

where

$$\lambda_1=\sqrt{\left(l\omega\right)^2+\left(e_1\omega\right)^2}, \tag{43}$$

$$\lambda_2=\sqrt{\left(l\omega\right)^2+\left(e_2\omega\right)^2}, \tag{44}$$

$$\lambda_3=\sqrt{\left(l\omega\right)^2+\left(e_3\omega\right)^2}, \tag{45}$$

$$\lambda_4=\sqrt{\left(l\omega\right)^2+\left(e_4\omega\right)^2}, \tag{46}$$

$$\lambda_5=\sqrt{\left(k\omega\right)^2+\left(e_5\omega\right)^2}, \tag{47}$$

$$\lambda_6=\sqrt{\left(k\omega\right)^2+\left(e_6\omega\right)^2}, \tag{48}$$

$$\lambda_7=\sqrt{\left(k\omega\right)^2+\left(e_7\omega\right)^2}, \tag{49}$$

$$\lambda_8=\sqrt{\left(k\omega\right)^2+\left(e_8\omega\right)^2}, \tag{50}$$

$$\lambda_0=\sqrt{\left(l\omega\right)^2+\left(k\omega\right)^2}. \tag{51}$$

The general solution of the equation is

$$Z_i\left(z\right)=K_{1i}e^{-\lambda_i z}+K_{3i}e^{\lambda_i z}\quad i=0,1,2,\ldots,8, \tag{52}$$

where K_{1i} and K_{3i} are constants. The boundary conditions (zero scalar potential for $z=\pm\infty$),

$$Z_{\psi 1i}\left(z\right)=K_{1i}e^{-\lambda_i z}\ \text{ for }\ i=0,1,2,\ldots,8 \tag{53}$$

$$Z_{\psi 3i}\left(z\right)=K_{3i}e^{\lambda_i z}\ \text{ for }\ i=0,1,2,\ldots,8. \tag{54}$$

In region 2, the equation is similar to equation (42) and replaces the 0 with the down side of equation (31). The solution is,

$$Z_i\left(z\right)=K_{2i}e^{-\lambda_i z}+T_{2i}e^{\lambda_i z}-\frac{MC}{\lambda_i^{\,2}\mu_r}g\left(k\right)e_i\omega \quad \text{for}\ \ i=1,2,3,4 \tag{55}$$

$$Z_j\left(z\right)=K_{2j}e^{-\lambda_j z}+T_{2j}e^{\lambda_j z}-\frac{MC}{\lambda_j^{\,2}\mu_r}g\left(l\right)e_j\omega, \quad \text{for}\ j=5,6,7,8 \tag{56}$$

$$Z_0\left(z\right)=K_{20}e^{-\lambda_0 z}+T_{20}e^{\lambda_0 z}, \tag{57}$$

where K_{2i}, T_{2i}, K_{2j}, T_{2j}, K_{20} and T_{20} are constants. The above constants can be calculated with the boundary conditions. The expression for the magnetic flux density in region 3 is,

$$\begin{aligned}B_{3x}=&-\sum_{k=1}^{\infty}\sum_{l=1}^{\infty}B_r k\omega K_{30}e^{\lambda_0 z}\cos\left(k\omega x\right)\sin\left(l\omega y\right)\\&-\sum_{k=1}^{\infty}\sum_{l=1}^{\infty}\sum_{u=1}^{\infty}B_r\sin\left(l\omega y\right)\sum_{i=1}^{4}K_{3i}e^{\lambda_i z}e_i\omega\cos\left(e_i\omega x\right)\\&-\sum_{k=1}^{\infty}\sum_{l=1}^{\infty}\sum_{u=1}^{\infty}B_r k\omega\cos\left(k\omega x\right)\sum_{j=5}^{8}K_{3j}e^{\lambda_j z}\sin\left(e_j\omega y\right)\end{aligned} \tag{58}$$

$$\begin{aligned}B_{3y}=&-\sum_{k=1}^{\infty}\sum_{l=1}^{\infty}B_r l\omega K_{30}e^{\lambda_0 z}\sin\left(k\omega x\right)\cos\left(l\omega y\right)\\&-\sum_{k=1}^{\infty}\sum_{l=1}^{\infty}\sum_{u=1}^{\infty}B_r l\omega\cos\left(l\omega y\right)\sum_{i=1}^{4}K_{3i}e^{\lambda_i z}\sin\left(e_i\omega x\right)-\\&\sum_{k=1}^{\infty}\sum_{l=1}^{\infty}\sum_{u=1}^{\infty}B_r\sin\left(k\omega x\right)\sum_{j=5}^{8}K_{3j}e_j\omega e^{\lambda_j z}\cos\left(e_j\omega y\right),\end{aligned} \tag{59}$$

$$B_{3z} = -\sum_{k=1}^{\infty}\sum_{l=1}^{\infty} B_r \lambda_0 K_{30} e^{\lambda_0 z} \sin(k\omega x)\sin(l\omega y)$$
$$-\sum_{k=1}^{\infty}\sum_{l=1}^{\infty}\sum_{u=1}^{\infty} B_r \sin(l\omega y)\sum_{i=1}^{4} \lambda_i K_{3i} e^{\lambda_i z} \sin(e_i \omega x) \quad (60)$$
$$-\sum_{k=1}^{\infty}\sum_{l=1}^{\infty}\sum_{u=1}^{\infty} B_r \sin(k\omega x)\sum_{j=5}^{8} \lambda_j K_{3j} e^{\lambda_j z} \sin(e_j \omega y),$$

where for $\mu_r = 1$, and

$$K_{3i} = \frac{Cg(k) e_i \omega}{2\lambda_i^2}\left(e^{-\lambda_i m_t} - e^{-\lambda_i m_b}\right) \quad i = 1,2,3,4 \quad (61)$$

$$K_{3j} = \frac{Cg(l) e_j \omega}{2\lambda_j^2}\left(e^{-\lambda_j m_t} - e^{-\lambda_j m_b}\right) \quad j = 5,6,7,8, \quad (62)$$

$$K_{30} = \frac{a_k a_l}{2\lambda_0}\left(e^{-\lambda_0 m_t} - e^{-\lambda_0 m_b}\right). \quad (63)$$

III. OPTIMIZATION OF THE NEW MAGNET ARRAY

Observing the magnet array proposed by this paper and the magnet array used by Jansen [4], the only difference is magnets of horizontally magnetized direction. Figure 5 shows the ratio between the higher harmonics and the analytical model in *z*-component of the magnetic flux density along the air gap length. The analytical model of the magnet array used in this paper is obtained by taking the first harmonic of the magnetic flux density and τ_m/τ takes 0.68 [4].

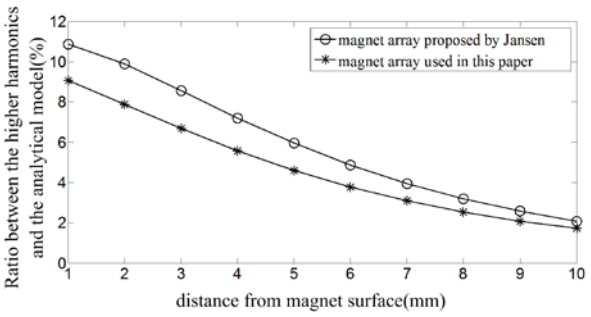

Fig. 5. Ratio between the higher harmonics and the analytical model in *z*-component of the magnetic flux density along the air-gap length.

The magnet array with hexagon magnets has lower ratio than the magnet array used by Jansen. The hexagon magnets can reduce the higher harmonics. The expressions of the magnetic flux density are too complicated to take the first harmonic of the *z*-component as the analytical model used in the real time control for planar motor. Then the effective amplitude is applied as an alternative method. The analytical model of this new 2-D Halbach array can be generalized as in [9],

$$B_{3eff}(\vec{x}) = e^{\sqrt{2}\omega z}\begin{bmatrix} B_{xy}\cos(\omega x)\sin(\omega y) \\ B_{xy}\sin(\omega x)\cos(\omega y) \\ B_z \sin(\omega x)\sin(\omega y) \end{bmatrix}, \quad (64)$$

where B_{xy} and B_z are the effective amplitudes of the magnetic flux density at z = -7.5 mm, and can be calculated as,

$$B_z = B_{3z}^{47}(0.5\tau, 0.5\tau, z_u) \Big/ e^{\sqrt{2}\omega z_u} \quad (65)$$

$$B_{xy} = B_z / \sqrt{2}. \quad (66)$$

The amplitude of *z*-component of the magnetic flux density can be predicted with equation (60) using Matlab. The maximum amplitude of the *z*-component of the harmonic at 4 mm below the bottom of the magnet array is less than 6×10^{-5} T when k = 1, l = 49, and u = 49, which is much less than geomagnetic field (about 6×10^{-5} T) [2]. So the harmonic components can be ignored in optimization if any one of the harmonic numbers (k, l, or u) is more than 47. The approximate expression of the *z*-component of the magnetic flux density is,

$$B_{3z}^{n} = -\sum_{k=1}^{n}\sum_{l=1}^{n} B_r \lambda_0 K_{30} e^{\lambda_0 z} \sin(k\omega x)\sin(l\omega y)$$
$$-\sum_{k=1}^{n}\sum_{l=1}^{n}\sum_{u=1}^{n} B_r \sin(l\omega y)\sum_{i=1}^{4} \lambda_i K_{3i} e^{\lambda_i z} \sin(e_i \omega x) \quad (67)$$
$$-\sum_{k=1}^{n}\sum_{l=1}^{n}\sum_{u=1}^{n} B_r \sin(k\omega x)\sum_{j=5}^{8} \lambda_j K_{3j} e^{\lambda_j z} \sin(e_j \omega y)$$

where n = 47. Both the width and length of the area are half pitch is chosen to be the objective region. This square area is placed in the 4 mm below the bottom of the array, and a 25 × 25 points matrix of the area is taken. The horizontal thrusts [6], which reflect the main performance of a planar motor are generated by *z*-component of the magnetic flux density. The minimization of higher harmonics of the *z*-component is the objective function obtained using equations (64) to (67),

$$f\left(\frac{\tau_m}{\tau}\right) = \left|\frac{\sum_{m=1}^{25}\sum_{n=1}^{25} B_{3zh}(S_{mn}) - \sum_{m=1}^{25}\sum_{n=1}^{25} B_{3zeff}(S_{mn})}{\sum_{m=1}^{25}\sum_{n=1}^{25} B_{3zeff}(S_{mn})}\right| \times 100\% \quad (68)$$

where $S_{mn} = (0.02m\tau, 0.02n\tau, -0.0075)$.

The genetic algorithm toolbox of Matlab is used. The optimization parameters and variables are shown in Tables I and II, respectively. The flowchart of the parameter optimizing procedure using genetic algorithm (GA) [13] is shown in Fig. 6. The stall generations are 100, and the others use the default setup.

Table I: Optimization parameters.

Parameters	**Symbol**	**Value**	**Unit**
Pole pitch	τ	0.025	m
Position of the top surface of the array	m_t	0.0035	m
Position of the bottom surface of the array	m_b	-0.0035	m
Remanence of the permanent magnets	B_r	1.24	T

Table II: Optimization variable.

Optimization variable	**Constrain**
τ_m/τ	[0,1]

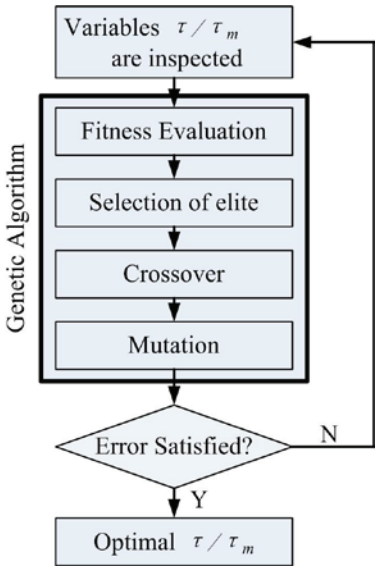

Fig. 6. The genetic algorithm process.

The fitness values of τ_m/τ shown in Fig. 7, illustrate that after 20 number of iteration the error reaches to an acceptable value. The minimization of the objective function can be obtained if τ_m/τ takes 0.41.

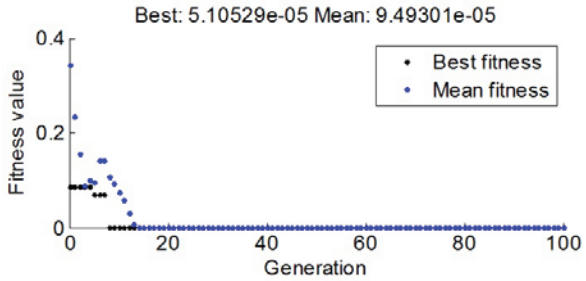

Fig. 7. Generation iteration process.

The magnetic flux density at 4 mm below the magnet array is shown in Fig. 8 when τ_m/τ takes 0.41. Figure 8 (a) is predicted with function shown in equation (61). Figure 8 (b) is calculated by 3-D finite-element model [13]. It can be found that Fig. 8 (b) approximates to Fig. 8 (a). The difference of the peak values between Fig. 8 (a) and Fig. 8 (b) is less than 0.01 T, which is 1.76 % of the peak value of Fig. 8 (a).

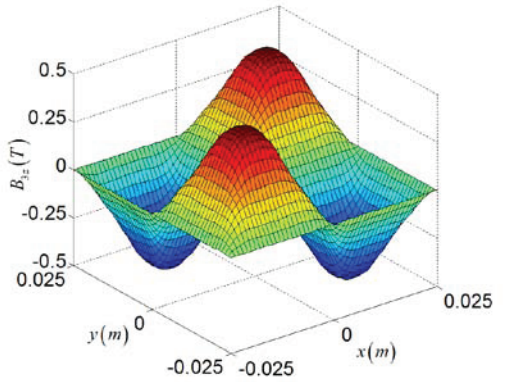

(a)

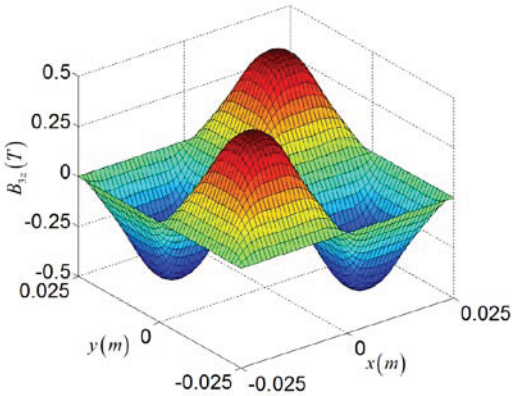

(b)

Fig. 8. Magnetic flux density, (a) calculated by the harmonic model and (b) calculated by the finite element method.

IV. SIMULATION AND COMPARISION

The Halbach array used by Jansen [4] has the same optimization parameters shown in Table I, and the results are shown with taking different optimization variable values in Table III.

Table III: Parameters compared.

Magnet array	τ_m/τ	$f(\tau_m/\tau)$
Proposed by this paper	0.41	0.0109%
Used by Jansen	0.68	6.277%

From Table III, the harmonic model is taken to obtain the sum for all the higher harmonics of z-component of the magnetic flux density on the plane, which is 4 mm below the magnet array surface. The sum of the magnet array proposed by this paper and used by Jansen is shown in Figs. 9 and 10, respectively.

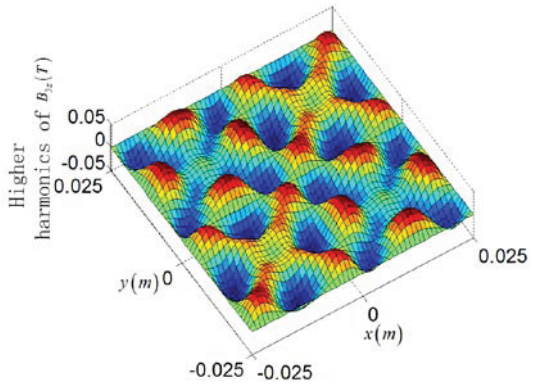

Fig. 9. The sum of all the higher harmonics components of the magnet array proposed by this paper.

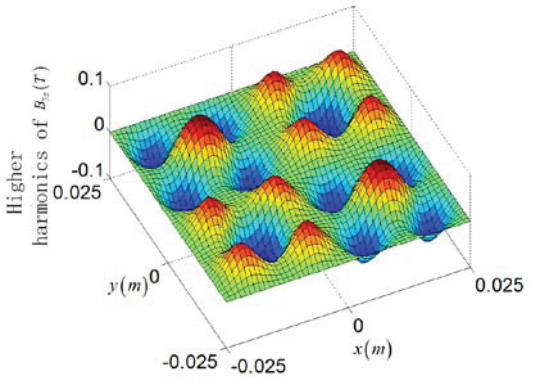

Fig. 10. The sum of all the higher harmonics components of the magnet array used by Jansen.

It is found that the sum for higher harmonics of z-component of the magnet array proposed by this paper is smaller and smoother than the magnet array used by Jansen. The peak value of higher harmonics of *z*-component of the magnet array proposed by this paper is 0.04097 T, which is 50.88 % of the peak value of the magnet array used by Jansen. If the magnet array proposed by this paper is used in the planar motor, the force ripple will be smaller than the planar motor in which the magnet array used by Jansen.

The peak value of *z*- and *x*-components of the magnetic flux density along the air-gap length from the magnet array surface are shown in Figs. 11 and 12, respectively. Comparing the curves in Figs. 11 and 12, the *z*-component of the magnetic flux density of the magnet array proposed by this paper is much larger than the magnet array used by Jansen, and the *x*-component of the magnetic flux density of the magnet array proposed by this paper is smaller.

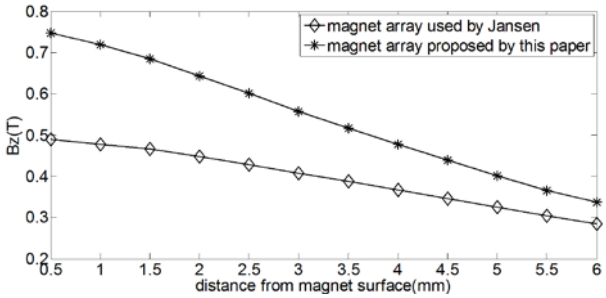

Fig. 11. Peak value of the *z*-component of the magnetic flux density along air-gap length.

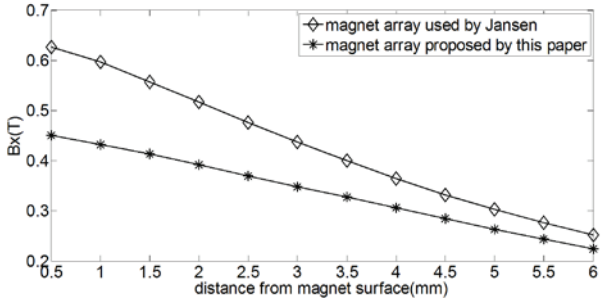

Fig. 12. Peak value of the *x*-component of the magnetic flux density along air-gap length.

V. CONCLUSION

The assumption of the air in the magnet array in the harmonic model derivation does not exist due to the compact structure. The hexagon

magnets can reduce the higher harmonics when compared with the magnet array used by Jansen. The analytical model is obtained by using the effective amplitude. The genetic algorithm is applied to minimize the higher harmonics of the *z*-component of the magnetic flux density of magnet array. Comparing with the magnet array used by Jansen, the higher harmonics of *z*-component of the magnetic flux density of this magnet array is much smaller, which will reduce the force ripple of the planar motor. The *z*-component of the magnetic flux density is larger and the *x*-component of the magnetic flux density is smaller.

ACKNOWLEDGMENT

Research was supported by National Natural Science Foundation of China (No. 51375194).

REFERENCES

[1] J. Compter, "Electro-dynamic planar motor," *Precision Eng.*, vol. 28, pp. 171-180, 2004.

[2] H.-S. Cho, C.-H. Im, and H.-K. Jung, "Magnetic field analysis of 2-D permanent magnet array for planar motor," *IEEE Trans. Magn.*, vol. 37, no. 5, Sep. 2001.

[3] H.-S. Cho and H.-K. Jung, "Analysis and design of synchronous per-manent-magnet planar motors," *IEEE Trans. Energy Convers.*, vol. 17, no. 4, pp. 492-499, Dec. 2002.

[4] J. Jansen, C. Van Lierop, E. Lomonova, and A. Vandenput, "Modeling of magnetically levitated planar actuators with moving magnets," *IEEE Trans. Magn.*, vol. 43, no. 1, pp. 15-25, Jan. 2007.

[5] J. Jansen, C. Van Lierop, E. Lomonova, and A. Van-Denput, "Magnetically levitated planar actuator with moving magnets," *in Proc. IEEE Int. Electric. Machines and Drives Conf.*, vol. 1, pp. 272-278, May 2007.

[6] W. Min, M. Zhang, Y. Zhu, B. Chen, G. Duan, J. Hu, and W. Yin, "Analysis and optimization of a new 2-D magnet array for planar motor," *IEEE Trans. Magn.*, vol. 46, no. 5, May 2010.

[7] Y. Zhang, Z. Yang, M. Yu, K. Lu, Y. Ye, and X. Liu, "Analysis and design of double-sided air core linear servo motor with trapezoidal permanent magnets," *IEEE Trans. Magn.*, vol. 47, no. 10, Oct. 2011.

[8] L. Huang, X. Huang, H. Jiang, and G. Zhou, "Comparative study of magnetic fields due to types of planar permanent magnet array," *International Conference on Electrical and Control Engineering*, vol. 10, 2010.

[9] J. Peng and Y. Zhou, "Modeling and Analysis of a new 2-D Halbach array for magnetically levitated planar motor," *IEEE Trans. Magn.*, vol. 49, no. 1, pp. 618-627, Jan. 2013.

[10] A. Shiri and A. Shoulaie, "Investigation of frequency effects on the performance of single-sided linear induction motor," *Applied Computational Electromagnetics Society (ACES) Journal*, vol. 27, no. 6, pp. 497-504, June 2012.

[11] K. Binns, P. Lawrenson, and C. Towbridge, *The Analytical and Numerical Solutions of Electrical and Magnetic Fields*, Chichester, England: *John Wiley & Sons*, 1994.

[12] A. Nejadpak, M. Barzegaran, and O. Mohammed, "Evaluation of high frequency electromagnetic behavior of planar inductor designs for resonant circuits in switching power converters," *Applied Computational Electromagnetics Society Journal*, vol. 26, no. 9, pp. 737-748, 2011.

[13] E. Schmidt and M. Hofer, "Application of the sliding surface method with 3D finite element analyses of a hybrid magnetic bearing," *25th Annual Review of Progress in Applied Computational Electromagnetics (ACES)*, pp. 440-445, Monterey, California, March 2009.

Guangdou Liu received the M.S. degree in Mechanical and Electronics Engineering from China University Of Petroleum, Shandong, China, in 2009, and is currently working toward the Ph.D. degree in Mechanical and Electronics engineering at the Huazhong University of Science Technology. His research interests include magnetic fields and magnetic devices.

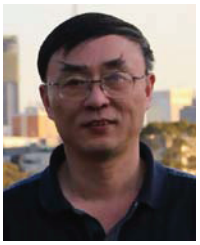

Yunfei Zhou received the B.S. degree in Mechanics from Zhejiang University, Hangzhou, China, in 1982, and the M.S. and Ph.D. degrees in Mechanical and Electronic Engineering from Huazhong University of Science and Technology, Wuhan, China, in 1989 and 1993, respectively. He is currently a Professor in Department of Mechanical and Electronic Engineering, Huazhong University of Science and Technology. His research interests include numerical control technology, high-precision motion control, microelectronic device, and precision servo motor control.

GHz-Frequency Electromagnetic Interference Suppression Technique using Magnetic Absorber for Hard Disk Interconnector

S. Osaklang [1], A. Keawrawang [1], A. Siritaratiwat [1], V. Ungvichian [2], R. Sivaratana [3], K. Prachumrasee [4], and A. Kruesubthaworn [4]

[1] KKU-Seagate Cooperation Research Laboratory,
Department of Electrical Engineering, Khon Kaen University, Khon Kaen, 40002, Thailand
arkom@elec.kku.ac.th, apirat@kku.ac.th

[2] College of Engineering and Computer Science,
Florida Atlantic University, Boca Raton, FL 33431, USA
ungvich@fau.edu

[3] Seagate Technology (Thailand) Co., Ltd.,
1627, Teparak Road, Samutprakarn, 10270, Thailand
Roong.Sivaratana@seagate.com

[4] Faculty of Applied Science and Engineering,
Khon Kaen University, Nong Khai Campus,
NongKhai, 43000, Thailand
krispr@kku.ac.th, anankr@kku.ac.th

Abstract ─ An electromagnetic interference (EMI) suppression technique for gigahertz (GHz) frequency region of hard disk interconnector, namely trace suspension assembly interconnector (TSAI) is presented. The BSR-1 absorber is selected and filled in between conductor traces of the interconnector. The attenuation of radiated and conducted EMIs are calculated and analyzed by using simulation software based on finite integral technique. From the results, it is found that the proposed technique can suppress radiated EMI from 16 μV to 0.5 μV in all frequency regions up to 20 GHz and the conducted EMI can be suppressed up to 0.7 Watt in a range of 0.9 GHz – 4.0 GHz with the same structure of TSAI.

Index Terms - Electromagnetic coupling, electromagnetic interference, interconnector, and interference suppression.

I. INTRODUCTION

To improve the data transfer rate of high speed hard disk drives (HDDs), the operating frequency has to be increased. However, the effects of EMI have to be suppressed because these effects can degrade the recording head in HDD as reported in [1, 2]. EMI can be classified as two types, which are radiated and conducted EMI. The EMI mechanism of both, including the three components includes source, path, and victim [3].

The radiated EMI from a cell phone, which causes the recording head degradation, has been reported [1, 2]. As the results, the signal integrity affected by an external EMI can cause latent failure to the sensitive components in HDDs [4, 5]. For conducted EMI, the EMI can interfere with both analog and digital signals, which is used in the read/write channels of HDDs [6]. In addition, the write-to-read crosstalk in trace suspension assembly interconnector (TSAI) is an example of the conducted EMI, which is reported in [7, 8]. Consequently, the effects of radiated and

Submitted On: Sept. 6, 2012
Accepted On: Sept. 29, 2013

1054-4887 © 2013 ACES

conducted EMI on the TSAI are a new challenge to design with low EMI.

A flexible printed circuit ribbon without a cover layer connects the HDD heads to an amplifier via TSAI behaving like an antenna [9]. Then, the TSAI can pick up the EMI signal and can cause failures in magnetic recording heads, which are severe problems [3]. Thus, one approach to mitigate the EMI is the overcoat of the interconnector traces with absorbing magnetic material [10, 12]. A drawback of this technique is an increase in the size of the TSAI, hence, it is undesirable for HDD applications.

The aim of this study is to find a new EMI suppression technique on TSAI based on the filling commercialized BSR-1 [13] absorber in the gap between copper traces of TSAI. A physical advantage over the previous approach [10, 12] is that the original TSAI dimensions have not been changed. The absorption properties of the BSR-1 with the radiated and conducted EMI on TSAI are presented. The results throughout this study are determined by using the finite integral technique in CST Microwave Studio [14].

II. INTERFERENCE MODEL FOR TSAI

The form factors of HDD have several dimensions, which consist of 1.8-, 2.5-, and 3.5-inch. The 2.5-inch drive is the main market of HDD technology that mostly uses in present [15]. Then, the selected TSAI is approximately 35 mm in length, which is used in 2.5-inch drives and is used in this simulation. As show in Fig. 1 (a), the TSAI is comprised six copper traces, which are 1 heater trace for flying height control, 2 read traces, 1 ground trace, and 2 write traces. From Fig. 1 (b), it is only two out of six copper traces, which are chosen to exhibit the effect to the active components of radiated [16] and conducted EMI [10].

The selected TSAI structure is supported by a 20 μm of stainless steel with the grooves being filled by BSR-1 between two copper traces are modeled. A 10 μm polyimide dielectric substrate has a permittivity of 3.5 and a dielectric loss tangent of 0.003. To investigate the EMI suppression properties of BSR-1 on TSAI, the simulations begin with the magnetic film thickness (t_m) of zero (no filling BSR-1 absorber), 3, 6, 9, 12, 15, and 18 μm (100% filling BSR-1 absorber).

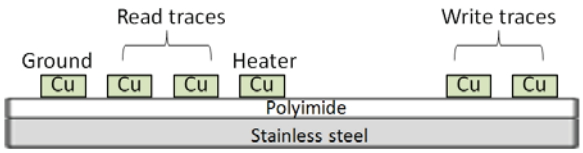

(a)

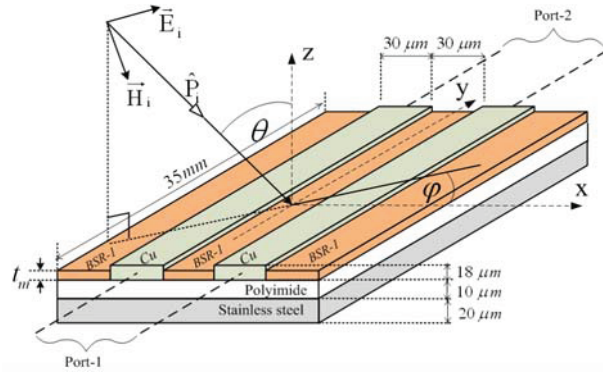

(b)

Fig. 1. (a) Cross-sectional geometry of TSAI [8] and (b) model of conduction EMI and radiation EMI.

The simulations of the radiated EMI are shown in Fig. 1 (b). The TSAI is exposed to the 1 V/m incident field of 20 GHz bandwidth Gaussian pulse. It achieves the maximum coupling, when the propagating field is oriented, such that an E-field is perpendicular to the plan of incident (the elevation angle $\theta = 90^{o}$, and azimuth angle $\varphi = 90^{o}$) [17].

The radiated noise can be measured when the 50 Ω of load impedances are terminated at both ends of TSAI. The occurrence of the radiating noise voltage at the far-end terminal of the TSAI is determined by coupling voltage (V_{FE}) where the active components are located [17]. The radiated EMI suppression effected by using BSR-1 on the TSAI is defined as the shielding effectiveness (SE), which is given by equation (1) [18],

$$SE = 20\log(V_{FEwithout-filled} / V_{FEwith-filled}) \ . \quad (1)$$

For the conducted EMI simulation, the port label is defined to calculate *S*-parameters obtained

from the CST simulation software as shown in Fig. 1 (b). Both reflection coefficient (S_{11}) and transmission coefficient (S_{12}) are evaluated to analyze the conducted EMI on the interconnector [11]. The evaluation of conducted EMI suppressed on TSAI by using BSR-1 can be estimated by power absorption, which is defined as the ratio of loss power to input power (P_{loss}/P_{in}), using the following equation [13],

$$P_{loss}/P_{in} = 1-\left(|S_{11}|^2+|S_{21}|^2\right) . \quad (2)$$

The electromagnetic properties of BSR-1 are depicted in Fig. 2. The major parameters determining the absorbability comprise a real-part permeability (μ') an imaginary-part permeability (μ'') and a magnetic loss tangent (tan δ_m). The tan δ_m represents an absorption performance of the material. As seen in Fig. 2, the maximum tan δ_m occurs around 10 GHz – 14 GHz, this means that the material provides a good absorption performance around 10 GHz [19].

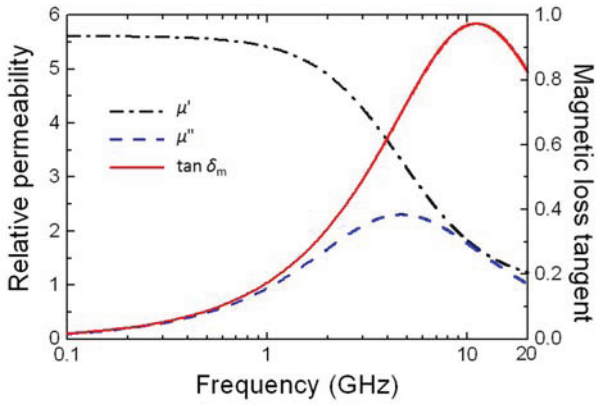

Fig. 2. Material properties of BSR-1.

The absorption ability of BSR-1 material is indicated by reflective loss (*RL*). It is given by equation (3) [19],

$$RL = -20\log\left|\frac{Z_{in}-50}{Z_{in}+50}\right| \quad (3)$$

$$Z_{in} = \sqrt{\frac{\mu'-j\mu''}{\varepsilon'-j\varepsilon''-j\sigma/(\omega\varepsilon_0)}} \cdot \tanh\left(\frac{jd\omega}{c}\sqrt{(\mu'-j\mu'')\left(\varepsilon'-j\varepsilon''-j\sigma/(\omega\varepsilon_0)\right)}\right) , \quad (4)$$

and

$$\omega = 2\pi f \quad , \quad (5)$$

where $Z_{in}, \mu', \mu'', \varepsilon', \varepsilon'', \varepsilon_0, \sigma, f, d,$ and c represent impedance of incidence wave, real part of permeability, image part of permeability, real part of permittivity, image part of permittivity, permittivity of vacuum, conductivity, frequency of electromagnetic wave, thickness of material, and light speed, respectively [19].

As seen in Fig. 3, the *RL* of BSR-1 significantly decreases with increasing t_m and frequency according to the details in [19]. This can be explained by the magnetic loss, which is inversely proportion when frequency and t_m were increased [19]. It is likely to be one of good candidates for EMI suppressor at this frequency region. Hence, the EMI absorption ability on TSAI is also explained in this study.

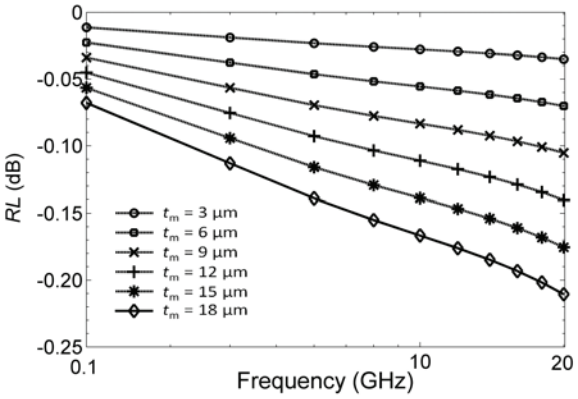

Fig. 3. Reflective loss of BSR-1with various magnetic film thickness (t_m).

III. RESULTS AND DISCUSSIONS

A. Suppression characteristics for the radiated EMI

In this section, the effects of BSR-1 absorber on the coupling voltage (V_{FE}) and shielding effectiveness (SE) are analyzed. The V_{FE} versus frequency with various t_m for the examined structures are shown in Fig. 4. A considerable amount of decoupling at GHz is observed with increasing t_m because the decrement of V_{FE} with increasing t_m is evaluated. For $t_m \geq 15$ μm, the lowest of V_{FE} is obtained at all frequency regions. Besides, the fluctuation of V_{FE} from dimensional resonance at around 17 GHz – 19 GHz is removed. It is a desirable characteristic for the decoupling signal because both fewest and

smoothest of V_{FE} are achieved. This effect is due to a higher magnetic loss from a higher surface impedance of absorber with increasing absorber thickness [19]. In addition, the suppression of radiated EMI is obtained by increasing t_m because of the attenuated V_{FE} by increment of t_m. Furthermore, the TSAI with $t_m \geq 15$ μm can suppress a large of coupling voltage from 16 μV into 0.5 μV at all regions.

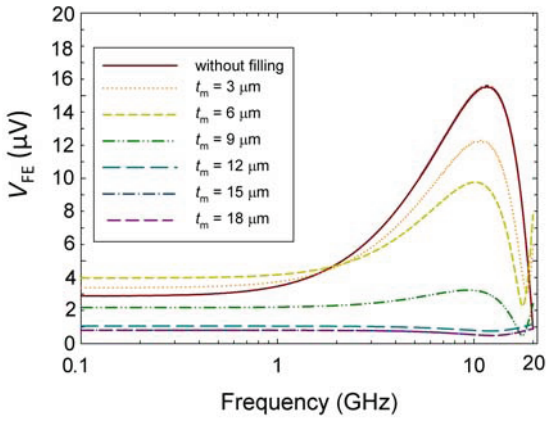

Fig. 4. Coupling voltage (V_{FE}) with various magnetic film thicknesses (t_m).

Figure 5 shows the SE of TSAI, which is calculated from equation (1). It is seen that the SE is above 10 dB for frequency below 1 GHz as well as rapidly increasing as a function of frequency from 1 GHz to 10 GHz. In addition, the SE reaches the maximum of 30 dB at 12 GHz. After that, SE is dramatically decreased from frequency over 13 GHz and attains 10 dB at 19 GHz. However, the SE is decreasing below 10 dB for 19 GHz – 20 GHz range, which is the undesirable characteristic for the radiated EMI suppression. As the results, the shielding of radiated EMI over 10 dB at 0 GHz – 19 GHz and the highest of 30 dB at 12 GHz are achieved for TSAI with 100% filling BSR-1 absorber. Hence, TSAI with 100% filling of BSR-1 absorber is the best choice to suppress the radiated EMI, which is appropriate at 0 GHz to 19 GHz region with the greatest performance at 12 GHz.

B. Suppression characteristics for the conducted EMI

The S_{11} and S_{21} versus frequency with various t_m are depicted in Fig. 6. Both S_{11} and S_{21} decrease with the increasing of t_m and frequency. This is because the absorption of the conducted currents caused by magnetic loss (see in Fig. 3) is proportional to t_m and frequency [19]. From Fig. 6, it is clearly observed that a magnitude of S_{11} and S_{21} decrease with increasing t_m. For all regions, the S_{11} obtains below -10 dB with the t_m above 3 μm and provides the minimum with t_m of 18 μm (100% filling BSR-1 absorber). For the S_{21}, it decreases as frequency increases, however, the level of S_{21} decreased when t_m increased. In addition, the maximum attenuation at over 1 GHz is achieved with 100% filling BSR-1 absorber. Also, the suppression ability of TSAI in case of conducted EMI can be controlled in 1 GHz to 20 GHz by varying t_m.

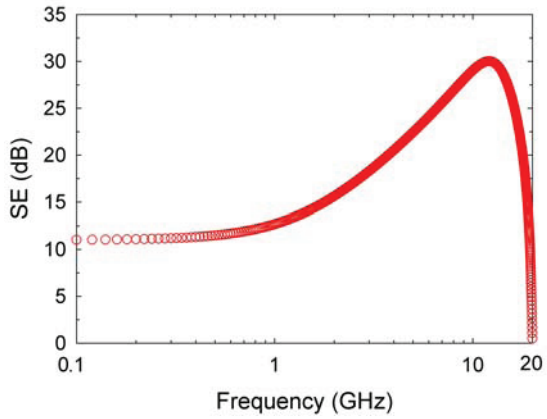

Fig. 5. Frequency dependence of shielding effectiveness (SE) in dB.

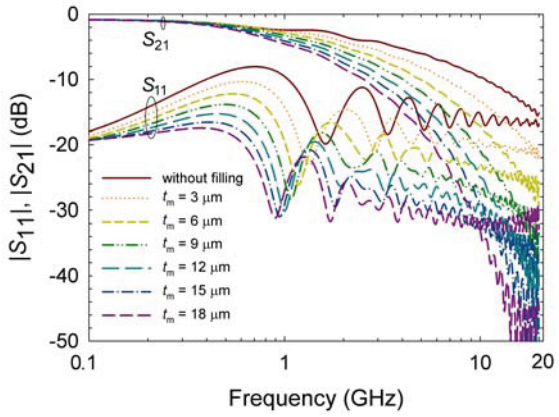

Fig. 6. *S*-parameters with various magnetic film thickness (t_m).

Figure 7 shows P_{loss}/P_{in} as a function of frequency with various t_m. It is found that the P_{loss}/P_{in} rapidly increases as frequency increases. It is according to the results shown in Fig. 6. From Fig. 8, P_{loss}/P_{in} of the 100% filling BSR-1 on TSAI begins to rise up to 0.7 GHz and tends to decrease around 0.3 GHz. This means that the filling BSR-1 absorber on TSAI can tune the absorption frequency region. Furthermore, the pure power absorbed is calculated by the difference between P_{loss}/P_{in} with and without 100% filling BSR-1 absorber, which is represented by $\Delta P_{loss}/P_{in}$ as a solid line in Fig. 8. It is found that the $\Delta P_{loss}/P_{in}$ initiates rise at 0.1 GHz and rapidly increases to 0.7 W. This means that the conducted EMI can be suppressed up to 0.7 W and normalized by 1 W of the input power in a range of 0.9 GHz – 4.0 GHz. Thus, the proposed technique is an outstanding approach to suppress the conducted EMI in the GHz region.

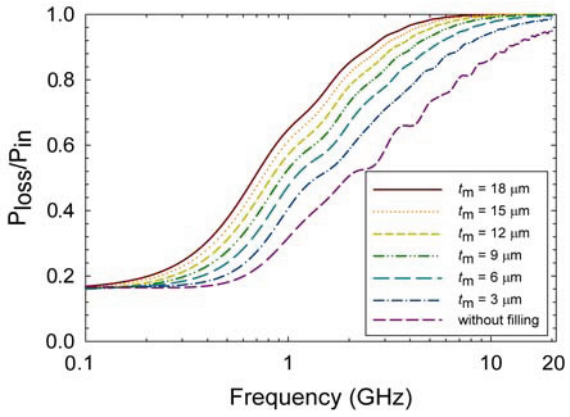

Fig. 7. The ratio of loss power to input power (P_{loss}/P_{in}), with various magnetic filling thickness (t_m).

IV. CONCLUSIONS

A novel electromagnetic interference suppression technique using magnetic material in the gap between the trace suspension assembly interconnector (TSAI) is proposed. The attenuations of radiated and conducted emissions are analyzed by using simulation software based on finite integral technique. From the radiated results, it is found that the proposed technique, especially the 100% filled TSAI provides the lowest of 0.5 μV of the coupling voltage. In addition, the shielding effectiveness of the 100% filled TSAI shows the greatest performance at 12 GHz according to the electromagnetic properties of the absorber material. For conducted emission, the results show that the power absorption decreased with increasing the absorber thickness and the large of absorbability of 0.7 W in a range of 0.9 GHz – 4.0 GHz is provided. Hence, this technique is an alternative technique that is suitable for practical TSAI design to provide a good immunity for EMI reduction at GHz region.

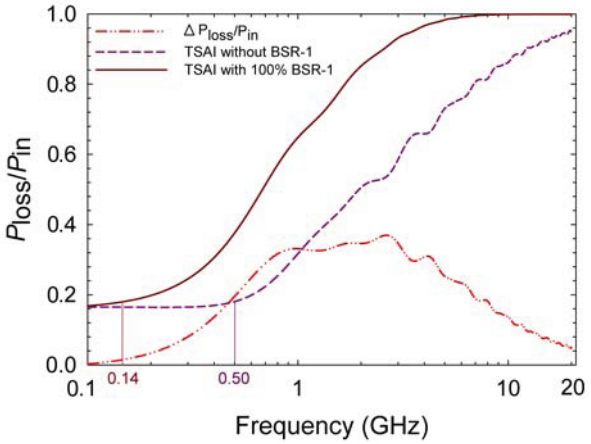

Fig. 8. The ratio of loss power to input power (P_{loss}/P_{in}) and the difference of P_{loss}/P_{in} between TSAI with and without 100% filling BSR-1 absorber ($\Delta P_{loss}/P_{in}$).

ACKNOWLEDGMENT

This work was financially supported by the Thailand Research Fund under the TRF Advanced Research Scholar Program, under Grant BRG5280019 with partially support by Khon Kaen University and the Office of the Higher Education Commission of Thailand, under UDC scholarship of Mahasarakham University. Also, the authors wish to express their sincere gratitude to Department of Telecommunication Engineering, King Mongkut's Institute of Technology Ladkrabang, Bangkok, Thailand for CST software.

REFERENCES

[1] V. Kraz and A. Wallash, "The effects of EMI from cell phones on GMR magnetic recording heads and test equipment," *J. Electrostat.*, vol. 54, pp. 39-53, Jan. 2002.

[2] A. Wallash and D. Smith, "Electromagnetic interference (EMI) damage to giant magnetoresistive (GMR) recording heads," *EOS/ESD Symposium*, pp. 368-374, 1998.
[3] C. R. Paul, *Introduction to Electromagnetic Compatibility*, pp. 3-496, Wiley & Sons, Inc., USA, 1992.
[4] A. Kruesubthaworn, R. Sivaratana, V. Ungvichian, and A. Siritaratiwat, "Testing parameters of TMR heads affected by dynamic-tester induced EMI," *J. Magn. Mater*., vol. 316, pp. 142-144, Feb. 2007.
[5] A. Kruesubthaworn, A. Pratoomthip, A. Siritaratiwat, and V. Ungvichian, "Anomalous magnetic responsiveness of giant magnetoresistive heads under specific electromagnetic interference frequencies using quasi static tester," *J Appl. Phys*., vol. 103, pp. 07F538, Mar. 2008.
[6] I. Ranmuthu, P. M. Emerson, K. Maggio, H. Jiang, A. Manjekar, B. E. Bloodworth, and M. Guastaferro, "A design for high noise rejection in a Pseudo differential preamplifier for hard disk drives," *IEEE J. of Solid State Circuits*, vol. 35, no. 6, pp. 911-914, June 2000.
[7] K. Prachumrasee, A. Siritaratiwat, V. Ungvichian, R. Sivaratana, and A. Kaewrawang "A methodology to identify crosstalk contributor from 6-line suspension assembly interconnect of ultra-high capacity hard disk drives," *ACES Journal*, vol. 27, no. 1, pp. 22-27, Jan. 2012.
[8] K. Klaassen, J. Contreras, and J. Van Peppen, "Read/write electronics front-end systems for hard disk drives," *IEEE Trans. Magn*., vol. 40, no. 1, pp. 263-268, Jan. 2004.
[9] G. Shinh, N. Nakhla, R. Achar, M. Nakhla, A. Dounavis, and I. Erdin, "Fast transient analysis of incident field coupling to multiconductor transmission lines," *IEEE Trans. Electromagn. Compat.*, vol. 48, no. 1, pp. 57-73, Feb. 2006.
[10] S. Onuma, H. Nagura, H. Fujimuri, and T. Masumoto, "Noise suppression effect of nanogranular Co-based magnetic thin films at gigahertz frequency," *IEEE Trans. Magn*., vol. 40, no. 4, pp. 2712-2715, July 2004.
[11] B. Drnovsek, J. Koselj, A. Znidarsic and V. Bregar, "Study of coupling on parallel microstrip line due to magnetic-loaded absorber sheet," *IEEE Trans. Magn*., vol. 44, no. 11, pp. 3801-3804, Nov. 2008.
[12] M. Yamaguchi, K. Kim, T. Kuribara, and K. Arai, "Thin film noise suppressor integrated in a transmission line," *IEEE Trans. Magn*., vol. 38, no. 5, pp. 3183-3185, Sep. 2002.
[13] Emerson and Cuming Microwave Products. http://www.eccosorb.com/products-eccosorb-bsr.htm.
[14] CST GmbH, Germany, CST Microwave Studio, 2010.
[15] M. Kryder and C. Kim, "After hard drives what comes next?," *IEEE Trans. Magn*., vol. 45, no. 10, pp. 3406-–3413, Oct. 2009.
[16] S. Osaklang, A. Kruesubthaworn, R. Sivaratana, P. Supnithi, V. Ungvichian, A. Keawrawang, and A. Siritaratiwat, "A practical crosstalk reduction technique applied to high-density hard disk interconnecting assembly traces," *IEEE Trans. Magn*., vol. 47, no. 10, pp. 4014-4017, Oct. 2011.
[17] S. Sali, "Coupling of electromagnetic fields to coplanar striplines with discontinuities," *IEE Proc. H*., vol. 140, no. 6, pp. 481-487, Dec. 1993.
[18] M. Rau, A. Iftermie, O. Baltag, and D. Costandache, "The study of the electromagnetic shielding properties of a textile material with amorphous microwire," *Advances in Electrical and Computer Engineering*, vol. 11, no. 1, pp. 18-22, 2011.
[19] J. Huo, L. Wang, and H. Yu, "Polymeric nanocomposite for electromagnetic wave absorption," *J. Mater. Sci*., vol. 44, no. 15 pp. 3917-3927, June 2009.

Arkom Kaewrawang obtained his B.Eng. (EE), Horn, from Khon Kaen University, M.Eng. (EE) from Chulalongkorn University, and Ph.D. from Shinshu University, Japan. He has done researches with HDD industry in the area of magnetic materials and high frequency effects to recording heads. He has published more than 20 international articles with many outstanding awards from various sources.

Apirat Siritaratiwat received his B.Eng. (EE) from Khon Kaen University in 1992. After working in industry for few years, he joined the Department of Electrical Engineering, Khon Kaen University in 1994 and continued his postgraduate study at the University of Manchester, UK, between 1995-1999. He has served in many managerial positions such as Head of Department, Assistant to President for Research Affairs, Vice President of KKU etc. He has done researches in HDD and been one of pioneer researchers of ESD/EOS and EMI in recording heads. Since his researches are mainly jointed with HDD industry, it leaded to the establishment of the KKU-Seagate Cooperation Research Laboratory and the I/U CRC in HDD Component where he was Director. He has published more than 100 articles and held 6 pending patents.

Vichate Ungvichian was born in Bangkok, Thailand. He received his Ph.D. degree in Electrical Engineering specialized in Electromagnetic from the Ohio University, Athens, Ohio, in 1981.Since 1982, he has been with the Department of Electrical & Computer Engineering and Computer Science, Florida Atlantic University, Boca Raton, Florida, USA. He is a Full Professor and in the past 28 years as the Director of the EMI Lab. He is a senior member of IEEE, Advisor of IEEE FAU Student Chapter and Advisor of τβπ Engineering Honor Society.

Roong Sivaratana is a Senior Director of Engineering at Seagate Technology (Thailand), responsible for TH R&D Activities. He received a B.Eng. in EE from KMITN in 1986, M.Eng. in EM from Chulalongkorn University, and M.S. in EBM from University of Warwick. Beside engineering works in Seagate, he is also a member of engineering advisory committee at SUT and KMITL, a member of KKU's activities promotion committee, as well as an industry adviser to Cluster/Program Management Office (CPMO under NSTDA).

Krisada Prachumrasee obtained his B.Eng. (EE), M.Eng. (EE) and Ph.D. in Electrical Engineering from Khon Kaen University in 2006, 2010 and 2013, respectively. Now, he is a lecturer at Khon Kaen University, Nong Khai campus. His research interests are and EMI/EMC in magnetic recording heads, and EMI/EMC in telecommunication.

Anan Kruesubthaworn obtained his B.Eng. and Ph.D. in Electrical Engineering from Khon Kaen University in 2002 and 2008, respectively. After that, he had joined Seagate Technology (Thailand) Ltd. for 3 years. Now, he is a lecturer at Khon Kaen University, Nong Khai campus and he is the pioneer to establish the engineering field at this campus. His research interests are EMC in nano electronic devices and telecommunication systems.

Verification of Nonlinear Characteristics of Radar Angular Glint by Surrogate Data Method

Jin Zhang, Zhiping Li, Cheng Zheng, and Jungang Miao

School of Electronic and Information Engineering
Beijing University of Aeronautics and Astronautics, Beijing, 100191, P. R. China
zhangjin850224@139.com, zhiping_li@buaa.edu.cn, zhengcheng@sina.com, jmiaobremen@buaa.edu.cn

Abstract ─ In this paper, we present a nontrivial verification of nonlinear characteristics of angular glint by the surrogate data method. Glint is a key cause of target loss in radar detections. Prediction and suppression of glint is a hot topic. Firstly, glint data of a typical target are calculated by GRECO method for two motions. As glint is calculated by quadric surface calculations, it is nonlinear in mathematical nature. The surrogate data method is explained and workflow is summarized to verify the nonlinear traits of glint. Surrogate methods of phase randomized Fourier transform and amplitude adjusted Fourier transform are illustrated. Test statistics of higher order moments and time reversibility are given. Lorenz model is simulated as a standard nonlinear model to verify effectiveness of workflow, and nonlinear verification criteria are drawn. A new parameter is designed to measure the powerfulness of nonlinearity. Finally, nonlinear verifications for the two angular glint series are given. Results are illustrated in figures and data and they agree with nonlinear criterion. This paper lays the foundations for chaotic verifications of glint.

Index Terms ─ **A**ngular glint, GRECO, nonlinear verification criterion, and surrogate data method.

I. INTRODUCTION

Since 1959, when the angular glint concept was firstly proposed, it has attracted great interest among electromagnetic diffraction and stealth researchers [1-3]. The primary cause of angular glint is the interaction among each reflection unit of the extended target. When the radar is in operation, angular glint could cause the antenna to jitter, which increases the tracking loss probability. When the target approaches nearer, this phenomenon becomes more evident. Researchers have drawn two conclusions on the relationship between RCS and angular glint: (1) the two are negatively correlative and (2) they are neither correlative nor independent [4-6].

Then two problems arise for further research on glint. The first is how to calculate angular glint precisely; the second is how to verify the nonlinear physical nature of glint and find solutions to suppress glint effects, as several suppression methods such as polarization and frequency diversities have been proposed.

In this paper, for the first problem, we have developed a software package based on phase gradient method (PGM) and GRECO, and glint results are calculated for straight line and rotary motions, which are typical routes across the radar detection range. These results agree well with measurements [7-8]. For the second problem, each angular glint is treated as time series by nonlinear science theories and their nonlinearities are verified by the surrogate data method.

As glint is calculated by nonlinear expressions (quadric surface equations) by GRECO [9], the problem of whether it is nonlinear in physical nature is proposed. The nonlinearity verification is performed in two steps. Firstly, this paper has elaborated the procedures of a known method for diagnosing nonlinearity, the surrogate data method and summarized its workflow, including the surrogate data generations (phase randomized Fourier transform and amplitude adjusted Fourier transform, PRFT and AAFT) and test statistics selection (higher order moments and time reversibility, TC3 and Trev) and their algorithms.

Submitted On: Oct. 31, 2012
Accepted On: Sept. 16, 2013

1054-4887 © 2013 ACES

After that, the results of Lorenz model (publicly accepted nonlinear model) are obtained as a verification of this workflow, and a set of nonlinear verification criterion are proposed. A new parameter (relative length of confidential interval, (RLCI)) to test the powerfulness of nonlinearity is proposed. Secondly, angular glint is verified by the same workflow to verify their nonlinearity. It is apparent that, considering the criterion, angular glint series possess clear nonlinear traits, which is a milestone that points out further chaotic traits of glint.

II. GLINT CALCULATION BY PHASE GRADIENT METHOD AND GRECO

A. GRECO algorithm explanation

As glint is not easily captured in radar detections, theoretical calculation and simulation methods are usually applied. In electromagnetic diffraction theories, any target with more than two scattering centers can generate angular glint. Two types of physical concept are accepted by the majority: the tilt of energy flow [8] and PGM [2], both of which are theoretical. The first is realized by the calculation of the scattering electromagnetic field energy flow; the second is more useful for actual phase measurements of angular glint. It has been verified that in isotropic media and under geometrical optics approximations, the two techniques are identical in physical nature [8].

The GRECO method was developed for RCS real time calculation, and results of several typical targets are given [9]. A similar software has been developed by us, and glint is calculated by PGM [10]. Compared with publicized results, glint calculation accuracies by GRECO are acceptable [10, 11].

In GRECO, each pixel is regarded as a scattering center and all the pixels of a target are calculated, and the angular glint is computed for the target in a trajectory [10]. The calculation setup and target is shown in Fig. 1. In the optical range, the scattering field of the target can be modeled as the vectorial sum of the echo fields of each scattering center. Let d_N be the distance between each scattering center, R and r_N are distances between the center and the radar ($R \approx r_N$), and $R >> d_N$, $R >> \lambda$, the total scattering field received can be derived as,

$$E^S = \sum_{i=0}^{N} E_n^S \exp\left[-j\left(2kr_N - \delta_N\right)\right] \tag{1}$$

where E_n^S and δ_N are the amplitude and phase of the scattering field. The relation between the incident and the scattering field is,

$$\begin{bmatrix} \mathbf{E}_1^s \\ \mathbf{E}_2^s \end{bmatrix} = \begin{bmatrix} \mathrm{Q}_{11} & \mathrm{Q}_{12} \\ \mathrm{Q}_{21} & \mathrm{Q}_{22} \end{bmatrix} \begin{bmatrix} \mathbf{E}_1^i \\ \mathbf{E}_2^i \end{bmatrix} \tag{2}$$

where 1 or 2 denotes vertical or horizontal polarization of the incident or scattering field, and [Q] is the equivalent scattering matrix given by,

$$[\mathbf{Q}] = \mathrm{e}^{\mathrm{i}\varphi_{11}} \begin{bmatrix} \sqrt{\sigma_{11}} & \sqrt{\sigma_{12}}\,\mathrm{e}^{\mathrm{i}(\varphi_{12}-\varphi_{11})} \\ \sqrt{\sigma_{21}}\,\mathrm{e}^{\mathrm{i}(\varphi_{21}-\varphi_{11})} & \sqrt{\sigma_{22}}\,\mathrm{e}^{\mathrm{i}(\varphi_{22}-\varphi_{11})} \end{bmatrix} \tag{3}$$

where $\sigma_{1,2}$ and $\varphi_{1,2}$ are the amplitude and phase of the scattering field for different polarizations. From equation (2), when the incident wave is spherical, the wave front of the scattering field is astigmatic, whose curvature is shown in [Q]. The curvature radii of the scattering fields for two polarizations are given by,

$$\frac{1}{\rho_{1,2}} = \frac{1}{2}\left[\mathrm{Q}_{11} + \mathrm{Q}_{22} \pm \sqrt{\left(\mathrm{Q}_{11} - \mathrm{Q}_{22}\right)^2 + 4\mathrm{Q}_{22}{}^2}\right]. \tag{4}$$

With the target DXF model (perfect conductor) and GRECO, the back-scattering fields are calculated using,

$$\begin{cases} \mathbf{E}_{\perp}^{\mathbf{S}} = \sum_{n=1}^{N} \left(\mathbf{e}_{\mathbf{n}\perp}^{\mathbf{i}} \bullet \mathbf{E}_{\mathbf{n}}^{\mathbf{S}} + \mathbf{e}_{\mathbf{n}\perp}^{\mathbf{i}} \bullet \mathbf{E}_{\mathbf{n}}^{\mathbf{d}}\right) \\ \mathbf{E}_{\parallel}^{\mathbf{S}} = \sum_{n=1}^{N} \left(\mathbf{e}_{\mathbf{n}\parallel}^{\mathbf{i}} \bullet \mathbf{E}_{\mathbf{n}}^{\mathbf{S}} + \mathbf{e}_{\mathbf{n}\parallel}^{\mathbf{i}} \bullet \mathbf{E}_{\mathbf{n}}^{\mathbf{d}}\right) \end{cases} \tag{5}$$

where the scattering field of the n[th] surface and the n[th] edge are represented by $\mathbf{E}_{\mathbf{n}}^{\mathbf{S}}$ and $\mathbf{E}_{\mathbf{n}}^{\mathbf{d}}$, and the total scattering field is their vectorial sum,

$$\mathbf{E}^{\mathbf{S}} = \sum_{n=1}^{N} \left(\mathbf{e}_{\mathbf{n}}^{\mathbf{i}} \bullet \mathbf{E}_{\mathbf{n}}^{\mathbf{S}} + \mathbf{e}_{\mathbf{n}}^{\mathbf{i}} \bullet \mathbf{E}_{\mathbf{n}}^{\mathbf{d}}\right). \tag{6}$$

Under the irradiation of uniformed plane or spherical wave, the beam front of the target is astigmatic, with the phase front of,

$$\phi = \frac{2\pi}{\lambda}\left\{\mathrm{R} + \frac{1}{2}[\mathrm{b}]^{\mathrm{T}}\,\mathrm{Q}(\mathbf{r})[\mathrm{b}]\right\}. \tag{7}$$

In which $[\mathrm{b}]^{\mathrm{T}} = [\mathrm{R}\theta + \mathrm{R}\varphi], [\mathrm{r}, \theta, \varphi]$ is the unit vector in spherical coordinate, Q(R) is the curvature matrix of the scattering wave. The edge and surface scattering centers are all included in GRECO simulations in this paper. The final expressions of angular glint of a complicated target can be given by using the PGM as [11],

$$\begin{cases} e_\theta = \dfrac{r(\nabla\phi)_\theta}{(\nabla\phi)_R} \\ e_\varphi = \dfrac{r(\nabla\phi)_\varphi}{(\nabla\phi)_R} \end{cases} . \quad (8)$$

From equations (7) and (8), angular glint is related not only to R, but also to the astigmatic beam front [b]. These relations are quadric surface expressions, which are typical nonlinear and different from linear differential relations. Therefore, a hypothesis that glint is nonlinear in physical nature when treated as a time series is proposed, and it is verified to be true by the surrogate data method. More importantly, nonlinear is the prerequisite for chaos by nonlinear science theories. These discussions are shown in sections 2 and 3.

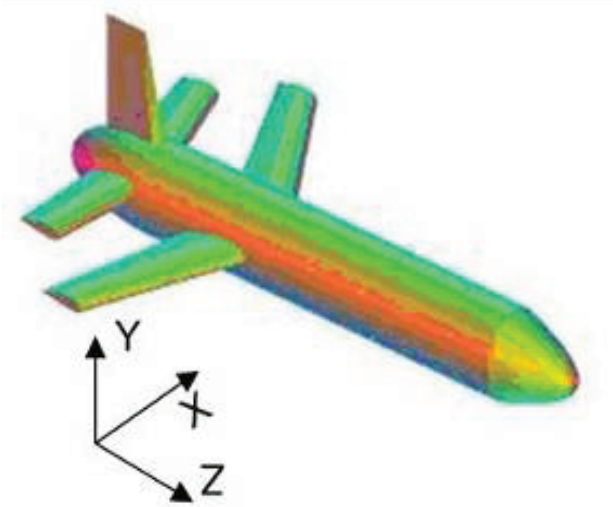

Fig. 1. Target for GRECO simulation [10].

B. Glint calculation by GRECO

The target selected is the same as in [9], and the glint of straight line motion (glint 1) is firstly simulated, which is regarded as the most common trajectory for a target. The motion diagram and results are shown in Figs. 2 and 3.

The second simulation setup is the rotary motion (glint 2), which yields much larger fluctuations in actual scattering centers than glint 1. The target moves in the orthogonal plane to the vector around the origin. The simulation setup and results are shown below in Figs. 4 and 5.

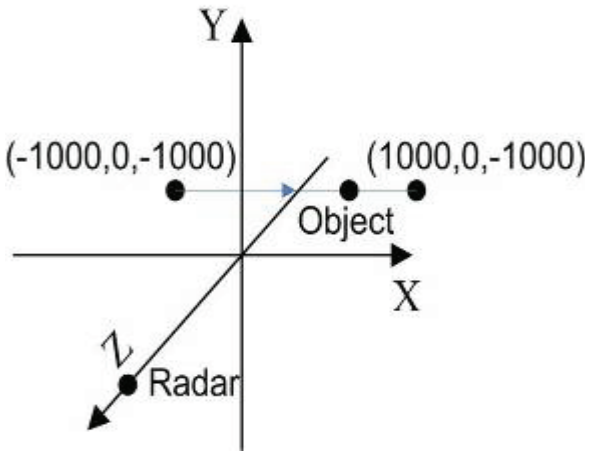

Fig. 2. Glint 1 simulation movement.

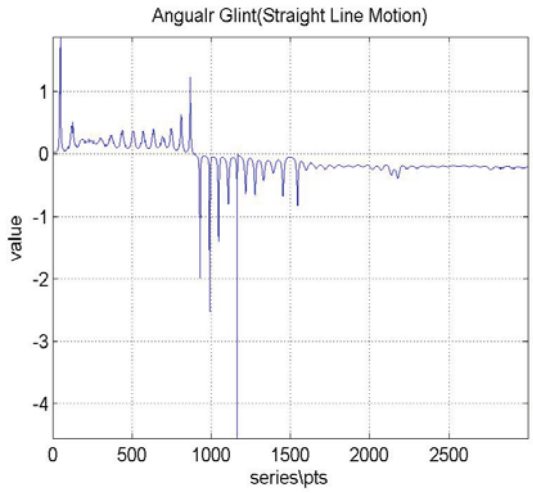

Fig. 3. Glint 1 simulation result.

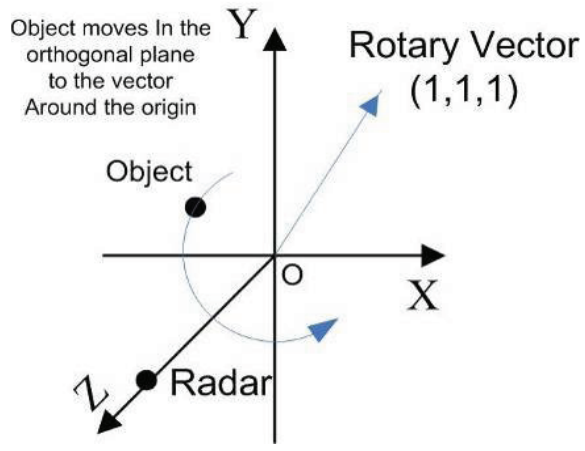

Fig. 4. Glint 2 simulation movement.

The glint simulation parameters are summarized in Table I.

Table I: Greco simulation parameters.

Motion	Straight Line	Rotary
Frequency	10 GHz	10GHz
Polarization	VV	VV
Incident Electric Field Intensity	1V/m	1V/m
Incident Direction	-Z	-Z
Calculation Plane	Azimuth	Azimuth
Glint Unit	meter	meter
Calculation Points	3600	18000

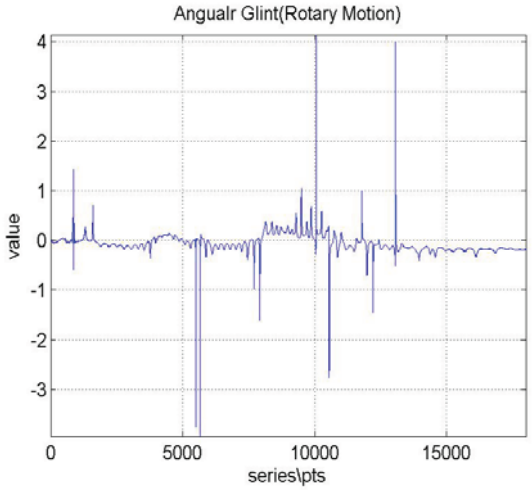

Fig. 5. Glint 2 simulation result.

III. SURROGATE DATA METHOD AND CALCULATION EXMAPLE OF LORENZ ATTRACTOR

A. Surrogate data method introduction

There are several methods to verify nonlinearity for time series. As glint calculation is done for every observation time interval in the trajectory, and can be regarded as time series. The surrogate data method can diagnose nonlinearity in noisy series and low dimension chaos, whereas typical chaotic verification approaches are unable to do so [12]. For our purpose a generalization of the typical application of this method is required. Therefore, the workflow of surrogate data method is summarized below in Fig. 6 [12].

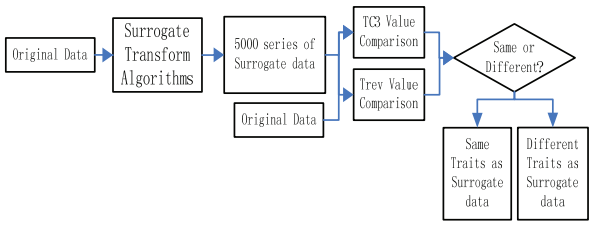

Fig. 6. Surrogate data method work flow.

The general operation of surrogate data workflow is summarized as:

1) Linear stochastic algorithms are designed (phase randomized Fourier transform and amplitude adjusted Fourier transform, PRFT and AAFT), and the original data (Lorenz or glint data) are calculated with these methods to generate a large number of surrogate data.

2) The original data and surrogated data series are measured by two statistical parameters, higher order moments and time reversibility (TC3 and Trev), whose types are specially selected for powerful nonlinear detections.

3) If the values of these parameters for original and surrogated data are notably different, the original data is nonlinear; if not, the data is linear [12]. Moreover, the powerfulness of nonlinearity is clarified by the RLCI, which is a newly proposed parameter.

B. Surrogate data generation

As angular glint is derived from nonlinear differential expressions, it is assumed that angular glint is powerfully nonlinear. For surrogate data generation, two typical algorithms to distinguish powerful nonlinear are applied: the first is PRFT (method 1) [13]. Given a time series x(t) of N values sampled by regular interval times Δt, the discrete Fourier transform can be written as,

$$X(f) = \mathcal{F}\{x(t)\} = \sum_{N=0}^{N-1} x(t_N) e^{2\pi i f n \Delta t} = A(f) e^{i\phi(f)}. \quad (9)$$

Then a random phase, which is chosen uniformly from [0, 2π] is added to the phase, and the surrogate data is given by equation (10), and this result has the same power spectrum and autocorrelation function as the original data.

$$X'(f) = F^{(-1)}(A(f) e^{i\phi(f)+i\varphi(f)}) = F^{(-1)}(X(f) e^{i\phi(f)})). \quad (10)$$

The second surrogate generation method is AAFT

(method 2) [13]. It is assumed that h is a nonlinear transform and is monotonic. Firstly h^{-1} is simulated by reordering normal white noise to the rank of x(t), then any possible nonlinear dynamics are destroyed by phase randomization (derived data set y^{FT}). Finally, h is simulated by reordering the original data to the rank order of y^{FT}.

C. The selections of test statistics

After the surrogate data have been generated, nonlinearity verification can be conducted by comparing the statistical verification parameters of the original data and the surrogate data. The two statistical parameters of TC3 and Trev are selected for powerful nonlinear diagnosis [14-16],

$$\mathrm{TC3}\left(\{x_n\},\tau\right)=\frac{\left\langle\left(x_n x_{n-\tau} x_{n-2\tau}\right)\right\rangle}{\left|\left\langle x_n x_{n-\tau}\right\rangle\right|^{\frac{3}{2}}} \tag{11}$$

$$Trev(\{x_n\},\tau)=\frac{\left\langle(x_n-x_{(n-\tau)})^3\right\rangle}{\left\langle(x_n-x_{(n-\tau)})^2\right\rangle^{(3/2)}}, \tag{12}$$

where the time lag τ is chosen by the first minimum value of the auto mutual information function of $\{x_n\}$, and $\langle x\rangle$ denotes mean values.

D. Calculation example of Lorenz attractor

The Lorenz attractor can be calculated by [14],

$$\begin{cases}\dfrac{dx}{dt}=-\sigma(y-x)\\ \dfrac{dy}{dt}=-xz+rx-y\\ \dfrac{dz}{dt}=xy-bz\end{cases}. \tag{13}$$

The time step is chosen as 0.025, and the constants σ, r, b are set as 0.1, -0.1, and 0.02, data length is 18000 and the x axis series is simulated, as shown in Fig. 7. The test statistics comparisons are shown in Fig. 8.

TC3 values are shown as appearance probability (y-axis) versus TC3 values (x-axis) in Fig. 8, and for the surrogate data (blue bars) and for original Lorenz data (red bar). Similar results are shown in Fig. 9 for AAFT surrogate method. The surrogate data method test results of Lorenz attractor are summarized in Table II. Also, the RLCIs and the overall length of all test statistical values are given. Their explanations are given in the next section.

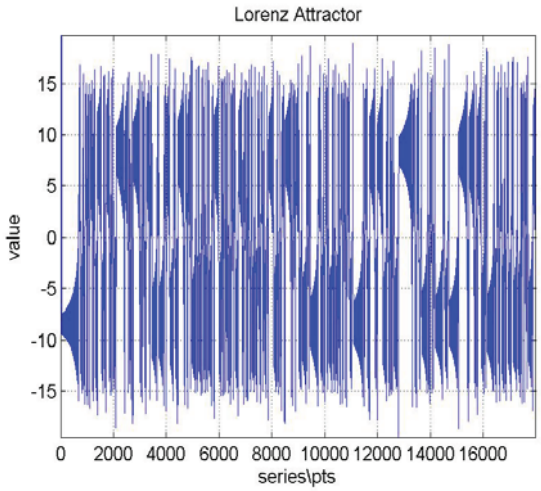

Fig. 7. Lorenz surrogate data (x series).

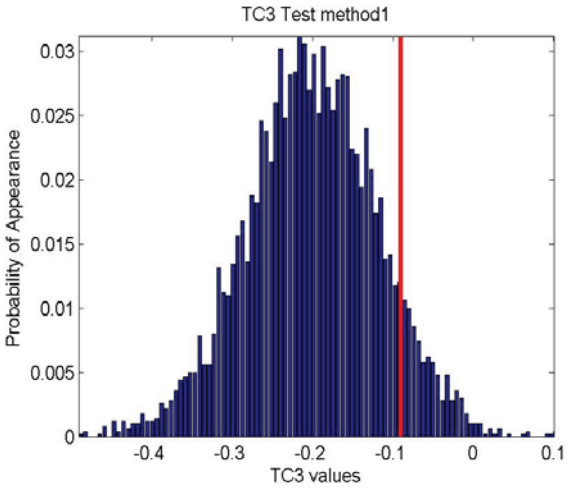

Fig. 8. Lorenz surrogate data test (PRFT, TC3).

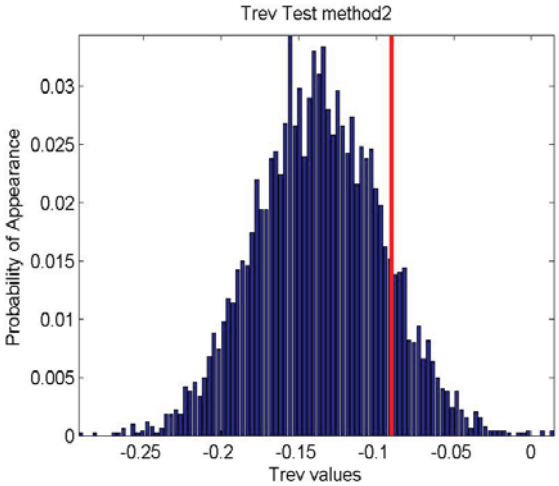

Fig. 9. Lorenz surrogate data test (AAFT, Trev).

Table II: Surrogate data results for Lorenz.

Surrogate Method	**PRFT**		**AAFT**	
Test Statistic	TC3	Trev	TC3	Trev
Test Statistic Value (Original Data)	-0.09	-0.08	-0.09	-0.08
Confidential Interval	-0.16~ -0.26	-0.16~ -0.25	-0.12~ -0.17	-0.12~ -0.17
RLCI	□□□ □□	□□□ □□	14.3%	16.7%

Table III: Surrogate tests for straight-line glint.

Surrogate Method	**PRFT**		**AAFT**	
Original Data	**Straight-Line Glint**			
Test Statistic	TC3	Trev	TC3	Trev
Value (Original Data)	-0.46	-0.44	-0.44	-0.45
Confidential Interval	-0.90~ -0.71	-0.90~ -0.78	-0.90~ -0.58	-0.98~ -0.52
RLCI	□□□ □	□□□ □	8.3%	12.4%

Table IV: Surrogate tests for rotary glint.

Surrogate Method	**PRFT**		**AAFT**	
Original Data	**Straight-Line Glint**			
Test Statistic	TC3	Trev	TC3	Trev
Value (Original Data)	-0.61	-0.60	-0.60	-0.58
Confidential Interval	-1.30~ -0.91	-1.40~ -0.90	-0.90~ -0.70	-1.00~ -0.70
RLCI	□□□ □□	□□□ □□	8.1%	10.2%

E. Nonlinear verification criterion

From canonical references and Lorenz model, the verification criteria for powerful nonlinearity are concluded as [15-17]:

1) The test statistics values of the original data are different from the values of surrogated data, or more precisely, they fall outside the confidence intervals of the values of surrogated data. The boundary of intervals can be determined by a probability range (in this case ≥ 0.025).

2) The RLCI defined in equation (13) are in inverse ratio of the intensity of nonlinearity. If the RLCI values are smaller than the results of Lorenz model (shown in Table II), it can be determined that they are more powerfully nonlinear than Lorenz,

$$\mathrm{RLCI} = \frac{\mathrm{length(confidence\ interval)}}{\mathrm{length(all\ values)}}. \qquad (14)$$

It can be seen from Table II that TC3 and Trev values of the Lorenz data all fall outside the surrogate data confidence intervals. Also, the RLCI values are shown. The results show that Lorenz data are powerfully nonlinear, and agree with common sense in nonlinear science.

IV. NONLINEAR VERIFICATION OF ANGULAR GLINT SERIES BY SURROGATE DATA METHOD

The glint data simulated in Figs. 3 and 4 are verified by the surrogate data test workflow of Fig. 6. The test statistics comparisons of the straight line motion glint are shown in Fig. 10, and similar results are shown in Fig. 11 for rotary motion glint. The two surrogate test results are also summarized in Tables III and IV.

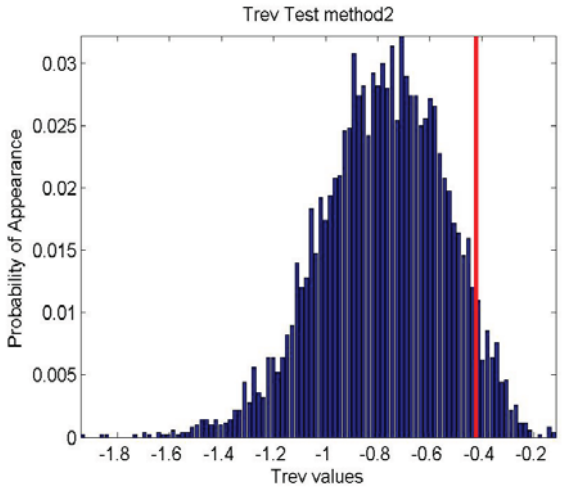

Fig. 10. Glint 1 surrogate data test (AAFT, Trev).

It can be observed that even by a narrower confidence interval boundary of probability 0.02, large differences are still clearly observed among the straight line motion glint and its surrogated data sets. In other words, the statistics values of the straight line glint fall outside the confidence intervals. Also, the RLCI values of straight line glint are smaller than Lorenz model. For rotary glint, all the TC3 and Trev values fall outside the confidence intervals of its surrogate data sets, and the RLCI values are also smaller than Lorenz.

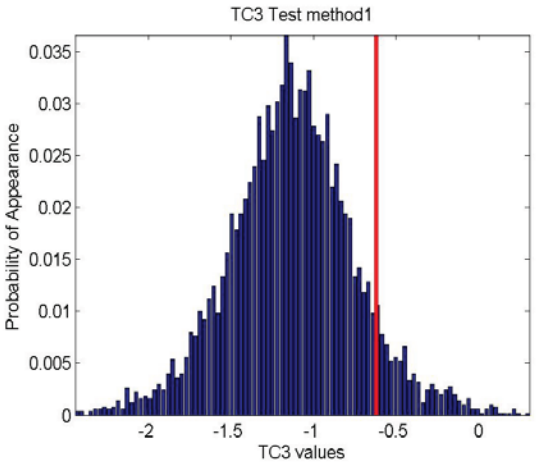

Fig. 11. Glint 2 surrogate data test (PRFT, TC3).

Therefore, considering the nonlinear verification criterion stated above, both straight line glint and rotary motion glint have been proved to possess powerful nonlinear traits, even more powerful than Lorenz model, which is a prerequisite for chaotic verifications. If angular glint is proved to be chaotic, then corresponding prediction and suppression techniques can be applied in the DSP unit of radar receivers. By these techniques, target information errors caused by angular glint can be lowered.

V. CONCLUSION

In this paper, the nonlinearity of radar angular glint is verified by the surrogate data method. Firstly, two angular glint series of a typical target are calculated by the Greco method. Secondly, the fundamentals of surrogate data method and its work flow are stated, and the nonlinearity verification criteria are demonstrated. A new verification parameter (RLCI) is proposed, and the effectiveness of this method is proved by Lorenz model. Finally, the nonlinearity traits of angular glint are proved by comparisons with the Lorenz model results and the verification criteria with all the details of nonlinear verifications are given and analyzed.

Nonlinearity is the first milestone in verifying the chaotic traits of angular glint. If nonlinearity is not proved, chaotic verification is meaningless. Even if chaos is proved without nonlinearity proof, it is not persuasive. After the nonlinear verification of angular glint, several preliminary chaotic verifications of angular glint series have been proposed with clear chaotic traits [18]. In chaotic science theories, if a time series is chaotic, then there are several ways to perform predictions and oscillation reductions. As angular glint is harmful for effective detection and could cause target loss, its predictions and reductions are critical in the radar signal processing. Therefore, the research results in this paper are nontrivial.

REFERENCES

[1] D. Howard, "Radar target glint in tracking and guidance system based on echo signal phase distortion," *Proc. of NEC*, pp. 840-849, May 1959.

[2] J. Lindsay, "Angular glint and the moving, rotating, complex radar target," *IEEE Trans. on Aerospace and Electronics Systems*, vol. 4, pp. 164-173, March 1968.

[3] J. Dunn and D. Howard, "Radar target amplitude angle and Doppler scintillation from analysis of the echo signal propagating in space," *IEEE Trans. on Microwave Theory and Techniques*, vol. 16, no. 9, pp. 715-728, Sep. 1968.

[4] R. Sinm and E. Graf, "The reduction of radar glint by diversity techniques," *IEEE Trans. on Antenna and Propagation*, vol. 19, no. 4, pp. 462-468, 1971.

[5] R. Ostrovityanov and F. Basalov, *Statistical Theory of Extended Radar Targets*, Translated from Russian (Barton. W. F, Barton. D. K), MA: Artech House, Ch. 1-Ch. 3, 1985.

[6] G. Stadhu and A. Saylor, "A real-time statistical radar target model," *IEEE Trans. on Aero . and Electro. Systems*, vol. 21, no. 4, pp. 490-507, 1985.

[7] H. Yin, S. Deng, R. Yingzheng, et al, "On the derivation of angular glint from backscattering measurements of each relative phase," *Acta Electronica Sinica*, vol. 9, pp. 36-40, 1996 (in Chinese).

[8] H. Yin and P. Huang, "Unification and comparison between two concepts of radar target angular glint," *IEEE Trans on Aer ospace and Electronics Systems*, vol. 31, no. 2, pp. 778-783, 1995.

[9] M. Juan, M. Ferrando, and L. Jofre, "GRECO: graphical electromagnetics computing for RCS

prediction in real time," *IEEE Antennas and Propagation Magazine*, vol. 35, no. 2, April 1993.
[10] Q. Dehua, *All-band Electromagnetic Scattering Computation for Complex Targets: Method Studies and Application Software*, Ph.D Dissertation, Dept. Elect. Eng., Beijing Univ. of Aerosnautics and Astronatics, Beijing, P. R. China, 2004 (in Chinese).
[11] N. Huansheng, F. Ning, and W. Baofa, "Visual computing method of radar glint for complex target," *Chinese Journal of Electronics*, vol. 15, no. 2, pp. 356-358, 2006 (in Chinese).
[12] D. Prichard, "Generating surrogate data for time series with several simultaneously measured variables," *Physical Review Letters*, vol. 73, no. 7, August 1994.
[13] D. Kugiumtzis, "Surrogate data test for nonlinearity including nonmonotonic transforms," *Physical Review E*, vol. 62, no. 1, pp. 25-28, July 2000.
[14] C. Merkwirth, U. Parlitz, et al. "TSTOOL User Manual," Version 1.11, 2002.4.[2011.10.13].
[15] T. Schreiber and A. Schmitz, "Surrogate time series," *Physica D*, vol. 142, pp. 346-382, 2000.
[16] J. Theiler, et al, "Using surrogate data to detect nonlinearity in time series in: nonlinear modeling and forecasting SFI studies in the sciences of complexity," vol. 7, Reading, MA: Addospm-Wesley, pp.163-188.
[17] D. Kugiumtzis, "Statically transformed autoregressive process and surrogate data test for nonlinearity," *Physical Review E* , vol. 66, 025201(R), 2002.
[18] J. Zhang and J. Miao, "The verification of chaotic characteristics of radar angular glint," *Progress in Electromagnetic Research B*, vol. 43, pp. 295-311, 2012.

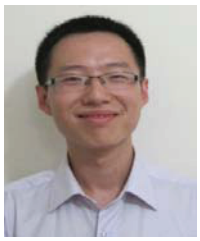

Jin Zhang was born in Beijing, P. R. China, in 1985. He received his B.S and M.S degrees from school of electronic and information engineering, Beijing University of Aeronautics and Astronautics, in 2007 and 2010. He is now pursuing for his Ph.D degree in the same institute, and majors in radar and radiometer system design.

He is interested in radar detection and target characteristic researches, and is also engaged in developing synthetic aperture interferometric radiometer imagers, which are applied in security checks. He is also doing researches in millimeter-wave FOD radar designs, in the lab of electromagnetic engineering. He has published 5 papers in the areas of radar target glint, radiometer imager design and FOD radar theories and applications.

Zhiping Li was born in 1982, in Shandong province, P. R. China. She received her B.S degree in Northwestern Polytechnic University in Shan'Xi province, and her Ph.D degree from school of electronic and information engineering, Beijing University of Aeronautics and Astronautics in 2010. She is now working as a teacher and tutor of M.S in the lab of electromagnetic engineering.

She is interested in radar system design, remote sensing and synthetic aperture interferometric radiometer and imager design and related theories and applications, especially in RCS and black body theories. She has published 8 papers in related areas.

Cheng Zheng was born in 1983, in Beijing, P. R. China. He received his B.S degree in 2006 from school of electronic and information engineering, Beijing University of Aeronautics and Astronautics, and now is pursuing his Ph.D degree in the same institute, and majors in radar and radiometer system design.

He is interested in radar system design, remote sensing and synthetic aperture interferometric radiometer and imager design and related theories and applications, especially in digital signal processing researches of these systems. He has published 4 papers in radar system, radiometer theory and digital signal processing areas.

Jungang Miao was born in 1963, in Hebei province, P. R. China. He received his B.S in 1982, in the National Defense University in Hunan province, and received his Ph.D in Bremen University, Germany, in 1998. He worked as a Professor in the remote sensing research institute of Bremen University until 2003, when he came to school of electronic and information engineering, Beijing University of Aeronautics and Astronautics. He works as a Professor and head of electromagnetic engineering lab up to the present.

He is interested in microwave and millimeter-wave radiation, diffraction and near-field detection, remote sensing, radar system, signal processing, antenna and electromagnetic calculations, and has published more than 50 papers in international journals and conferences.

Microstrip Patch Antenna Covered With Left Handed Metamaterial

E. Dogan[1], E. Unal[1], D. Kapusuz[1], M. Karaaslan[1], and C. Sabah[2]

[1] Department of Electrical and Electronics Engineering
University of Mustafa Kemal, 31200, Iskenderun, Hatay, Turkey
esradogan0688@gmail.com, eunal@mku.edu.tr, dilekkapusuz@gmail.com, mkaraaslan@mku.edu.tr

[2] Department of Electrical and Electronics Engineering, Middle East Technical University - Northern Cyprus Campus, Kalkanli, Guzelyurt, TRNC / Mersin 10, Turkey
sabah@metu.edu.tr

Abstract ─ We present gain characteristics of microstrip patch antennas covered with metamaterial substrate composed of split-ring resonators (SRRs) and metallic strip. To determine the performance of the SRR-metallic strip mounted on microstrip patch antenna, the metamaterial has been proposed as an effective medium with extracted constitutive parameters. Simulation results are supported by experimental measurements. The experimental results confirm that the metamaterial covered patch antenna improves gain by an amount of -5.68 dB (% 60.3) as well as radiation pattern (-8 dB to +20 dB) at WLAN communication.

Index Terms - Effective parameters, FDTD, gain, patch antenna, metamaterial, and split ring resonator.

I. INTRODUCTION

Microstrip patch antenna is one of the most commonly used antenna in portable communication devices due to compact, conformal, low cost, and ease of fabrication properties. Although it offers many advantages as mentioned, it has some disadvantages, which result from conductor and dielectric losses. Beside this, gain reduction and poor directionality are also observed in this antenna due to surface waves [1]. Conductor and dielectric losses can be minimized by using perfect conductor and low loss dielectric substrate, but these choices result in higher fabrication cost. Gain, bandwidth enhancement, miniaturization, and broadband directionality can be provided by using metamaterial structures [2-6].

Metamaterials are man-made structures designed to have properties that may not be found in nature. These structures may have both negative effective permittivity and permeability at the same frequency range. It provides negative effective refractive index over a certain frequency region(s) [7]. These properties of metamaterial provide novel application opportunities to several disciplines, such as microwave and optical cloaking, focusing of images, and sensing of biological and chemical substances.

Metamaterials have also many application areas for novel antenna systems [8-11]. One of the important applications of metamaterials is miniaturization of the microstrip antennas with different types of artificial materials. The conventional way of reducing the antenna size is to use high permittivity substrate. This approach reduces the wavelength of the signal in the substrate [12]. But, this design results in more energy consumption due to high permittivity, since it decreases the impedance bandwidth of the antenna. Another way is removing the substrate to minimize the effective dielectric constant. This application restricts the wave to travel in the substrate, hence, improving the gain of the patch antenna has been possible [13, 14]. However, the maximum gain enhancement does not exceed to 2 dB with all these techniques and the directionality also does not change too much. Hence, many different solutions have been proposed to overcome these problems, such as utilization of metamaterials with patch antenna [15-18].

Submitted On: Feb. 21, 2013
Accepted On: Oct. 31, 2013

1054-4887 © 2013 ACES

This article describes a novel way to enhance both the gain and directionality of patch antenna used for WLAN applications. Split-ring resonators (SRRs) responsible for negative permeability and metal strip responsible for negative permittivity are used to improve both gain and directionality of patch antenna. The effective permittivity of the strip and the permeability of SRRs were evaluated by using both finite element method (FEM) based high frequency structure simulator (HFSS) and finite difference time domain method (FDTD) based computer simulation technique (CST). The dimensions of the inclusions (SRRs and strip) were optimized to realize negative values for the constitutive parameters at the operating frequency of the antenna. SRRs and metal strips were fabricated with optimum dimensions to provide negative constitutive parameters at 2.4 GHz. The fabricated metamaterial was mounted on microstrip patch antenna to observe the effects on it. The measurement results are in good agreement with simulation data. It has been noticed that the metamaterial considerably enhances the gain of the patch antenna.

II. METAMATERIAL DESIGN AND CONSTITUTIVE PARAMETERS

Figure 1 illustrates the front and the back side of metamaterial structure, which consists of both circular SRR and metallic strip (MS). The combined structure was designed on two sides of 10 mm × 10 mm × 1.6 mm FR4-epoxy ($\varepsilon_r = 4.4$, $\mu_r = 1$, and dielectric loss tangent $\tan\delta = 0.02$). While SRR produce a response like magnetic materials and exhibit negative permeability, MS acts as a strong dielectric structure and exhibits negative permittivity[19].

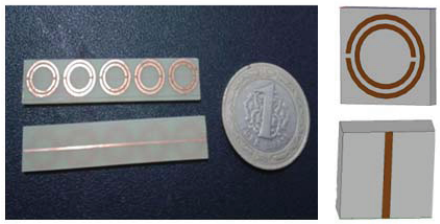

Fig. 1. Front and back view of metamaterial.

All the dimensions of the SRR and MS are optimized by HFSS to achieve negative permittivity and permeability at 2.4 GHz. The TEM wave is applied to the metamaterial. E-field is applied parallel to the MS and H-field is applied normal to the plane of SRR. It means that the system has directional dependency. The periodicity of one unit cell with SRR-MS was obtained by assigning perfectly electric conductor-PEC (side normal to E-field) or perfectly magnetic conductor-PMC (side normal to H-field) to the sides of the unit cell. The constitutive parameters were evaluated from the scattering parameters (S_{11} and S_{21}) by using Nicolson Ross Weir (NRW) approximation [20, 21],

$$z = \sqrt{\frac{(1+S11)^2 - S21^2}{(1-S11)^2 - S21^2}} \quad (1)$$

$$n = \frac{j}{kod}\ln\left(\frac{S21}{1-S11\frac{z-1}{1+z}}\right) \quad (2)$$

$$\varepsilon_{eff} = n/z \; ; \; \mu_{eff} = n.z \quad (3)$$

where z, d, and k_0 represent the impedance, thickness of the metamaterial, and free space wave number, correspondingly. The effective permittivity, permeability, and refractive index are denoted by ε_{eff}, μ_{eff}, and n, respectively. The simulations are realized up to 6 GHz. All of the electromagnetic constitutive parameters are negative at 2.4 GHz. Hence, this structure can be used as negative refractive index metamaterial with patch antenna operating at this frequency as shown in Fig. 2.

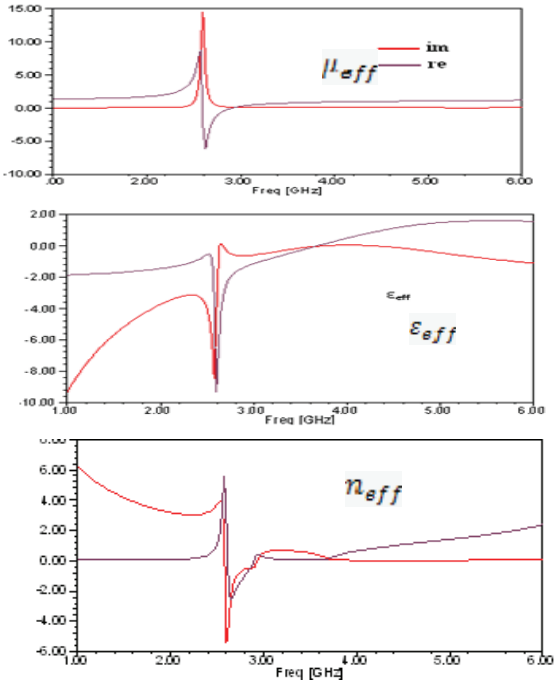

Fig. 2. Effective parameters of metamaterial.

Microstrip patch antenna was fabricated to operate at frequency range in which permittivity and permeability of metamaterial utilized with this antenna are negative. In this study, the frequency of 2.4 GHz is chosen for the operating frequency of microstrip patch antenna in which specifications are shown in Table 1.

Table 1: Dimensions of patch antenna on FR4 laminate.

Parameter	**Magnitude**	**Unit**
Operating frequency	2.4	GHz
Patch length(L)	59	mm
Patch Width(W)	42.4	mm
Laminate length (Lg)	75	mm
Feed	coaxial	-
Laminate Thickness	1.6	mm

The microstrip patch antenna was fabricated on an FR4 substrate ($\varepsilon_r = 4.4$, $\mu_r = 1$, and dielectric loss tangent $\tan\delta = 0.02$). The evaluated results were obtained by HFSS and CST simulators and measured results of microstrip patch antenna without metamaterial are shown in Fig. 3. Return loss measurement was realized by using ENA Series Network Analyzer (E5071B). While return loss (gain value) $-S_{11}$ value of the patch antenna is -13.68 dB in HFSS and -16.64dB in CST, measured value is only -9.42 dB. The difference between measured and simulated values of the antenna results from measurement errors and fabrication process.

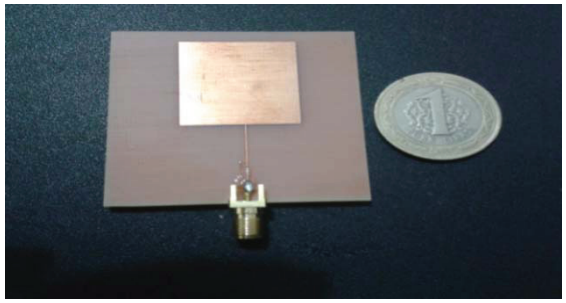

S11	HFSS	CST	Measurement
Patch Antenna	-13.68dB	-16.64 dB	-9.42 dB

Fig. 3. Microstrip patch antenna without metamaterial and return losses in dB.

Effect of the metamaterial on the return loss of the microstrip patch antenna was investigated by placing metamaterial on it. The SRR-MS structure was fabricated to obtain negative constitutive parameters at 2.4 GHz and it was periodically mounted on microstrip antenna as shown in Fig. 4.

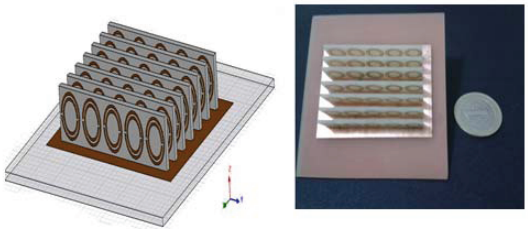

Fig. 4. Fabrication of patch antenna-metamaterial system.

The direction of the metamaterial is important to improve the gain of the patch antenna, since the metamaterial has anisotropic behavior. Therefore, they were mounted such that center of SRR is parallel to H-field and MT is parallel to E-field direction of the antenna. The distance between the periodically arranged metamaterials was 2 mm. The simulated and measured results of microstrip patch antenna covered with metamaterial are shown in Fig. 5. While the return loss decreases down to -20.27 dB in HFSS simulation and -23.33 dB in CST simulation, it was observed -15.1 dB in measurement at 2.4 GHz. This means 60.3 % enhancement of the antenna gain (return loss) with respect to antenna without metamaterial. The enhancement results of antenna with and without metamaterial is indicated in Table 2. Good gain improvement (return loss) is obtained for all of HFSS-CST and measurement results. Although, measured return loss (S_{11}) of the patch antenna with metamaterial indicates several modes at different frequencies as shown in Fig. 5 (c), but these modes are not sufficient to mention about new extra radiation frequencies. Since the return losses of these extra modes are higher than -10 dB.

Table 2: Comparison of simulation and measurement results of return loss (S_{11}).

	HFSS	CST	Measurement
without MTM	-13.6812 dB	-16.64 dB	-9.42 dB
with MTM	-20.2712 dB	-23.33 dB	-15.1 dB
Gain	-6.59 dB	-6.69 dB	-5.68 dB

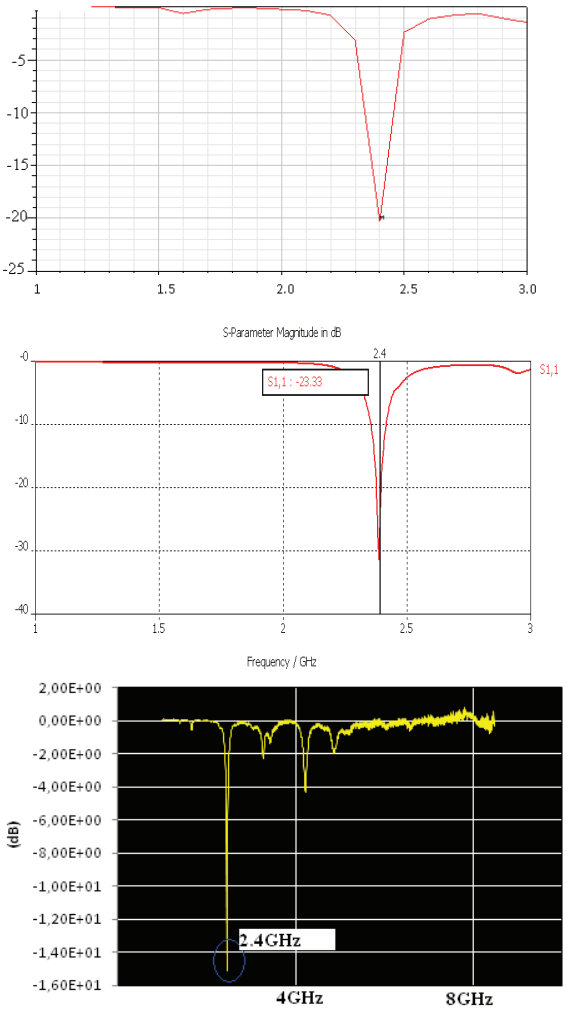

Fig. 5. (a) HFSS simulation, (b) CST simulation, and (c) measurement results of patch antenna with metamaterial.

It is well known that the radiation pattern of the antenna with and without metamaterial give exact idea about the gain of the antenna system, since the return loss (S_{11}) is not enough alone to decide the antenna performance. The radiation patterns of the patch antenna with and without metamaterial are evaluated by HFSS as shown in Figs. 6 and 7. The radiation patterns of H-plane are simulated at every 30^0 between $0^0/180^0$. Although the maximum radiation gain of the antenna without metamaterial is -8 dB (Fig. 7), it reaches up to +20 dB for antenna with metamaterial (Fig. 6). These exhibits that metamaterial doesn't only provide minimization of return loss (S_{11} value) but also gives a chance to enhancement of the antenna gain.

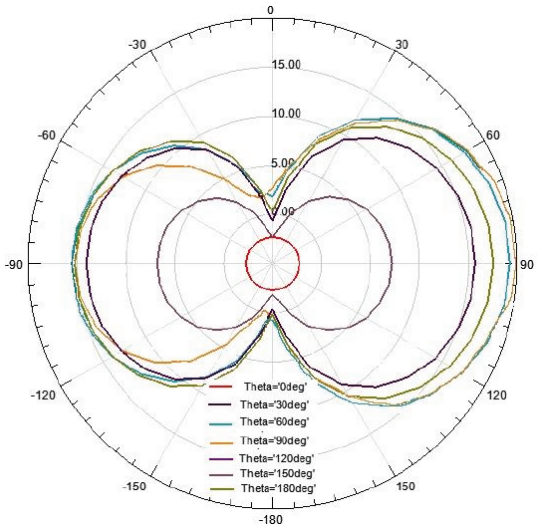

Fig. 6. HFSS simulation of radiation pattern of patch antenna with metamaterial.

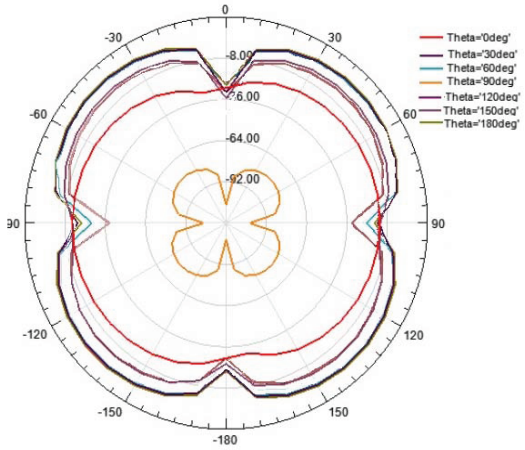

Fig. 7. HFSS simulation of radiation pattern of patch antenna without metamaterial.

Beside the simulations of radiation pattern, some measurements were also realized to observe the effect of metamaterial on patch antenna by using MATS1000. The HFSS simulation for patch antenna without metamaterial and measurement result for patch antenna with metamaterial are shown in Fig. 8. Two different antennas were used at the measurements. One of them is metamaterial mounted patch antenna and the other one is ring antenna to observe the radiation pattern of H-plane. Whereas simulation result of H-plane radiation gain is around -72 dB, measurement result is much better (-47.5 dB). These results indicate the enhancement of antenna radiation gain due to the metamaterial.

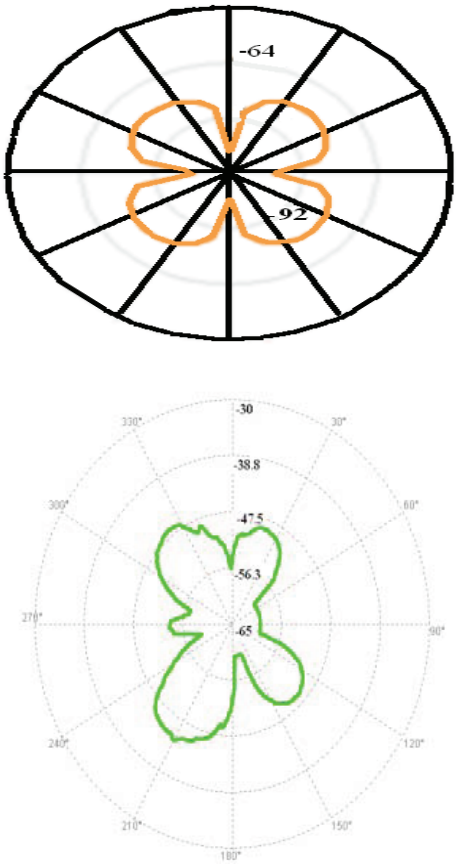

Fig. 8. Simulation and measurement radiation pattern results of patch antenna without and with metamaterial (H-plane).

III. CONCLUSIONS

In this study, simulation, fabrication, and measurement are investigated for microstrip patch antenna covered with metamaterial composed of SRR and MS. The results show that good improvement in the antenna characteristics in terms of gain is achieved. The gain of the microstrip patch antenna with metamaterial is increased by 6.69 dB from simulation and 5.68 dB from measurement. It can be concluded that microstrip patch antenna based on metamaterial exhibits improvement on the antenna gain performance. Therefore, metamaterials provide potential application areas to antenna researchers, such as improvement of the gain or radiation properties of any type of antenna.

REFERENCES

[1] R. Waterhouse, *Microstrip Patch Antennas—A Designer's Guide*, Kluwer Academic Publishers, Boston, MA, 2003.

[2] M. Palandoken, A. Grede, and H. Henke, "Broadband microstrip antenna with left-handed metamaterials," *IEEE Trans. Antennas Pr opag.*, vol. 57, pp. 331-338, 2009.

[3] S. Burokur, M. Latrach, and S. Toutain, "Theoretical investigation of a circular patch antenna in the presence of left-handed mematerial," *IEEE Antennas Wirel. Propag. Lett*. vol. 4, pp. 183-186, 2005.

[4] T. Liu, X.-Y. Cao, J. Gao, Q. Yang, and W.-Q. Li, "Design of miniaturized broadband and high gain metamaterial patch antenna," *Microwave Opt. Technol. Lett.*, vol. 53, pp. 2858-2861, 2011.

[5] M. Veysi and A. Jafargholi, "Directivity and bandwidth enhancement of proximity-coupled microstrip antenna using metamaterial cover," *Applied Computational Electromagnetics Society (ACES) Journal*, vol. 27, no. 3, pp. 261-270, March 2012.

[6] A. Jafargholi and M. Kamyab, "Dipole antenna miniaturization using single-cell metamaterial," *Applied Computational Electromagnetics Society (ACES) Journal*, vol. 27, no. 3, pp. 261-270, March 2012.

[7] R. Ziolkowski, "Double negative metamaterial design, experiment and applications," *IEEE Trans. Microwave Theory Tech.*, vol. 51, pp. 396-399, 2003.

[8] J. Liu, W. Shao, and B. Wang, "A dual-band metamaterial design using double SRR structures," *Applied Computational Electromagnetics Society (ACES) Journal*, vol. 26, no. 6, pp. 459-463, June 2011.

[9] M. Tang, S. Xiao, D. Wang, J. Xiong, K. Chen, and B. Wang, "Negative index of reflection in planar metamaterial composed of single split-ring resonators," *Applied Computational Electromagnetics Society (ACES) Journal*, vol. 26, no. 3, pp. 250-258, March 2011.

[10] W. Abdouni, A-C. Tarot, and A. Sharaiha, "Realization of a compact patch antenna over an artificial magneto-dielectric substrate," *24th Annual Review of Progressin Applied Computational Electromagnetics (ACES)*, pp. 149-152, Niagara Falls, Canada 2008.

[11] C. Fazi, S. Shi, I. Mirza, and D. Prather, "Split ring resonator slab modeling for a metamaterial loaded loop antenna," *23rd Annual Review o f Progress in Applied Computational Electromagnetics (ACES)*, pp. 117-122, Verona, Italy, March, 2007.

[12] Z. Szabo, G. Park, R. Hedge, and E.-P. Li, "A unique extraction of metamaterial parameters based on kramers–kronig relationship," *IEEE Trans. Microwave The ory Tech.*, vol. 58, pp. 2646-2653, 2010.

[13] Y. Lo, "Theory and experiment on microstrip antennas," *IEEE Trans. Antennas Propag.*, vol. 27 pp. 137-145, 1979.
[14] R. Hwang and S. Peng, "Surface-wave suppression of resonance- type periodic structures," *IEEE Trans. Antennas Propag.*, vol. 51, pp.1221-1229, 2003.
[15] S. Yeap and Z. Chen, "Microstrip patch antennas with enhanced gain by partial substrate removal," *IEEE Trans. Antennas Propag.*, vol. 58, pp. 2811-2816, 2010.
[16] J. Colburn and Y. Rahmat-Samii, "Patch antennas on externally perforated high dielectric permittivity material," *Electron Lett.* vol. 31, pp. 1710-1712, 1995.
[17] H. Mosallaei and K. Sarabandi, "Antenna miniaturization and bandwidth enhancement using a reactive impedance substrate," *IEEE Trans. Antennas Propag.*, vol. 52, no. 52, pp. 2403-2414, 2004.
[18] P. Ikonen, S. Maslovski, and S. Tretyakov, "PIFA loaded with artificial magnetic material: Practical example for two utilization strategies," *Microwave Opt. Technol. Lett*., vol. 46, no. 46, pp.554-556, 2005.
[19] P. Ikonen, S. Maslovski, C. Simovski, and S. Tretyakov, "On artificial magneto dielectric loading for improving the impedance bandwidth properties of microstrip antennas," *IEEE Trans. Antennas Propag.*, vol. 54, pp. 1654-1662, 2006.
[20] A. Nicolson and G. Ross, "Measurement of the intrinsic properties of materials by time domain techniques," *IEEE Trans. on Instrum. and Measur.*, vol. 19, pp. 377-382, 1970
[21] W. Weir, "Automatic measurement of complex dielectric constant and permeability at microwave frequencies," *Proceedings of the IEEE* , vol. 62, no. 62, pp. 33-36, 1974.

EsraDoğan received the B.S degree in Electrical – Electronics Engineering from Mustafa Kemal University in 2010 and M.S degree from Mustafa Kemal University,Hatay in Electrical Electronics Engineering in 2012. She has worked as lecturer in Mustafa Kemal University. Her current research interests are left hand metamaterial, metamaterial antenna design, metamaterial antenna applications, antenna design and testing, antenna arrays and numerical methods.

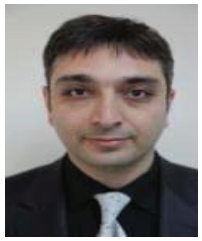

Muharrem Karaaslan received the PhD degree in Physics Department from University ofÇukurova, Adana,Turkey, in 2009. He is the coauthor of about 20 scientific contributions published in international journals and peer-reviewed conference proceedings. His research interest includes the applications of metamaterials in the analysis andsynthesis of antennas, waveguides and textile.

EminÜnal received the PhD degree in Electrical and Electronics Engineering from University of Gaziantep, Turkey, in 1994. He is the coauthor of about 20 scientific contributions published in international journals and peer-reviewed conference proceedings. His research interest includes Frequency selective surfaces and metamaterials.

DilekKapusuz received the associate degree in Industrial Electronics Department from 9 Eylül University, İzmir, Turkey,in 2001, and B.S degree as an Electronics Teacher in Electronics and Computer Education Department from Kocaeli University Technical Education Faculty, Kocaeli ,Turkey, in 2007. She has carried out some studies on SRR Structures and Metamaterials as to present her Certificate of Completion Project between the years of 2005-2006. Also a conference paper of her on Multi-strip monopole antenna for UWB applications has been approved and published in IEEE Signal Processing and Communications Applications Conference that took place, Mugla, Turkey, in April in 2012.

Cumali Sabah received the B.Sc., M.Sc., and Ph.D. degrees in electrical and electronics engineering from the University of Gaziantep, Turkey. He is currently with Middle East Technical University - Northern Cyprus Campus. His research interests include the microwave and electromagnetic investigation of unconventional materials and structures, wave propagation, scattering, complex media, metamaterials and their applications.

2013 INSTITUTIONAL MEMBERS

DTIC-OCP LIBRARY
8725 John J. Kingman Rd, Ste 0944
Fort Belvoir, VA 22060-6218

AUSTRALIAN DEFENCE LIBRARY
Northcott Drive
Canberra, A.C.T. 2600 Australia

BEIJING BOOK CO, INC
701 E Linden Avenue
Linden, NJ 07036-2495

DARTMOUTH COLLEGE
6025 Baker/Berry Library
Hanover, NH 03755-3560

DSTO EDINBURGH
AU/33851-AP, PO Box 830470
Birmingham, AL 35283

SIMEON J. EARL – BAE SYSTEMS
W432A, Warton Aerodome
Preston, Lancs., UK PR4 1AX

ENERGY KEN LIBRARY
PO Box 300613
Jamaica, NY, 11430

ENGINEERING INFORMATION, INC
PO Box 543
Amsterdam, Netherlands 1000 Am

ETSE TELECOMUNICACION
Biblioteca, Campus Lagoas
Vigo, 36200 Spain

GA INSTITUTE OF TECHNOLOGY
EBS-Lib Mail code 0900
74 Cherry Street
Atlanta, GA 30332

TIMOTHY HOLZHEIMER
Raytheon
PO Box 1044
Rockwall, TX 75087

HRL LABS, RESEARCH LIBRARY
3011 Malibu Canyon
Malibu, CA 90265

IEE INSPEC
Michael Faraday House
6 Hills Way
Stevenage, Herts UK SG1 2AY

INSTITUTE FOR SCIENTIFIC INFO.
Publication Processing Dept.
3501 Market St.Philadelphia, PA
19104-3302

LIBRARY – DRDC OTTAWA
3701 Carling Avenue
Ottawa, Ontario, Canada K1A OZ4

LIBRARY of CONGRESS
Reg. Of Copyrights
Washington DC, 20559

LINDA HALL LIBRARY
5109 Cherry Street
Kansas City, MO 64110-2498

MISSOURI S&T
400 W 14th Street
Rolla, MO 56409

MIT LINCOLN LABORATORY
244 Wood Street
Lexington, MA 02420

NATIONAL CHI NAN UNIVERSITY
Lily Journal & Book Co, Ltd
20920 Glenbrook Drive
Walnut, CA 91789-3809

JOHN NORGARD
UCCS
20340 Pine Shadow Drive
Colorado Springs, CO 80908

OSAMA MOHAMMED
Florida International University
10555 W Flagler Street
Miami, FL 33174

NAVAL POSTGRADUATE SCHOOL
Attn:J. Rozdal/411 Dyer Rd./ Rm 111
Monterey, CA 93943-5101

NDL KAGAKU
C/0 KWE-ACCESS
PO Box 300613 (JFK A/P)
Jamaica, NY 11430-0613

OVIEDO LIBRARY
PO BOX 830679
Birmingham, AL 35283

DAVID PAULSEN
E3Compliance
1523 North Joe Wilson Road
Cedr Hill, TX 75104-1437

PENN STATE UNIVERSITY
126 Paterno Library
University Park, PA 16802-1808

DAVID J. PINION
1122 E Pike Street #1217
SEATTLE, WA 98122

KATHERINE SIAKAVARA
Gymnasiou 8
Thessaloniki, Greece 55236

SWETS INFORMATION SERVICES
160 Ninth Avenue, Suite A
Runnemede, NJ 08078

YUTAKA TANGE
Maizuru Natl College of Technology
Maizuru, Kyoto, Japan 625-8511

TIB & UNIV. BIB. HANNOVER
Welfengarten 1B
Hannover, Germany 30167

UEKAE
PO Box 830470
Birmingham, AL 35283

UNIV OF CENTRAL FLORIDA
4000 Central Florida Boulevard
Orlando, FL 32816-8005

UNIVERSITY OF COLORADO
1720 Pleasant Street, 184 UCB
Boulder, CO 80309-0184

UNIVERSITY OF KANSAS – WATSON
1425 Jayhawk Blvd 210S
Lawrence, KS 66045-7594

UNIVERSITY OF MISSISSIPPI
JD Williams Library
University, MS 38677-1848

UNIVERSITY LIBRARY/HKUST
Clear Water Bay Road
Kowloon, Honk Kong

CHUAN CHENG WANG
8F, No. 31, Lane 546
MingCheng 2nd Road, Zuoying Dist
Kaoshiung City, Taiwan 813

THOMAS WEILAND
TU Darmstadt
Schlossgartenstrasse 8
Darmstadt, Hessen, Germany 64289

STEVEN WEISS
US Army Research Lab
2800 Powder Mill Road
Adelphi, MD 20783

YOSHIHIDE YAMADA
NATIONAL DEFENSE ACADEMY
1-10-20 Hashirimizu
Yokosuka, Kanagawa,
Japan 239-8686